A photograph of a wind farm. In the foreground, a single wind turbine is visible, its blades angled upwards. In the background, another wind turbine stands in a field of green crops. A line of trees and some small buildings are visible further back.

Master of Science thesis

Prandtl tip loss factor assessed

S.F. Ramdin

Prandtl tip loss factor assessed

MASTER OF SCIENCE THESIS

For obtaining the degree of Master of Science in Aerospace
Engineering at Delft University of Technology

S.F. Ramdin

January 31th, 2017



Copyright © S.F. Ramdin
All rights reserved.

DELFT UNIVERSITY OF TECHNOLOGY
DEPARTMENT OF
AERODYNAMICS, WIND ENERGY, FLIGHT PERFORMANCE AND PROPULSION

The undersigned hereby certify that they have read and recommend to the Faculty of Aerospace Engineering for acceptance a thesis entitled "**“Prandtl tip loss factor assessed”**" by **S.F. Ramdin** in partial fulfillment of the requirements for the degree of **Master of Science**.

Dated: January 31th, 2017

Head of department: _____
dr.ir. B.W. van Oudheusden

Supervisor: _____
dr.ir. A.H. van Zuijlen

Reader: _____
dr. ir. J.G. Schepers

Reader: _____
dr. ir. C.J. Simao Ferreira

Summary

The Blade Element Momentum theory (BEM) is widely used for the design of wind turbine blades and predicting aerodynamic loads because of its ability to compute fast and reasonable results. The downside is that there is a need for correction factors in order to improve the results due to numerous simplifications in BEM. In this thesis the Prandtl tip loss factor, that serves as a correction for the assumption of infinite number of blades in BEM, is assessed on its performance.

It is discussed that four parameters in the derivation of the Prandtl tip loss factor can be evaluated in multiple ways, resulting in 72 Prandtl tip loss factor variations. These four parameters are defined as the radius r_2 related to the distance between the helical wake sheets, the radius r_3 related to the tangential velocity component, the axial induction factor a and the tangential induction factor a' .

The Prandtl tip loss factors are compared to analogous tip loss factors from CFD and vortex method results. To obtain the CFD tip loss factor this thesis discusses three methods to extract the induced velocities from the CFD computations, however for each method there exists multiple limitations. The method that subtracts the upwash from the flow by modelling the blades as bound vortex lines is accepted because it performs more consistent, conform expectations and it is verified with results from the University of Stuttgart.

ECN's free wake lifting line method AWSM code is used to retrieve a vortex method tip loss factor. This code is first validated with measurements from the NewMexico experiment. This validation shows that the results of the code are remarkably close to the experiment. To be able to retrieve a tip loss factor in high resolution, limitations of the code are identified and overcome.

The assessment of the tip loss factors is done for five rotors at a wide-range of operational conditions. The sensitivity study shows that the performance of the Prandtl tip loss factors are dependent on the tip speed ratio. The lack of accounting for the radial movement of the flow is identified as a possible reason of less accurate results near the tip of the blade. Furthermore, four Prandtl tip loss factors are recognized as the best performing tip loss factors. These have in common that r_2 and a are evaluated locally, instead of at the tip or taking the averaged value. The dependency on the choice of r_3 and a' is negligible for the four best Prandtl tip loss factors.

This thesis identifies the limitations of the current Prandtl tip loss factor and provides possible solutions to improve the accuracy of the Prandtl tip loss factor and consequently the BEM implementation. The study therefore contributes to more efficient wind turbines and better load predictions.

Acknowledgements

In this chapter, I would like to address that this thesis would not be successful without the help of my supervisors and others.

The weekly meetings with Gerard Schepers (ECN) have been of immense importance for this thesis and myself. With his knowledge, care and patience on personal and work-related level, I am grateful that I had the privilege to have Gerard as my supervisor. In the same breath I would also like to thank Koen Boorsma (ECN), because his guidance and enthusiasm proved to be of great help during my thesis study. The third individual person I would like thank is Sander van Zuijlen (TU Delft) from who I was able to receive advice in the process of the thesis.

Furthermore, my time at ECN would not have been so enjoyable without all the interns and employees with who I shared lunches, dinners and multiple other activities outsides the work environment for which I am thankful for.

Lastly, I have to thank my family and friends back home. Although I was largely separated from them during these last months, they made sure I had to relax and enjoy life outside of the thesis life. I am looking forward to start with a new adventure with you by my side!

Delft, The Netherlands
January 31th, 2017

S.F. Ramdin

Contents

Summary	vi
Acknowledgements	ix
List of Figures	xix
List of Tables	xxi
Acronyms	xxv
List of Symbols	xxvii
1 Introduction	1
1.1 Motivation	1
1.2 Objective	3
1.3 Methodology	4
1.4 Outline	5
2 Aerodynamics models	7
2.1 CFD	7
2.2 Vortex methods	8
2.3 BEM	11
3 Prandtl tip loss factor	19
3.1 Derivation	19
3.2 Variations	27
3.3 Results in literature	30

4 Computational Setup	35
4.1 Rotors	35
4.2 CFD	38
4.2.1 Description	38
4.2.2 Determination of the angle of attack	38
4.2.3 Tip loss factor	41
4.3 Vortex method	42
4.3.1 Description	42
4.3.2 Validation	43
4.3.3 Tip loss factor	43
4.4 BEM	44
4.4.1 Description	44
4.4.2 Tip loss factor	44
4.5 Sensitivity study	45
5 Results	49
5.1 CFD	49
5.1.1 Determination of the angle of attack	49
5.1.2 Tip loss factor	59
5.2 Vortex method	62
5.2.1 Validation	62
5.2.2 Tip loss factor	69
5.3 Simplified rotor	78
5.3.1 Variations of Prandtl tip loss factor	78
5.3.2 Sensitivity study	83
5.4 Real rotors	96
5.4.1 Per rotor	96
5.4.2 General trends	106
6 Conclusion and recommendations	113
6.1 Conclusion	113
6.2 Recommendations	115
References	117
A Additional explanations and results of determining the angle of attack from CFD	121
A.1 Post-processing	121
A.2 UVL method	122
A.3 UDV method	125
A.4 Remaining results	128
A.4.1 Monitor point location dependency	128
A.4.2 Spanwise dependency	128
A.4.3 Tip loss factor	128

B Remaining vortex method validation results	143
B.1 Axial traverse	143
B.2 Radial traverse	143
B.3 Azimuthal traverse	143

List of Figures

1.1	Growth of wind power installations in the EU	2
2.1	Bound, trailing and shed vortices	9
2.2	A vortex filament for which the Biot-Savart law holds	9
2.3	One-dimensional flow across an actuator disk, resulting in a streamtube .	12
2.4	Velocity triangle for a blade section	14
3.1	The simplified helical wake structure for a three-bladed rotor with a finite number of blades	20
3.2	Curving of the flow around the helical disks	20
3.3	The Joukowski transform shown for a unit circle and circle with an offset to the origin resulting in a flat plate and an airfoil, respectively	22
3.4	Visualization of the helical wake sheets, the angle between helical wake sheets ϵ_w , the screw pitch h and distance between two helical wake sheets d	26
3.5	Normal forces for the NREL experimental rotor compared to the computed results of Blade Element Momentum theory (BEM) with different tip loss factors at different wind speeds	32
3.6	Bar chart of the relative differences of annual energy production for 8 tip loss factors	33
4.1	The twist angle and the chord distributions for the Mexico, AVATAR, Innwind, NREL Phase VI and NewBlade rotors	36
4.2	The variation of the axial induction factor and azimuthal averaged axial induction factor for an optimum rotor operating at its design tip speed ratio	41
5.1	The axial induction factor and inflow angle results from the two inverse BEM method for the AVATAR rotor at 6 m/s	50
5.2	The axial induction factor and inflow angle results from the two inverse BEM method for the Innwind rotor at 6 m/s	51
5.3	The axial induction factor and inflow angle results from the two inverse BEM method for the NREL Phase VI rotor at 15 m/s	52

5.4	The AVATAR rotor plane showing the locations of the monitor points used in the upwash methods	53
5.5	The dependency of the positioning of the monitor points on the number of sections N for the upwash methods	53
5.6	The axial induced velocity u_{ind} (top) and inflow angle ϕ (bottom) results from UVL (left) and UDV (right) for the AVATAR rotor at 6 m/s	55
5.7	The results from UVL minus the results from UDV for the AVATAR rotor at 6 m/s	57
5.8	The results from all four methods to extract the angle of attack α from the CFD results for the AVATAR rotor at 6 m/s, shown for two monitor point positions	58
5.9	The results from all four methods to extract the angle of attack α from the CFD results for the Innwind rotor at 9 m/s, shown for two monitor point positions	60
5.10	Three methods to estimate the axial induction factor a along the blade span from the CFD results for the AVATAR rotor at 6 m/s	61
5.11	The computed axial induction factor a , azimuthal averaged axial induction factor \bar{a} and tip loss factor F extracted from the UVL method for the AVATAR rotor at 6 m/s	63
5.12	Load distributions from New Mexico experiment, BEM and AWSM	66
5.13	Axial force F_{ax} and torque Q from New Mexico experiment, BEM and AWSM	67
5.14	Inboard and outboard axial traverse for 15 m/s	68
5.15	Upstream and downstream radial traverse for 15 m/s	70
5.16	Azimuthal traverse for 15 m/s at sections $r = 82\%R$ and $92\%R$	71
5.17	Calculation of the azimuthal averaged axial induction factor \bar{a} with the rotor plane and 9 o'clock method for the Mexico rotor at 15 m/s	73
5.18	Results of the axial induction factor a obtained from the external field module with default settings for LCO and WCO for the Mexico rotor at 15 m/s	74
5.19	Effect of varying the setting for the from 0.05 to 0.95 in 18 steps	75
5.20	Effect of varying the setting for the from 0.01 to 0.996 in 18 steps	76
5.21	The azimuthal averaged axial induction factor \bar{a} and axial induction factor a plotted for the Mexico rotor at 15 m/s obtained from the 9 o'clock method and increasing the discretization of the blade using interpolation, respectively	77
5.22	The AWSM tip loss factor F_{AWSM} for the Mexico rotor at 15 m/s, calculated with the results from figure 5.21	77
5.23	The azimuthal averaged axial induction factor \bar{a} , axial induction factor a and circulation Γ for the NewBlade rotor at 8 m/s and 534.761 rpm, with pitch angle θ set to 0°	79
5.24	The effect of the number of sections N on the AWSM tip loss factor	82
5.25	The 72 Prandtl tip loss factors shown for the NewBlade rotor at design conditions	82
5.26	The AWSM tip loss factor and a variety of Prandtl tip loss factor, after the code checks which tip loss factors show similar results	83
5.27	The AWSM tip loss factor, the rotor's best tip loss factor (F_{30}) and the ECN tip loss factor (F_{71})	84

5.28	The azimuthal averaged axial induction factor \bar{a} and circulation Γ for 5 pitch angles θ between -3° to 8°	85
5.29	The AWSM and a variety of Prandtl tip loss factors for 5 pitch angles θ between -3° to 8°	86
5.30	The AWSM tip loss factors for 5 pitch angles θ between -3° to 8° showing the slight lowering of the values	87
5.31	The AWSM, the rotor's best (F_{30}) and the ECN (F_{71}) tip loss factor for 5 pitch angles θ between -3° to 8°	88
5.32	The azimuthal averaged axial induction factor \bar{a} and circulation Γ for 4 settings of the wind velocity V_∞ resulting in different tip speed ratios	89
5.33	The AWSM tip loss factors 4 wind velocity V_∞ and thus 4 tip speed ratios	91
5.34	The AWSM, the rotor's best (F_{30}) and the ECN (F_{71}) tip loss factor for the 4 wind velocities V_∞ settings	92
5.35	The results for the azimuthal averaged axial induction factor \bar{a} and circulation Γ , by multiplying the rotational velocity Ω and wind velocity V_∞ with the same factor, resulting in an unchanged tip speed ratio λ	93
5.36	The AWSM tip loss factor, the rotor's best (F_{30}) and the ECN (F_{71}) tip loss factor after multiplying the rotational velocity Ω and wind velocity V_∞ with the same factor, resulting in an unchanged tip speed ratio λ	94
5.37	The wake development downstream the blade computed by AWSM	95
5.38	The azimuthal averaged axial induction factor \bar{a} and circulation Γ with equipping the NewBlade rotor with 2, 3 and 4 blades	95
5.39	The AWSM tips loss factor and a variety of the Prandtl tip loss factors for the NewBlade rotor with 2, 3 and 4 blades	97
5.40	The AWSM tip loss factor, the rotor's best (F_{30}) and the ECN (F_{71}) tip loss factor for the rotor with 2, 3 and 4 blades	98
5.41	The results for the azimuthal averaged axial induction factor \bar{a} and circulation Γ for the Mexico rotor at 4 conditions	99
5.42	This figures shows for the Mexico rotor, the angle of attack α when the wind velocity $V_\infty = 10 \text{ m/s}$ and the lift polars for the three airfoils which are used in the blade design	100
5.43	The AWSM tip loss factor versus the rotor's best (F_{22}), overall best (F_{13}) and the ECN (F_{71}) Prandtl tip loss factors for the Mexico rotor at 4 different operational conditions	101
5.44	The azimuthal averaged axial induction factor \bar{a} and circulation Γ for the AVATAR rotor at 4 different operational conditions	102
5.45	The AWSM tip loss factor versus the CFD tip loss factor, rotor's best (F_6), overall best (F_{13}) and the ECN (F_{71}) Prandtl tip loss factors for the AVATAR rotor at 4 different operational conditions	103
5.46	The azimuthal averaged axial induction factor \bar{a} and circulation Γ for the Innwind rotor at 5 different operational conditions	104
5.47	The AWSM tip loss factor versus the CFD tip loss factor, rotor's best (F_6), overall best (F_{13}) and the ECN (F_{71}) Prandtl tip loss factors for the Innwind rotor at 5 different operational conditions	105
5.48	The azimuthal averaged axial induction factor \bar{a} and circulation Γ for the NREL Phase VI rotor at 3 operational conditions	106

5.49	The AWSM tip loss factor versus the rotor's best (F_{24}), overall best (F_{13}) and the ECN (F_{71}) Prandtl tip loss factors for the NREL rotor at 3 different operational conditions	107
5.50	The differences of the overall best tip loss factor (F_{13}) and the ECN (F_{71}) tip loss factor compared to the AWSM tip loss factor measured at three radial positions	108
5.51	The differences of the overall best tip loss factor (F_{13}) and the ECN tip loss factor (F_{71}) compared to the AWSM tip loss factor measured at three radial positions, with the modified AWSM code in where the radial velocity V_z is fixed to zero	110
5.52	The averaged differences of the 72 Prandtl tip loss factor compared to the AWSM tip loss factor considering all simulations done in this thesis	111
A.1	The two types of slices in Tecplot used to reduce the CFD data set	122
A.2	The axial induced velocity u_{ind} (top) and inflow angle ϕ (bottom) results from UVL (left) and UDV (right) for the AVATAR rotor at 9 m/s	129
A.3	The axial induced velocity u_{ind} (top) and inflow angle ϕ (bottom) results from UVL (left) and UDV (right) for the Innwind rotor at 6 m/s	130
A.4	The axial induced velocity u_{ind} (top) and inflow angle ϕ (bottom) results from UVL (left) and UDV (right) for the Innwind rotor at 9 m/s	131
A.5	The axial induced velocity u_{ind} (top) and inflow angle ϕ (bottom) results from UVL (left) and UDV (right) for the NREL Phase VI rotor at 7 m/s .	132
A.6	The axial induced velocity u_{ind} (top) and inflow angle ϕ (bottom) results from UVL (left) and UDV (right) for the NREL Phase VI rotor at 15 m/s	133
A.7	The results from all four methods to extract the angle of attack α from the CFD results for the AVATAR rotor at 9 m/s, shown for two monitor point positions	134
A.8	The results from all four methods to extract the angle of attack α from the CFD results for the Innwind rotor at 6 m/s, shown for two monitor point positions	135
A.9	The results from all four methods to extract the angle of attack α from the CFD results for the NREL Phase VI rotor at 7 m/s, shown for two monitor point positions	136
A.10	The results from all four methods to extract the angle of attack α from the CFD results for the NREL Phase VI rotor at 15 m/s, shown for two monitor point positions	137
A.11	The computed axial induction factor a , azimuthal averaged axial induction factor \bar{a} and tip loss factor F extracted from the UVL method for the AVATAR rotor at 9 m/s	138
A.12	The computed axial induction factor a , azimuthal averaged axial induction factor \bar{a} and tip loss factor F extracted from the UVL method for the Innwind rotor at 6 m/s	139
A.13	The computed axial induction factor a , azimuthal averaged axial induction factor \bar{a} and tip loss factor F extracted from the UVL method for the Innwind rotor at 9 m/s	140
A.14	The computed axial induction factor a , azimuthal averaged axial induction factor \bar{a} and tip loss factor F extracted from the UVL method for the NREL Phase VI rotor at 7 m/s	141

B.1	Inboard and outboard axial traverse for 10 m/s	144
B.2	Inboard and outboard axial traverse for 24 m/s	145
B.3	Upstream and downstream radial traverse for 10 m/s	146
B.4	Upstream and downstream radial traverse for 24 m/s	147
B.5	Azimuthal traverse for 10 m/s at sections $r = 82\%R$ and $92\%R$	148
B.6	Azimuthal traverse for 24 m/s at sections $r = 82\%R$ and $92\%R$	149

List of Tables

3.1	Overview of literature that discusses tip loss factors	34
4.1	General design data and operational conditions for the Mexico, AVATAR, Innwind, NREL Phase VI and NewBlade rotors	37
4.2	Operational conditions of the used CFD results.	38
4.3	Overview of operational conditions for which the NewBlade rotor is subjected to	47
5.1	Accepted number of sections N for the AVATAR, Innwind and NREL Phase VI rotors for the upwash methods	54
5.2	Comparison of calculating three Prandtl tip loss factor inside the iterative loop or afterwards with the ECN BEM code and a self-made BEM code .	79
5.3	The settings for the r_2 , a , r_3 and a' resulting into the 72 Prandtl tip loss factors	81
5.4	Per rotor the best Prandtl tip loss factor and the overall best tip loss factor	109
5.5	The parameter settings for the best performing Prandtl tip loss factors, which show identical results	112

Acronyms

AAT Average Azimuthal Technique.

AVATAR AdVanced Aerodynamic Tools for lArge Rotors EU project.

AWSM Aerodynamic Windturbine Simulation Module.

BEM Blade Element Momentum theory.

CFD Computational Fluid Dynamics.

DNS Direct Numerical Simulation.

DTU Technical University of Denmark.

ECN Energy research Center of the Netherlands.

ECN Aero-Module ECN's in-house aerodynamic simulation software containing the BEM and AWSM models.

EERA European Energy Research Alliance.

Ellipsys3D Incompressible RANS CFD solver 'Ellipsys3D'.

ForWind Joint center of wind energy research in Oldenburg.

Innwind Innovative (10-20MW) offshore rotor EU project.

LES Large Eddy Simulation.

Mexico Model EXperiments In Controlled Conditions rotor.

Mexnext International Energy Agency (IEA) Wind Task 29 Mexnext project.

New Mexico New Model EXperiments In Controlled Conditions.

NREL National Renewable Energy Laboratory.

OpenFOAM Open source Field Operation And Manipulation - a CFD solver.

PIV Particle Image Velocimetry.

RANS Reynolds-Averaged Navier-Stokes.

TU Delft University of Technology Delft.

UDV Upwash from Distributed Vorticity.

UVL Upwash from bound Vortex Line.

List of Symbols

Alphanumeric

a	axial induction factor	-
A	cross-sectional area	m^2
a'	angular induction factor	-
\bar{a}	azimuthal averaged axial induction factor	-
c	chord	m
C	curve	m
C_d	drag coefficient	-
C_l	lift coefficient	-
C_{l_0}	zero angle of attack lift coefficient	-
C_n	normal force coefficient	-
C_t	tangential force coefficient	-
d	distance between two helical wake sheets	m
D	drag force	N
e_n	normal unit vector	-
e_r	radial unit vector	-
e_t	tangential unit vector	-
F	tip loss factor	
F_{ax}	axial force	N
F_n	normal force	N/m
F_t	tangential force	N/m
h	screw pitch	m
L	lift force	N
LCO	lifting line cut-off radius	-
\dot{m}	mass flow rate	kg/s
N	number of sections	-
N_b	number of blades	-
p	pressure	N/m^2

Q	torque	$\text{N} \cdot \text{m}$
r	radial position	m
R	blade radius	m
Re	Reynolds number	-
R_m	rotation matrix	-
s	boundary of a closed domain	-
S	surface	m^2
t	time	s
T	thrust	N
U	one-dimensional velocity	m/s
u_{ind}	axial induced velocity	m/s
\mathbf{V}	velocity vector	m/s
V_∞	wind velocity	m/s
V_{rel}	relative velocity	m/s
V_θ	azimuthal velocity	m/s
V_x	axial velocity	m/s
V_y	tangential velocity	m/s
V_z	radial velocity	m/s
WCO	wake cut-off radius	-

Greek letters

α	angle of attack	°
β	local blade angle (pitch angle + twist angle)	°
ϵ	twist angle	°
ϵ_w	angle between helical wake sheets	°
γ	yaw angle	°
Γ	circulation	m/s
λ	tip speed ratio	-
μ	viscosity	$\text{kg}/(\text{m} \cdot \text{s})$
Ω	rotational velocity	rad/s
ϕ	inflow angle	°
ϕ_{vp}	velocity potential	m^2/s
ψ	azimuth angle	°
ψ_{sf}	stream function	m^2/s
ρ	density	kg/m^3
σ	solidity	-
θ	pitch angle	°
ξ	vorticity	1/s

Subscripts

ax	axial value	-
d	disc value	-
w	wake value	-
rel	relative value	-
n	normal	-

t	tangential	-
max	maximum value	-
∞	free stream value	-

Chapter 1

Introduction

In this thesis the Prandtl tip loss factor, that serves as a correction for the assumption of infinite number of blades in Blade Element Momentum theory (BEM), will be assessed on its performance. This introduction will first explain the motivation of the research, followed by the objectives in the second section. The third section will briefly sketch the methodology and the final section will describe the structure of the report.

1.1 Motivation

Wind energy has evolved into a significant part of the European energy mix over the last years. Figure 1.1 shows the growth of the wind power installations in the EU. For the next 15 years several scenarios expect that the amount of installed capacity will at least double compared to 2014, covering almost 25 % of the electricity demand in the EU (see European Wind Energy Association (2015)). To achieve this, more and larger wind turbines will be designed.

The design of wind turbine blades is performed by an iterative process with the use of BEM. This is a relative simple theory that allows for relatively accurate load predictions without the use of extensive computational power. It should be considered that to assess the loading for the entire 20 years lifetime of a wind turbine, up to 7.2 million¹ aerodynamic computations have to be done, as stated by Schepers (2012). The computation time of aerodynamic methods for wind energy purposes is therefore critical. BEM has proven to be the most efficient in the design process with the current and expected computer capacity.

The downside is that because BEM consists of multiple simplifications, there is a need for correction factors in order to improve the results. In this thesis the focus will be on the tip loss factor, which corrects the simplification that the wind turbine consists

¹Schepers (2012, p. 5): "based on 120 time series (i.e. 6 realizations at 20 wind speeds) of 10 minutes and a time step of 0.01 seconds."

FIGURE 1.2: CUMULATIVE WIND POWER INSTALLATIONS IN THE EU (GW)

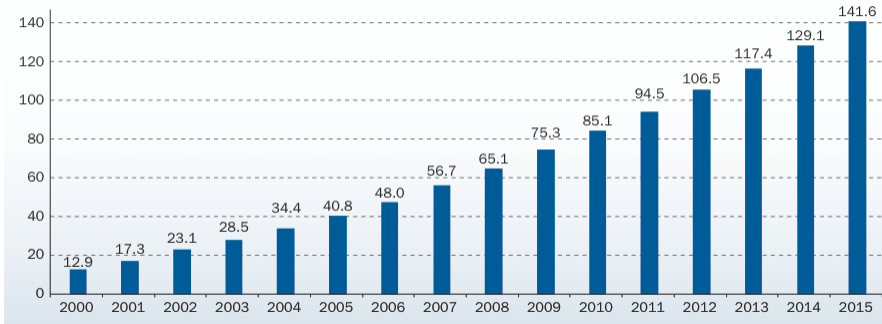


Figure 1.1: The cumulative wind power installations in the EU expressed in GW, visualizing the growth of wind energy over the last 15 years (European Wind Energy Association, 2016, figure 12).

of an infinite number of blades. The accuracy of the loading at the tip of the blades is strongly affected due to this simplification. However comparisons of several tip loss factors show deviating results up to $\pm 5\%$ of the annual energy production for a 10.06 m diameter rotor (Branlard, Dixon, and Gaunaa (2013)), indicating disagreement between the tip loss factors.

From the first derivation done by Prandtl (1921), there have been many attempts to improve the tip loss factor (the latest published by Maniaci and Schmitz (2016)). These are mostly variations on the Prandtl tip loss factor. Though, at least an equal amount of articles can be found that show that the current tip loss factors still suffer from over-predicting the loads at the tips, or, when the results are acceptable, it is due to that the conditions closely resemble the conditions for which the tip loss factors are calibrated.

Advanced numerical methods, such as CFD (Computational Fluid Dynamics (CFD)) and vortex methods, show possibilities to investigate the flow field at the blades in higher detail. This thesis will show that these methods can also be used to investigate the performance of the tip loss factor, although new hurdles must be faced. One of the main hurdles is that CFD theory does not explicitly value the induced velocities, as other methods do. Furthermore, concerning the tip loss factor, most literature only test one to a few tip loss factors applied to two rotors operating at a small amount of different conditions. A broad perspective of possible improvements that holds universally is therefore missing.

1.2 Objective

Section 1.1 motivates to carry out the current thesis, which has the higher purpose to improve the Prandtl tip loss factor. However, to be able to enhance the accuracy of the Prandtl tip loss factor, it should be known first to what extent the Prandtl tip loss factor is correct and to what extent it is not. This leads to the following objective for the thesis:

To identify the limitations of the Prandtl tip loss factor by assessing the Prandtl tip loss factor for a variety of conditions and rotors and by comparing the results to higher fidelity modelling techniques, such as CFD and vortex methods.

To support the objective, several sub-objectives can be formulated:

1. *Retrieve a tip loss factor from CFD that is apparent to the Prandtl tip loss factor.*
In order to do so, the induced velocities should be recovered from the CFD results. This is done by translating the CFD variables to engineering variables. This should enable comparisons of CFD results with results from the other methods, which can intrinsically value the induction of the rotor. When this is achieved, a definition should be created to value the non-uniformities of the flow.
2. *Retrieve a tip loss factor from a vortex method code that is apparent to the Prandtl tip loss factor.*
Firstly, the validation of the vortex method code is done by using experimental results. Secondly, the definition of the amount of non-uniform flow from the previous sub-objective can be used to create the tip loss factor, where the extraction of the induced velocities from vortex methods is far more easy.
3. *Analyse the results of all the variations of the Prandtl tip loss factor for multiple conditions.*
From the derivation of the Prandtl tip loss factor it will be shown that there are 72 Prandtl tip loss factor variations possible. It is evident that these variations will lead to different results. An analysis of these results is necessary in order to be able to validate the Prandtl tip loss factor.
4. *Compare the tip loss factors from Prandtl, the vortex method and CFD for multiple rotors to map trends and differences.*
This will identify the needed improvements of the Prandtl tip loss factor in a more broader sense than what is done until now.

The added value of this thesis will be that, when the objective is accomplished, it will provide a clear picture on how the performance of the Prandtl tip loss factor can be compared to higher fidelity methods, what the effect is of the variations of the Prandtl tip loss factor and if there are certain conditions or variables that show similar or deviating results for multiple rotors. Therefore, this thesis will help improving the prediction of tip loads by using a corrected tip loss factor in BEM and thus lead to more effective and (cost) efficient wind turbine designs.

1.3 Methodology

This research is conducted in collaboration with Energy research Center of the Netherlands (ECN). ECN provides the numerical tools and results but also knowledge from other projects. In the in-house developed ECN Aero-Module code (see Boorsma, Grasso, and Holierhoek (2011); Boorsma, Hartvelt, and Orsi (2016) for more details) a BEM solver and free wake lifting line vortex code are incorporated. The power of this combination is that the same input files are used for the two numerical methods, minimizing the possibility of errors. The free wake lifting line vortex code is named as Aerodynamic Windturbine Simulation Module (AWSM) (Van Garrel (2003)).

This AWSM code will be validated with the measurements from the New Model EXperiments In Controlled Conditions (New Mexico) project (for more details on this project see Boorsma and Schepers (2014) and Boorsma et al. (2016)). This analysis is done within the International Energy Agency (IEA) Wind Task 29 Mexnext project (Mexnext), described by Schepers et al. (2012, 2014). The objective of this project is to investigate multiple wind aerodynamic phenomena. As a result of an earlier phase where experiments on the Model EXperiments In Controlled Conditions rotor (Mexico) were carried out, new measurements were done on the same rotor, with improvements on the experimental set-up. These improved measurements are annotated by New Mexico.

From the AWSM simulations a tip loss factor will be calculated and compared to the many variations of the Prandtl tip loss factor used in BEM. Multiple rotor data is available at ECN, enabling to perform an extensive analyse using AWSM and BEM. Furthermore, the operation conditions can be easily adjusted, which is also helpful in the assessment of the Prandtl tip loss factor.

For the use of CFD data, results are available from the AdVanced Aerodynamic Tools for lArge Rotors EU project (AVATAR) (Schepers et al. (2015)). In this project an European Energy Research Alliance (EERA) consortium of 11 research institutes and 2 industry partners work together to analyse the aerodynamics of large (10 MW+) wind turbines. The two rotors that will be used in this thesis are called the AVATAR and Innwind rotor. The CFD calculations are done with Incompressible RANS CFD solver 'Ellipsys3D' (Ellipsys3D) (described by Ivanell, Mikkelsen, Sørensen, and Henningson (2008)). The extraction of the engineering variables such as angle of attack, axial induction factor and inflow angle fall under the 'lifting line benchmark' defined in Work Package (WP) 2 Task 2.1 - 3D Rotor Aerodynamics. Due to the availability of CFD results for the NREL Phase VI rotor (this rotor is described by Hand et al. (2001)), these are also used in this benchmark.

The CFD flow field calculations allow to visualize the non-uniform flow due to the finite number of blades in high detail. However, for this thesis the objective is to investigate the validity of the Prandtl tip loss factor. The CFD results are therefore only used to serve this objective. A first hurdle is the extraction of engineering variables in order to form an equivalent tip loss factor from CFD. Several methods for translating the CFD variables to engineering variables will be discussed. One method will be accepted such that the scope will return on the tip loss factor.

From this methodology, it is clear that some side-steps are needed to be able to achieve the objective, however this will strengthen the assessment of the Prandtl tip loss factor.

1.4 Outline

This report is structured into six chapters. Chapter 1 illustrates the motivations, objectives and methodology of the thesis. To be able to understand the different aerodynamic models, chapter 2 gives a description on CFD, vortex methods and BEM. The strong and weak points of each model are discussed with respect to each other. The full derivation, variations and results in literature of the Prandtl tip loss factor will be shown in chapter 3. In the fourth chapter the computational setup is explained. This concerns which rotors are used and in which operational conditions but also how the results of the aerodynamic models are used. Chapter 5 will show the results in the order of sub-objectives given in section 1.2. Finally, the conclusions of this thesis and recommendations for further research are given in chapter 6.

Chapter 2

Aerodynamics models

Three groups of aerodynamic models can be distinguished that differ in conceptual background, complexity and accuracy. This chapter will start with the description of the highest fidelity model CFD, the vortex method as the second highest fidelity model one and finally the most simple model BEM.

2.1 CFD

Computational Fluid Dynamics (CFD) is the family name comprising the numerical methods to solve the Navier-Stokes equations. The equations describe in essence the conservation of mass, conservation of momentum and the conservation of energy. These three fundamental physical laws state, in respective order, that

1. mass can not be created or destroyed but only can rearrange,
2. the forces exerted on an element always equal the mass times the acceleration of the element (Newton's second law), and
3. energy can not be created or destroyed but only can change in form.

Multiple forms of the equations exist due to different perspectives, simplifications and assumptions. In wind turbine aerodynamics the assumption of incompressible flow can be made as the total flow velocity regime is assumed to be lower than a third of the speed of sound. This leads to the simplification that only the conservation of mass and conservation of momentum, given in equations (2.1) and (2.2) respectively, are needed to solve for the unknown variables pressure p and velocity vector \mathbf{V} .

$$\nabla \cdot \mathbf{V} = 0 \tag{2.1}$$

$$\rho \left(\frac{\partial \mathbf{V}}{\partial t} + \mathbf{V} \cdot \nabla \mathbf{V} \right) = -\nabla p + \mu \nabla^2 \mathbf{V} \quad (2.2)$$

In these equations ρ is the constant density, time t , and viscosity μ . Also it should be noted that body forces (such as gravity) are neglected. Equations (2.1) and (2.2) hold for three-dimensional steady or unsteady, viscous or inviscid, incompressible flow. For performing the calculations the flow field is discretized into points, where connecting lines form the grid or mesh. The flow properties are only calculated at these grid points. A closed-form analytical solution (input can be a random point) to the Navier-Stokes equations is stated as one of the seven millennium prize problem (Clay Mathematics Institute (2016)), indicating the difficulty of solving the equations without making simplifications.

There are in general three levels of fidelity concerning CFD, namely Direct Numerical Simulation (DNS), Large Eddy Simulation (LES) and Reynolds-Averaged Navier-Stokes (RANS). In short, it can be said that the three differ in which level the turbulence is calculated and/or modelled. DNS resolves the smallest scale of turbulence, for LES the smaller scales are modelled and for RANS only the mean is captured, although it is known that turbulence consists of large fluctuations. To overcome this, several turbulence models exist to model the turbulence fluctuations and can be divided into algebraic models and turbulence energy equation models.

For wind energy aerodynamics RANS models are used as they offer the lowest computational price with the ability to resolve the flow field physically in very high detail compared to the engineering methods such as BEM and vortex methods. CFD can be coupled with engineering methods to specifically focus the CFD computations on the wake dynamics and use the engineering methods to perform the blade loading calculations, as for example described by Ivanell et al. (2008).

To be better able to compare the value of the three aerodynamic models, it is emphasized that because CFD solves the flow field from the physical point of view, aerodynamic effects due to the rotation of the blades, stall at the blades and other highly three-dimensional flow effects are solved intrinsically, without the need of knowledge on for example the airfoils used along the blades. It will be shown that this is the biggest advantage of CFD compared to vortex methods and BEM, which are methods based on the engineering point of view.

2.2 Vortex methods

By further simplifying the flow to an incompressible, inviscid and irrotational flow, vortex methods can be established. These methods are able to approximate the aerodynamic properties of a blade by modelling the blade as for example a lifting line (other possibilities are discussed later). This lifting line can be seen as a bound vortex with strength Γ . Confined to Helmholtz vortex theorem - stating that 1) along a vortex filament, which is a line of strength Γ , the strength is constant and that 2) this vortex filament must form a closed path or extend to the boundaries of the flow - the bound vortex must continue with two trailing vortices downstream from the end of the blades closed by an shed vortex. Figure 2.1 shows this for three sections at the fourth time step and visualizing the development of the wake.

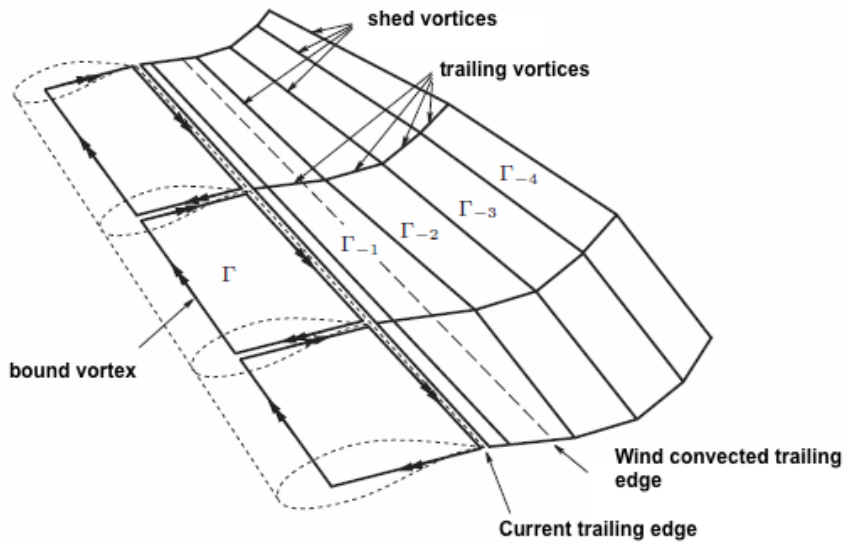


Figure 2.1: Defining the terminology for the bound, trailing and shed vortices (Van Garrel, 2003, figure 9 modified). The dashed lines indicate the three blade sections.

Each blade and wake section influences each other, which can be calculated with the Biot-Savart law. This law is applicable for incompressible inviscid flow and relates the strength Γ of each vortex to induced velocities at the point of interest due to this vortex. The equation (2.3) gives the relation.

$$d\mathbf{V} = \frac{\Gamma}{4\pi} \int_{-\infty}^{+\infty} \frac{dl \times r}{|r|^3} \quad (2.3)$$

In this universal form, dl is the segment and r is the distance vector from the point of interest to the segment, visualized by figure 2.2. This point of interest can be anywhere in the flow field.

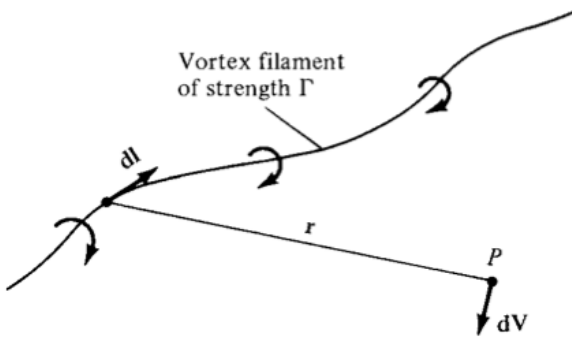


Figure 2.2: Visualization of the vortex filament with strength Γ , the segment dl and the distance vector r to a point of interest P (Anderson, 2011, figure 5.8).

The vortex strength (or circulation) Γ is however not known. Fortunately, Kelvin's theorem states that the rate of change of the total circulation in a flow is zero, or in other

words saying that the total circulation stays constant in the flow field. Therefore, a distribution of Γ is first assumed and by an iterative algorithm, which is given next, the real values are solved.

1. Assume a distribution of vortex strength Γ_j along the discretized blade.
2. Obtain the total onset velocity at all control points located in each section by the summation of the induced velocity (calculated by equation (2.3)), the wind velocity and the distance that the control points have travelled divided by the time step.
3. Calculate the angle of attack α , which is defined as the angle between the chord c and relative velocity V_{rel} , with the components of the total onset velocity.
4. Determine the lift coefficient C_l corresponding to this angle of attack α from airfoil data and calculate the circulation Γ_{C_l} by rewriting the Kutta-Joukowski equation, given in equation (2.4), that relates the lift force to the circulation for a two-dimensional section with chord c .

$$L = \rho \Gamma V_\infty c \quad (2.4)$$

5. Add the difference between Γ_j and Γ_{C_l} to Γ_j , with underrelaxation factor k , such that:

$$\Gamma_j = \Gamma_j + k(\Gamma_j - \Gamma_{C_l}) \quad (2.5)$$

6. Go back to the first step if no convergence is reached for Γ_j . If there is convergence the pressure differences are obtained from the Bernoulli equation, which is valid for inviscid incompressible flow, given in equation (2.6). As discussed in section 2.1 the velocity field and pressure are the two only physical unknown quantities for an incompressible flow and therefore all other flow properties can be calculated from the circulation Γ .

$$p + \frac{1}{2} \rho V^2 = \text{constant} \quad (2.6)$$

It should be stressed that airfoil data is used and thus the quality of the result is dependent on the quality of the airfoil data. Also, wake effects such as expansion, distortion and tip vortex roll-up can be modelled, if the wake is free to induce on its own (free wake) instead of that the wake is modelled as a fixed structure (prescribed wake). Next to this, the discretization of the blade as a lifting line is only one method. A better representation is considering the blade as multiple lifting surfaces, achieved by dividing the blade into sections in spanwise direction. Further discretizing these sections in chordwise direction leads to the panel method, which also accounts for the thickness of the section. Furthermore, as already mentioned in the previous section, a hybrid setup of vortex methods and CFD can improve the accuracy of (especially wake) results.

From this section it should be clear that vortex methods can only be used for certain flow regimes. The accuracy of the solutions at the blade depend on which vortex method is used and how the airfoil data is obtained. Because CFD solves the flow equations without exactly knowing of the existence of the airfoil (the airfoil is 'replaced' by boundary

conditions), it can calculate the velocities and forces at the blade without the need for airfoil data.

Though, there are several strong points of vortex methods. First of all, vortex methods are significantly less computational expensive compared to CFD. Secondly, it is clear that vortex methods are able to capture the flow field up- and downstream of the rotor, where BEM, which will be discussed in the next section, averages the induced effects to one value for each annulus in the rotor plane. Therefore, the induction of the rotor is better predicted with vortex methods than with BEM. Furthermore, if the wake is allowed to convect freely, effects such as vortex roll-up, wake expansion and distortion will improve the results even more.

2.3 BEM

Blade Element Momentum theory (BEM) is a combination of blade element theory with two-dimensional momentum theory. Both theories will be discussed in this section including the coupling of the two. BEM offers very fast calculations allowing the use of it in an iterative design process of wind turbine blades with reasonable loads estimation. The reason why it is such an efficient method may be due to the fact that the theory is designed from a (wind or propeller) rotor's aerodynamic perspective. This perspective focusses on how the kinetic energy from the wind is transformed into mechanical energy; both theories calculate the thrust and torque resulting from the interaction of the wind rotor with the flow.

In theory, the most optimal rotor will have extracted all the energy from the flow, such that the flow that interacts with the rotor blades has no energy left and thus must be at rest afterwards. In practice this does not happen due to the simple fact that such rotor can not be designed. Therefore the flow only slows down behind the rotor, resulting into different flow properties upstream and downstream of the rotor. The momentum theory is based on this concept, where the blade element theory is looking from the blade point of view. Both are discussed next separately, starting with momentum theory.

Momentum theory In one sentence, the momentum theory solves the integral form of the Navier-Stokes equations (given in the conservative form in equations (2.1) and (2.2)) for inviscid, incompressible, steady and irrotational flow by defining an one-dimensional control volume. This control volume consist of the flow far upstream the rotor, the flow far downstream the rotor and the rotor represented as an actuator disk. This is a theoretical disk through where the air can flow continuously without any friction. It is this disk that extracts the kinetic energy from the flow and creates a pressure difference at the disk. The flow upstream and the slowed down flow downstream the rotor form a stream-tube which defines a boundary over where no flow crosses. Furthermore, by the assumption that the flow is incompressible, the stream-tube must expand due to the deceleration of the flow behind the rotor. This is visualized in figure 2.3, in where also the labelling of the different one-dimensional variables is given.

From one-dimensional linear momentum theory (rewriting equation (2.2) for this simplified flow) it is stated that the force due to pressure difference at the disk T is equal to

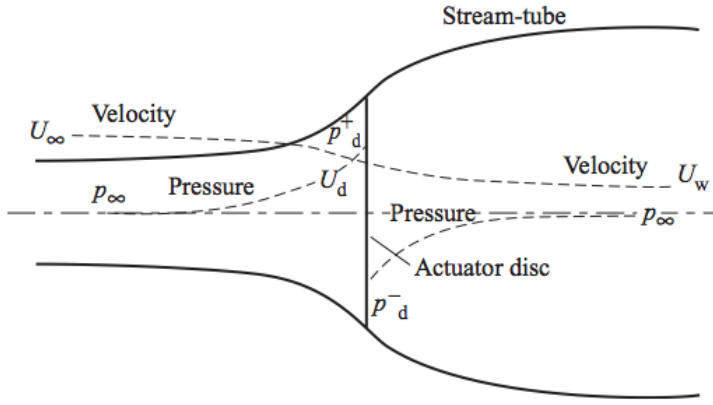


Figure 2.3: The stream-tube, velocity and pressure profile plotted along the actuator disk. The subscripts d and w stand for disk and wake respectively (Burton et al., 2001, figure 3.2). The direction of the flow is from left (upstream) to right (downstream).

the rate of change of momentum, shown in equation (2.7).

$$T = U_\infty(\rho A_\infty U_\infty) - U_w(\rho A_w U_w) \quad (2.7)$$

The continuity equation (equation (2.1)) states that the mass flow rate \dot{m} stays the same in the stream-tube, and therefore with equation (2.8), equation (2.7) can be rewritten to equation (2.9).

$$\dot{m} = \rho A_\infty U_\infty = \rho A_d U_d = \rho A_w U_w \quad (2.8)$$

$$T = \dot{m}(U_\infty - U_w) \quad (2.9)$$

The thrust T can also be evaluated by the pressure difference over the actuator disk. This pressure difference can be calculated with applying the Bernoulli equation (equation (2.6)) up- and downstream and subtracting them from each other, resulting in equation (2.10).

$$(p_d^+ - p_d^-) = \frac{1}{2}\rho(U_\infty^2 - U_w^2) \quad (2.10)$$

A second equation for thrust T is therefore given in equation (2.11).

$$T = (p_d^+ - p_d^-)A_d = \frac{1}{2}\rho(U_\infty^2 - U_w^2)A_d \quad (2.11)$$

Combining equations (2.8), (2.9) and (2.11) yields to the interesting equation which shows that, in this aerodynamic representation, the velocity at the actuator disk is the average of the velocity far upstream and downstream, shown in equation (2.12).

$$U_d = \frac{U_\infty + U_w}{2} \quad (2.12)$$

The velocity at the disk is then defined as the free-stream velocity minus a velocity variation due to the extraction of kinetic energy. The streamwise component of this velocity variation is denoted as the axial induction factor a times the far upstream velocity U_∞ resulting in equation (2.13). It will become clear that the axial induction factor is an important variable for wind aerodynamic analyses.

$$U_d = U_\infty(1 - a) \quad (2.13)$$

The thrust equation can therefore be written into equation (2.14).

$$T = 2\rho U_\infty^2 a(1 - a) A_d \quad (2.14)$$

Considering only an annulus of the actuator disk with area δA_d , the thrust δT is given in the next equation.

$$\delta T = 2\rho U_\infty^2 a(1 - a) \delta A_d \quad (2.15)$$

Until this point it is considered that the actuator disk is not rotating and thus the angular momentum is equal to zero. In case of a rotating disk, the flow in the wake does not behave only linear but also rotates in opposite direction to the disk. The moment associated with this is called torque Q . The torque on an annulus of the rotating actuator disk can be calculated by the multiplication of the mass flow rate through this annulus with the tangential momentum and the radius of the annulus. The tangential velocity component is expressed as $\Omega r(1 + a')$ with rotational velocity Ω , radial position r and angular induction factor a' , noting that the tangential velocity thus increases across the disk. The difference of tangential velocity is related to the angular induction factor a' and to visualize the different velocity components figure 2.4 is given. The torque δQ for an annulus with area δA_d is therefore calculated with equation (2.16).

$$\delta Q = \rho \delta A_d U_\infty (1 - a) 2\Omega a' r^2 \quad (2.16)$$

In equations (2.15) and (2.16) the annulus area δA_d is equal to equation (2.17).

$$\delta A_d = 2\pi r \delta r \quad (2.17)$$

Next, the blade element theory will show alternative equations for δT and δQ , which allows the coupling of the theories.

Blade element theory Where momentum theory does not include the local blade design in the calculations but does, in some sense, acknowledge the wake, blade element theory divides the blade into several sections with the possibility to have different airfoil properties for each section without considering the flow away from these sections. Such a section has the length δr in spanwise direction, chord c and is located at radial position r . The steady incompressible inviscid flow interacts with the section in only two-dimensional sense (radial flow is assumed to be zero). Therefore, the local forces on each section can

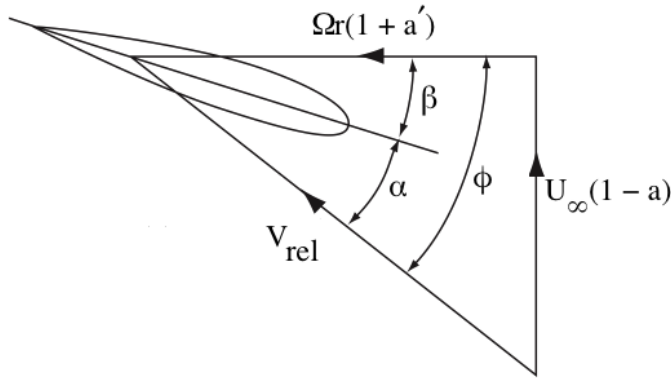


Figure 2.4: The composition of the relative velocity V_{rel} , axial velocity $U_\infty(1-a)$ and tangential velocity $\Omega r(1+a')$ with the angles inflow angle ϕ , angle of attack α and local blade angle (pitch angle + twist angle) β (Burton et al., 2001, figure 3.14 modified).

be calculated by aeronautical analogy, where due to the different radial position r and airfoil design, the forces will vary along the blade. The lift force δL and drag force δD for a cross-section given in figure 2.4 are perpendicular and tangential to the relative velocity V_{rel} , respectively, with the equations given next.

$$\delta L = \frac{1}{2} \rho V_{rel}^2 C_l c \delta r \quad (2.18)$$

$$\delta D = \frac{1}{2} \rho V_{rel}^2 C_d c \delta r \quad (2.19)$$

It should be noted that for the stated incompressible inviscid flow, it is argued (by for example Burton et al. (2001), Lindenburg (2003) and Wilson and Lissaman (1974)) if the drag force D should be included or not. Though, as this chapter focusses on the differences between the aerodynamic models, the discussion whether drag force is let aside. To allow the inclusion of drag force in BEM if preferred, the drag force D is not set to zero in the following equations.

The relative velocity V_{rel} is obtained by equation (2.20) and the lift coefficient C_l , drag coefficient C_d and chord c are assumed to be known from the blade design. Note that the lift coefficient C_l and drag coefficient C_d depend on the angle of attack α and are obtained from the airfoil data. Thus similar to vortex methods, the accuracy of the results depend on the accuracy of the acquired $C_l(\alpha)$ and $C_d(\alpha)$.

$$V_{rel} = \sqrt{[U_\infty(1-a)]^2 + [\Omega r(1+a')]^2} \quad (2.20)$$

From the lift force L and drag force D the step to thrust T and torque Q is easily made, as the thrust is the force in the direction of the plane of the rotation (same direction as the tangential velocity $\Omega r(1+a')$ in figure 2.4) and the torque is as the moment around the direction of flight (same direction as the axial velocity $U_\infty(1-a)$ in figure 2.4).

Therefore, the inflow angle ϕ is used to transpose the lift force L and drag force D to these axes, resulting in the local forces normal force δF_n and tangential force δF_t , given in equations (2.21) and (2.22).

$$\delta F_n = \delta L \cos \phi + \delta D \sin \phi \quad (2.21)$$

$$\delta F_t = \delta L \sin \phi - \delta D \cos \phi \quad (2.22)$$

Finally, the blade element theory equations for the thrust and torque are shown next, where it is seen that the local forces δF_n and δF_t are multiplied with the number of blades N_b in order to calculate the annulus values for δT and δQ . This is only allowed for axial flow (yaw angle γ is equal to zero). For yaw flow one should take the different blade contribution separately into consideration.

$$\delta T = \frac{1}{2} \rho V_{rel}^2 (C_l \cos \phi + C_d \sin \phi) c N_b \delta r \quad (2.23)$$

$$\delta Q = \frac{1}{2} \rho V_{rel}^2 (C_l \sin \phi - C_d \cos \phi) c N_b r \delta r \quad (2.24)$$

Therefore, these equations calculate the thrust T and torque Q for the same annulus as equations (2.15) and (2.16).

BEM With the last conclusion on the similarities of the equations, equation (2.15) can be set equal to equation (2.23) and equation (2.16) to equation (2.24). This is the essence of Blade Element Momentum theory (BEM). The equations are then rewritten such that the variables that are unknown from the blade design (α , a and a') but are dependent on the flow conditions can be solved.

To do so, with trigonometric relations, the relative velocity V_{rel} can be expressed in the axial and tangential velocities, using figure 2.4. In this figure it can also be seen that the inflow angle ϕ is a summation of an angle that is dependent on the flow (angle of attack α) with an angle that is dependent on the blade design and settings (local blade angle (pitch angle + twist angle) β), expressed once more in equation (2.28).

$$\tan \phi = \frac{U_\infty(1-a)}{\Omega r(1+a')} \quad (2.25)$$

$$\cos \phi = \frac{\Omega r(1+a')}{V_{rel}} \quad (2.26)$$

$$\sin \phi = \frac{U_\infty(1-a)}{V_{rel}} \quad (2.27)$$

$$\phi = \alpha + \beta \quad (2.28)$$

Now equating the thrust equations from both theories (equation (2.15) and equation (2.23)) results in an equation for the axial induction factor a , with the solidity σ (expressing the ratio of the amount of area that is covered by the rotor in the annulus) and the normal force coefficient C_n given in equations (2.30) and (2.31), respectively.

$$a = \frac{1}{\frac{4\sin^2\phi}{\sigma C_n} + 1} \quad (2.29)$$

$$\sigma = \frac{N_b c}{2\pi r} \quad (2.30)$$

$$C_n = C_l \cos \phi + C_d \sin \phi \quad (2.31)$$

The same is done for the torque equations (equation (2.16) and equation (2.24)) resulting in an expression for the angular induction factor a' (given in equation (2.32)) with the tangential force coefficient C_t given in equation (2.33).

$$a' = \frac{1}{\frac{4\sin\phi\cos\phi}{\sigma C_t} - 1} \quad (2.32)$$

$$C_t = C_l \sin \phi - C_d \cos \phi \quad (2.33)$$

For each annulus the axial induction factor a and angular induction factor a' can now be calculated with an iterative algorithm:

1. Assume initial values for a and a' for each section (i.e. a and a' are function of r).
2. Compute the inflow angle ϕ with equation (2.25).
3. Compute the angle of attack α with equation (2.28).
4. Determine the lift coefficient C_l and drag coefficient C_d corresponding to the calculated angle of attack using airfoil data.
5. Calculate new values for axial induction factor a and angular induction factor a' with equations (2.29) and (2.32), respectively.
6. Check if there is convergence comparing the new and old values for a and a' . If a certain tolerance is not reached, go back to step 2. If the results are accepted, the thrust, torque, lift force and drag force can be calculated with equations (2.15), (2.16), (2.18) and (2.19), respectively.

Assumptions and limitations BEM Now that BEM is explained mathematically, it is good to reflect what is done and for which assumptions this is acceptable, to be able to compare it to CFD and vortex methods. To derive the momentum theory it is assumed that the flow is inviscid, incompressible, steady and irrotational and moving from upstream to downstream direction. The wind rotor is modelled as a rotating actuator disk, which can be seen as a rotor with an infinity number of blades that allows the air to continuously flow through it and is responsible for a pressure jump at the disk. As it is assumed that the force acting on an annulus is only due to this pressure jump (evaluated locally), it is implicitly assumed that there is no interaction of flow between the annuli. Therefore the thrust is uniform over the rotor area or in other words, the induction is uniform. With the assumption that the pressure far upstream and far downstream the rotor is the same, it can be therefore stated that the wake structure is modelled as a cylinder, rotating with the opposite rotational velocity of the wind rotor. For the blade element theory the same assumptions are done, with the emphasize on that there is no radial flow (independent annuli) and axis-symmetric inviscid, incompressible, steady flow.

The consequence of these assumptions is that there are limitations for which BEM can be used. To correct the limitations, and thus broaden the applicability of BEM, several modifications can done. A complete overview is given by Schepers (2012), however a few are discussed shortly next.

- Turbulent wake state corrections: a negative wake velocity (theoretical flow reversal) in BEM is possible when a is higher than 0.5 (calculated by inserting equation (2.13) in equation (2.12) and rewriting the equation for U_w). In this case, the assumption that the flow only moves from upstream to downstream direction is thus not satisfied, which leads to a breakdown of the momentum theory. In reality, the assumption of the stream-tube does not hold as the wake will interact with the flow outside the stream-tube, resulting into turbulent flow in the wake. Corrections can be implemented that extend the algorithm for when the loading (expressed by axial induction factor a or thrust coefficient) is above a certain critical value. Literature shows several critical values for which the momentum theory breaks down, based on empirical results (see Wilson and Lissaman (1974), Manwell, McGowan, and Rogers (2009)). Glauert (1926) was the first to note this type of correction and therefore the different variations on correcting the momentum theory for highly loaded rotors are usually denoted as Glauert corrections.
- Radial flow corrections: BEM is capable of calculating local forces due to the assumption that there is no radial dependency of sections or in other words, the flow is treated as a two-dimensional flow. However due to the rotation of the blades the flow does have a component in radial direction, measured by several (Ronsten (1992), Schreck and Robinson (2002), Lindenburg (2003), Herráez, Stoevesandt, and Peinke (2014)). In short, the Coriolis force that is present due to the rotation drives the boundary layer ("viscous part of the flow") towards the trailing edge. For inboard radial sections where the angle of attack α is high (combine equations (2.25) and (2.28) for low values of r), this force acts as a favourable pressure gradient and therefore counteracts the adverse pressure gradient, resulting in delay of separation of the boundary layer and the possibility of achieving higher lift coefficients. When

the conditions are such that there is already separation, the Coriolis force is responsible for so-called centrifugal pumping of the separated flow towards more outboard sections (see for more detailed explanations Himmelskamp (1945), Harris (1966), Eggers and Digumarthi (1992), N. N. Sørensen, Michelsen, and Schrek (2002) or Montgomerie (2004)). There exist quite a few different stall delay corrections in literature due to different approaches and fitting to different experimental data (see Snel and Van Holten (1995), Chaviaropoulos and Hansen (2000), Lindenburg (2003), Bak, Johansen, and Andersen (2006), Breton, Coton, and Moe (2008)).

- Finite number of blades corrections: The momentum theory models the rotor as an actuator disk, which can be seen as a rotor with an infinite number of blades. It is evident that this is a strong simplification, resulting in an assumed uniform flow in the rotor plane and a full, cylindrical shaped wake for the flow conditions stated earlier. Physically, a rotor with finite number of blades will show non-uniformities in the flow field as some flow particles will have to interact with the blades and other particles will not. Furthermore, the wake will shape to a helical structure with still allowing the concept of a stream-tube, although additional non-uniform flow arises at the edges of the stream-tube in the wake part. From the point of view which considers complete uniform as perfect, these non-uniform flow regimes can be denoted as losses. Prandtl (1921) was the first who attempted to describe these losses and therefore the correction associated to the infinite number of blade assumption is known as the Prandtl tip loss correction. This correction is the essence of this thesis and therefore it will be derived in detail in the next section, from which it also will be clear why it is called a tip loss factor. When the Prandtl tip loss factor is implemented, the results will show that the factor gives the ratio of the azimuthal averaged axial induction factor versus the local axial induction factor, which can be related to the momentum theory and blade element theory, respectively.

From the derivation and the listing of assumptions and limitations of BEM it is clear that some physical aerodynamic properties are not well captured by the theory, especially when comparing to CFD and vortex methods: flow field properties can not be calculated (as CFD is able to do) and aerodynamic effects due to the flow up- and downstream are not properly included (as vortex methods are able to do), let alone the fact that there are corrections needed to approach a better solution of the flow in the rotor plane. Then again, this encourages the incentive to use CFD and vortex methods to improve BEM, with maintaining BEM's main advantage of a immensely fast method to analyse the loading on a wind turbine rotor.

Chapter 3

Prandtl tip loss factor

Introduced in the previous chapter, the Prandtl tip loss factor corrects BEM for modelling the rotor with an infinite number of blades. Due to the importance the full derivation will be done in this first section. It will be clear that the tip loss factor described by Prandtl (1921) is not directly suitable for BEM and therefore multiple implementations exist, which will be discussed in the section 3.2.

3.1 Derivation

A rotor transforms kinetic energy from the flow into mechanical energy. The flow downstream the rotor is called the wake. This downstream flow has also been enforced to rotate. When considering that the blades have a constant bound circulation over the total span, the wake created by a number of blades will consist of the same number of single vortices that are trailed from the tips. A visualization is given in figure 3.1.

In case of a non-constant circulation along the blade, the same helical wake structure will be formed but now by vortex sheets. In both cases, the wake consists of streamlines of the flow. The wake can therefore be seen as impermeable or solid sheets for flow outside of the wake.

When observing the wake in figure 3.1 in the $x'' - y''$ plane and rotating the frame such that the trailed tip lines are vertical, figure 3.2 can be drawn. In this figure the top wake lines are drawn in bold thick lines in a new reference $x' - y'$ frame, with the dashed lines indicating that the lines are cut. Note that although the first and fourth vertical lines should be connected as these originate from the same blade, this is not shown. Furthermore, the lines are called wake sheets because in this two-dimensional visualization it is of no importance if the wake consists of only trailed tip vortices or vortex sheets. The distance between the wake sheets is defined as d .

With the assumption of that the wake sheets are impermeable, the undisturbed flow close to the tips of the wake sheets will curve around the tips. The level of curvature

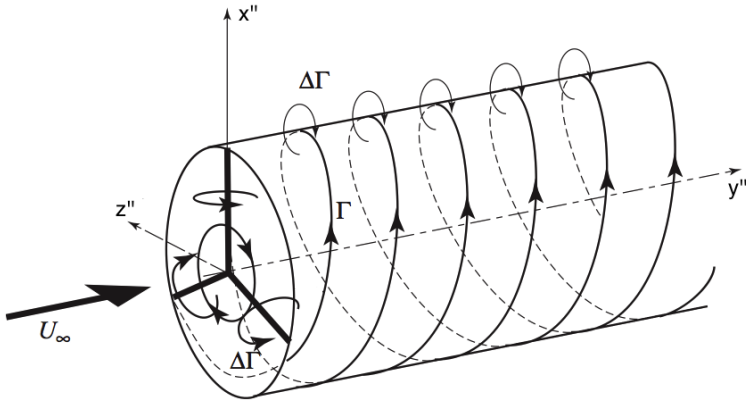


Figure 3.1: The simplified (no wake expansion and distortion) helical wake structure for a three-bladed rotor with a finite number of blades (Burton et al., 2001, figure 3.7). When assuming constant circulation along the blades, vortices are trailed only from the tip of the blades. Note that the reference frame is chosen differently from what is conventional, because this will help to understand the derivation of the Prandtl tip loss factor.

is dependent on the distance between the sheets and the strength of the shed vortices. When the rotor would consist of an infinite number of blades, infinite number of trailed tip vortices would be shed, hence resulting in a cylindrical wake structure. Therefore, curvature of the undisturbed flow near the tip of the wake sheets would be allowed, leading to complete uniform flow (again, neglecting the wake expansion and distortion).

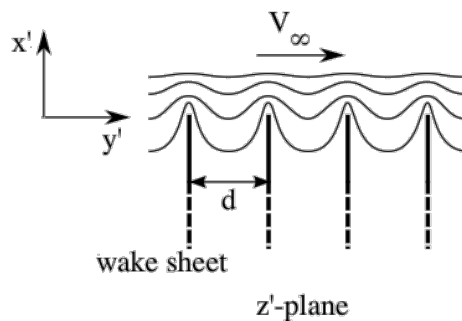


Figure 3.2: The flow over the four impermeable wake sheets curves around them, which shows the non-uniform behaviour of the flow (Branlard, 2011, figure 2.7 modified). The distance between the wake sheets is d . Note the reference frame labelling (lowercase letters).

The curvature of the flow is thus related to the amount of non-uniform flow. Prandtl was able to describe this flow mathematically as an addition to the paper of Betz and Prandtl (1919) (and later published his own paper (Prandtl (1921))). Prandtl's approach was to value the loss of circulation due to the interaction of the flow with the helical wake compared to a rotor with infinite number of blades, by using screw engineering analogy to describe the helical wake and conformal mapping to describe the flow. As commonly done, Prandtl only discusses the highlights of his work. Branlard (2011) shows the beginning

of the derivation but because 1) he uses the same notations for different variables, 2) the used notation differs from other literature and 3) the derivation is of great importance for this thesis, the derivation is given next and completed, in the order and syntax which it is most logic to the author.

Prandtl uses conformal mapping to describe the curvature of the flow around the wake sheets. In general, conformal mapping transforms variables from complex geometries to simpler geometries (or vice versa), with preservation of original angles and orientations, by a mathematical transformation function. For these simpler geometries, the flow field is often also known. In this case the flow field around a circle will be used as the simpler case, where figure 3.2 shows the complex case. The Joukowski's transform function will map the flow around the circle to the complex case.

For two-dimensional potential flow, the flow field around a circle can be described by superimposing elementary uniform flow with doublet and vortex flow. Using Joukowskii's transform function given in equation (3.1) this circle geometry can be transformed to an airfoil in a new complex reference frame. The notation in equation (3.1) uses arbitrary symbols which should be replaced when the equation is being used, where ξ^* is the transformed variable, σ^* is some length and ψ^* is the original variable (the stars symbols are used to prevent confusion with other variables that use the same Greek letters).

$$\xi^* = \psi^* + \frac{(\sigma^*)^2}{\psi^*} \quad (3.1)$$

With figure 3.2, it can be concluded that the wake sheets can be seen as infinity number of individual flat plates in y' -direction of semi-infinite length in x' -direction, which imposes an extra level of difficulty. When this is overcome, the same Joukowski's function can be used to describe the flow field over the flat plates.

Let's first define the circle and the flow field around this circle. Consider the circle to be in the complex z -plane with axes x and y and such that $z = x+iy$. The circle center is located at the origin of the reference frame and has radius b . Therefore, the circle is described by equation (3.2).

$$z = b \exp[i\theta] \quad (3.2)$$

Inserting this equation in the Joukowski transform, noting that $\psi^* = z$ and defining the transformed variable $\xi^* = Z$, results in equation (3.3), with constants c_1 and c_2 equal to equations (3.4) and (3.5), respectively.

$$\begin{aligned} Z &= b \exp[i\theta] + \frac{(\sigma^*)^2}{b} \exp[-i\theta] = \left(b + \frac{(\sigma^*)^2}{b} \right) \cos \theta + i \left(b - \frac{(\sigma^*)^2}{b} \right) \sin \theta \\ &= c_1 \cos \theta + i c_2 \sin \theta \end{aligned} \quad (3.3)$$

$$c_1 = \left(b + \frac{(\sigma^*)^2}{b} \right) \quad (3.4)$$

$$c_2 = \left(b - \frac{(\sigma^*)^2}{b} \right) \quad (3.5)$$

Considering a circle with radius $b = \sigma^* = 1$ and $\theta = [0; 2\pi]$, the result shows that with the Joukowski transform the unit circle in the z -plane is mapped as a line segment stretching from -2 to 2 on the real axis (imaginary part is zero) in the complex Z -plane. This is visualized in solid (red) lines in figure 3.3. For a circle with center just shifted slightly, it is seen that the Joukowski transform results in an airfoil in Z -plane. Therefore the Joukowski transform is commonly used for airfoil design (Pozrikidis (2011)).

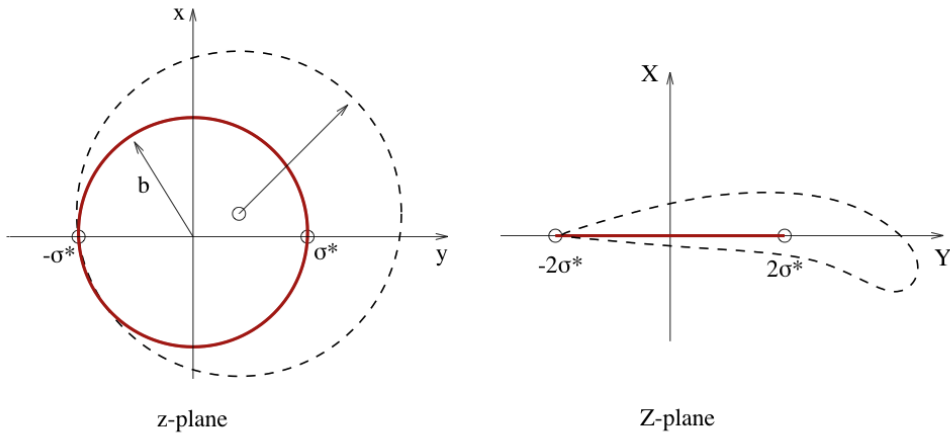


Figure 3.3: The transformation of the red circle with radius b and its center located at the origin of the z -plane (left) to the red flat plate in the Z -plane (right) is done by the Joukowski transform (equation (3.1)). When the center of the circle has an offset to the origin of the axis system, the Joukowski transform maps the circle to an airfoil, as shown by the dashed lines. (Pozrikidis, 2011, figure 7.12.3 modified).

The flat plate in figure 3.3 will be later related to the wake sheets drawn in figure 3.2. First the flow field over the circle is given in equation (3.6). Considering two-dimensional potential flow, it can be seen that the flow field is a summation of uniform flow, doublet flow and vortex flow.

$$w(z) = V_\infty \left(z - \frac{b^2}{z} \right) - \frac{i\Gamma}{2\pi} \log z \quad (3.6)$$

In this equation $w(z)$ is the complex potential and Γ the circulation strength of the elementary vortex flow. In general, the complex potential can be expressed by the velocity potential ϕ_{vp} and stream function ψ_{sf} , as done in equation (3.7). To be clear, the z variable in equation (3.6) is the same z variable that describes the circle in the z -plane.

$$w = \phi_{vp} + i\psi_{sf} \quad (3.7)$$

The geometry and the flow field are thus completely known in the z -plane. Furthermore, the Joukowski transform showed how the circle in the z -plane can be related to a flat plate stretching from $[-2; 2]$ in the Z -plane.

Though, as the z' -plane in figure 3.2 indicates, there are more than one flat plates of semi-infinite length, with respect to what the flow at the tip feels. In mathematical form, the geometry of the wake sheets can be described by $x' \in [-\infty; 0]$ and $y' = kd$ with $k \in \mathbb{Z}$ and distance between two helical wake sheets d . The repeating order of the wake sheets can be described using the complex exponential function and $z' = x' + iy'$, such that

$$\exp\left[\frac{\pi z'}{d}\right] = \exp\left[(x' + iy')\frac{\pi}{d}\right] = \exp\left[\frac{\pi x'}{d}\right] \exp[ik\pi] = \exp\left[\frac{\pi x'}{d}\right] \begin{cases} 1, & k \in 2\mathbb{Z}, \\ -1, & k \in 2\mathbb{Z}+1 \end{cases}$$

This exponential equation maps the wake sheets from figure 3.2 for $x' \in [-\infty; 0]$ to segments in the domain of $[0; 1]$, making it a finite problem, with the segments covering $[-1; 1]$. The two parts of the answer are covered by transforming the equation (another form of mapping) to the next form, where Z' is thus covering the finite segments from $[-1; 1]$.

$$z' = \frac{d}{\pi} \log Z' \quad (3.8)$$

Note that only two wake sheets are mapped by the exponential function, but with the knowledge that the flow is assumed to be symmetric and repetitive over the rest of the wake sheets, this causes no problem in order to describe the non-uniform flow. Now, the combination of the previously described separated ingredients will lead to the expression which is known as the Prandtl tip loss factor. This is described in the following steps.

1. The segments in the Z' plane are, by no coincidence, similar to the segments in the earlier discussed Z -plane, with half the length. Therefore, multiplying Joukowski's transform (equation (3.1)) with a half and knowing that the transformed variable $\xi = \frac{1}{2}Z = Z'$, the original variable $\psi^* = z$ and $\sigma^* = b = 1$ and inserting this in equation (3.8), results in:

$$z' = \frac{d}{\pi} \log \left[\frac{1}{2} \left(z + \frac{1}{z} \right) \right] \quad (3.9)$$

To once more clarify, the z' -plane is shown in figure 3.2 and the z -plane is where the circle with the known flow field is described (left-side of figure 3.3).

2. The complex potential describes the flow field around the circle as a function of z , which is shown in equation (3.6). Combining this equation with equation (3.7) and noting that the objective is to describe only the non-uniform flow (in other words, the parts with V_∞ are ignored), the equation can be rewritten for z , which is shown next.

$$z = \exp \left[\frac{2\pi}{\Gamma} (\phi_{vp} + i\psi_{sf}) \right] \quad (3.10)$$

3. The complex exponential equation (3.10) can be inserting into equation (3.9), noting that the term in between square brackets in equation (3.9) is equal to the $\cos(z)$ when z is complex, defined by the Euler equation. Therefore, combining equation (3.10) with equation (3.9) results in:

$$z = \frac{d}{\pi} \log \cos \left[\frac{2\pi}{\Gamma} (\phi_{vp} + i\psi_{sf}) \right] \quad (3.11)$$

4. By defining the boundary of the circle as a streamline of the flow field ($\psi_{sf} = 0$) and by equating the real parts of the last equation with $z = x + iy$, results in an equation for the potential ϕ_{vp} .

$$\phi_{vp} = \pm \frac{\Gamma}{2\pi} \arccos \exp \left[\frac{x\pi}{d} \right] \quad (3.12)$$

5. Note that \pm in equation (3.12) comes from the fact that $\cos(\alpha) = \cos(-\alpha)$. The x -coordinate is defined in z -plane (in where the circle is defined), although the wish is to describe the flow in rotor analogy (Z -plane). The x -coordinate gives the distance with respect to the reference frame origin. Now imagining a rotor blade, the distance from an arbitrary radial section r_1 to the tip is equal to r_1-R (the need of the subscript will become clear later). Therefore, the x -coordinate in rotor geometry can be seen as the distance between r_1-R . This leads to the following equation.

$$\phi_{vp} = \pm \frac{\Gamma}{2\pi} \arccos \exp \left[-\pi \frac{R - r_1}{d} \right] \quad (3.13)$$

6. The objective of Prandtl was to describe the non-uniform flow compared to the undisturbed flow V_∞ . Considering the flow far above the edges of the wake sheets drawn in figure 3.2, the flow is equal to this V_∞ . This is used to find a limit for the Prandtl tip loss factor.

From the complex potential given in equation (3.7), the complex velocity in the z' -plane (figure 3.2) can be calculated by differentiating the complex potential $w(z)$ to z' .

$$\frac{dw}{dz'} = \frac{dw}{dz} \frac{dz}{dz'} \quad (3.14)$$

The first derivative dw/dz is obtained from equation (3.6), where it was discussed that the uniform flow component is ignored. The second derivative dz/dz' is obtained from equation (3.9). This leads to the following velocity.

$$\frac{dw}{dz'} = -i \frac{\Gamma}{2d} \frac{z^2 + 1}{z^2 - 1} \quad (3.15)$$

Far away from the wake, the velocity $\frac{dw}{dz'}$ is equal to V_∞ . As it is discussed that complete uniform flow is the ideal case, V_∞ is set to one, such that a value lower than one would indicate the existence of non-uniform flow. This limiting case is reached

when $|z| \rightarrow \infty$ (so a position far from the circle given in figure 3.3), therefore resulting in the following condition.

$$\Gamma = 2d \quad (3.16)$$

The result of this limiting case can be used in equation (3.13) to form the following equation for the scaled velocity potential.

$$\phi_{vp} = \pm \frac{d}{\pi} \arccos \exp \left[-\pi \frac{R - r_1}{d} \right] \quad (3.17)$$

7. Finally, to have a factor that describes the non-uniform flow with values between 0 and 1, equation (3.17) is divided by d . Also, the absolute difference between two extrema of the velocity potential, denoted by when the plus-minus sign is equal to a minus and a plus, is two. This leads to the Prandtl tip loss factor given next.

$$F = \frac{2}{\pi} \arccos \exp \left[-\pi \frac{R - r_1}{d} \right] \quad (3.18)$$

In words, this equation is equal to 1 when there is only uniform flow (limiting case of $|z| \rightarrow \infty$) and equal to a value between 0 and 1 when there is non-uniform flow between two wake sheets divided by distance d .

Note that the derivation shown here, is as how Prandtl derived it. Glauert did his own derivation but as the result is the same, it is not discussed here. In present literature the tip loss factor is sometimes named as the Prandtl-Glauert tip loss factor, which has nothing to do with how the derivation is performed, but is due to the fact that Glauert made some assumptions, that are necessary to implement the tip loss factor into BEM. This will be discussed in the next section, but this section will first conclude on defining the distance between two helical wake sheets d .

Relative to the rotor plane, the wake sheets shedding from the rotor blades are actually tilted. Therefore, figure 3.2 is redrawn to show this angle, given as figure 3.4.

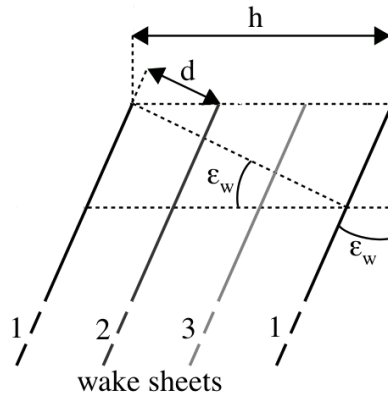


Figure 3.4: Visualization of the helical wake sheets, the angle between helical wake sheets ϵ_w , the screw pitch h and the distance between two helical wake sheets d (Branlard, 2011, figure 2.8 modified). The numbers indicate that the first and last wake sheet originated from the first blade, the second wake sheet from the second blade and the third wake sheet from the third blade. The screw pitch h is thus the axial distance for which the helical wake sheet has made one single revolution.

The figure shows the side-view of the wake, where it convects downstream to the right. It consists of three helical sheets, where the first and the last drawn lines are in essential the wake sheets originating from the same blade and are thus connected. Though, to clarify the definition of distance between two helical wake sheets d , the figure does not indicate this. The variable h in the figure gives the axial distance for which the helical sheet has made one single revolution. **One revolution equals the circumference of a circle with radius r_2** (if the tip is taken, $r_2 = R$) and because the sheets are convecting under the angle ϵ_w , the equation for h is given in equation (3.19).

$$h = 2\pi r_2 \tan \epsilon_w \quad (3.19)$$

Now from the figure it is easily deduced that d is the distance between two consecutive threads, or in this case, the distance from one helical sheet to the next. With the number of blades N_b and the angle between helical wake sheets ϵ_w this results in equation (3.20).

$$d = \frac{h}{N_b} \cos \epsilon_w \quad (3.20)$$

Some reflection should be done in order to fully understand what the derivation tells. Prandtl tries to describe the amount of curving flow around the wake structure, where the curved flow is labelled as the losses compared to the ideal situation of complete uniform flow. The resulting equations are formed by using the elementary potential vortex flow to describe the circular motioned flow. It can be seen that, when combining equations (3.19) and (3.20) in equation (3.18), the only not-design related variable and thus the only variable that is dependent on the operational conditions is the angle between helical wake sheets ϵ_w . In Prandtl's model, for a given rotor, the losses are thus only dependent on this angle, assuming that the wake is perfect helical structure.

Furthermore, Prandtl assumes that the blades have a constant circulation along the span of the blades, resulting in a wake consisting of only trailed vortices from the outer ends of the blades. However, it is known that circulation distributions are not perfectly constant for real rotors. For the derivation of the tip loss factor, figures 3.2 and 3.4 only visualize the side-view of the wake and the two-dimensional flow that interacts with the edges does not change by this fact. Thus the conclusion that must be done here is that in this form, the Prandtl tip loss factor can not describe all the non-uniformities.

A second assumption that is important in the discussion on how valid the Prandtl tip loss factor is, is the assumption that the wake is a perfect helical wake. In reality, there is wake expansion due to deceleration of the incompressible flow, tip vortex roll-up due to the matching of the flow over the upper surface of the blade with the lower surface of the blade at the tip and wake distortion depending on the amount of loading. When including these effects the wake can not be represented as a perfect helix. It is therefore evident that there will be deviating results visible, when conditions are such that this assumption is not valid any more.

Finally, it must also be noted that the current form of the tip loss factor is not applicable for the use in BEM. The next section will show that, besides to the already discussed limitations, more consideration have to be made in order to be able to correct BEM properly.

3.2 Variations

As discussed in the previous section, the only variable that can not be related to known design variables of the rotor is angle between helical wake sheets ϵ_w . However, because BEM models the wake resembling a cylindrical-tube and not as a helical wake (after all the Prandtl tip loss factor is there to correct this), this angle is not defined in BEM. It is therefore needed to estimate this angle. For the wake that is just shed from the rotor and thus propagates with the same axial and rotational velocity similar to the rotor, the velocity triangle shown in figure 2.4 holds for the wake sheets close to the rotor. For this reason, in order to apply the Prandtl tip loss factor in BEM, it is assumed that angle between helical wake sheets ϵ_w is equal to the inflow angle ϕ . This assumption is less true when moving downstream in the wake. The wake dynamics are related to the loading of the rotor such that a highly loaded rotor will produce a less perfect helical wake compared to a lightly loaded one. Consequently it is said that the angle between helical wake sheets ϵ_w is equal to the inflow angle ϕ assuming a lightly loaded rotor. On the other hand, the far wake dynamics will have a decreasing influences on the rotor dynamics, which is expressed by the Biot-Savart law given in equation (2.3).

The inflow angle ϕ can be determined with equations (2.25) to (2.27). As the angle should be evaluated at the same position for which the screw pitch h in equation (3.19) is evaluated, the inflow angle ϕ is a function of radius r_2 . Depending on the accuracy and implementation for which one desires to evaluate the inflow angle, several values for r_2 , a and a' can be used. This results in that many variations of the Prandtl tip loss factor can be found. Equations (3.18) to (3.20) are combined to embody all the variations. The Prandtl tip loss factor in this new form is given in equation (3.21). In this equation, the importance of the distinction between r_1 from equation (3.13) where translation of the

x -coordinate to rotor analogy was done, and r_2 from equations (3.19) and (3.20) which are used to determine the distance between two helical wake sheets d , is now clear. The velocity components are given in equations (3.22) and (3.23), from which it can be seen that a third radius r_3 is related to the tangential velocity V_t .

$$F = \frac{2}{\pi} \arccos \left[\exp \left(-\frac{N_b}{2} \frac{R - r_1}{r_2} \frac{\sqrt{V_n^2 + V_t^2}}{V_n} \right) \right] \quad (3.21)$$

$$V_n = U_\infty(1 - a) \quad (3.22)$$

$$V_t = \Omega r_3(1 + a') \quad (3.23)$$

In the BEM equations, the Prandtl tip loss factor is then inserted into equations (2.29) and (2.32), such that the new equations for the axial induction factor a and the a' are as following.

$$a = \frac{1}{\frac{4F \sin^2 \phi}{\sigma C_n} + 1} \quad (3.24)$$

$$a' = \frac{1}{\frac{4F \sin \phi \cos \phi}{\sigma C_t} - 1} \quad (3.25)$$

The most common Prandtl tip loss factor is often called the Prandtl-Glauert tip loss factor, as Glauert (1935) made the assumptions that r_1 , a , a' , r_2 and r_3 should be all evaluated locally ($r_1 = r_2 = r_3 = r$). Another common tip loss factor is the one described by Burton et al. (2001). Burton et al. (2001) ends up, though by taking a different path of assumptions, with a tip loss factor almost identical to the one of Glauert (1935). Compared to the general form above, he assumes that a' is equal to zero and that for the relative velocity V_{rel} given in equation (2.20) both a and a' are zero, however for calculating the inflow angle ϕ with equation (2.27) a is not zero. With the tip speed ratio λ given in equation (3.26), this leads to equation (3.28). The two forms of the tip loss factor are given in the equations (3.27) and (3.28) to show the different appearances.

$$\lambda = \frac{\Omega r}{U_\infty} \quad (3.26)$$

$$F_{Glauert} = \frac{2}{\pi} \arccos \left[\exp \left(-\frac{N_b}{2} \left(\frac{R - r}{r} \right) \frac{1}{\sin \phi(r)} \right) \right] \quad (3.27)$$

$$F_{Burton} = \frac{2}{\pi} \arccos \left[\exp \left(-\frac{N_b}{2} \left(\frac{R - r}{r} \right) \sqrt{1 + \left(\frac{\lambda(r)}{1 - a(r)} \right)^2} \right) \right] \quad (3.28)$$

These are just two of many examples that can be found in literature. By taking different combinations of assumptions, the list of variations is long, for which the following should give insight in:

1. The radius r_1 is always evaluated locally because this radial position is used to calculate the distance from this position to the tip of the blade.
2. The radial position r_2 can be defined locally ($r_2 = r$) or at the tip ($r_2 = R$) (2 possibilities).
3. The same holds for the r_3 in equation (3.23): $r_3 = r$ or $r_3 = R$ (2 possibilities).
4. For the value of the axial induction factor a articles can be found that set it to zero, use the local or tip values or use the local or tip azimuth averaged values, resulting into 5 possibilities.
5. The value of the angular induction factor a' is most of the times set to zero. In other cases the local or tip values are used (3 possibilities).

This already leads to $2 \times 2 \times 5 \times 3 = 60$ possible variations.

Next to this, by making the analogy to roller bearing in where bearings slide between two surfaces, it can be discussed that the tip trailing vortices convect at the edge of the wake, dividing the wake from the free-stream flow. Therefore, these tip vortices travel with an average of the velocity outside of the wake U_∞ and the velocity just inside the wake $U_\infty a(R)$. Though due to that the release of the tip vortices is not precisely concentrated at the tip, Lindenburg (2003) multiplies the latter velocity with \sqrt{F} , resulting in an extra iterative loop needed for solving F . Snel and Van Holten (1995) discuss that a factor of 1/2 is sufficient in acknowledging the spread tip vortices. To maintain the generality and easiness of the equations, any factor is excluded here and V_n is simply calculated by taking the average of the two velocities (Snel and Schepers (2009) also showed that this is a good approximation), as given in equation (3.29). The assumptions that can be made for r_2 , r_3 and angular induction factor a' still hold, thus the roller bearing analogy results into $2 \times 2 \times 3 = 12$ extra variations.

$$V_n = U_\infty \left(1 - \frac{a(R)}{2} \right) \quad (3.29)$$

Besides the already discussed ones from Glauert (1935), Burton et al. (2001) and Lindenburg (2003), there exist two more often used tip loss factors annotated by their inventors, namely Goldstein (1929) and Shen, Mikkelsen, Sørensen, and Bak (2005). Similar to Prandtl (1921), Goldstein (1929) continued the work of Betz and Prandtl (1919), leading to an exact solution of describing the circulation for an optimal rotor by the use of Bessel functions. By assessing the differences between this circulation to the one from a rotor with infinite number of blades, a tip loss factor can be formed. However, due to the complexity of Goldstein's theory, implementation of the exact solutions into the BEM theory has not been achieved in such a way that it will not diminish the elegant and simple setup of the BEM theory. Furthermore, the theory is based on an optimal rotor, which is a strong simplification on its own. Shen et al. (2005) proposed a tip loss factor equivalent to the Prandtl tip loss factor for the force coefficients and used fitting techniques to determine the constants in his formulation. Compared to the general equations for the Prandtl tip loss factor that can lead to many variations as discussed in this section, the

tip loss factors of Goldstein (1929) and Shen et al. (2005) are thus seen as two completely different factors.

Furthermore, similar to Shen et al. (2005), Wilson and Lissaman (1974) and De Vries (1979) discuss that the Glauert tip loss factor should also be used to correct the force coefficients (because it is observed that the loading is still overestimated, which will be discussed in the next section). However, as shown by Shen et al. (2005), both lead to a misconception: applying the tip loss factor, the inflow angle ϕ reduces and thus indeed lower values for the loading are calculated, though the same two-dimensional airfoil data is used, where it is known that due to the finite span, this airfoil data is not correct. Note that, in this thesis only the effect of the tip loss factor is assessed, so the correctness of the use of two-dimensional airfoil data for both BEM and vortex methods is out of the scope for this research.

In short, this section discusses the many variations and forms that exists of the tip loss factor. The next section will show there is no consensus on which tip loss factor should be used, by comparing several results from experiments and numerical methods.

3.3 Results in literature

In recent literature, several papers can be found that show comparisons concerning tip loss factors. First, figure 3.5 from Shen et al. (2005) shows that a decay of the normal force at the tip, similar to the experimental results, is modelled when implementing a tip loss factor. It also shows that Shen's tip loss factor performs good, which is expected as he fits his tip loss factor to the experimental results. The results when applying Shen's tip loss factor to other rotors and conditions show deviations due to its empirical origin, indicating that the general validity of the tuned correction could be improved.

Branlard (2011) shows that the differences of results using several tip loss factors for calculating the annual energy production for two wind speeds are large, see figure 3.6. This is an important figure as it visualizes that the performance of the tip loss factors is dependent on the operational conditions. However, it must be noted that though the effect of the tip loss factor on the annual energy production is interesting, the accuracy of predicting the loading at the tip is even more interesting. An overview figure showing the effect of the tip loss factor on the loads has not been found in literature.

Similar to Shen et al. (2005), Breton et al. (2008), Schepers et al. (2014) and Koh and Ng (2016) show that the tip loss factors used in BEM in general overpredict the loads at the tip compared to experimental results. It is discussed that this overprediction can be related to the use of two-dimensional airfoil data in BEM where the flow is far from two-dimensional at the tip. Micallef (2012) devoted his Ph.D dissertation to this, where he extensively discussed the three-dimensional flow at the blades of a wind turbine. A way to overcome the use of two-dimensional airfoil data is to use CFD for creating three-dimensional airfoil data. This data can then be used in BEM, for which now no tip corrections are needed as this is covered by the airfoil data. The results of this approach is given by Johansen and Sørensen (2004) and Yang, Shen, Xu, Hong, and Liu (2014) and show that the new results from BEM are more in line with the CFD results. However, the extraction of the angle of attack α in order to obtain the airfoil data from CFD is

not self-evident due to the difficulty of defining the angle knowing that the flow is far from two-dimensional. Several methods exists for which Hansen, Sørensen, Sørensen, and Michelsen (1997), Johansen and Sørensen (2004) and Shen, Hansen, and Sørensen (2006, 2009) are examples. The next chapter will be partly devoted on this topic.

As discussed in section 2.2, vortex methods are built with the same engineering variables as BEM. Furthermore, compared to BEM they intrinsically includes three-dimensional effects such as tip vortices roll-up, wake expansion and distortion. Therefore, vortex methods are also used to improve tip loss factors. Schepers (2012) describes the use of a free wake lifting line code to develop a tip loss factor and compares it to the Prandtl tip loss factor. No improvements on the Prandtl tip loss factor are done but the differences in results hint that the Prandtl tip loss factor does not cover all the non-uniformities in the flow. Branlard et al. (2013) creates a circulation-based database in which the tip loss function for every circulation distribution is stored. These calculations are done by using a free-wake vortex code. Next, the BEM circulation is compared with the database, requiring an extra loop of calculations, where the algorithm searches for the best fit, resulting in an approximation of the tip loss function. The results show a clear improvement, however the method is depending on the size and accuracy of the database. In the present study it is preferred to create insights for a more generalized tip loss factor.

Two other examples on how vortex methods can be used for improving BEM are discussed in the papers of J. N. Sørensen, Dag, and Ramos-Garcia (2014) and Maniaci and Schmitz (2016). J. N. Sørensen et al. (2014) discusses that the induced effects of the wake on the tip of the blade has a decambering effect and therefore lowers the forces compared to what is modelled originally. The proposed decambering correction is applied next to the Prandtl tip loss factor and shows indeed improvements for the theoretical rotor and the National Renewable Energy Laboratory (NREL) 5MW rotor. However, J. N. Sørensen et al. (2014) states his correction is not enough and suggest improving the Prandtl tip loss factor on its own. Maniaci and Schmitz (2016) also state that the wake effects should be acknowledged in BEM. They create a modified Glauert tip loss factor by fitting it to results from free wake vortex panel code, and state that with this approach the wake effects are included. The results are promising, however the modified tip loss factor is dependent on two variables, which must be known upfront but vary for each rotor and operational conditions.

This literature review shows much recent activity on developing a better tip loss factor based on more physical methods than the simplified concept used by Prandtl. Shortcomings are seen in all these studies which then forms the motivation for this study. Moreover in section 3.2 several implementations of the tip loss factor are discussed and the effect of these differences in implementation are never assessed. Possibly one implementation outperforms the others. Furthermore, with the exception of Johansen and Sørensen (2004), all the discussed papers only look at the results by (experimentally) modelling a maximum of two rotors (see table 3.1) and therefore there exists a lack of generality. This creates an incentive to perform a parametric study of the tip loss factor applied on multiple rotors to gain insight on possible wider-spread improvements.

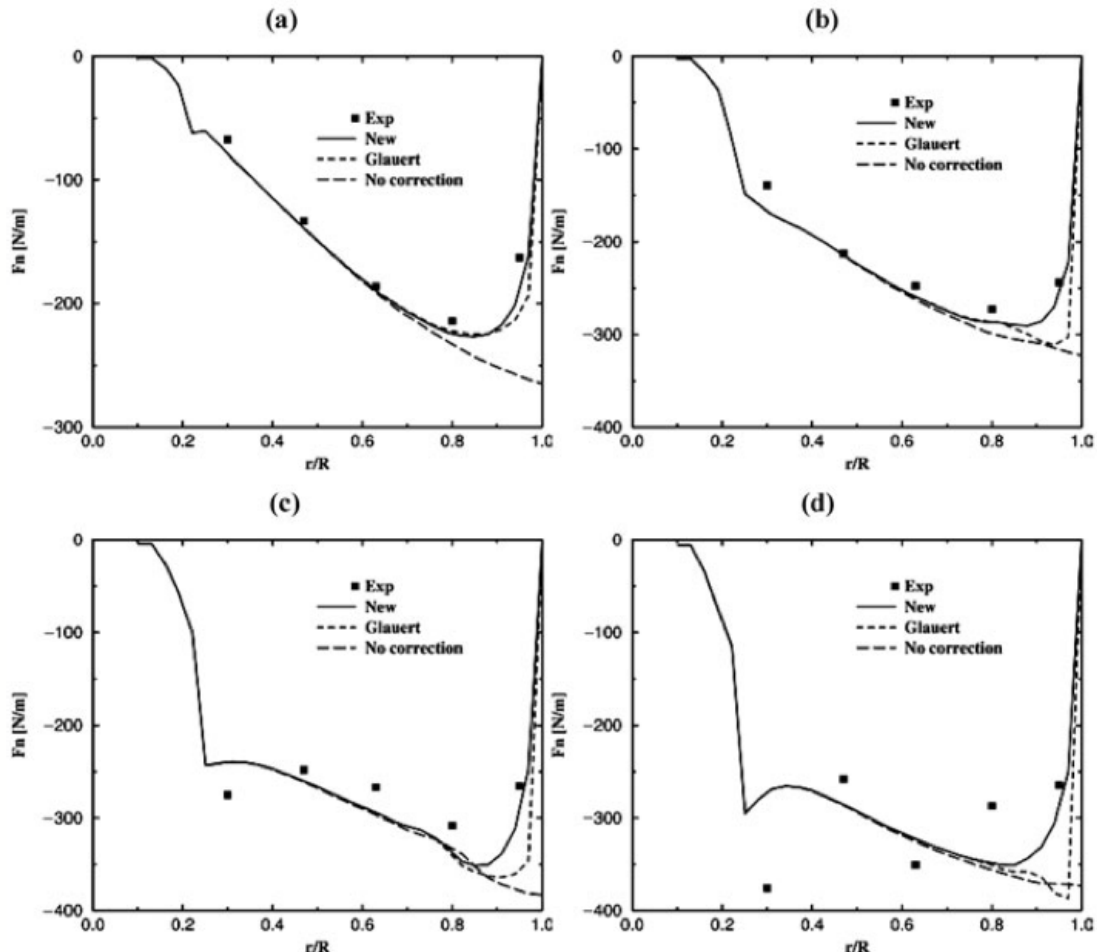


Figure 3.5: Normal forces for the NREL experimental rotor compared to the computed results of BEM with different tip loss factors at different wind speeds: (a) 7 m/s ($\lambda = 5.4$), (b) 10 m/s ($\lambda = 3.8$), (c) 13 m/s ($\lambda = 2.9$) and (d) 15 m/s ($\lambda = 2.5$) (Shen et al., 2005, figure 4). The label "new" stands for Shen's tip loss factor. The figure shows the improvements of results at the tip when there is a tip loss factor applied.

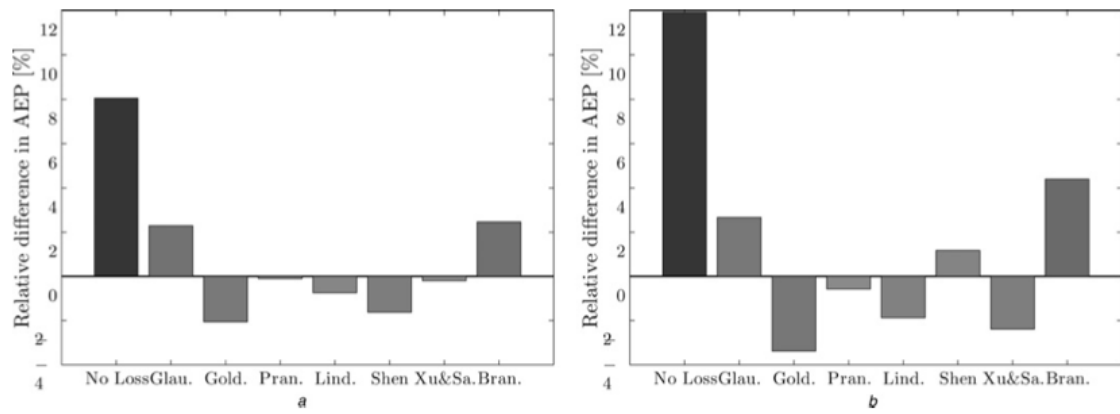


Figure 3.6: The relative difference of the annual energy production is calculated with respect to the average of annual energy production from all the simulations, when using several tip loss factors. Thus, a difference close to zero indicates that the used tip loss factor is performing close to the average. However, as the left and the right figures show the result for two different wind speeds, the results are deviating from one case to the other, and therefore no conclusions can be drawn on the comparison (Branlard et al., 2013, figure 1).

Paper	Rotor(s) used	Relevant key topic
Branlard et al. (2013)	only circulation distributions	tip loss factor database from vortex method
Breton et al. (2008)	NREL Phase VI	overview of results of mainly stall-delay factors but also a few tip loss factors
Johansen and Sørensen (2004)	NREL Phase VI, Danish 95kW Tellus, Danish 500 kW Nordtank	obtaining three-dimensional airfoil data from CFD and implemented in BEM
Koh and Ng (2016)	rotor of Bahaj et al (2007) ¹ , rotor of Mycek et al. (2014) ²	tip loss factor effects shown for tidal turbines
Maniaci and Schmitz (2016)	NREL Phase VI, NREL 5MW	modified Glauert tip loss factor by fitting it to vortex method results
Schepers (2012)	Mexico, Danish 100kW Tellus	vortex method tip loss factor compared to Prandtl tip loss factor
Shen et al. (2005)	Swedish WG 500, NREL experimental rotor	new tip loss factor created by fitting applied to force coefficients
J. N. Sørensen et al. (2014)	NREL 5MW	additional decambering tip factor
Yang et al. (2014)	Mexico	obtaining three-dimensional airfoil data from CFD and implemented in BEM

Table 3.1: This table gives an overview of the papers which discusses the tip loss factors and the rotors used.

¹Bahaj, Molland, Chaplin, and Batten (2007)

²Mycek, Gaurier, Germain, Pinon, and Rivoalen (2014)

Chapter 4

Computational Setup

In this chapter necessary explanations and code descriptions are given. The first section will start to give an overview on which blades are used. The three following sections will describe the aerodynamic models CFD, vortex code AWSM and the BEM code, respectively. In these sections also details will be given on the additional difficulties that have to be overcome in order to achieve the objective. The final section will give the setup for the study that is done on the effect of different operational conditions on the Prandtl tip loss factor.

4.1 Rotors

The assessment of the Prandtl tip loss factor is done by investigating the results of five rotors. The Mexico and NREL Phase VI rotors are relatively small and have been tested in wind tunnel experiments. The AVATAR and Innwind rotors are large (10 MW+) reference wind turbines, designed for the purpose to investigate the aerodynamics of the next generation of rotors. The fifth rotor is designed by the author.

Prandtl's derivation is based on a rotor with constant circulation. It is known that a blade with a constant circulation distribution along its span will only have trailed root and tip vortices. In other words, the variation of the axial induction factor along the span will be less for a blade that is approaching an almost constant circulation distribution. Therefore, the fifth rotor named as NewBlade is designed, which is based on the Mexico rotor, such that its circulation is close to constant, by optimizing the twist angle distribution.

The overall geometry and operational conditions are given in table 4.1. To give an overview on the twist angle and chord distributions, figure 4.1 plots both versus the normalized radius. Since the NewBlade rotor is based on the design of the Mexico rotor, the chord distribution is very similar, resulting in that the differences between them are hardly visible in figure 4.1b.

As can be seen in table 4.1, the rotors are exposed to a wide range of operational conditions. However, the CFD simulations are not performed for all rotors and conditions,

which will be discussed in section 4.2. Furthermore, the NewBlade rotor is used for a sensitivity study on the Prandtl tip loss factor. Section 4.5 will elaborate on this.

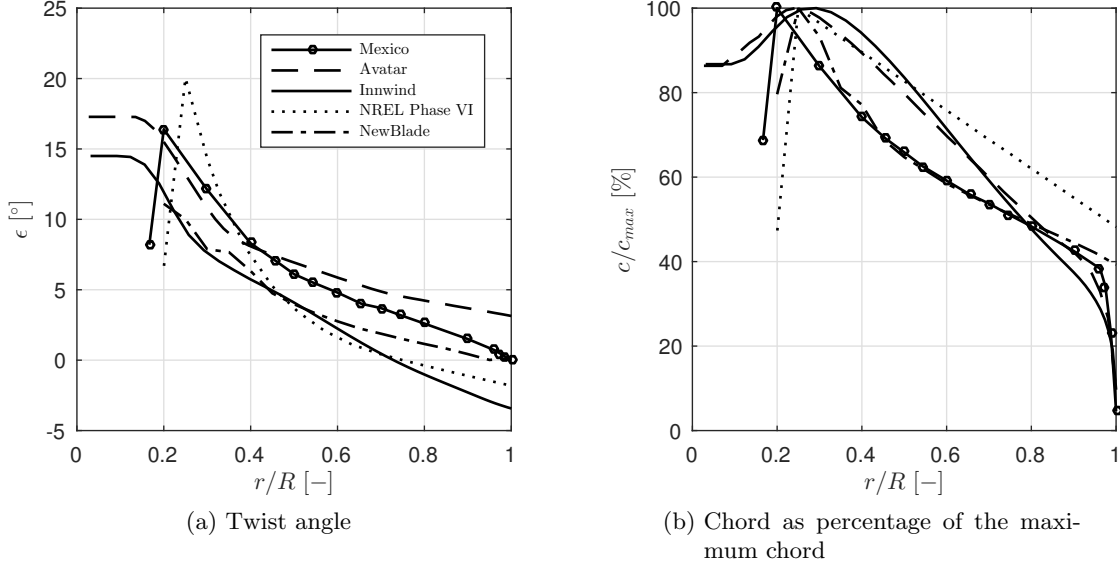


Figure 4.1: The twist angle and the chord distributions for the Mexico, AVATAR, Innwind, NREL Phase VI and NewBlade rotors. The chord is expressed as the percentage to the maximum chord, given in table 4.1.

	Mexico	AVATAR	Innwind	NREL Phase VI	NewBlade
Number of blades N_b [-]	3	3	3	2	3
Blade radius R [m]	2.25	102.88	89.17	5.03	1
Root radius [m]	0.21	2.8	2.8	0.19	0.1
Maximum chord c [m]	0.24	6.23	6.23	0.74	0.13
Pitch angle θ [$^\circ$]	-2.3	0	0	0	0
Hub height [m]	5.49	132.7	119.02	12.19	5.5
Rotational velocity Ω [rpm]	425.1	6/7.733/6/6	6/6/7.229/9.6/9.6	71.7	534.761
Wind velocity V_∞ [m/s]	10/11.9/15/24	6/9/11.55/15.4	6/7/9/16/21.3	5/6.74/10	4.7/5.71/6.67/ 8/10/13.325
Tip speed ratio λ [-]	10.02/8.42/6.68/4.17	10.77/9.26/5.60/4.20	9.33/8.00/7.5/5.60/4.21	7.55/5.60/3.78	11.91/9.81/8.40/ 7/5.60/4.20
Airfoil used	Cylinder RISO-A121 DU91-W250 NACA-64418	Cylinder DU600eq DU396 DU346 DU300 D240	Cylinder FF-W3-600 FF-W3-480 FF-W3-360 FF-W3-301 FF-W3-241	Cylinder S809	Cylinder Flat plate ¹

Table 4.1: General design data and operational conditions for the Mexico, AVATAR, Innwind, NREL Phase VI and NewBlade rotors.

¹Flat plate airfoil data for angles of attack between -12° and 12° . For angles of attack lower and higher than these values, the values for -12° and 12° , respectively, are used.

4.2 CFD

As already mentioned in the previous section, not all the operational conditions from table 4.1 can be simulated with CFD, simply due to the fact that this computational power is not available. The section will therefore first elaborate on which results are available. After this, the problem and possible solutions of extracting engineering variables from CFD results is explained. Finally, a definition of the CFD tip loss factor is discussed in section 4.2.3.

4.2.1 Description

CFD RANS results from the AVATAR, Innwind and NREL Phase VI rotors are available and used in this thesis. The AVATAR and Innovative (10-20MW) offshore rotor EU project (Innwind) results have been produced for the deliverable 2.3 'Power curve predictions' (N. N. Sørensen, Hansen, García, Florentie, and Boorsma (2014)) within the AVATAR project. Ellipsys3D from the Technical University of Denmark (DTU) is used as the CFD solver, which is an incompressible RANS solver (see N. N. Sørensen et al. (2014) for more details). The blades are fully meshed, with the same cell sizes for both rotors. The simulations for the NREL Phase VI rotor are performed by ForWind with the open-source CFD software OpenFOAM. Due to the assumptions of periodicity of time and space for axis-symmetric conditions, only one blade is meshed and half of the flow field is calculated.

For all the simulations the flow is uniform non-yawed without shear. An overview of the operational conditions is found in table 4.2. For all conditions the pitch angle, cone angle and tilt angle are set to zero. The datasets contain the mesh point locations, relative pressures and three-dimensional velocity components. Due to the immense size, they are initially post-processed by Tecplot and Paraview (the different file formats required the use of both programs) and finally with Matlab.

	AVATAR	Innwind	NREL Phase VI
Wind velocity V_∞	6/9	6/9	7/15
Rotational velocity Ω	6/7.733	6/7.229	71.7
Tip speed ratio λ	10.77/9.26	9.33/7.5	5.39/2.52

Table 4.2: Operational conditions of the used CFD results. The pitch angle, cone angle and tilt angle are set to zero.

In order to be able to define a tip loss factor that relates to the Prandtl tip loss factor, it would be beneficial to express the physical quantities resulting from the CFD computations in the 'same language' of BEM (and vortex methods), containing engineering variables such as the inflow angle ϕ , axial induction factor a and circulation Γ . This is discussed next.

4.2.2 Determination of the angle of attack

When going back to the equations which explained BEM and the Prandtl tip loss factor (section 2.3 and chapter 3, respectively), it can be concluded that the key (missing)

variable to determine all other missing variables is the angle of attack α . When the angle of attack is known, the inflow angle ϕ can be calculated with equation (2.28), and by obtaining the local force coefficients from the pressure differences, the rest of the equations can be calculated.

The definition of the angle of attack is purely two-dimensional. Figure 2.4 gives the simplified definition of the angle of attack α used in BEM. However, due to the presence of the blade section and the created downwash when the blade is finite (i.e. in three-dimensional case), the relative velocity component will not be straight but curved nearby the blade section. The effective angle of attack will therefore be different from the geometrical angle of attack drawn in figure 2.4. Thus, depending on where one would pick a point in the flow field, the direction of the relative flow would be different from another point, ergo the effective angle of attack would be different. To be able to compare the same angles from BEM and the vortex method with CFD results, it is desired to obtain the geometrical angle of attack from CFD but maintaining the effect of the three-dimensional flow on the angle.

With this knowledge, there exist multiple methods to extract the engineering variables or the airfoil characteristics, as others call them. Four are discussed shortly.

- Inverse BEM: the BEM equations given in section 2.3 are used in the same manner, except that the force coefficient equations (2.31) and (2.33) are replaced by the following equations.

$$C_n = \frac{F_n}{\frac{1}{2}\rho V_{rel}^2 c} \quad (4.1)$$

$$C_t = \frac{F_t}{\frac{1}{2}\rho V_{rel}^2 c} \quad (4.2)$$

In these equations, the normal force F_n and tangential force F_t are determined from the pressure differences calculated by CFD, see equations (4.3) and (4.4).

$$F_{n,i} = \oint p \cdot e_n ds \quad (4.3)$$

$$F_{t,i} = \oint p \cdot e_t ds \quad (4.4)$$

Hence, the induced velocities are calculated from the loads which are integrated from the CFD pressure distributions, illustrating that the airfoil data as used in the 'normal BEM' are not needed. The other steps remain the same. Corrections for three-dimensional flow, such as the tip loss factor, are not needed because the corresponding effects are incorporated in the pressure computations. Though, it is evident that because BEM is an one-dimensional theory, the accuracy may be questionable.

- Average Azimuthal Technique (AAT): this is a method described by Hansen et al. (1997) and Johansen and Sørensen (2004). For one radial section, the annular averaged axial velocity upstream and downstream can be plotted versus the distance to the rotor. The axial velocity at the rotor is then obtained by interpolating the results. A simpler approach is to take just one point upstream and one point downstream, both at the same distance from the rotor. From the approximated axial velocity at the section, the a can be calculated with equation (2.13), and therefore the angle of attack can be determined with the use of the velocity triangle (figure 2.4).

This method shows reasonable results for the midboard sections, where the annular averaged velocity is close to the real axial velocity. Beside this important matter, the method can only be used in axial flow conditions.

- Upwash from bound Vortex Line (UVL): this is one of the two methods from Shen et al. (2006, 2009), where in both methods the upwash is subtracted from the velocity field, in order to calculate the angle of attack from the corrected velocity components. The methods differ in the way the upwash strength is determined. In this first method, Shen et al. (2006) model the blade as multiple sections, which have a point vortex located at the quarter chord point. These vortices induce an upwash at a certain monitor point that can be calculated with the Biot-Savart law (equation (2.3)). The local forces are calculated from the pressure distribution and with the inflow angle, which is first estimated and later is determined from the velocity components, illustrating the need for an iterative loop. The strength of the point vortex can be calculated with the Kutta-Joukowski equation (equation (2.4)).

Opposite to AAT, no averaging is done and therefore this method should give results closer to the reality, near the root and the tip. It is also applicable for yawed conditions, which makes the method more valuable. However, monitor point positions, where the angle of attack is evaluated, chosen close the point vortex singularities will lead to convergence problems.

- Upwash from Distributed Vorticity (UDV): the induction at the monitor point can also be calculated by modelling a distributed vorticity along each airfoil section. This method is described by the same authors as from the UVL method (Shen et al. (2009)). By assuming that the Bernoulli equation (equation (2.6)) holds, the distributed vorticity can be calculated, knowing that it is equal to curl of the velocity field. Again, with the Biot-Savart law the upwash at a monitor point is determined, and finally the angle of attack is calculated with the upwash corrected velocity components.

Because the vorticity strengths are directly calculated from the pressure distribution, there is no need for an iterative loop. The difficulty of this method is to determine the sign that gives the direction of each vorticity point. Besides that the sign is opposite for the lower and upper surface, the sign also changes for areas with separated flow. However, the monitor point can be chosen closer to the airfoil due to the fact that there is no concentrated point vortex singularity.

For this thesis, where the local flow near the tips is of interest, it is evident that AAT is not a preferable method. To allow comparisons and because of the easiness to implement

the inverse BEM, the other three methods are used. More details on the UVL and UDV methods are presented in appendix A. The results are discussed in the next chapter.

4.2.3 Tip loss factor

When the engineering variables are determined, i.e. the induced velocities in the rotor plane and the induced velocity at the blade, a tip loss factor that is similar to the Prandtl tip loss factor should be formed.

The derivation showed that the Prandtl tip loss factor corrects the axial induction factor and angular induction factor for the non-uniform behaviour of the flow. Since the variables from the CFD results already incorporate the non-uniformities, a ratio has to be formed differently to express the level of non-uniform flow. Figure 4.2 plots the axial induction factor a and azimuthal averaged axial induction factor \bar{a} after correcting them with the Prandtl tip loss factor in the BEM equations. When the Prandtl tip loss factor is not applied, the lines in figure 4.2 would not show any differences. Therefore, the differences at the tip indicate the effect of the Prandtl tip loss factor and thus it is stated that the tip loss factor from the CFD results can be defined as equation (4.5).

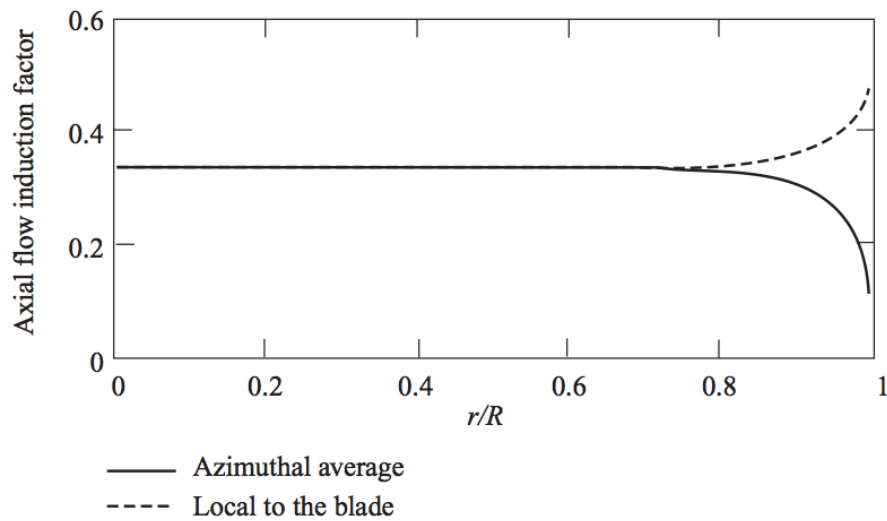


Figure 4.2: The variation of the axial induction factor (dashed line) and azimuthal averaged axial induction factor (solid line) for an optimum rotor operating at its design tip speed ratio (Burton et al., 2001, figure 3.36).

$$F_{CFD} = \frac{\bar{a}}{a} \quad (4.5)$$

In this equation, the azimuthal averaged axial induction factor \bar{a} is determined by annulus averaging a sufficient number of axial induction factor a , which are evaluated by one of the previously discussed methods.

4.3 Vortex method

The vortex method that will be used is made available by ECN and it is named as Aerodynamic Windturbine Simulation Module (AWSM). The details of the code will be given briefly. Part of the thesis is to validate the code. Hence, the set-up of the validation is explained next. To determine a tip loss factor, the same equation as in section 4.2.3 can be used. Opposite to the situation of CFD, vortex methods like AWSM provide engineering variables such as induced velocities relatively straightforward, although some extra computations are needed to calculate the azimuthal averaged axial induction factor \bar{a} . This is discussed at the end of this section.

4.3.1 Description

The used vortex method is the non-linear free wake lifting line vortex code AWSM, which is part of ECN's in-house aerodynamic simulation software containing the BEM and AWSM models (ECN Aero-Module). The main theory on vortex methods is already explained in section 2.2, but specific points will be discussed here.

As the blade is modelled as a lifting line, the thickness of sections are not taken into account. The forces can be derived from the circulation Γ , which is acting at the quarter chord point of each section, with use of the Kutta-Joukowski equation (equation (2.4)). For numerical stability, a so-called cut-off radius (LCO) is introduced, for cases when evaluation points are in proximity of the vortex singularities. This cut-off radius is an user-defined percentage of the vortex line element and is added to the value in the denominator of the Biot-Savart law (equation (2.3)). The discretization of the elements is defined in the input.

Similar to the previous cut-off radius, there is the wake cut-off radius WCO , for the same reason as the lifting line cut-off radius LCO . The wake develops as shown in figure 2.1. To assure full development of the wake and proper induced effects, the numbers of wake points should be such that the wake has convected at least a distance of three rotor diameters. The code allows to set the amount of self-influences of the wake, or in other words, defining the free wake properties. By setting the number of free wake points equal to the number of total wake points, the full wake is modelled as a free wake. Since the induced effects of the far wake on the blade are less and less profound when moving away from the rotor and the calculations of the far wake are expensive, the last part of the wake is set to be a prescribed wake. The convecting wake velocity can also be adjusted but for the simulations done in this research, it is kept to the default fixed velocity, which depends on the wake induction and onset velocity (see section 2.2).

The simulation code requires one input file containing information on which aerodynamic model should be run (BEM or AWSM), the blade design (size, twist angles and which airfoil data should be used, etc), rotor design (number of blades, hub and tower design, etc), environment (density, wind conditions, etc), operational conditions and simulation settings. In other files the airfoil and wind data is stored. An extra module called the external field module can be activated to calculate the flow field and pressure coefficients on user-defined locations. This module will be used extensively in this research.

For every blade, the aerodynamic properties of each section are outputted. Furthermore, the wake discretization with its circulation strength are also written to text files. When the external field module is used, an additional text file is created. The post-processing of the results is done with Matlab.

4.3.2 Validation

To illustrate the quality of results, AWSM is validated with data from the New Mexico experiment. In this experiment improvements are done on the experimental set-up and additional measurements are done, compared to its predecessor. Both experiments use the same Mexico rotor. Similar to the Mexico experiment, in the New Mexico experiment measurements are done for three wind velocity, corresponding to a turbulent wake state (10 m/s), the design condition (15 m/s) and a separated flow condition (24 m/s). The rotational velocity Ω in the simulations is set to 44.52 rad/s (corresponding to 425.1 rpm), and the pitch angle θ is set to -2.3° .

It must be noted that AWSM has already been validated with an experiment run with the NREL experimental rotor and with the Mexico rotor, both reported in the manual of ECN Aero-Module (Boorsma and Grasso (2016)). For both cases, the manual shows the comparisons of the radial distribution of the normal and tangential forces for axial flow and the azimuthal variation of these sectional forces at five positions along the blade for yawed flow. For the NREL rotor, there is also a dynamic inflow validation done.

The validation in this study will deviate from the chosen approach in the manual. It will be comparable to what is done by Schepers et al. (2012), because this will open the possibility to use the benchmark results originated from the participants of Mexnext. Schepers et al. (2012) show the results from the Mexico experiment compared to a variety of aerodynamics codes (CFD and vortex methods), including AWSM, concerning loads and velocity traverses comparisons for axial and yawed flow. Since yawed flow is outside of the scope of the thesis, this validation will be focussed on axial flow.

4.3.3 Tip loss factor

For the same reasons as discussed in section 4.2.3, the tip loss factor is defined similarly to equation (4.5), see equation (4.6).

$$F_{AWSM} = \frac{\bar{a}}{a} \quad (4.6)$$

From the output files, the axial induction factor a can be calculated with equation (2.13). The determination of the azimuthal averaged axial induction factor \bar{a} requires extra computations, which is done by the use of the external field module. With this module additional evaluation points can be defined. For this purpose, the module can be used in two ways:

1. Rotor plane method: the additional evaluation points are spread out in the entire rotor plane. The azimuthal averaged axial induction factor \bar{a} is then calculated at one time step, corresponding to one azimuthal position of the rotor blades.

2. 9 o'clock method: the additional evaluation points are only specified along a line, for example at 9 o'clock if one would imagine the rotor plane upfront. For this method, the azimuthal averaged axial induction factor \bar{a} is calculated by averaging the values from a full rotation of the rotor.

The results will show that the computational time, resolution of the results and simulation settings will play an important role in calculating the AWSM tip loss factor.

4.4 BEM

Also the BEM code is made available by ECN. A short description is given first and secondly the used variation of the Prandtl tip loss factor in ECN's code is discussed.

4.4.1 Description

The BEM code in the ECN Aero-Module is more advanced compared to the BEM description in section 2.3, to be able to account for dynamic inflow or yawed flow. Without going into detail, this is done by discretizing each annulus of the rotorplane into separated stream-tubes for all the blades. Depending on the type of wind conditions, the code checks the convergence of the azimuthal averaged axial induction factor or the axial induction factor. Since all wind conditions in this research are uniform axial, the code stops when there is convergence of the axial induction factor.

The input files are the same as discussed in section 4.3, with specific parameters for the BEM simulation. One obvious parameter is to turn on or off the Prandtl tip loss factor in the calculations. The same holds for the Prandtl root loss factor, which is a similar correction factor that influences the results near the root. The location of the root vortex can also be adjusted. Finally, as described in section 2.3, there is the unresolved discussion on whether to include the drag in the induction calculation and how to correct BEM for when the momentum theory breaks down. Therefore, the code gives the option to include the drag and to set the critical value of the axial induction factor a for which the turbulent wake state model should be used.

For the simulations done in this thesis, most settings are set to default, resulting in a critical value of axial induction factor a of 0.38 and the exclusion of the drag. Furthermore, the Prandtl root and tip loss factors are turned off, as these calculations are done afterwards. The results will show that the difference between calculating the Prandtl tip loss factor in the iterative loop compared to calculating the Prandtl tip loss factor afterwards only differ to a small percentage.

4.4.2 Tip loss factor

The derivation of the Prandtl tip loss factor in chapter 3 showed that there are many variations. Although the settings for the BEM simulations will be such that the Prandtl tip loss factor will not be used in the iterative loop, it is interesting to know that the coded tip loss factor in ECN Aero-Module is comparable to one of the roller bearing analogy tip

loss factors. The coded tip loss factor is labelled as F_{ECN} and is formed, in terminology described with equations (3.21) to (3.23), by setting r_2 and r_3 to R and using the tip values for a and a' . The resulting equations are given next.

$$F_{ECN} = \frac{2}{\pi} \arccos \left[\exp \left(-\frac{N_b}{2} \frac{R-r}{R} \frac{\sqrt{V_n^2 + V_t^2}}{V_n} \right) \right] \quad (4.7)$$

$$V_n = U_\infty \left(1 - \frac{a(R)}{2} \right) \quad (4.8)$$

$$V_t = \Omega R (1 + a'(R)) \quad (4.9)$$

4.5 Sensitivity study

It is obvious that the many variations of the Prandtl tip loss factor will lead to different results. Therefore, the NewBlade rotor will be used to evaluate all of them, to a wide range of operational conditions, as it was discussed in section 4.1 that this rotor satisfies the constant circulation assumption made by Prandtl. AWSM simulations will be used to verify the results of the variations.

The derivation of the Prandtl tip loss factor showed that the only variable dependent on the operational conditions, is the angle between helical wake sheets ϵ_w . For implementation the tip loss factor in BEM, this angle is estimated to be the same as the inflow angle ϕ . By comparing the equation for the inflow angle ϕ given in equation (2.25) with the equation for the tip speed ratio λ given in equation (3.26) (where it is common to set the a and a' to zero in this equation), it can also be said that the Prandtl tip loss factor only depends on tip speed ratio λ .

Furthermore, from the knowledge that the vortex method AWSM incorporates vortex roll-up, wake expansion and distortion, it is interesting to see what the effect is of changing the wind velocity V_∞ or rotational velocity Ω , separately or in the same manner, as these variables affect the wake properties differently.

These considerations motivate to define several cases, which are discussed next.

1. Original: the NewBlade rotor is run at the design conditions.
2. Pitch angle: in order to see the effect of loading on the blades, the pitch angle θ is changed and the twist angle ϵ distribution is adjusted to keep the circulation constant. In essence, this case will thus compare different blades, to ensure that the assumption of Prandtl is met.
3. Wind velocity: by changing the wind velocity V_∞ , the tip speed ratio λ is changed.
4. Rotational velocity: the tip speed ratio λ can also be changed by setting the rotational velocity Ω to other values. This is done in this case.

5. Fixed tip speed ratio: for this case the wind velocity V_∞ and rotational velocity Ω are changed such that the tip speed ratio λ is kept the same. This is done to see the effect of different wake convection.
6. Number of blades: to see the effect of the number of blades N_b on the Prandtl tip loss factor, simulations are done with two and four blades (ECN Aero-Module does not allow other values).

Table 4.3 gives the defined cases and the corresponding settings.

Note that these cases are additional to the already discussed settings in the previous sections. The other and NewBlade rotors are subjected to the conditions shown in tables 4.1 and 4.2, depending on the aerodynamic model used.

Variable \ Case	Original	Pitch angle ²	Wind velocity	Rotational velocity	Fixed tip speed ratio	Number of blades
Number of blades N_b	3	3	3	3	3	2/4
Pitch angle θ [°]	0	-3/+2/+4/+5/+8	0	0	0	0
Rotational velocity Ω [rpm]	534.761	534.761	534.761	320.856/427.809/ 641.713/748.665	320.856/427.809/ 641.713/748.665	534.761
Wind velocity V_∞	8	8	13.33/10/6.67/ 5.71/4.7	8	4.8/6.4/9.6/11.2	8
Tip speed ratio λ [-]	7	7	4.2/5.6/8.4/ 9.8/11.9	4.2/5.6/8.4/9.8	7	7

Table 4.3: The NewBlade rotor is subjected to different cases for which this tables shows the operational settings.

²The NewBlade rotor is re-designed to assure a constant circulation by changing the twist angle distribution.

Chapter 5

Results

In this chapter the results will given in the order of the stated sub-objectives in section 1.2. Therefore, section 5.1 will start on extracting the angle of attack from CFD results, where after the tip loss factor defined in equation (4.5) is calculated. The second section will show the validation of AWSM and how to determine a similar tip loss factor. Section 5.3 will discuss the 72 variations of the Prandtl tip loss factor by using the NewBlade rotor. The results of the sensitivity study are also given and explained. The last section will assess the Prandtl tip loss factors for the real rotors and show the general trends deducted from these results.

For visualizing arguments, one figure will only contain one legend that applies for all sub-figures in that specific figure, unless the sub-figures contain different or additional information.

5.1 CFD

In order to be able to compare BEM results including the tip loss factor with CFD results, the induced velocities must be known. When the angle of attack is extracted from the flow field and pressure computations, these velocities can be calculated. As introduced in section 4.2, the inverse BEM, Upwash from bound Vortex Line (UVL) and Upwash from Distributed Vorticity (UDV) methods are used to obtain this angle for their own reasons. The results of these methods are discussed in section 5.1.1. Following, section 5.1.2 will relate the CFD results to the definition of the tip loss factor.

5.1.1 Determination of the angle of attack

The angle of attack is determined for the rotors at operational conditions given in table 4.2. The AVATAR rotor will be used to present the results because most observations are applicable to the other rotors as well. If not, the deviating results will be also discussed. The remaining results can be found in appendix A.4.

The figures will show the axial induction factor a , axial induced velocity u_{ind} and inflow angle ϕ , because with these variables the results can be better explained. All three are functions of the angle of attack, hence the name of the section.

The results from the inverse BEM method are discussed first, whereafter the results of the two upwash methods are presented. At the end, a comparison is done, including results obtained from other participants in the Mexnext project for verification reasons.

Inverse BEM By calculating the force coefficients directly from the pressure values computed by CFD, an angle of attack can be relatively easily determined with the same BEM equations. However, due to that there are multiple forms of the BEM theory, especially considering the several correction factors which require different implementations, the results will differ. Therefore, two methods are discussed. The first inverse BEM method is based on the equations given in section 2.3 and calculating the force coefficients C_n and C_t with equations (4.1) and (4.2). The Glauert correction that is given in Hansen (2008) is used in case of high values of the axial induction factor a . Lindenburg (2003) provides a different inverse BEM algorithm. This one is used as the second inverse BEM method. In his implementation, Lindenburg (2003) uses the momentum break-down correction described by Wilson (1986) and also applies a Prandtl root and tip loss factor to correct the velocities for the distributed (instead of concentrated) induced effects of the trailed vortices.

The results for the AVATAR rotor at 6 m/s are given in figure 5.1. The inverse BEM methods seem to agree with each other, which is also the case for the AVATAR rotor at 9 m/s.

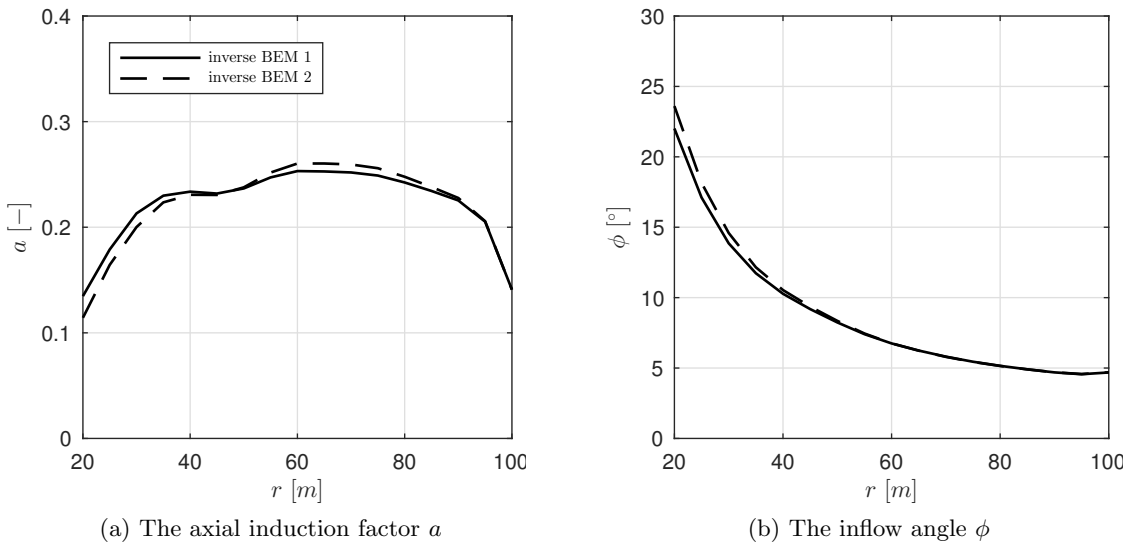


Figure 5.1: The results of the axial induction factor a and inflow angle ϕ from the two inverse BEM method for the AVATAR rotor at 6 m/s. The first method is the method including the Glauert correction given in Hansen (2008), where the second method is given in detail by Lindenburg (2003). It is seen that the methods agree on the results.

However, the methods show different results for the Innwind and NREL Phase VI rotors. Figure 5.2 plots the results for the Innwind rotor at 6 m/s, but the results for 9 m/s are similar. It can be seen that the axial induction factor a is close to or above the critical value for which the momentum theory breaks down (most corrections are active for $a > 0.4$). Therefore, the differences of the results can be explained by the fact that the two inverse BEM methods uses different momentum break-down corrections.

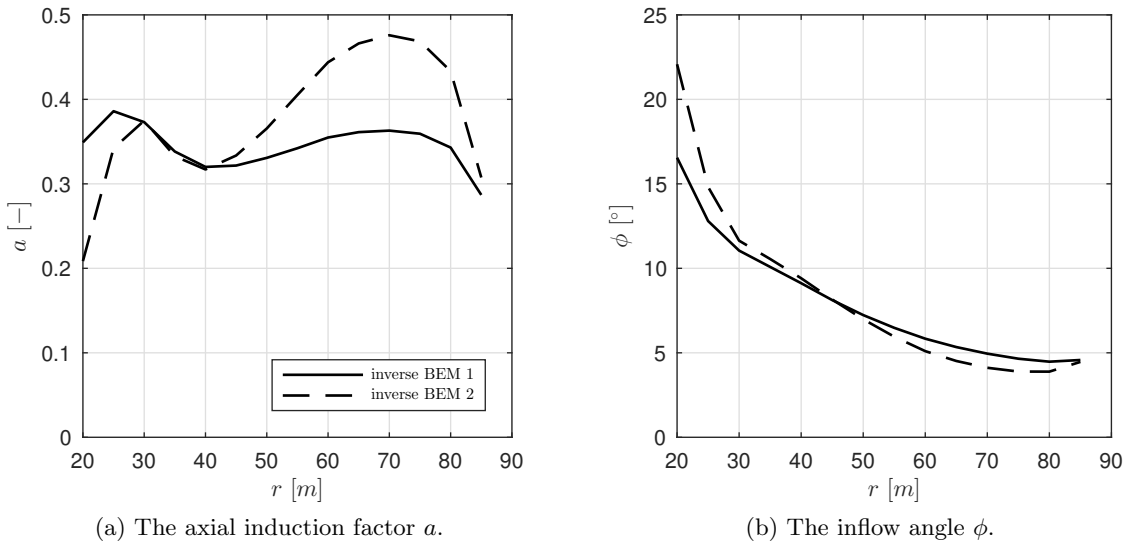


Figure 5.2: The two inverse BEM methods show deviating results for the Innwind rotor at 6 m/s, which can be explained by the use of a different momentum break-down correction, as the value for the axial induction factor a is indeed high.

This is not the reason for the deviating NREL Phase VI results, because figure 5.3 shows that the axial induction factor a is very low. Note that due to these low values, the scale of figure 5.3a is changed and the difference between the methods are stronger visible, compared to figure 5.2. By remembering the twist angle distribution given in figure 4.1a, the high values for inflow angle ϕ indicate that for this condition (15 m/s) the flow will be separated from the blade.

Upwash methods The results from the two upwash methods are discussed next. Where both methods subtract the upwash from the flow field, they differ on how the upwash is calculated. The UVL method models the lifting capabilities of each section as a point vortex located at the quarter chord point, resulting in resembling the blade as a lifting vortex line, where the UDV method models the lifting capabilities by distributed vorticity along the sectional surfaces. It is therefore expected that the results will differ when evaluating the angle of attack close to the blade, as the strength of the point vortex singularity is higher compared to when there is a distribution of vortices. This monitor point dependency is supposed to decrease for locations further away from the blade and hence the two methods will show similar results. In the scope of comparing the CFD results with the tip loss factor, the ideal case would be that there is minimum dependency on the location of the monitor point, in order to determine the induction factors properly.

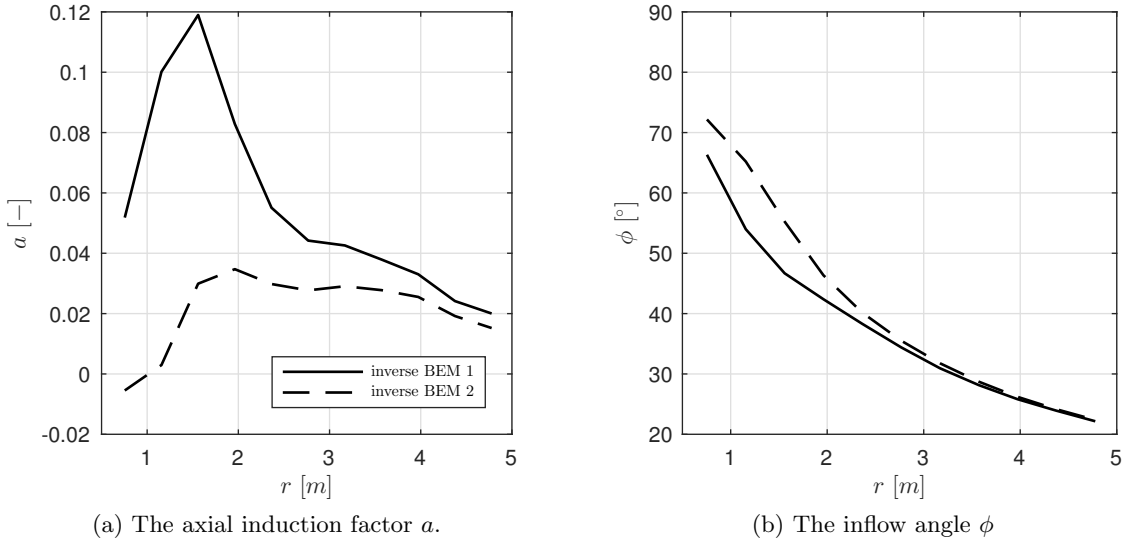


Figure 5.3: For the NREL Phase VI rotor at 15 m/s it is clear that the rotor operates in stall conditions, given that the inflow angle ϕ is high and the twist angle distribution along the span of the blade (see figure 4.1a).

Because the induced velocities in the rotor plane are of interest, the monitor points are placed in this plane and at distances in terms of the local chord c from the local leading edge, in a circular manner. Figure 5.4 visualizes 16 monitor points from $0.5c$ to $8c$ for one AVATAR blade which is in the 12 o'clock position. The points that coincide with the next blade will be discussed later. Although the distribution of the monitor points is set to be uniform (i.e. at $0.5c$, $1.0c$, $1.5c$, etc), it is seen that due to the deviating positions of the mesh points the actual distribution of where the angle of attack will be evaluated is less uniform. Without having done any computations, this first lesson learned is already clear.

The effect of the number of sections N on the results is investigated next. The blades are discretized with a fixed discretization step in order to model the induced effects in an uniform matter. After all, if a non-uniform sectional distribution is chosen, the computed upwash at a monitor point will be influenced stronger by the region of the blade where the discretization is denser. The AVATAR blade is divided in N sections from $r = 20$ m to $r = 100$ m. Figure 5.5 shows the effect of the number of sections on the results for the AVATAR blade at 9 m/s, when computing the inflow angle at several chord distances from the leading edge with both upwash methods for the radial section at $r = 60$ m.

For clarity, monitor points chosen at a larger distance from the leading edge are not plotted, because at these positions it is known that the upwash is less strong, leading to smaller differences for different values of the number of sections (this is already visible for the monitor points at $2c$ and $4c$). When choosing the monitor points closer to the blade than $0.5c$ both methods show irrelevant results, which will become clear later in this section.

For the both methods a clear convergence is visible in figure 5.5. These same trends can also be shown for the Innwind and NREL Phase VI rotors. The convergence is

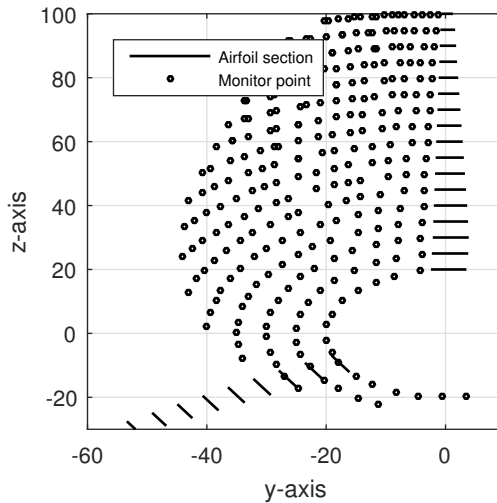


Figure 5.4: The AVATAR rotor plane showing the locations of the monitor points used in the upwash methods. The spread of monitor points is not uniform due to that the mesh is not uniform. At inboard sections, some monitor points are overlapping with the next blade, which will lead to fluctuations results at these monitor points.

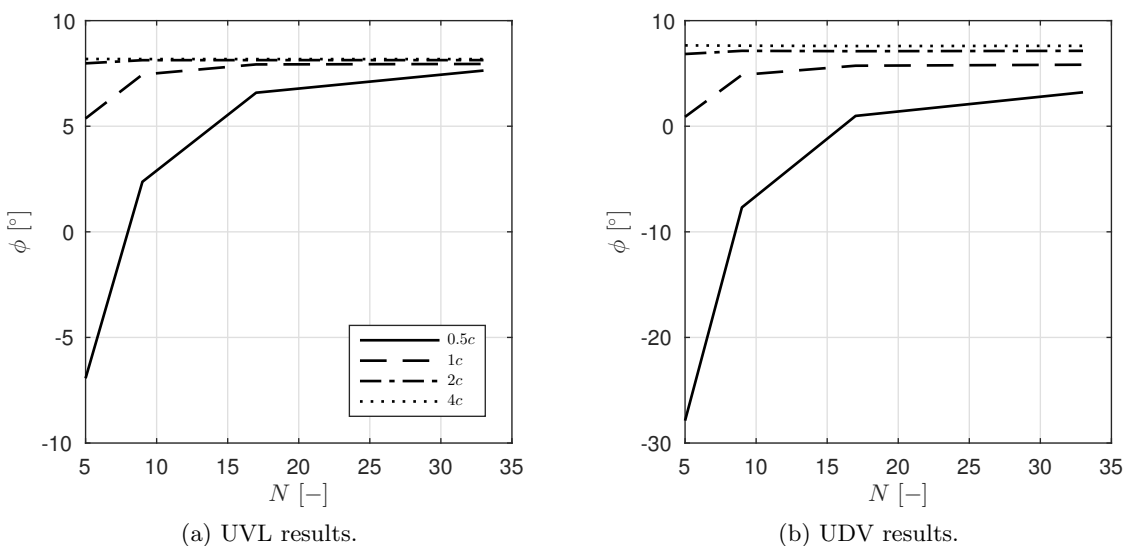


Figure 5.5: The inflow angle ϕ versus the number of sections N for the radial section at $r = 60$ m of the AVATAR rotor at 9 m/s, plotted for multiple monitor points. The number of sections N only has an influence on the monitor points chosen close to the airfoil.

explained by the fact that for a low number of sections, the upwash is computed with an overestimated strong influence of the root and tip sections. As this upwash is deducted from the velocity field, the inflow angle ϕ will be underestimated. This explains that the inflow angle ϕ values near the airfoil increases with increasing the number of sections.

A higher number of sections also means that there is more CFD data to process, resulting in longer computational times. Therefore, for the initial investigation of the accuracy of the upwash methods, a reasonable amount of number of sections is chosen based on results such as presented in figure 5.5. Table 5.1 gives an overview of the discretization setting used in the remaining part of the results.

	AVATAR	Innwind	NREL Phase VI
Discretization domain	20 m to 100 m	20 m to 85 m	15 % to 95 % of R
Discretization size	5 m	5 m	8 % of R
Number of sections N	17	13	11

Table 5.1: Accepted number of sections N for the AVATAR, Innwind and NREL Phase VI rotors.

For the sake of readable figures, not all results for every section are plotted. For example, figure 5.6 shows the results for the AVATAR rotor at 6 m/s for only five sections. The top sub-figures plot the axial induced velocity u_{ind} and the bottom sub-figures plot the inflow angle ϕ versus the position of the monitor points. The left-hand sub-figures show the results from the vortex line method (UVL) and the right-hand figures show the results calculated with the distributed vorticity method (UDV).

Several observations can be done here, which are universal for each rotor. As an example the AVATAR rotor at 6 m/s is taken, with the results shown in figure 5.6.

1. The most striking results are seen for the inboard section at 20 m with monitor points at 4.0 c to 6.0 c . The large fluctuating results are due to that at these positions, the monitor points are located very close to or even on the inboard section of the next blade. This can be seen in figure 5.4 for the first three sections. Note that in this figure the monitor points are placed at 0.5 c , 1.0 c , 1.5 c , etc, up to 8.0 c and thus for the radial section at 20 m, the positions at 4.0 c to 6.0 c are the 8th to 12th point, counting from the leading edge of the blade at 12 o'clock.
2. The effect of the point vortex singularity used in the vortex line method (UVL) is clearly visible for the section at 20 m:
 - Before the position of 5.0 c from the leading edge, the upwash strength is exaggerated in downward direction due to the point vortex, resulting in lower values for the axial induced velocity u_{ind} and higher values for the inflow angle ϕ , as seen in figures 5.6a and 5.6c.
 - At the position of 5.0 c it can be seen in figure 5.4 that the monitor point coincide with the section of the next blade. Thus, the monitor point is very close to the core of the singularity, leading to a jump in results.
 - For the monitor point positions just after 5.0 c , the nature of the point vortex singularity exaggerates the upwash, resulting in a higher values of axial induced

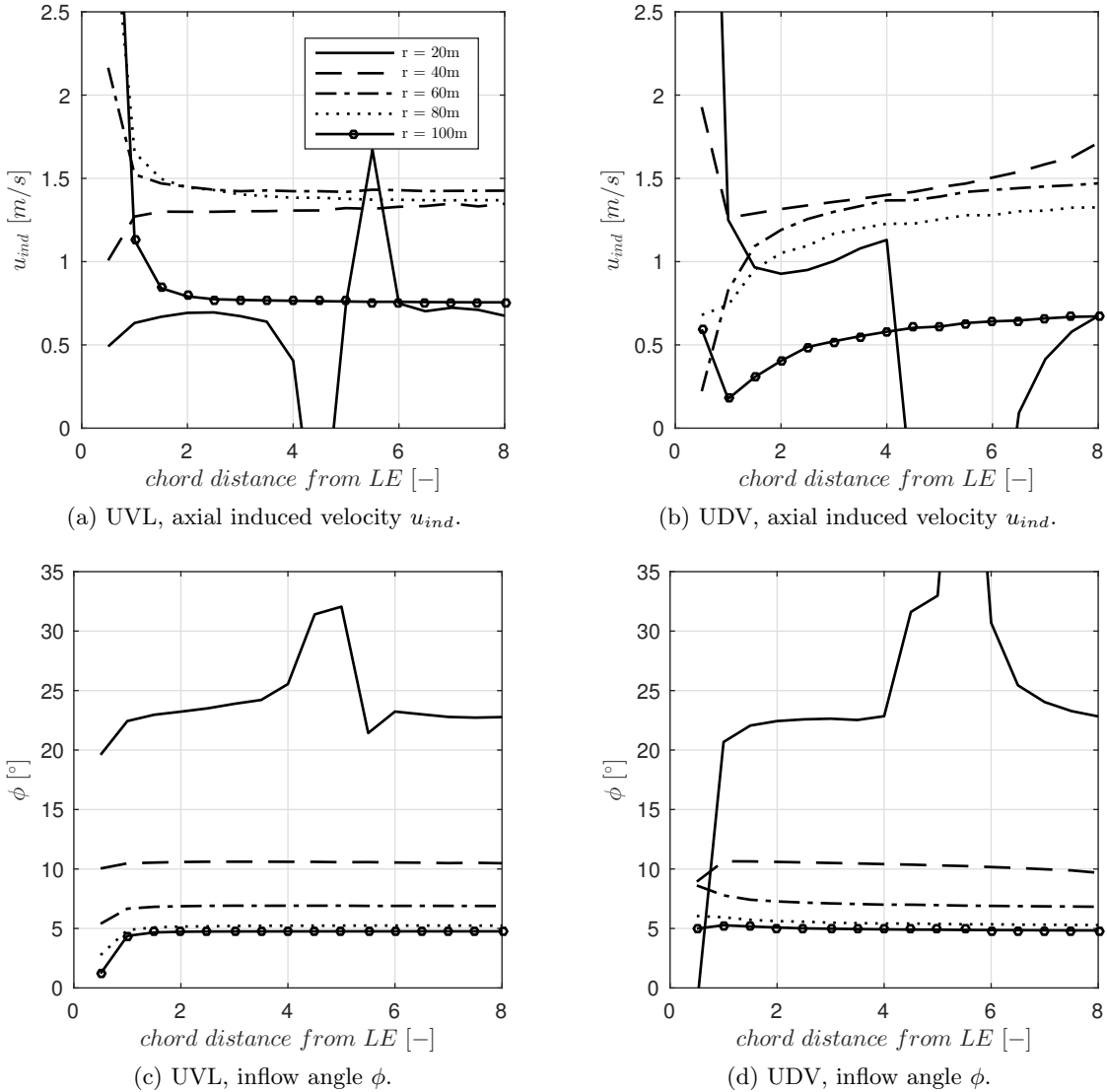


Figure 5.6: The axial induced velocity u_{ind} and inflow angle ϕ results from UVL and UDV for the AVATAR rotor at 6 m/s shown for five sections and monitor points located from $0.5c$, $1.0c$, $1.5c$, etc, to $8.0c$. The results especially deviate for the axial induced velocity u_{ind} and when the monitor points are positioned close to or on the next blade, shown for the monitor points between $4.0c$ and $6.0c$ of the section at $r = 20$ m.

velocity u_{ind} and lower values for the inflow angle ϕ . To help visualizing this, imagine that for the section drawn in figure 2.4, there is a point vortex placed at the quarter chord point in anticlockwise direction (because it is creating lift). Due to the placement of this point vortex, the vertical component in the velocity triangle will be smaller than drawn in the figure. This means that the value for the axial induction factor a and thus the axial induced velocity u_{ind} is higher and the inflow angle ϕ will be smaller, which is exactly visible in figures 5.6a and 5.6c.

3. The influence of the next section on the results from the distributed vorticity method (UDV) for the section at 20 m shows a strong downwash effect: the corrected flow field is in a stronger downward direction (vertical component in the velocity triangle, figure 2.4, is larger), resulting in higher and lower values for the axial induced velocity u_{ind} and inflow angle ϕ , respectively.
4. For the other sections, the UVL method shows convergence for the axial induced velocity u_{ind} when evaluating the variables at larger distances from the leading edge. This is less visible for the UDV method, especially for the inboard sections.
5. The comparison of values of the axial induced velocity u_{ind} between the two methods at higher number of chord distances show that the methods generally agree at this distance, except for the second plotted sections of each rotor, as these are again very close to the next blade. This is illustrated in figure 5.7 for the AVATAR rotor at 6 m/s. In this figure the differences between the two methods are plotted along the span of the blade for three monitor point locations.

For the other rotors and conditions the trends are the same, however the magnitude of the deviations are different, especially for the inboard sections. This will become clear when the axial induction factor a and inflow angle ϕ are plotted versus the span of the blade later on in this section.

6. Both methods show small dependency of the monitor point location on the calculated inflow angle ϕ . They also agree on the value of the angle, especially for the outboard sections. However, when being very critical, the UDV results show a slight decreasing effect on the inflow angle ϕ for increasing number of chord c distances. For the AVATAR rotor this is less pronounced compared to the results of the other rotors. Due to that at these distances the strength of the upwash is lower and the effect of the section is minimum, it is not understood why this difference is visible.
7. The expectation of more constant results independent on the choice of positioning the monitor points for the UDV method compared to the UVL method is not met. This is not understood at this moment. The analysis of the results is also difficult to assess, as it is not known what the truth is.

Except that the magnitude of the difference between methods are different, there are no observations that apply specifically to one rotor or operational condition, as shown in appendix A.4.

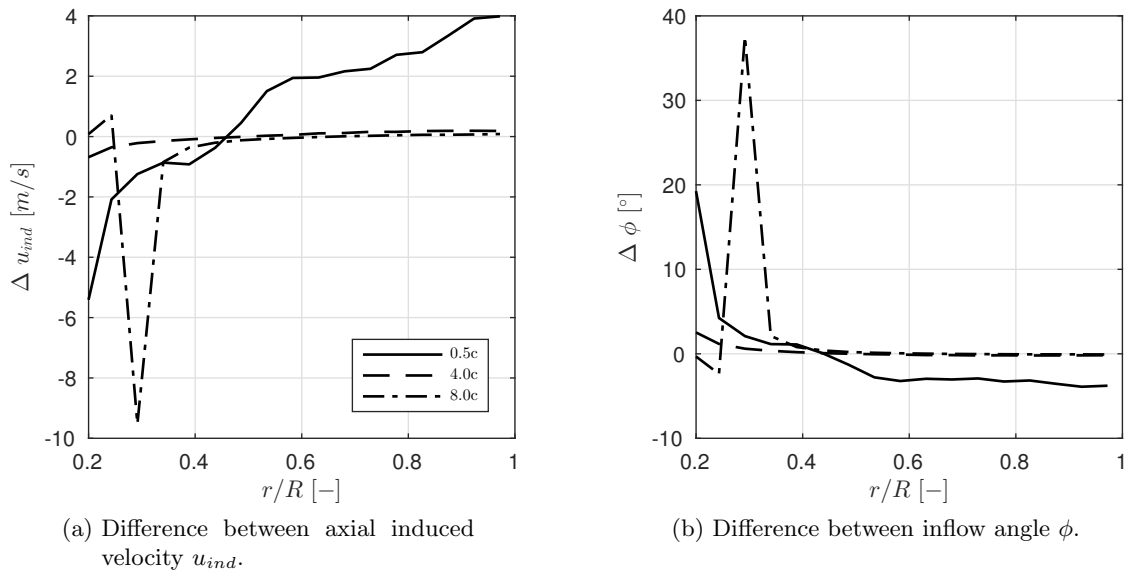


Figure 5.7: The results from UVL minus the results from UDV for the AVATAR rotor at 6 m/s for 3 monitor point positions. It can be seen that the methods at a larger distances from the leading edge are more similar, in contrary to the results for 0.5c. The inboard peak for 4.0c is due to that for this section the monitor points are close to or on the next blade.

Comparison of methods In order to plot the results from UVL and UDV versus the inverse BEM results, one monitor point location should be chosen. From the listed observations and figure 5.7 it can be concluded that the two upwash method agree for a monitor point not too close to leading edge but also not at a location for which the influences of the next blade is strong. Therefore, the location of 4c from the leading edge is chosen to compare the results with the inverse BEM results. The results from the first inverse BEM method are used, because the second method showed curved results for the Innwind results, where it is shown in appendix A.4 that the two upwash method do no show this behaviour. To keep the comparison clear, the second method is thus discarded.

Furthermore, as the subject of extracting the angle of attack α is a part of benchmark defined in the Mexnext project, results from other participants that uses same and several other methods are available to the author. Due to that the benchmark is still up and running, these results can not be shown in this thesis. Though, as Eva Jost from the university of Stuttgart has performed the same analysis with her implementation of the UVL method and is able to do this analysis for a very high number of sections, permission is asked and granted to show her results with the results discussed here.

The comparison of results for the AVATAR rotor at 6 m/s is given in figure 5.8. To see the difference between choosing the monitor point at 1.0c (Eva Jost did not provide the results at 0.5c) and 4.0c from the leading edge, both are plotted, with 1.0c on the left-hand side and 4.0c on the right-hand side. Furthermore, Eva Jost discretized the AVATAR blade into 103 sections.

It is encouraging to see that the results of the UVL methods are almost identical for 4.0c. From the analysis of the effect of the number of sections N it is expected to see

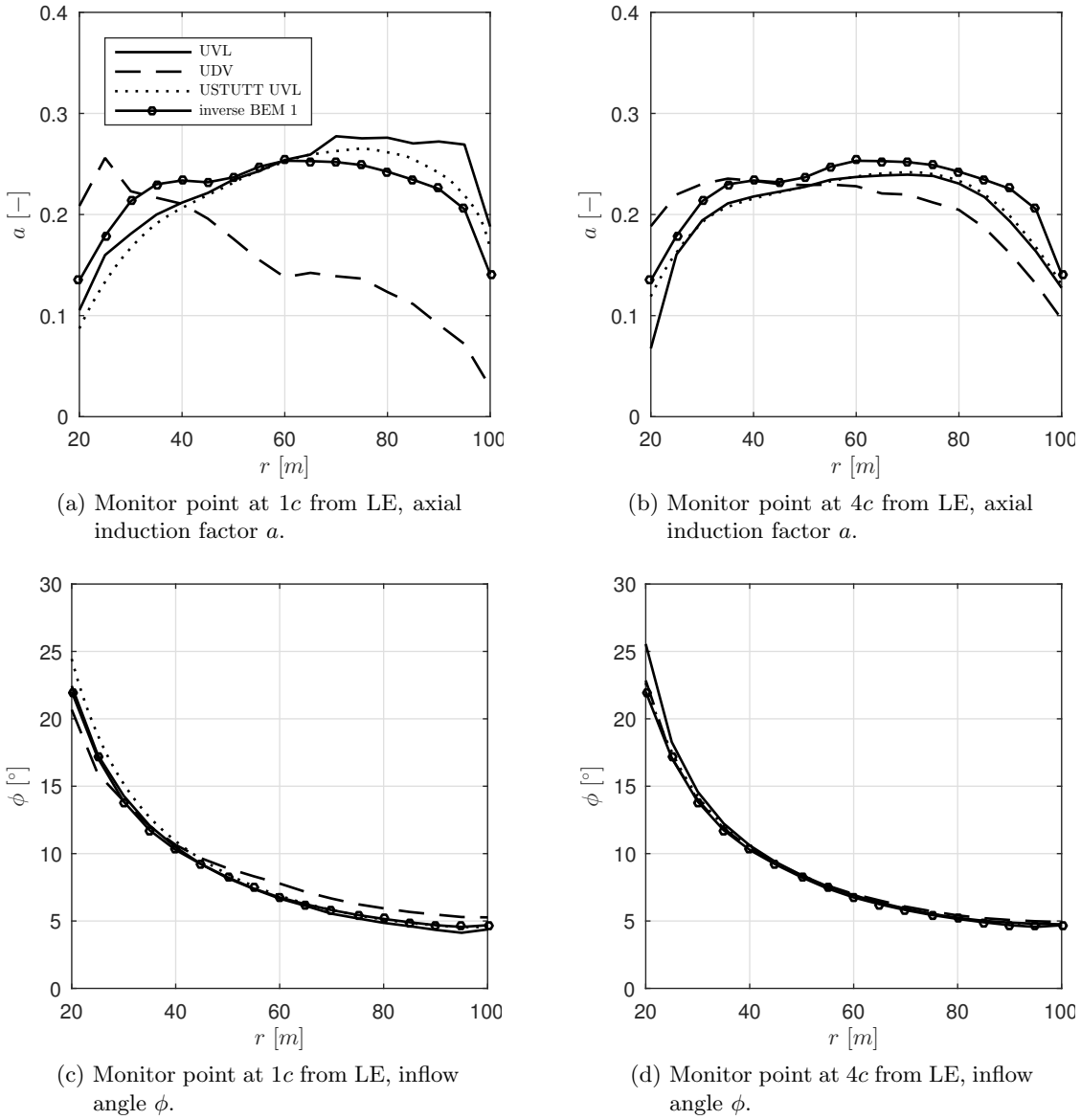


Figure 5.8: The results from all four methods to extract the angle of attack α from the CFD results for the AVATAR rotor at 6 m/s, shown for two monitor point positions. The UVL results from the University of Stuttgart (USTUTT) are obtained with discretizing the blade in 103 section compared to 17 sections in this thesis. Because the results are similar, the UVL method is verified. The UDV results at $1.0c$ deviate largely, but because it is not known what the exact truth is and the fact that the point vortex used in UVL is influencing the results at these locations, it is difficult to state which results are better.

deviating results between the two UVL methods when evaluating closer to the blade, which is visible in figure 5.8a. The inverse BEM method can not calculate the variables at different monitor positions, so these results are the same in the left and right figures. The UDV method at $1.0c$ produces mismatched results compared to the UVL method, which was expected from the observations done with figure 5.7, but it was not known which method was performing better at the smaller distances. From figure 5.8a it can be concluded that UDV does not give reasonable results monitor positions close to the blade, as the other three results are fairly comparable.

This is also true for the AVATAR rotor at 9 m/s , see figure A.7. For the other two rotors, UDV shows deviating results for the inboard sections even at $4.0c$. As an example, this is shown for the Innwind rotor at 9 m/s in figure 5.9, where the rest of the results can be found in appendix A.4. Although similar plots to figure 5.7 show that a moderate agreement is found for the axial induced velocity u_{ind} evaluated at $4.0c$, the differences are more exposed when plotting the axial induction factor a . The explanation may be found in investigated separated flow in these regions because then the equations for the UDV method are different as given in appendix A.3, however the provided CFD data does not allow to do this at the moment of writing this thesis. Furthermore, it is not expected that for these operational conditions the Innwind rotor operates in largely stalled conditions.

Conclusion

From this investigation it is clear that the results from the different methods tend to agree better when monitoring the angle of attack at a sufficient distance from the blades. However this is not always true for the UDV method. The results for the inverse BEM methods will differ when the conditions are such that the BEM equations have to be corrected. For the upwash methods, there is a dependency on the number of sections N and an even larger dependency on the placement of the monitor points. It seems that the UVL method provides results that are more in agreement with the expectations, although it is known that the point vortex influences the calculations strongly when the monitor points are placed close to the blade. Therefore, it might be that the truth may be somewhere in between the results.

5.1.2 Tip loss factor

Despite that the questions which remain on the extraction of the angle of attack, one method is chosen in order to create insights on the Prandtl tip loss factor.

The inverse BEM can not be used because of the evident reason that the induced velocities in the rotor plane can not be determined with this method. Both upwash methods showed a strong dependency on the locations of the monitor points, especially when choosing them close to the current or next blade. For larger distance from the leading edge, the UVL method seems to present a more constant convergence of the u_{ind} , which meets the expectations. However, the point vortex of UVL may exaggerate the upwash near the blade. But because the verification of this method to the results of University of Stuttgart is excellent and the UDV results are not fully understood, the UVL method is chosen to see if a relevant tip loss factor can be determined.

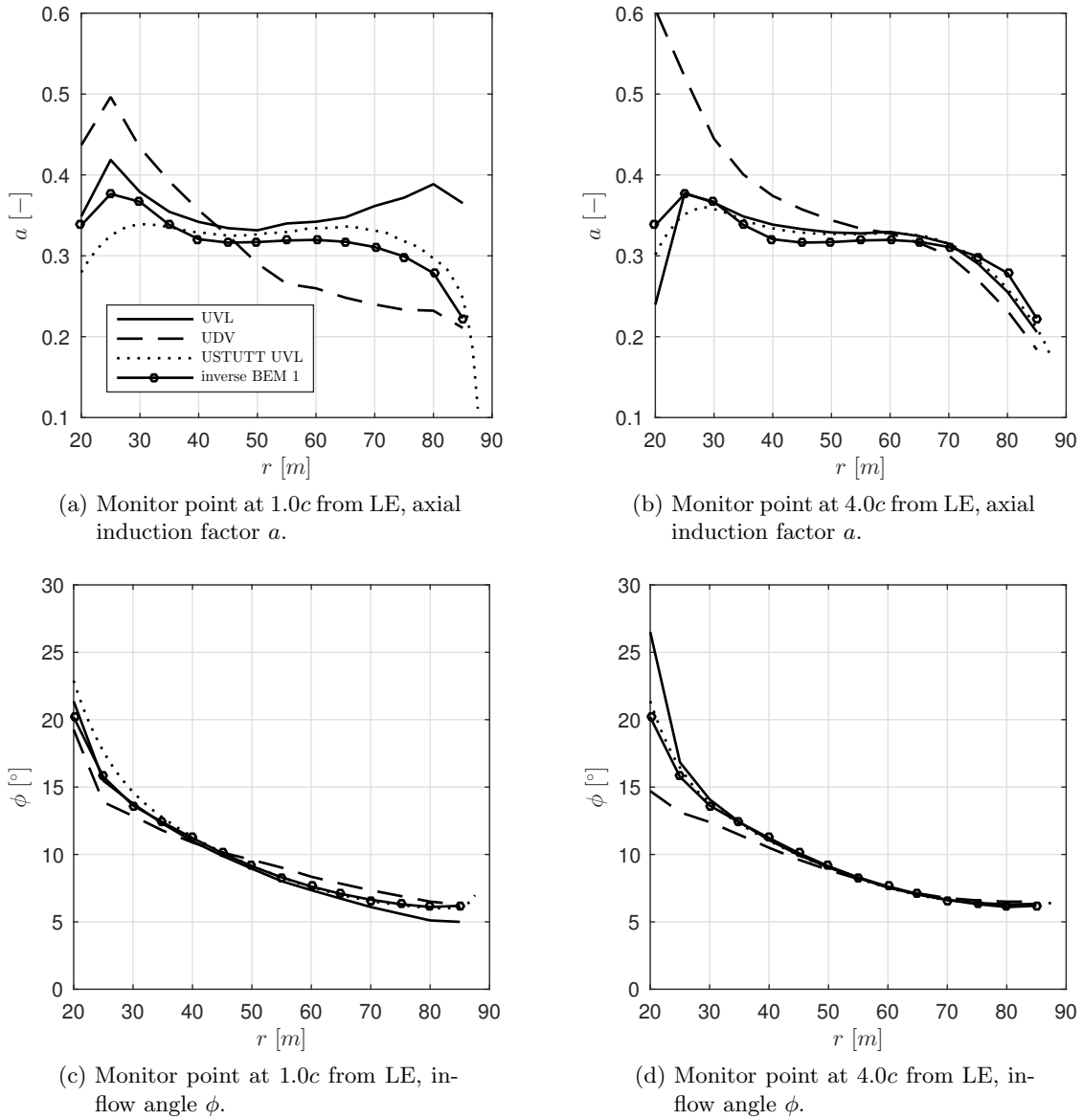


Figure 5.9: The results from all four methods to extract the angle of attack α from the CFD results for the Innwind rotor at 9 m/s , shown for two monitor point positions. In contrary to the results for the AVATAR rotor, the UDV method shows deviating results of the axial induced velocity u_{ind} at $4.0c$ for the inboard sections. This is also visible for the Innwind rotor at 6 m/s and the NREL Phase VI results, which can be found in appendix A.4.

The defined tip loss factor is given in equation (4.5) and repeated below.

$$F_{CFD} = \frac{\bar{a}}{a} \quad (4.5 \text{ revisited})$$

For calculating the axial induction factor a several ideas come to mind. One is to interpolate between the monitor points in front and behind the airfoil. However due to the point vortex located in the quarter chord point, it is known that the two points just in front and behind the rotor are influenced strongly by this singularity. An averaged on these two or more points could also be done.

The results of these ideas are shown in figure 5.10 for the AVATAR rotor at 6 m/s. In between two blades (thus similar to one third of the rotor plane), there are in total 2264 monitor points places in front of the 17 sections given in table 5.1. It is accepted that these monitor points are not fully uniform spread along the rotor plane, for the reasons discussed in the previous section. Because the number of points in the inboard annular rings is low (the next blade is relatively very close), the values for the sections at $r = 20$ m, 25 m and 30 m are not computed when using a number of points for the averaging.

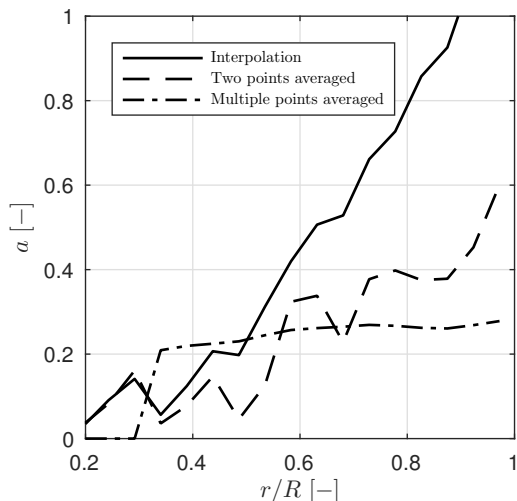


Figure 5.10: Three methods to estimate the axial induction factor a along the blade span from the CFD results for the AVATAR rotor at 6 m/s. The first method interpolates between the available results, the second method computes the average taking a monitor point just in front of the leading edge and just behind the trailing edge and the third method uses multiple points to do this averaging depending on the size of the section. Because the number of points for the inboard annular rings is low, the averaging is not done for these sections. The result show that only the multiple points averaging method leads to expected results.

The results show that the only reasonable method is the multiple points averaged method for estimating the axial induction factor a .

An approximated azimuthal averaged axial induction factor \bar{a} is calculated by computing the axial induced velocity u_{ind} for a high number of monitor points, such that the complete rotor plane is covered and then averaging these values per annular ring. This is similar to

the rotor plane method discussed in section 4.3. The monitor points that are very close to or on the blades are discarded from the computations.

Figure 5.11 gives the axial induction factor a , azimuthal averaged axial induction factor \bar{a} and the computed tip loss factor.

The resulting tip loss factor looks valid: midboard the flow is expected to be uniform and thus the tip loss factor should be close to one, where a decrease of the tip loss factor at the tip is anticipated due to higher non-uniformities. Therefore, the same is done for the other rotors. However, because for the NREL Phase VI rotor at 15 m/s the results for the axial induced velocity u_{ind} at the tip regions are only positive for monitor points at a minimum distance of $2c$ from the local leading edge (see figure A.6), the computations of the axial induction factor a and azimuthal averaged axial induction factor \bar{a} results into abnormal values.

The tip loss factor results will be used in section 5.4, where they will be plotted next to the AWSM tip loss factor and the Prandtl tip loss factors.

It must be stated that the accuracy of the determined tip loss factor from the CFD results is limited due to several reasons. First of all, it was discussed that the mesh points are not structured in the CFD data, resulting into a non-uniform distribution of the monitor point, not only in the rotor plane but also in axial direction. Furthermore, as it is known that the number of sections N is affecting the results for the upwash method close to the blades, a highest number of section should be chosen. Due to time restrictions, this could not be achieved. The comparison of the UVL results to other benchmark results showed that this method is still performing acceptable with a lower number of sections. Also, it is known that the upwash is exaggerated by the use of the point vortex, but because UDV showed convergence problems for regions where it is expected that the results should be constant and the results are not consistent comparing the results for the three rotors, this method is not used. Lastly, to determine the axial induction factor a an averaging is done of a number of monitor points close to the blade, because the other methods did not show reasonable results.

5.2 Vortex method

The second objective of the thesis is to show that vortex methods can be used to retrieve a vortex method tip loss factor which is similar to the Prandtl tip loss factor. The vortex method code used in this thesis is the AWSM code, explained in section 4.3. This section will first show the validation of this free wake lifting line AWSM code with measurements from the New Mexico experiment. After the code is validated, the development of the AWSM tip loss factor will be discussed.

5.2.1 Validation

In this section the free vortex lifting line code AWSM is validated with the New Mexico experiment. To run the AWSM simulations, ECN Aero-Module must be used, which also contains a BEM simulation. Therefore, as BEM results can easily be produced with the assurance that the same input files are used as for the AWSM simulations, the results

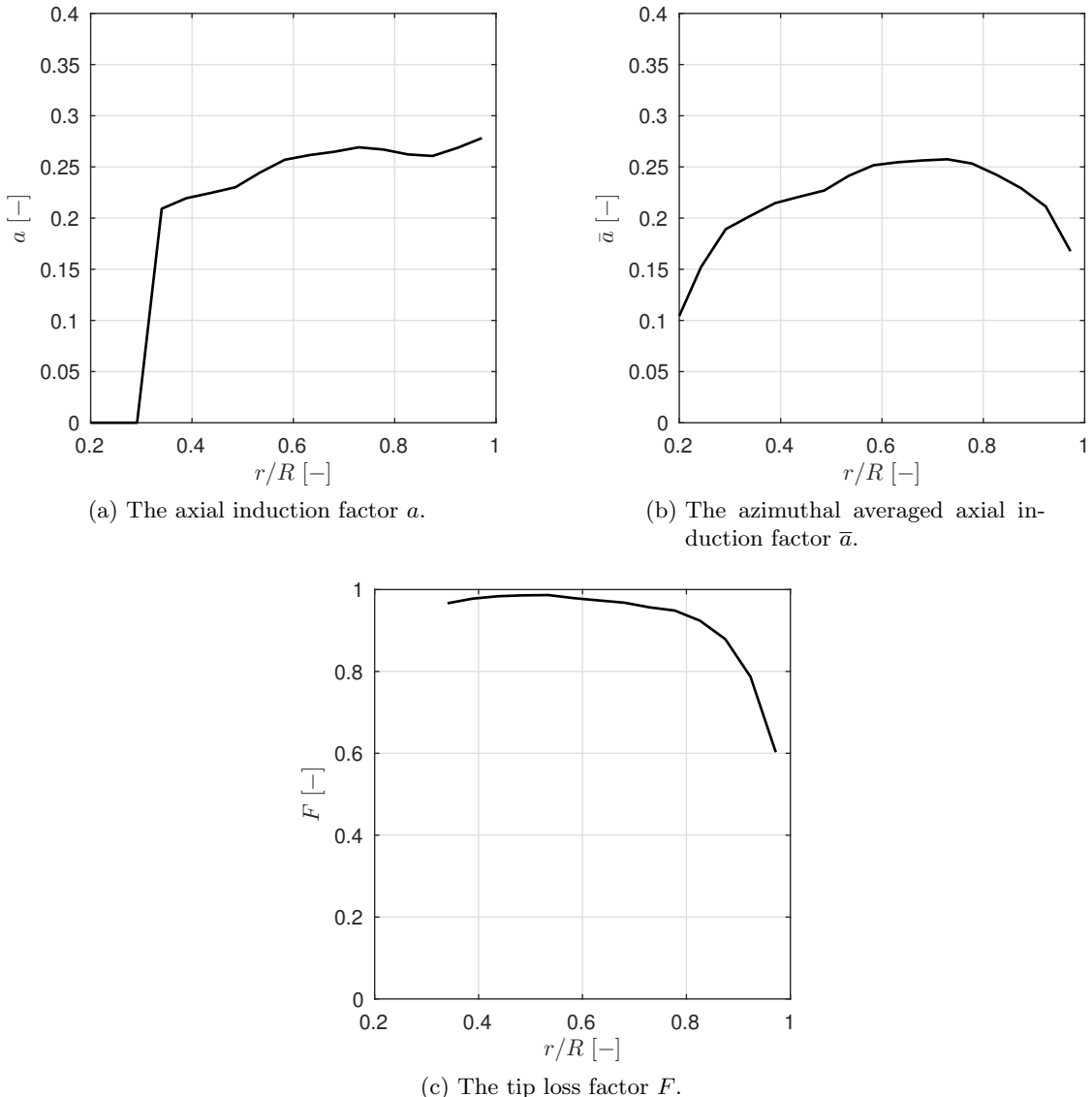


Figure 5.11: The computed axial induction factor a , azimuthal averaged axial induction factor \bar{a} and tip loss factor F extracted from the UVL method for the AVATAR rotor at 6 m/s. The shape of each variable comply with the expectations, although the used methods have not been validated. The same observations hold for the AVATAR rotor at 9 m/s, the Innwind rotor at both conditions and the NREL Phase VI rotor at 7 m/s, which are given in appendix A. The results for the NREL Phase VI rotor at 15 m/s are abnormal due to negative induced velocities.

will show a third candidate when comparing loads. Furthermore, the results discussed in this section are published in a conference paper, see Boorsma et al. (2016).

Similar to the Mexico experiment, the New Mexico experiment contain measurements for three wind tunnel velocities, corresponding to a turbulent wake state (10 m/s), the design condition (15 m/s) and a separated flow condition (24 m/s), when setting the rotational velocity Ω of the Mexico rotor equal to 44.52 rad/s (corresponding to 425.1 rpm). However, for the velocity traverses only the results of 15 m/s will be shown. The reader is referred to appendix B for the other conditions. The pitch angle θ is set to -2.3° .

The loads are discussed first, followed by the axial, radial and azimuthal velocity traverses.

Loads

Figure 5.12 shows the normal force F_n (left column) and tangential force F_t (right column) for the three velocities (divided by the rows). These forces are direct outputs from both BEM and AWSM simulations. It can be seen that for the New Mexico experiment, the forces are only given for five radial positions (25 %, 35 %, 60 %, 82 % and 92 % span). From the in total 125 pressure sensors along these sections, the data is postprocessed to the normal force and tangential force.

Overall, the magnitude of the normal force from both simulation models is very close to the measurements. Taking the scope of this thesis in consideration, it is once more shown that there is overprediction of the normal force at the tip of the blade (at 92 % span).

For the other four sections, the normal force results of the 10 m/s and 15 m/s cases are comparable; a good prediction for 25 % span, underprediction for 35 % and 82 % span and overprediction for 60 % span. The difference in over- and underprediction between the three middle sections can be related to the airfoil polar characteristics at these sections. First, both the airfoils at 35 % and 82 % span (the DU91-W2-250 and the NACA 63-418 respectively) have a comparable zero angle of attack lift coefficient where the airfoil at 60 % span (Risø A1-21) has a (approximately 33 %) higher zero angle of attack lift coefficient. Secondly, it is known that the two-dimensional airfoil polar data for the Risø A1-21 airfoil is acquired in a wind tunnel which features high turbulence intensity levels. Though, since the performance of low Reynolds number airfoils is highly dependent on the boundary layer, a low turbulence intensity level is necessary when acquiring airfoil polar data, in order to assure that the boundary layer is laminar. Thirdly, not the Risø A1-21 airfoil but the Risø A2-21 airfoil is used in the design of the blade, but because no airfoil polar measurements exist for this airfoil, the polar data from the Risø A1-21 airfoil is used. Due to these reasons a deviation in results at 60 % span compared to its neighbours is expected.

For 24 m/s the underprediction at the root sections can be related to the stall delay effect, although Snel, Houwink, and Bosschers (1994) rotational correction model is used in BEM and AWSM, to account for stall delay effects in the inboard region. Literature shows that in general, these corrections, including the one from Snel et al. (1994), tend to correct the calculations too far outboard compared to measurements (see Dumitrescu and Cardos (2011) and Guntur, Bak, and Sørensen (2012)) and also the results of the corrections depend on which rotor is used (this is shown by Bak et al. (2006), who compares several

stall delay models on three rotors). Furthermore, the differences at 60 % and 82 % span compared to the other two velocities could be related to the fact that for 24 m/s the flow is separated and thus the results depend on the quality of the airfoil polars for these high angles of attack.

The tangential force comparisons show that the two aerodynamic models are less close to the measurements compared to the normal force calculations, but it should be noted that because the tangential forces are lower in magnitudes, differences are enlarged more, opposed to the normal forces. Also, the experimental results shown in figure 5.12 are the outcome of post-processing the pressure measurements. The reduced resolution of the pressure sensors plays an important role in the determination of the tangential force. For the tangential forces at 24 m/s the three-dimensional effect in separated flow is probably the cause of the large deviations shown in figure 5.12f. Next to this, the correct modelling of separation of the aerodynamic models is dependent on the airfoil polar data.

Figure 5.13 shows the axial force and torque. These are calculated with equations (5.1) to (5.4). The axial force and the torque of the aerodynamic models are calculated using only the (interpolated) forces and angles at the five sections, similar to the five sections used in the experiment, to ensure a correct comparison. Furthermore the values for the normal force and tangential force at the root and tip are set to zero. A linear integration is finally done over the seven sections leading to the results shown in figure 5.13.

$$dF_{ax} = F_n \cos(\theta + \epsilon) + F_t \sin(\theta + \epsilon) \quad (5.1)$$

$$F_{ax} = N_b \int_0^R dF_{ax} dr \quad (5.2)$$

$$dQ = F_n \sin(\theta + \epsilon) + F_t \cos(\theta + \epsilon) \quad (5.3)$$

$$Q = N_b \int_0^R dQ dr \quad (5.4)$$

The in general overprediction of the normal force modelled in AWSM is visible in the axial force plot. The torque is more sensitive to the tangential force and especially for the 24 m/s case this is clearly visible. Note that the values shown in this figure should only be used for validation purposes as the calculations are done with limited spanwise resolution.

Axial velocity traverse

In the New Mexico experiment multiple stereo Particle Image Velocimetry (PIV) measurements are performed, where the details are described by Boorsma and Schepers (2014). The PIV sheets are located at 9 o'clock, when facing the rotor upfront, on the same height as the rotor center. The axial traverse measurements are done at two radial positions, $r = 0.5$ m (inboard) and $r = 1.5$ m (outboard), with the first blade in 12 o'clock position. In order to retrieve the flow field along these positions from AWSM, the external field

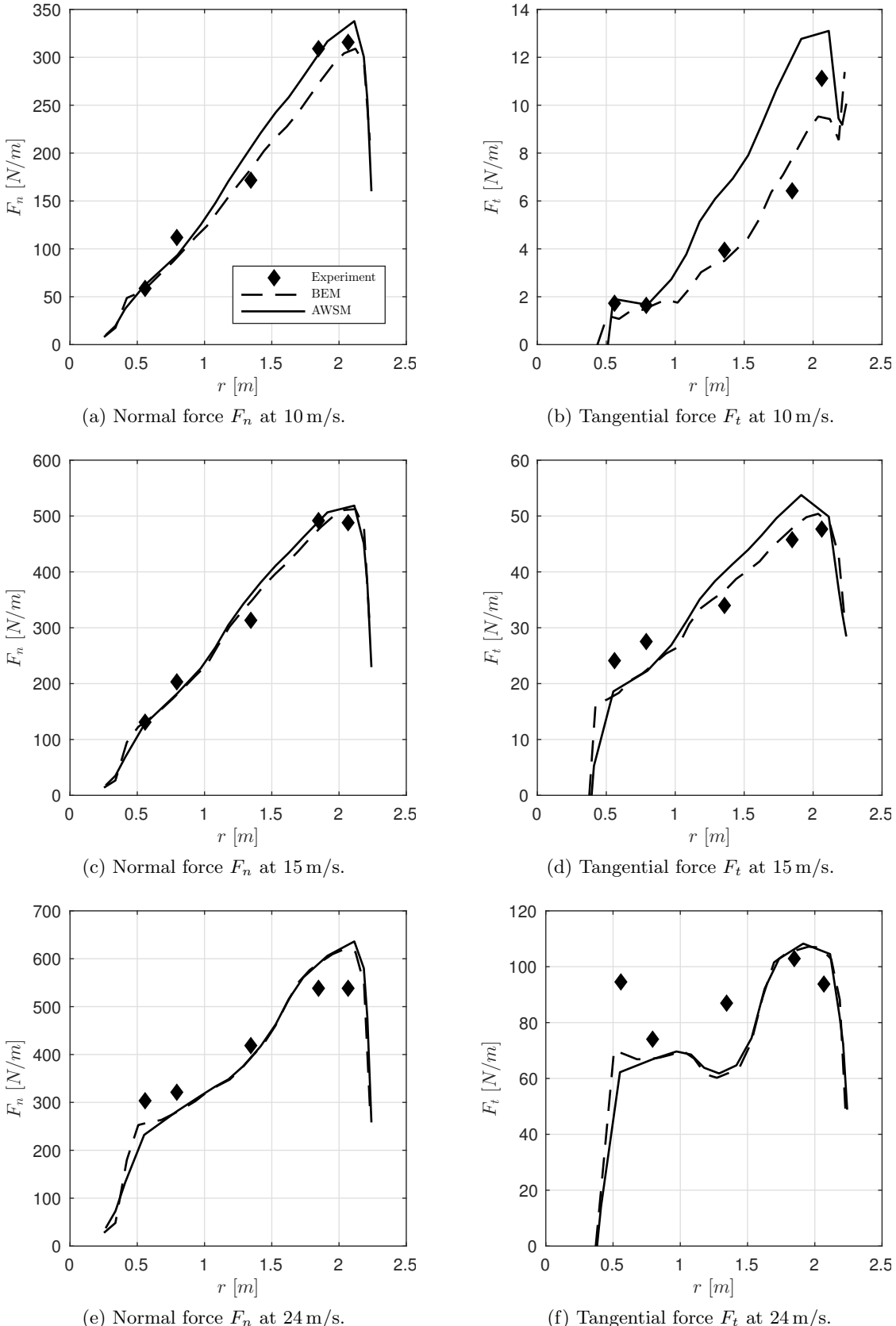


Figure 5.12: The load distributions (normal force F_n on the left and tangential force F_t on the right) from the New Mexico experiment, BEM and AWSM simulations for three velocities (top: 10 m/s, middle: 15 m/s and bottom: 24 m/s). It can be seen that the loads are predicted reasonable good, with differences that can be explained by the use of airfoil polar data and corrections in the aerodynamic models.

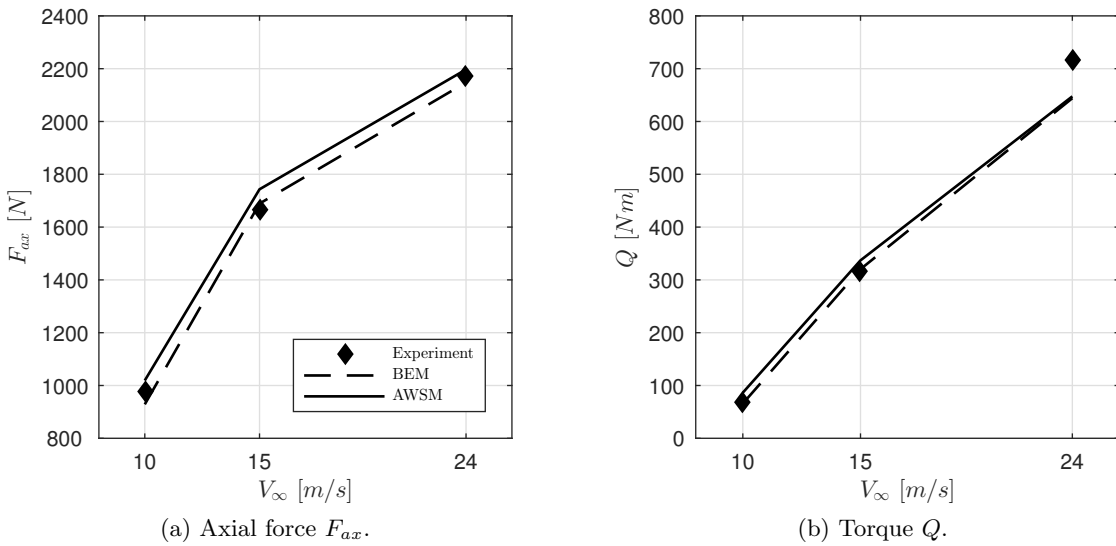


Figure 5.13: The axial force F_{ax} (left) and torque Q (right) from the New Mexico experiment, BEM and AWSM simulations for three velocities. It can be concluded that AWSM overpredicts the axial force F_{ax} and torque Q , with the exception of the torque Q computed for 24 m/s which can be attributed to the separation of flow in this condition.

module is used. The three velocity components are shown for the design condition case (15 m/s) per row in figure 5.14, where the left-hand sub-figures correspond to the inboard results and the right-hand sub-figures to the outboard results.

The induction of the rotor in the rotor plane is clearly visible. In general the results of AWSM are comparable with the experimental results. For the inboard traverse, the root vortex is causing the fluctuating results, which is visible from the AWSM and New Mexico results. However, due to the fact that the nacelle is not modelled in AWSM, some deviations are expected and visible. The outboard comparison shows good agreement on the velocity component in streamwise direction V_x . It is also seen that this velocity in the far wake approaches a value of half the velocity at the rotor plane, which is predicted by momentum theory (see section 2.3). For the other two components the difference can be explained by the fact that wake in AWSM does not account for viscous effects.

For the other two operational conditions, only outboard experimental results are available. However, the same observations on the outboard results can be made for these conditions. For these results the reader is referred to appendix B.

Radial traverse

Radial traverse PIV measurements are done just upstream (-0.30 m) and downstream (0.30 m) the rotor plane, along the same 9 o'clock sheet as described before. To focus on the passage of the second blade, measurements are done at 13 positions of the rotor with the azimuth angle non-uniform ranging from 10° to 110° (with 0° defined as the first blade being in the 12 o'clock position). The velocities are averaged over these azimuth angles.

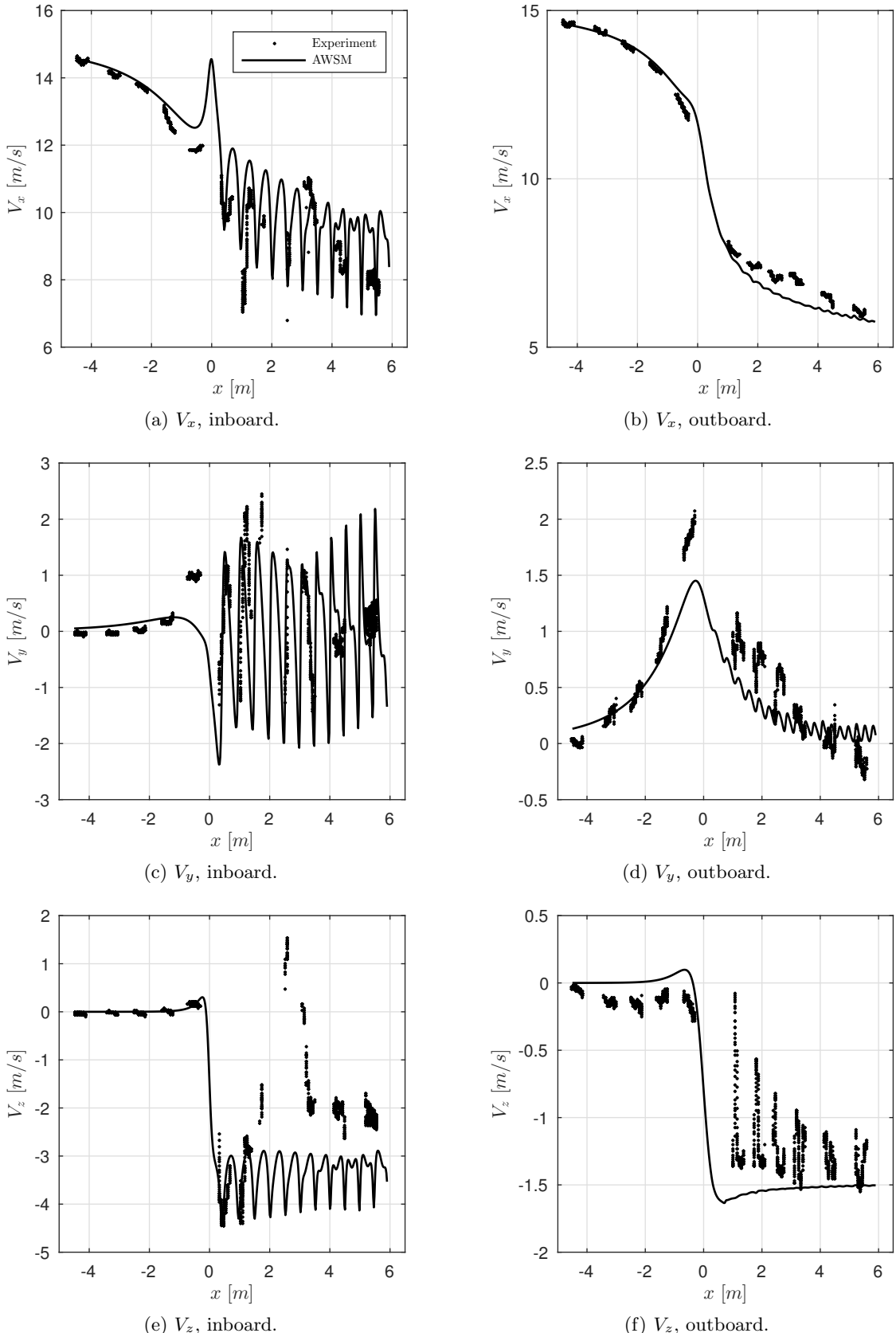


Figure 5.14: Inboard ($r = 0.5$ m) and outboard ($r = 1.5$ m) axial traverse for 15 m/s measured in the New Mexico experiment and computed by AWSM at the 9 o'clock position, with the first blade in 12 o'clock position. It is illustrated that AWSM is able to predict the velocity components close to the measurements.

Again, the external field module in ECN Aero-Module is used to calculate the same radial traverses from AWSM. The azimuthal averaged velocity component results for 15 m/s are given in figure 5.15 for the upstream (left) and downstream (right) traverses.

The AWSM results are in line with the New Mexico results, especially for V_x at the outboard part of the blade. The release of the trailed vortices is captured well by AWSM, however there is a small shift of the tangential velocity along the entire span. Similar to the axial traverse observations, differences due to the nacelle effect at the root are expected. As the measurements are done slightly downstream, it is furthermore satisfactory to see that AWSM is able to predict the velocities near and beyond the tip of the blade in agreement with the experimental results. This indicates that the tip vortex and wake expansion are correctly calculated on both the location and strength.

Azimuthal traverse

The same results from the radial traverse can be used to plot the velocity components as a function of the azimuth angle ψ , upstream (-0.30 m) and downstream (0.30 m) from the rotor plane. From the experiment, the PIV results for the five radial locations as described earlier (25 %, 35 %, 60 %, 82 % and 92 % of the span) are available. Though, it would be cumbersome to discuss all the results in this thesis, even if only the 15 m/s condition is chosen. Therefore, only the downstream results for the two most outboard are presented. Figure 5.16 shows the results for the radial position of 82 % R on the left and the radial position of 92 % R on the right for the 15 m/s condition.

The blade passage at $\psi = 30^\circ$ is clearly visible. Overall, the trends of the simulations are corresponding with the experimental results, even for these outboard sections, for which it is known that at this region three-dimensional aerodynamic effects are taking place. When evaluating the results critically, the level of induction close to blade passage is overestimated by AWSM, leading to lower magnitudes of the velocity components compared to what is measured. Also, the shift of the V_y velocities is similar to what has been seen before at the radial traverse results. For the two other wind conditions, the results are comparable to what is seen in figure 5.16, although these conditions involve a turbulent wake and separated flow.

Conclusion

Without extensively explaining differences between the New Mexico experiment and the AWSM results, this section has shown that AWSM performs closely to the measurements for the design condition and appendix B will illustrate the same for the other two conditions. It is to some extent remarkable how comparable the results are, even in the root and tip region, where it is known that the flow is far from uniform. Fortunately, based on this validation, AWSM can be accepted as reliable model for calculating wind aerodynamics.

5.2.2 Tip loss factor

Now that AWSM is validated, the code can be used to form a tip loss factor, which will allow comparisons with the Prandtl tip loss factor. As given in section 4.3, the AWSM tip

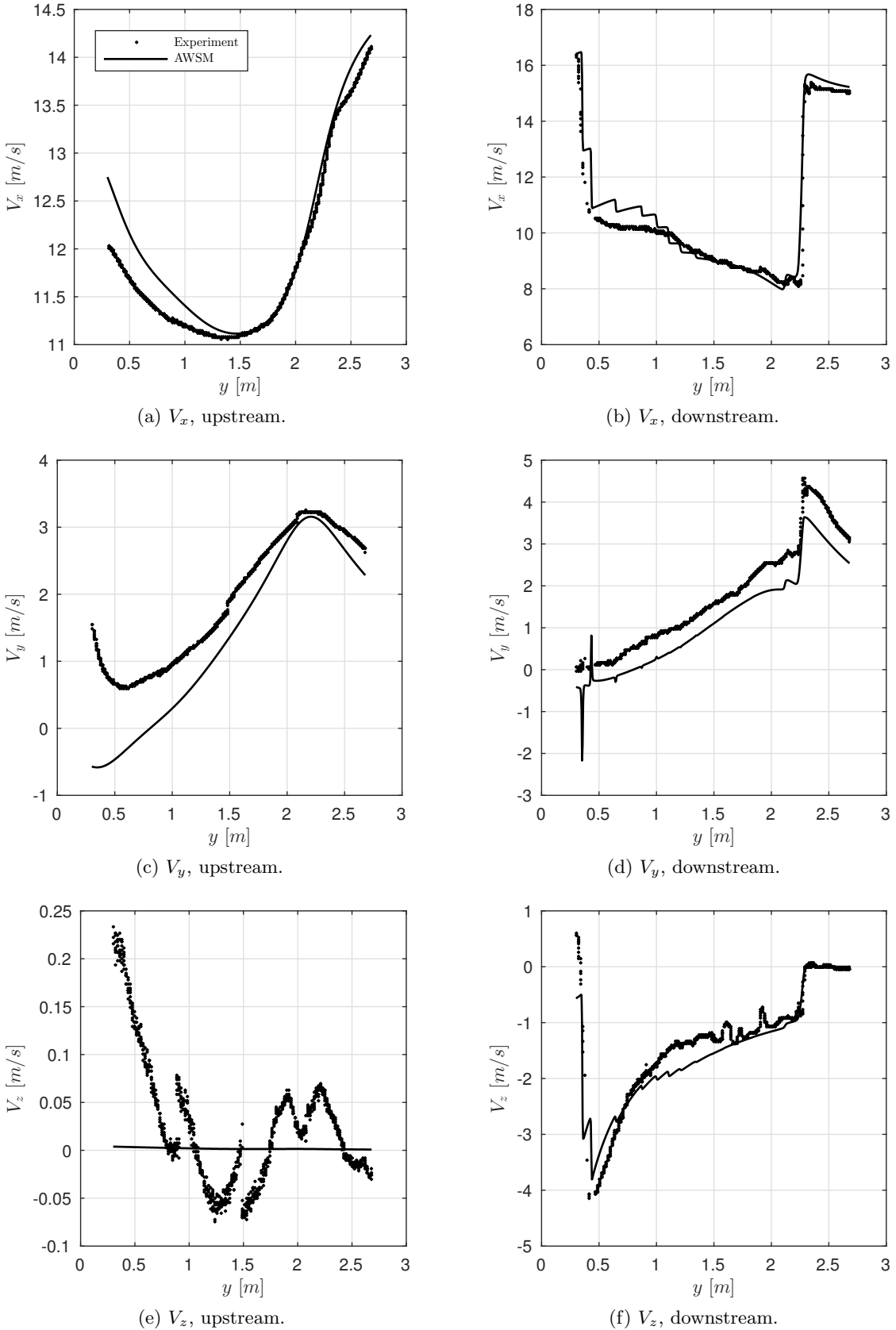


Figure 5.15: Upstream (-0.30 m) and downstream (0.30 m) radial traverse for 15 m/s measured in the New Mexico experiment and computed by AWSM. The velocity components are averaged over 13 rotor positions. The results show that AWSM is calculated the velocities accurately, with a small shift for the tangential velocity V_y .

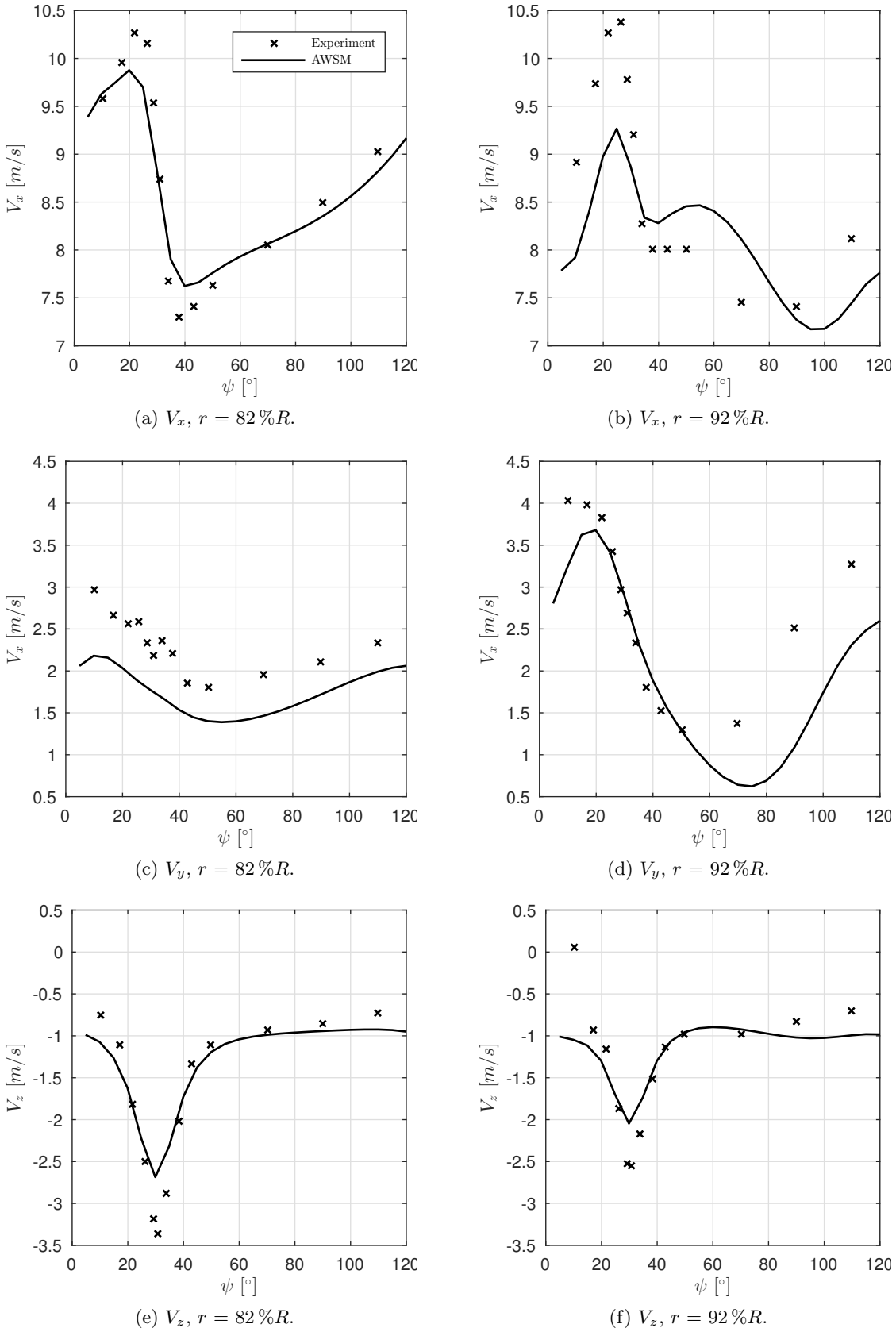


Figure 5.16: Azimuthal traverse for 15 m/s at sections $r = 82\%R$ and $92\%R$ measured and computed downstream (0.30 m) and averaged over 13 rotor positions, with the blade passage at $\psi = 30^\circ$. The results show that AWM is slightly underestimating the magnitudes of the velocity components at the blade passage.

loss factor is defined as the ratio between the azimuthal averaged axial induction factor \bar{a} and the axial induction factor a , see equation (4.6). This section will discuss on how both variables can be determined from the simulation code, starting with the azimuthal averaged axial induction factor \bar{a} .

$$F_{AWSM} = \frac{\bar{a}}{a} \quad (4.6 \text{ revisited})$$

Azimuthal averaged axial induction factor

As described in section 4.3, the external field module must be used in order to determine the azimuthal averaged axial induction factor \bar{a} . This can be done in two ways; with the rotor plane method and the 9 o'clock method. It will be shown that the methods have their own advantages and disadvantages. Because of the just discussed experimental and AWSM results for the Mexico rotor, this rotor will be used as an example.

A short description on the two methods is given first, starting with the rotor plane method. With the external field module, additional evaluation points are placed in the entire rotor plane, where the code will calculate the velocity components and the pressure coefficients at these points. Because the cone and tilt angles of every rotor in this thesis are set to zero, the definition of the rotor plane in this thesis is straightforward. The external field module allows to assign the evaluation points in a circular grid. In this case, the additional evaluation points resembles the monitor points discussed in section 5.1.1. Thus, the rotor plane will be similar to what is shown in figure 5.4, except that now the distribution is definitely uniform and the rotor plane is fully filled with evaluation points.

The 9 o'clock method earned its name thanks to the radial traverse measurements in the New Mexico experiment. It was discussed that the velocity components were measured by the PIV method in the sheets located at 9 o'clock, just up- and downstream the rotor plane, for 13 rotor positions. The azimuthal averaged values were presented as the radial traverse results. Using the external field module, the same has been done with the AWSM code, but for more azimuthal positions of the rotor. In this case, only a line of points is the input for the external field module, instead of a complete grid. Furthermore, the line can be defined anywhere in the rotor plane, as this thesis only deals with non-yawed flow, resulting in axis-symmetric flow.

For the rotor plane method, the rotor plane from the center to a position just after the tip is divided into 101 annular rings, with 150 evaluation points in each ring. The line for the 9 o'clock method contains 500 evaluation points. For both simulations the time step is chosen such that the rotor rotates with exactly 10° each step, although any value can be chosen (it will be discussed that this is not the case when determining the axial induction factor a). The results of the two methods for the Mexico rotor at 15 m/s and rotating with 425.1 rpm is given in figure 5.17.

It can be seen that the methods mostly produce the same results. The peak, which is only seen for the 9 o'clock method, is located very close to the tip. This is probably the effect of positioning an evaluation point on the tip vortex for when the blade is exactly coinciding with the 9 o'clock line, in combination with the lower azimuthal resolution (10° compared to 2.4° for the rotor plane method), but this will be discussed later in more

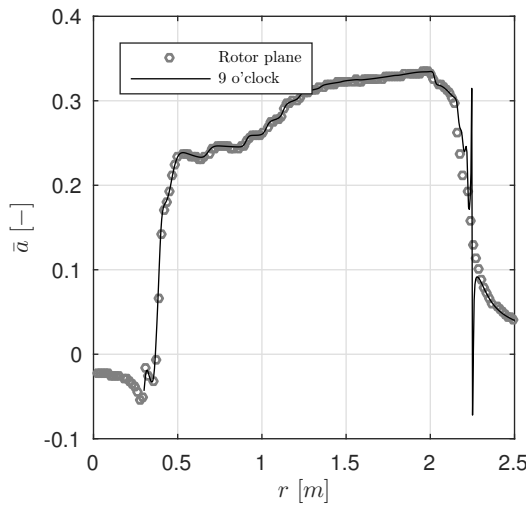


Figure 5.17: Calculation of the azimuthal averaged axial induction factor \bar{a} with the rotor plane and 9 o'clock method for the Mexico rotor at 15 m/s. The peak at the tip of the blade ($R = 2.25$ m) is the effect of position the evaluation point on the tip vortex in combination with the lower azimuthal resolution compared to the rotor plane method.

detail. In any case, this is an unwanted effect because this will lead to similar jumps when calculating the tip loss factor using this azimuthal averaged axial induction factor. However, the resolution of the 9 o'clock method along the blade is five times higher, where only less than a third of the computational time is needed compared to the rotor plane (4 hours versus 15 hours). Therefore, for the time being, a combination of both methods or interpolation at the tip for the 9 o'clock method is suggested in order to cope with the peak of the azimuthal averaged axial induction factor results at the tip.

Axial induction factor

Although the axial induction factor a can be directly calculated from the simulation outputs, the resolution of the result is constrained by the sectional resolution of the blade, when using the output files. It is common to discretize the blade up to 20 sections, when using AWSM, even for large rotors such as the AVATAR rotor ($R = 102.88$ m). This is due to the fact that, for example, doubling the number of sections for the Mexico rotor from 20 to 40 sections, quadruples the computational time (>20 hours) of the AWSM simulation.

As demonstrated before, the external field module can be easily used to compute velocities along a line with 500 points. In this case, the time step should be now chosen such that the blade will coincide precisely with the 9 o'clock line, otherwise the axial induction factor a are not calculated on the blade. Due to the use of the external field module for calculating both the azimuthal averaged axial induction factor \bar{a} and the axial induction factor a , no interpolation of results is needed, which will be the case when the axial induction factor a is computed directly from the output files.

For the same conditions as before, the results for the axial induction factor a using the 9 o'clock method for the Mexico rotor is given in figure 5.18.

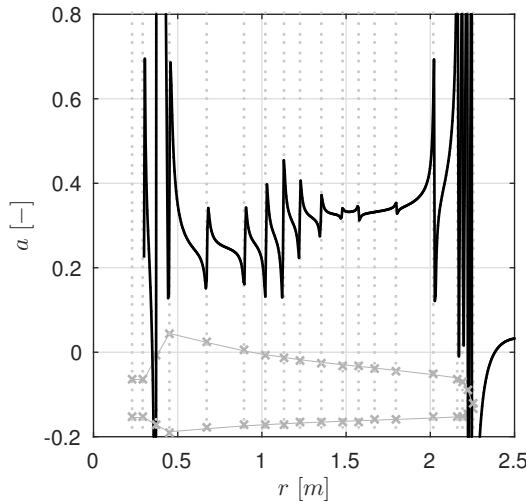


Figure 5.18: Results of axial induction factor a obtained from the external field module with default settings for lifting line cut-off radius LCO and wake cut-off radius WCO for the Mexico rotor at 15 m/s. With the discretization of the blade plotted in grey, it can be seen that the fluctuations of results are coinciding with the edges of each section, illustrating that the origin of the fluctuations are due to the vortices placed at these region.

The result show a lot of, at first unexpected, wiggles. However, when plotting the blade with the sectional discretization below it, it is immediately seen that the locations of these fluctuations coincide with the edges of each section (denoted by the cross markers). From the description of vortex methods in section 2.2 and from the visualization of figure 2.1, it is clear that for each section vortices are modelled at the edges these sections. Therefore, when placing an evaluation point near to such a vortex singularity, will result in these wiggled results, similar to what was discussed for the UVL method in section 5.1.

Section 4.3 introduced the lifting line cut-off radius (LCO) and the wake cut-off radius (WCO), which both set a vortex core to a finite size, so that when evaluating velocities close to this vortex, the solutions do not go to infinity. It is expected that changing these values (default settings are 0.01 and 0.2 for LCO and WCO , respectively) will affect the results shown in figure 5.18. Therefore, the sensitivity of these values are investigated next.

First, the wake cut-off radius WCO settings are changed from 0.05 to 0.95 in 18 steps. The choice of 18 simulations is made by predicting the total amount of computational time needed and the amount of computational power available for a period amount of time. The results are shown in figure 5.19, where it is visible that the setting has a large influence on the fluctuation magnitudes. Figure 5.19b provides a closer look. Although it can be concluded that the wiggles can be made smaller by choosing a certain WCO , they do not vanish completely. Setting WCO somewhere in between 0.5 and 0.7 (differences between the results in this range of WCO are negligible) give the smallest fluctuations.

For the lifting line cut-off radius LCO the same study is done, but now in the range of 0.01 to 0.996 in 18 steps and with setting WCO to 0.5. Surprisingly, at first, LCO does not seem to affect the axial induction factor a calculated on the blade, as visible in figure 5.20, although the lifting line cut-off radius LCO supposed to appoint fixed

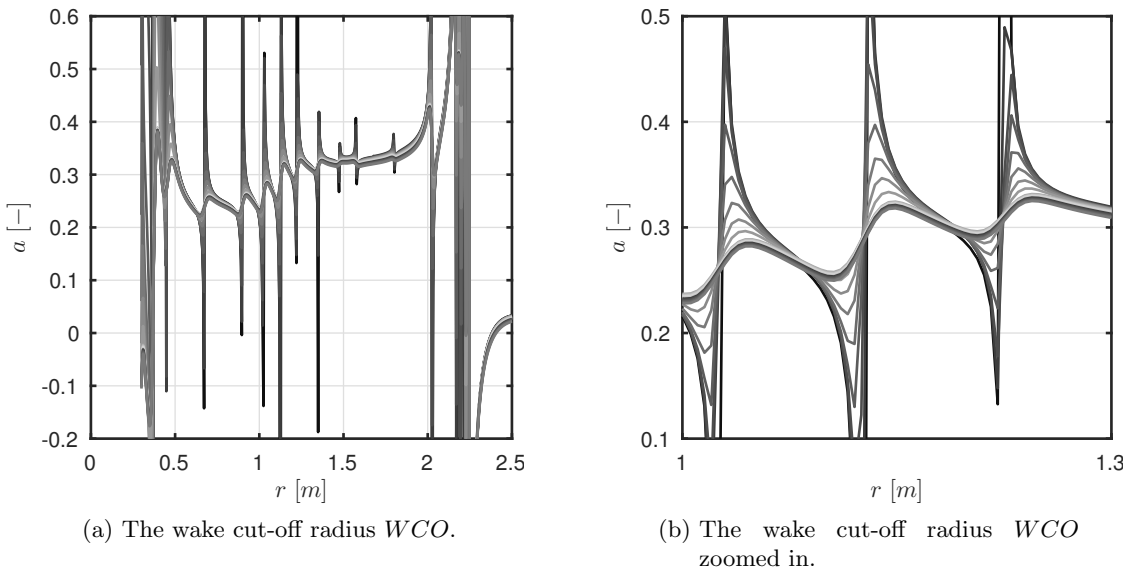


Figure 5.19: The effect of changing the value for the wake cut-off radius WCO , with keeping the value for lifting line cut-off radius LCO to default. In both figures, results for 18 different values are plotted ranging from 0.05 to 0.95. The right figure shows a magnification to see the effect closer. The differences of results for $0.5 < WCO < 0.7$ is very small and show the lowest magnitude of fluctuations.

lengths of the vortices cores along the blade. However, as the external field module is used to calculate the values on the blade although this external field module is designed to calculate the flow field elsewhere (hence the name of the module), it is explained that for these points only the wake cut-off radius WCO affects the results.

Figure 5.20a thus shows the results for the axial induction factor a with the best settings, concerning the wiggles. With such a high resolution, it is evident that points will be placed close to or on the edges of the sections. However, these wiggles will prolong when calculating the tip loss factor. Therefore, it must be reassessed if such a high resolution with acceptance on the fluctuations is more desirable over a smooth tip loss factor. With the knowledge that 72 Prandtl tip loss factors will be investigated later on in this chapter, it will be shown that the differences between tip loss factors for certain conditions are small. Therefore, it is decided to see if a more smooth axial induction factor a can be resolved.

One obvious solutions is to define the evaluation points manually (until now the first and last evaluation point with the desired number of intermediate points was sufficient input to create the 9 o'clock line) such that they are not close to the edges of the sections. However, it then also should be investigated what a sufficient distance from each edge is and because the magnitude of the vortices on the edges depend on the operational conditions, this will lead to excessive prior work.

Another solution is to decrease the size of the sections and compute the axial induction factor a from the output files. As previously discussed, this will lead to a large increase of computational time, but no time has to be spent on investigating what a good distribution of evaluation points is. Furthermore, to decrease the computational time, it is chosen that

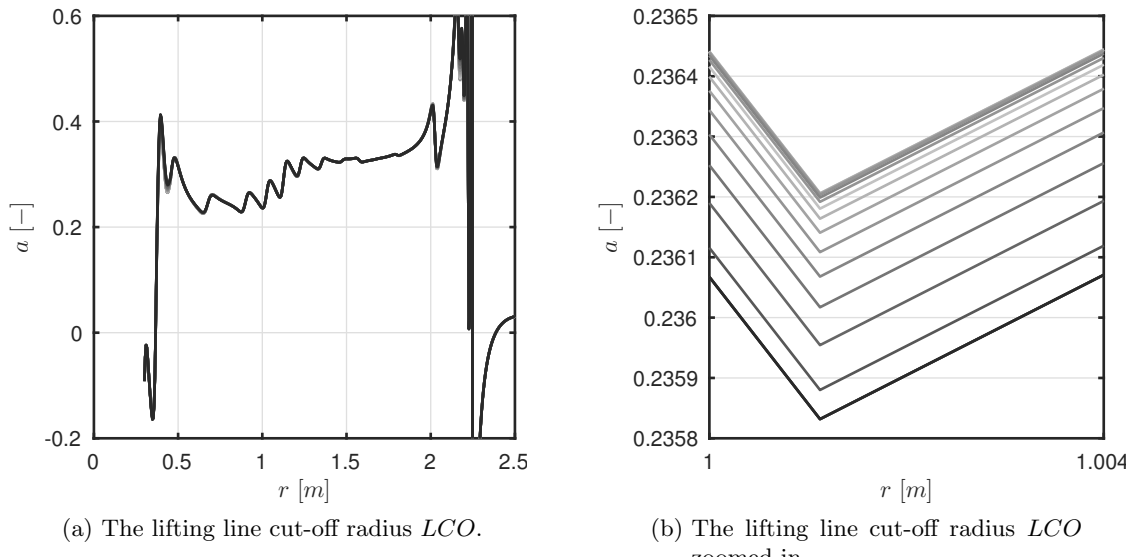


Figure 5.20: By setting the wake cut-off radius WCO to 0.5, the lifting line cut-off radius LCO is varied from 0.01 to 0.996 in 18 steps. From both figures it is clear that the effect is negligible and therefore it is decided to use the default setting of 0.02.

the discretization of the blade is more dense near the tip (defined as at least the last 20 % of the span). The sections can not be made too small, otherwise the vortices at the edges will be placed close to each other, leading to instability of the code. To some extent this can be controlled with LCO , however to keep the computational times restricted, it has been noticed that the value of LCO can remain as the default value.

For calculating the tip loss factor, the positions at where the axial induction factor a should match the positions at where the azimuthal averaged axial induction factor \bar{a} is calculated. Because the axial induction factor a are now computed at approximately the center of each section, the 9 o'clock evaluation points are set to the same positions. Consequently, there is no need for interpolations between the induction factors.

The results are shown in figure 5.21. It is visible that for these lower spanwise resolution, there is no peak of azimuthal averaged axial induction factor \bar{a} near the tip. Also, figure 5.21b shows a smoother axial induction factor a , with a visualization of the new discretization of the Mexico blade in grey. The results are similar to what is shown in figure 4.2, which showed the BEM results of an optimal three-bladed rotor after applying the Prandtl tip loss factor.

With equation (4.6) the corresponding tip loss factor is plotted in figure 5.22.

Conclusion

These results show how the vortex method code AWSM can be used to create a tip loss factor, with exploring all the options and limitations due to the theoretical setup of the code.

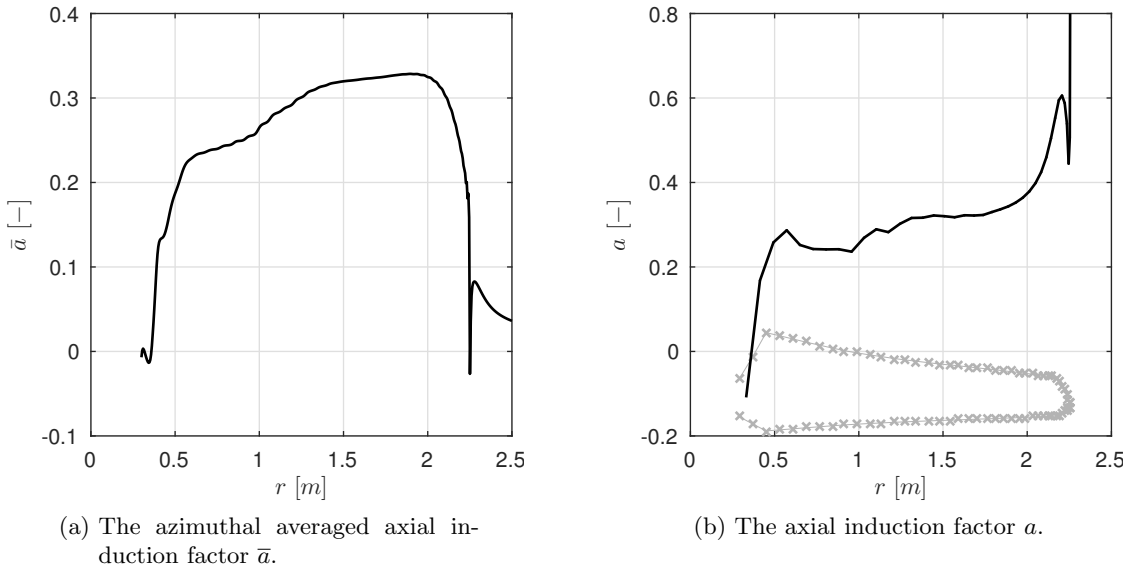


Figure 5.21: The azimuthal averaged axial induction factor \bar{a} and axial induction factor a plotted for the Mexico rotor at 15 m/s. The values for azimuthal averaged axial induction factor \bar{a} are obtained with the 9 o'clock method and the axial induction factor a are obtained by increasing the discretization of the blade using interpolation and extracting the values directly from the output files, shown in grey in the right plot.

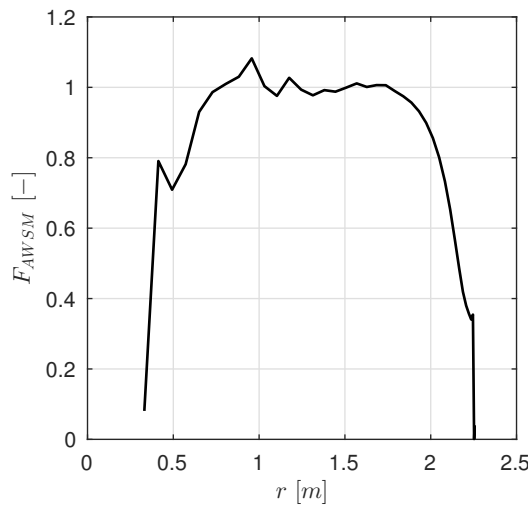


Figure 5.22: The AWSM tip loss factor F_{AWSM} for the Mexico rotor at 15 m/s, calculated with the results from figure 5.21.

5.3 Simplified rotor

In this section the variations of the Prandtl tip loss factor are assessed by using the simplified NewBlade rotor. At first, the rotor is subjected to the original design conditions, where after a sensitivity study is done by changing the operational conditions and design of the NewBlade rotor.

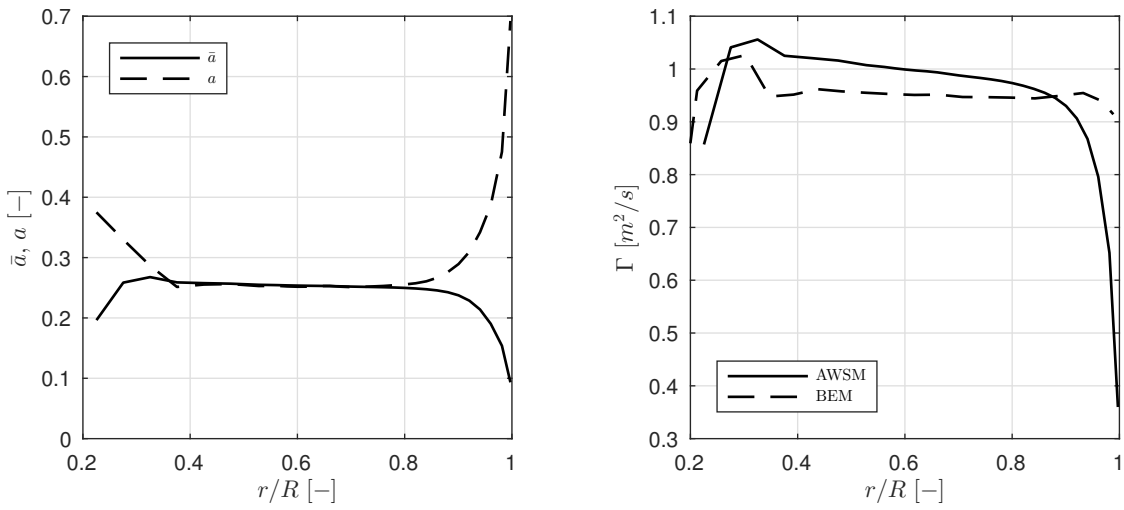
5.3.1 Variations of Prandtl tip loss factor

Chapter 3 showed that there are 72 possibilities which can be considered as a Prandtl tip loss factor. In fact, there are endless variations since the velocity of the tip trailing vortices, in the roller bearing analogy, can be set to infinite values. For example, Lindenburg (2003) multiplies this velocity with \sqrt{F} to account for the spread behaviour of the tip vortices, but which one of the 72 tip loss factors should be used as F ? Other articles can be found on measurements of the tip vortices, for example shown by Snel and Schepers (2009). Considering that until this moment no study has been performed on the variety of the Prandtl tip loss factor, the decision is made to limit the investigation to the stated 72 tip loss factors and thus declining further variations on the roller bearing analogy tip loss factors.

The rotor used for this assessment is the NewBlade rotor. This three-bladed rotor is based on the design of the Mexico rotor with simplified blades, see section 4.1 for more details. With the BEM simulation in ECN Aero-Module linked to Matlab, a design routine is created such that a constant circulation distribution along the span of the blade is made, to meet the assumption made by Prandtl in his derivation. The outcome for the circulation Γ is shown in figure 5.23b, when setting the rotational velocity Ω to 534.761 rpm, wind velocity V_∞ to 8 m/s and the pitch angle θ to 0°, resulting in a tip speed ratio λ of 7. It can be seen that for these conditions, there is some differences between the computed circulation by AWSM and BEM. It will be shown later that the difference tend to get smaller when the loading is lowered.

The corresponding loading for these conditions are plotted in figure 5.23a, which give the axial induction factor a and the azimuthal averaged axial induction factor \bar{a} calculated with AWSM. It can be seen that for these operational conditions the loading of the rotor is quite high, where the assumption of a lightly loaded rotor was necessary to be able to set the angle between helical wake sheets ϵ_w equal to the inflow angle ϕ . However, for the moment being, the correctness of the tip loss factor is not yet the topic of discussion. Also, different loading cases are investigated later on.

First it must be discussed how the variations of the Prandtl tip loss factor are implemented. Unfortunately, code adjustments to ECN Aero-Module could not be done. The implemented tip loss factor, based on the roller bearing analogy given in equation (4.7), could only be turned on or off with the current version of the code. It is known that the tip loss factor is calculated in the iterative loop (see section 2.3 for a description of BEM), but surprisingly the difference when including the tip loss factor in the loop and when calculating the tip loss factor after running BEM in ECN Aero-Module is only 7.1% at maximum. This gave the incentive to write an own BEM code in where any tip loss factor could be included and check if the same observation is true for the other variations



(a) The azimuthal averaged axial induction factor \bar{a} and axial induction factor a .

(b) The circulation Γ .

Figure 5.23: The azimuthal averaged axial induction factor \bar{a} , axial induction factor a and circulation Γ for the NewBlade rotor at $V_\infty = 8 \text{ m/s}$ and $\Omega = 534.761 \text{ rpm}$, with the pitch angle θ set to 0° .

Description	F_1	F_{42}	F_{71}
Maximum difference of tip loss factor results between own BEM and ECN BEM including the tip loss factor in the loop.	2.01 %	0.04 %	0.10 %
Maximum difference of results between including the tip loss factor in the loop or calculating it afterwards.	4.04 %	1.73 %	1.82 %

Table 5.2: Comparison of calculating three Prandtl tip loss factor inside the iterative loop or afterwards with the ECN BEM code and a self-made BEM code. Note that F_{71} is the ECN tip loss factor, given in equation (4.7). In table 5.3 the numbering of the tip loss factors is given.

besides the tip loss factor implemented in ECN's code. Table 5.2 shows the results for three tip loss factors which are chosen for their contrast compared to each other.

The variations of the tip loss factors are numbered so that they can be looked up in table 5.3 (the four parameters should be used in equations (3.21) to (3.23)). Using this table, it can be seen that F_1 evaluates r_2 , r_3 , a and a' in equations (3.21) to (3.23) all locally, where F_{42} evaluates these variables at the tip. F_{71} equals the ECN tip loss factor, also given in equation (4.7).

	r_2	a	r_3	a'
1	local	local	local	local
2	local	local	local	tip
3	local	local	local	0
4	local	local	tip	local
5	local	local	tip	tip

6	local	local	tip	0
7	local	tip	local	local
8	local	tip	local	tip
9	local	tip	local	0
10	local	tip	tip	local
11	local	tip	tip	tip
12	local	tip	tip	0
13	local	local averaged	local	local
14	local	local averaged	local	tip
15	local	local averaged	local	0
16	local	local averaged	tip	local
17	local	local averaged	tip	tip
18	local	local averaged	tip	0
19	local	tip averaged	local	local
20	local	tip averaged	local	tip
21	local	tip averaged	local	0
22	local	tip averaged	tip	local
23	local	tip averaged	tip	tip
24	local	tip averaged	tip	0
25	local	0	local	local
26	local	0	local	tip
27	local	0	local	0
28	local	0	tip	local
29	local	0	tip	tip
30	local	0	tip	0
31	tip	local	local	local
32	tip	local	local	tip
33	tip	local	local	0
34	tip	local	tip	local
35	tip	local	tip	tip
36	tip	local	tip	0
37	tip	tip	local	local
38	tip	tip	local	tip
39	tip	tip	local	0
40	tip	tip	tip	local
41	tip	tip	tip	tip
42	tip	tip	tip	0
43	tip	local averaged	local	local
44	tip	local averaged	local	tip
45	tip	local averaged	local	0
46	tip	local averaged	tip	local
47	tip	local averaged	tip	tip
48	tip	local averaged	tip	0
49	tip	tip averaged	local	local
50	tip	tip averaged	local	tip
51	tip	tip averaged	local	0
52	tip	tip averaged	tip	local

53	tip	tip averaged	tip	tip
54	tip	tip averaged	tip	0
55	tip	0	local	local
56	tip	0	local	tip
57	tip	0	local	0
58	tip	0	tip	local
59	tip	0	tip	tip
60	tip	0	tip	0
61	local	roller bearing	local	local
62	local	roller bearing	local	tip
63	local	roller bearing	local	0
64	local	roller bearing	tip	local
65	local	roller bearing	tip	tip
66	local	roller bearing	tip	0
67	tip	roller bearing	local	local
68	tip	roller bearing	local	tip
69	tip	roller bearing	local	0
70	tip	roller bearing	tip	local
71	tip	roller bearing	tip	tip
72	tip	roller bearing	tip	0

Table 5.3: In this table the settings for the r_2 , a , r_3 and a' as shown in equations (3.21) to (3.23) are defined, resulting in 72 variations of the Prandtl tip loss factor. The ECN tip loss factor is equal to F_{71} . For the roller bearing tip loss factors equation (3.29) is used for velocity component V_n . The grey highlighted tip loss factor are performing the best for all rotors and conditions, as discussed in section 5.4.2.

$$F = \frac{2}{\pi} \arccos \left[\exp \left(-\frac{N_b}{2} \frac{R-r}{r_2} \frac{\sqrt{V_n^2 + V_t^2}}{V_n} \right) \right] \quad (3.21 \text{ revisited})$$

$$V_n = U_\infty(1-a) \quad (3.22 \text{ revisited})$$

$$V_t = \Omega r_3(1+a') \quad (3.23 \text{ revisited})$$

From the results in table 5.2, it can be concluded that the tip loss factors can be calculated after running BEM with the tip loss factor disabled. The results of the BEM code in ECN Aero-Module (with the implemented Prandtl tip loss factor (F_{71}) de-activated) are therefore used to investigate the 72 Prandtl tip loss factors, which are calculated afterwards.

In line with the resolution complications that were discussed in section 5.2.2 for retrieving a tip loss factor from AWSM, figure 5.24 shows the difference of results when discretizing the last 20 % of the blade into four sections (low N) versus ten sections (high N), resulting in 0.13 difference at $r/R = 0.98$. A sufficient number of sections is therefore important, also to ensure that the code computes the tip loss factor close to the tip of the blade.

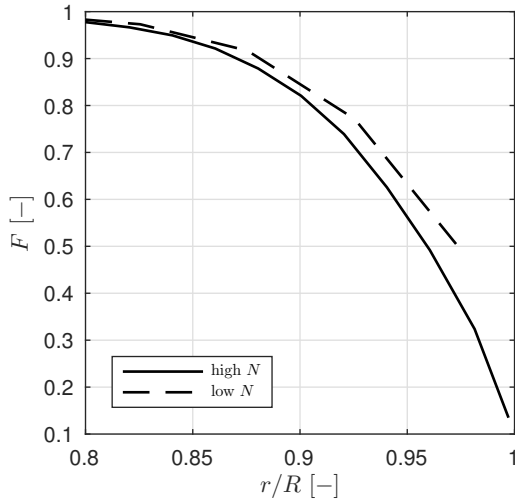


Figure 5.24: The effect of the number of sections N on the AWSM tip loss factor. It can be concluded that a high number of sections N should be chosen, but this choice is limited due to the instability effects of AWSM when the number of sections N is too high.

Now everything is set to perform comparisons. First of all, figure 5.25 shows the results when plotting all the 72 tip loss factors, using the same amount of grey values.

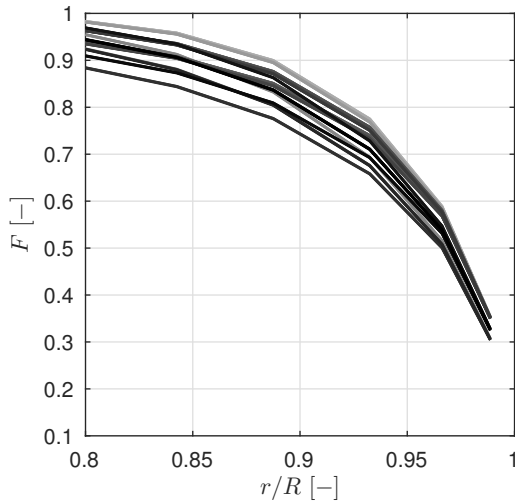


Figure 5.25: The 72 Prandtl tip loss factors shown for the NewBlade rotor at design conditions plotted in 72 grey values. Indicated by the several black lines, most of the tip loss factor show similar results.

It is immediately noticeable that, for at least these operational conditions, many tip loss factors show similar results, resulting in the dark black lines. To be able to focus on the results and not be overwhelmed by the many plotted lines, the code is modified to plot only those ones that differ in results for a minimum value in a certain defined region or point. As example, figure 5.26 is given, for which the tolerance is set to 0.01 at the 85 % of the span.

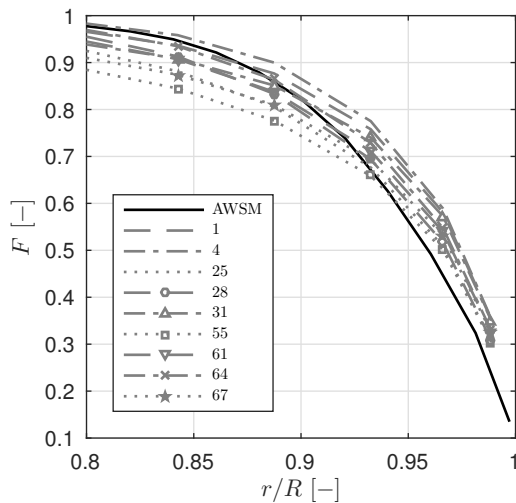


Figure 5.26: The AWSM tip loss factor and a variety of Prandtl tip loss factor, after the code checks which tip loss factors show similar results for a certain tolerance (in this case 0.01) at a specific radial position (in this case 85 % R). The numbering of the tip loss factors can be found in table 5.3.

For these restrictions, 9 different tip loss factors can be distinguished. Each of the 72 tip loss factors are labelled for which the legend in figure 5.26 gives the plotted tip loss factors. Table 5.3 can be used to see which settings of the r_2 , r_3 , a and a' belong to the labels and by remembering equations (3.21) to (3.23). Furthermore, in figure 5.26 the AWSM tip loss factor is also plotted. As it was discussed that vortex methods are better able to compute the induced effects of the rotor and include wake effects compared to BEM, the AWSM tip loss factor is treated as the desired tip loss factor.

The Matlab code is further extended to check which tip loss factor is performing the best, by calculating the absolute differences for each percent point in the tip region (from 80 % R to the tip) with the AWSM tip loss factor. The best tip loss factor is then defined as the one that performs the best on average (equal weighting) in this region. For all the conditions that the NewBlade rotor will be evaluated for in this thesis, the rotor's best tip loss factor is number 30 (see table 5.3 once again for the details). The discussion on why this tip loss factors performs the best, is kept for the last part of this chapter, when all the rotors are discussed. This rotor's best tip loss factor is plotted in figure 5.27, next to the AWSM results and the original ECN tip loss factor. In this case the difference is not astonishing, however there will be examples shown when the tip loss factors significantly differ. In similar ways, the results for the other conditions and rotors will be discussed in the remaining part of the thesis.

5.3.2 Sensitivity study

In this section, the performance of the 72 tip loss factors will be investigated for several conditions, by using the simplified NewBlade rotor. The goal is to understand why the tip loss factor behave like they do, in all sort of conditions. By doing so, it will outline the important parameters and this result will be used when assessing the tip loss factor for the more complex and real rotors.

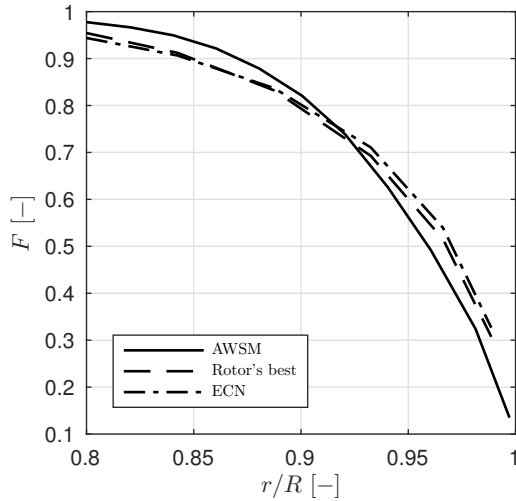


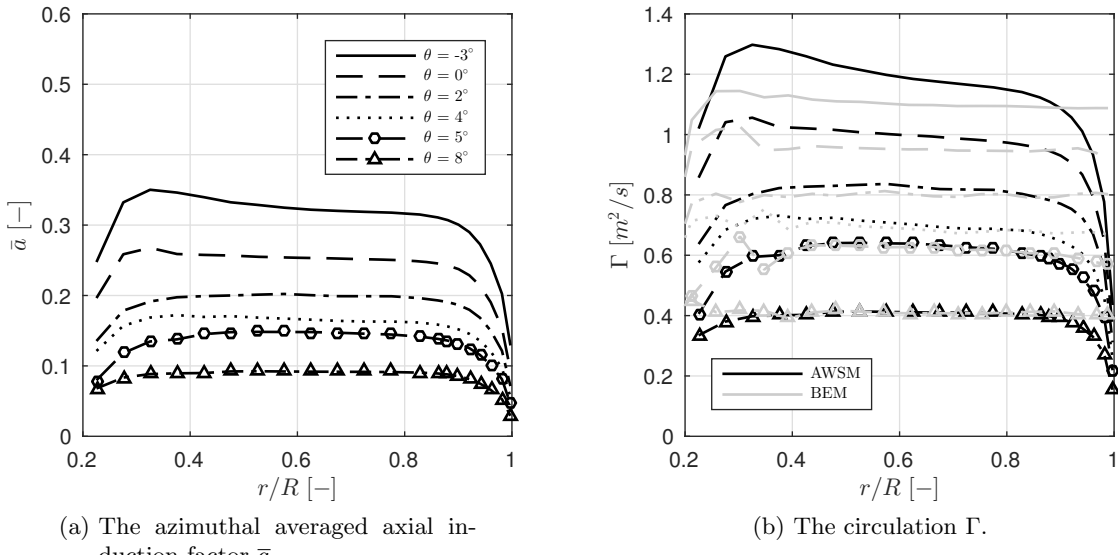
Figure 5.27: The AWM tip loss factor, the rotor's best tip loss factor (F_{30}) and the ECN tip loss factor (F_{71}). The two Prandtl tip loss factors show comparable results and are underpredicting (up to $92\%R$) or overpredicting (from $92\%R$) the non-uniform flow compared to AWM.

Pitch angle The loading of a rotor can be controlled by changing the pitch angle θ . From wind turbine aerodynamics, it is understood that the loading of the rotor will have an influence on the blade lifting properties and the wake structure. For example, lightly loaded rotors will experience separated flow at the blade, where for highly loaded rotors the wake will be in the turbulent state. It is the question what the role is of these and other effects on the tip loading. The derivation of the Prandtl tip loss factor also showed that the distance between two helical wake sheets d is an important parameter in the description of the tip losses. The dependency of the loading on the distance between two helical wake sheets will be also investigated.

With this in mind, the following is done. The NewBlade rotor is modified by setting a pitch angle θ and adjusting the twist angle ϵ , such that five loading cases can be investigated with keeping the circulation constant along the blade in order to comply with the assumptions made by Prandtl. This design routine is performed with BEM by computing the circulation Γ for each iterative loop and comparing it to the desired distribution. Adjustments to the twist angle ϵ are done by the algorithm, when the desired distribution is not met for a certain tolerance. The wind velocity V_∞ and rotational velocity Ω are kept to the original values (given in table 4.3).

The results for the loading and the circulation distribution are shown in figure 5.28. The azimuthal averaged axial induction factor \bar{a} is calculated with AWM and figure 5.28b shows the difference of the circulation Γ computed by the two aerodynamic models.

As expected, when pitching the blade into the flow (from 8° to -3°), the loading of the rotor will increase (higher azimuthal averaged axial induction factor \bar{a}). The difference between the computed Γ for lower values of the pitch angle θ can be explained by that, at these conditions, the two aerodynamic models differ in how they assess the momentum theory, as explained in chapter 2. AWM is better able to compute the inductions by the rotor. For when the induction is lower, the BEM results are closer to the AWM



(a) The azimuthal averaged axial induction factor \bar{a} .

(b) The circulation Γ .

Figure 5.28: The azimuthal averaged axial induction factor \bar{a} and circulation Γ for 5 pitch angles θ between -3° to 8° . The comparison of the circulation Γ computed by AWSM and BEM indicate that for higher loading cases (higher azimuthal averaged axial induction factor \bar{a}) the methods predict less comparable results due to the different assessment of the momentum theory.

results.

The computed tip loss factors for each pitch angle setting are given in figure 5.29, showing the AWSM tip loss factor compared to a number of Prandtl tip loss factors. As discussed in the previous section, the code only plots the tip loss factors which differ for a minimum value of 0.01 at radial position $85\%R$. The numbering of the tip loss factors can be used with table 5.3 to check which settings correspond to the factor.

From the results it can be seen that as the loading goes down in the order of sub-figures 5.29a to 5.29f, the tip loss factor values also lower slightly. Furthermore, the variety of the Prandtl tip loss factor tend to agree more for the lower loading cases. It can also be seen that the AWSM tip loss factor decays faster than any other.

The spread of the Prandtl tip loss factors, especially shown in figure 5.29a, is explained first. A negative pitch angle θ increases the inflow angle ϕ . Consequently, by remembering equation (3.19) and equation (3.20), the distances between the helical sheets will increase, again with the approximation that the inflow angle ϕ is equal to the angle between helical wake sheets ϵ_w . This gives the flow in between the blades and just over the tip of the blades the opportunity to wave in and out the sheets more heavily. The variations of the Prandtl tip loss factor are created by evaluating this non-uniform flow differently. It is thus evident that the differences between the tip loss factors are larger when there is more non-uniform flow. The opposite is true for when the blade is pitched such that the loading is lowered, which is shown in figure 5.29f.

The values for the tip loss factors slightly go down with pitching the blade out of the flow. Because this may not be immediately clear from figure 5.29, the AWSM tip loss

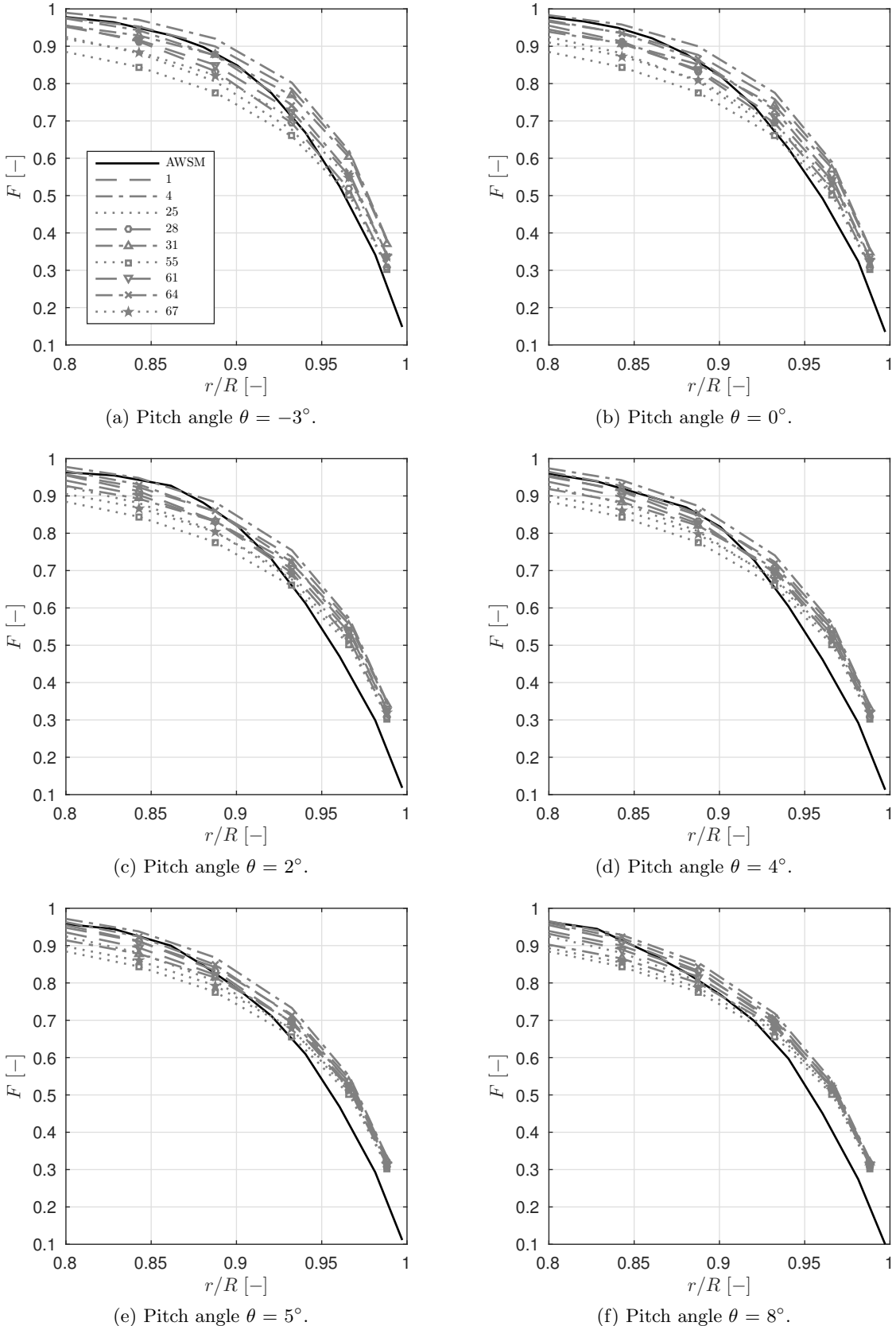


Figure 5.29: The AWSM and a variety of Prandtl tip loss factors for 5 pitch angles θ between -3° to 8° . Differences are explained by the effect of loading on the variations of the Prandtl tip loss factor and by the modelling of wake expansion and the trailing tip vortex. The numbering of the tip loss factors can be found in table 5.3.

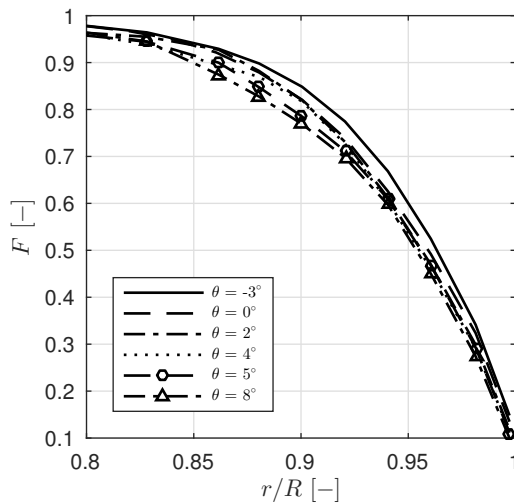


Figure 5.30: The AWSM tip loss factors for 5 pitch angles θ between -3° to 8° showing the slight lowering of the values explained by the movement of the trailedd tip vortex.

factors are plotted in one figure for the different pitch angles θ in figure 5.30. This can be explained by the effect of the trailedd tip vortex in time on the tip of the blades. For a highly loaded rotor ($\theta = -3^\circ$) it is known that the tip vortex moves more outboard compared to a lightly loaded rotor ($\theta = 8^\circ$). The velocity for which this tip vortex convects is determined by the tip speed ratio λ , as shown by Snel and Schepers (2009). In these cases, the tip speed ratio λ is fixed, so the convecting velocity of the tip vortex is similar for all cases. Therefore, when the radial position of the tip vortex does not change as much (lightly loaded rotor), it influences the tip at the blade more, resulting in an increase of non-uniform flow compared to when the tip vortex is convecting downstream and outboard (highly loaded rotor). Thus, the tip loss factor, which it is defined as unity for complete uniform flow and zero for complete non-uniform flow, will be lower for the high loading cases.

This effect of the tip vortex is also explained to be the reason of the larger decay of the AWSM tip loss factor compared to other ones. BEM does not model the tip vortex and such the results will deviate, especially at the tip, when the tip vortex remains closer to the blade, in case of lower loading.

With the variety of the tip loss factors discussed, figure 5.31 shows the AWSM, the rotor's best (F_{30}) and the ECN tip loss factor for the 5 pitch angle settings. The differences between the conventional tip loss factor (rotor's best) and the roller bearings tip loss factor (ECN's) is again small and is able to follow the AWSM tip loss factor for an acceptable level in the shown tip region.

In the discussed cases, the tip speed ratio λ is fixed and the pitch angle θ is changed. The next case will do the opposite, while still changing the loading of the blade.

Wind velocity and rotational velocity Different values for the tip speed ratio λ can be obtained by changing the wind velocity V_∞ or the rotational velocity Ω . Table 4.3 showed that there are 5 simulations done with different settings for the wind velocity and

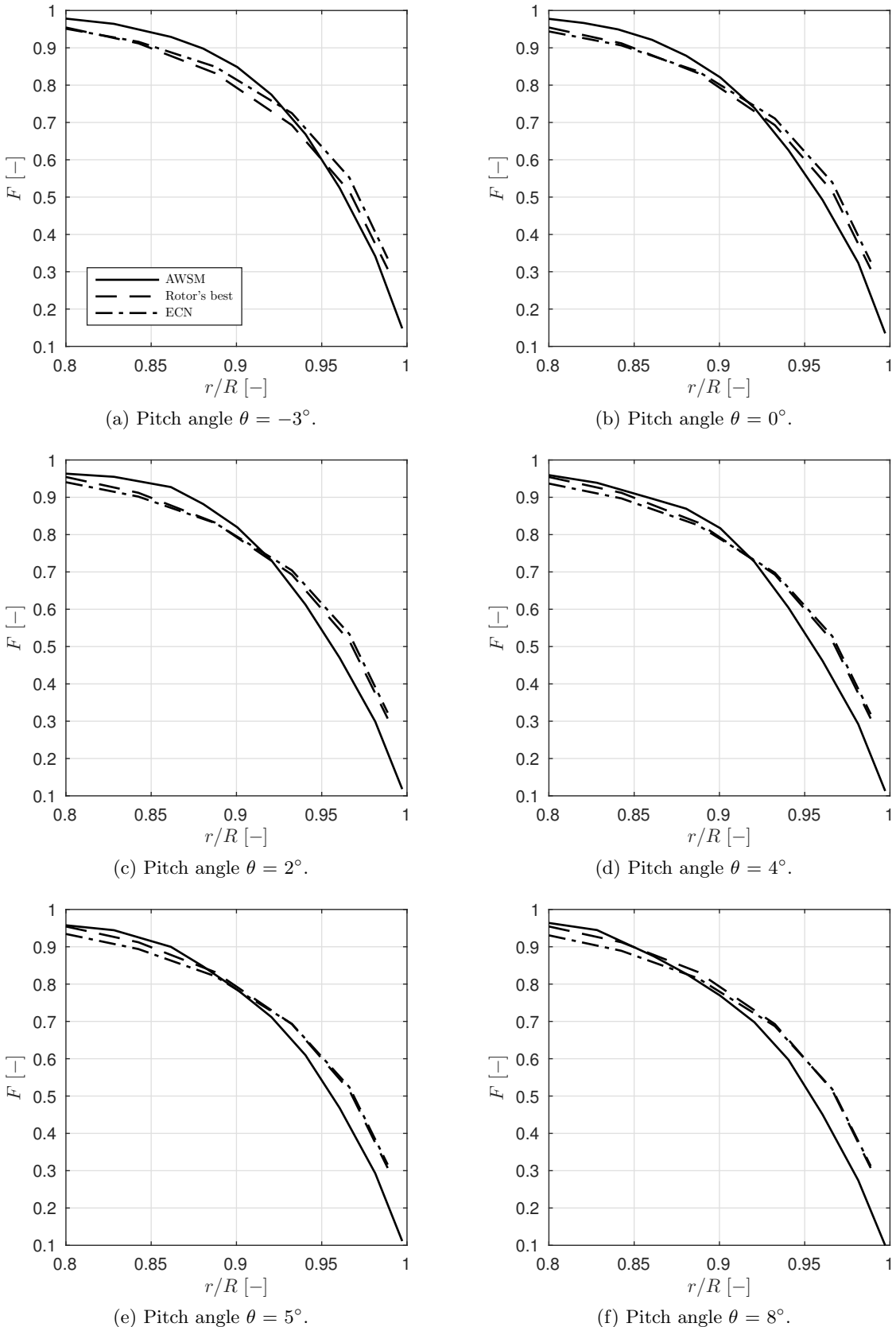
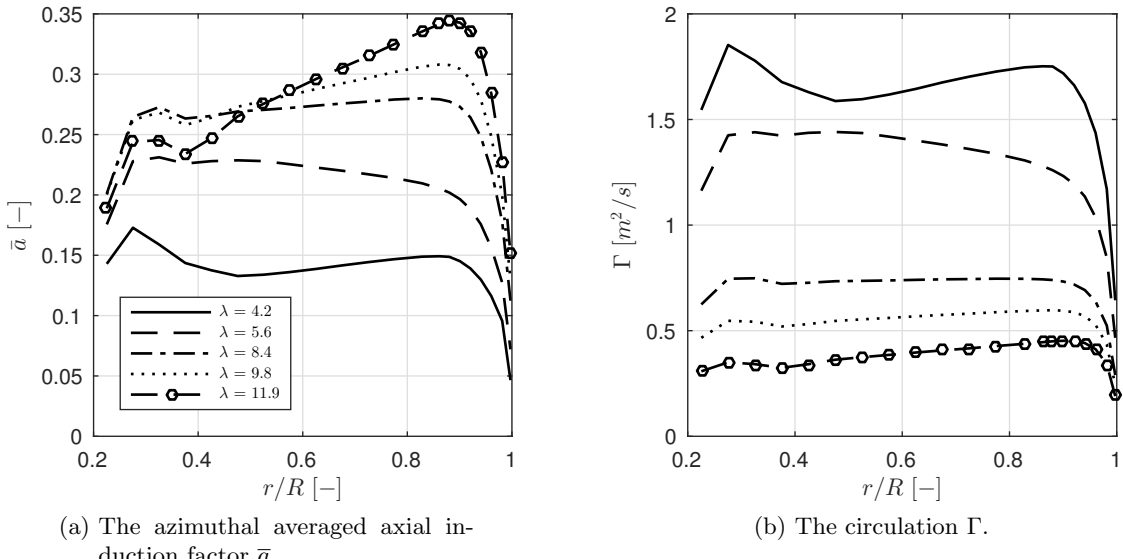


Figure 5.31: The AWM, the rotor's best (F_{30}) and the ECN (F_{71}) tip loss factor for 5 pitch angles θ between -3° to 8° . The deviations between the Prandtl tip loss factors are very small. Furthermore it is illustrated that both Prandtl tip loss factors are at first overpredicting the non-uniform flow, where this changes to underpredictions for the regions very close to the tip.

(a) The azimuthal averaged axial induction factor \bar{a} .(b) The circulation Γ .**Figure 5.32:** The azimuthal averaged axial induction factor \bar{a} and circulation Γ for 4 settings of the wind velocity V_∞ resulting in different tip speed ratios.

4 simulations for different values of rotational velocity, with keeping the other values the same. This is done such that each simulation for the rotational velocity case has a tip speed ratio λ similar to a simulation done for the wind velocity cases. Note that the original NewBlade rotor with zero pitch angle is used.

The motivation of this approach is to see whether the computations of non-uniform flow would be different when changing the loading of the rotor using the wind velocity V_∞ or the rotational velocity Ω . If, for a same tip speed ratio, there would be a difference noticeable, the curving movement of the flow near the blade compared to the undisturbed flow would not be captured fully with the derivation done by Prandtl. Fortunately, the results of the AWSM tip loss factors are the same when comparing the cases of changing the wind velocity V_∞ or the rotational velocity Ω , with maintaining the same tip speed ratio. Note that the Prandtl tip loss factors are also the same, but this was expected from the derivation. Therefore, only the results of the wind velocity cases are shown. Of course, also the effect of the tip speed ratio λ on the AWM tip loss factor and the variety of the Prandtl tip loss factor is of interest. This will be discussed next.

Figure 5.32 plots the azimuthal averaged axial induction factor \bar{a} , circulation Γ and the tip loss factor for different values of the wind velocity V_∞ . It can be seen in figure 5.32a that a higher tip speed ratio λ (low wind velocity V_∞) corresponds to a higher loading of the blade. The circulation distribution along the span is less uniform for a low tip speed ratio because at these conditions the angles of attack are close to stall values.

The tip loss factors for the 5 tip speed ratios are given in figure 5.33. What is directly visible is that for the higher loading case (figure 5.33e), the results are more diverse. The other four sub-figures show that the same 9 Prandtl tip loss factors as in figure 5.29. Furthermore, it is observed that when the loading is low, the tip loss factors agree better, there is more uniform flow predicted and the AWM tip loss factor shows a faster decay

compared to the Prandtl tip loss factors.

With increasing the tip speed ratio λ (lower wind velocity V_∞), the inflow angle ϕ is decreased. Similar to what was discussed for the pitch angle cases, it is therefore explained that the tip loss factor shows a fuller form compared to the lower tip speed ratios, due to the relation between the inflow angle ϕ and the distance between two helical wake sheets d .

Furthermore, the effect of the tip vortex is noticeable to some extent. For a low tip speed ratio λ the radial movement of tip vortex is small, however the convective velocity is high. The opposite is true when the tip speed ratio λ is high. Therefore, the tip vortex has influence on a larger part of the blade for the lower tip speed ratio λ , explaining that the faster decay of the AWSM tip loss factor starts earlier in figure 5.34a compared to figure 5.34e. Note that the strength of tip vortex is now also different for each λ (in contrary to what was discussed for the pitch angle cases), so in order to be able to explain the magnitude differences between the AWSM tip loss factor and, for example, the rotor's best tip loss factor, due to the tip vortex, both the movement and the strength of each tip vortex should be investigated.

Figure 5.34 gives the AWSM, the rotor's best and the ECN tip loss factor. Once again, it can be seen that the ECN tip loss factor is comparable to the rotor's best tip loss factors for the lower loading cases, however the differences at higher tip speed ratios are still small. For these cases it can be concluded that the ECN tip loss factor performs as good as the rotor's best.

Fixed tip speed ratio and zero pitch angle The effect of wake velocity is examined next. This is done by fixing the tip speed ratio λ and pitch angle θ , but changing the rotational velocity Ω and the wind velocity V_∞ with the same factor. By doing so, one could say that the effects that only depend on the time are investigated, as the loading stays the same but the velocity components in the velocity triangle (see figure 2.4) change in magnitude (but not the direction). Therefore, the wake velocities will be different. Note that the wake is modelled as mainly a free wake, with a prescribed structure for the far wake. This is done because it is known that the required computations for the free wake increases going further downstream, though the influence of the far wake on the blade properties is small, due to the larger distance to the blade. Furthermore, the transport velocity of the free wake (near the blade) is computed as a function of the operational conditions and the self-induction of the wake in the AWM simulations.

The rotational velocity Ω and wind velocity V_∞ are multiplied with 4 factors (0.6, 0.8, 1.2 and 1.4) compared to the original settings. Table 4.3 gives the corresponding values. The azimuthal averaged axial induction factor \bar{a} and circulation Γ are given in figure 5.35.

It can be seen that the loading is indeed close to identical. As expected, the circulation is different due to that the relative velocity V_{rel} is changed for each setting and shifted to the value belonging to the multiplication factor which was used.

However, the plots for the AWM and Prandtl tip loss factors do no show any differences (see figure 5.36). The effect of the wake velocity on the Prandtl tip loss factor was expected to be zero because the wake is not modelled BEM, in contrary to AWM. The two wake sheets originating from one blade at the same azimuth angle are plotted in

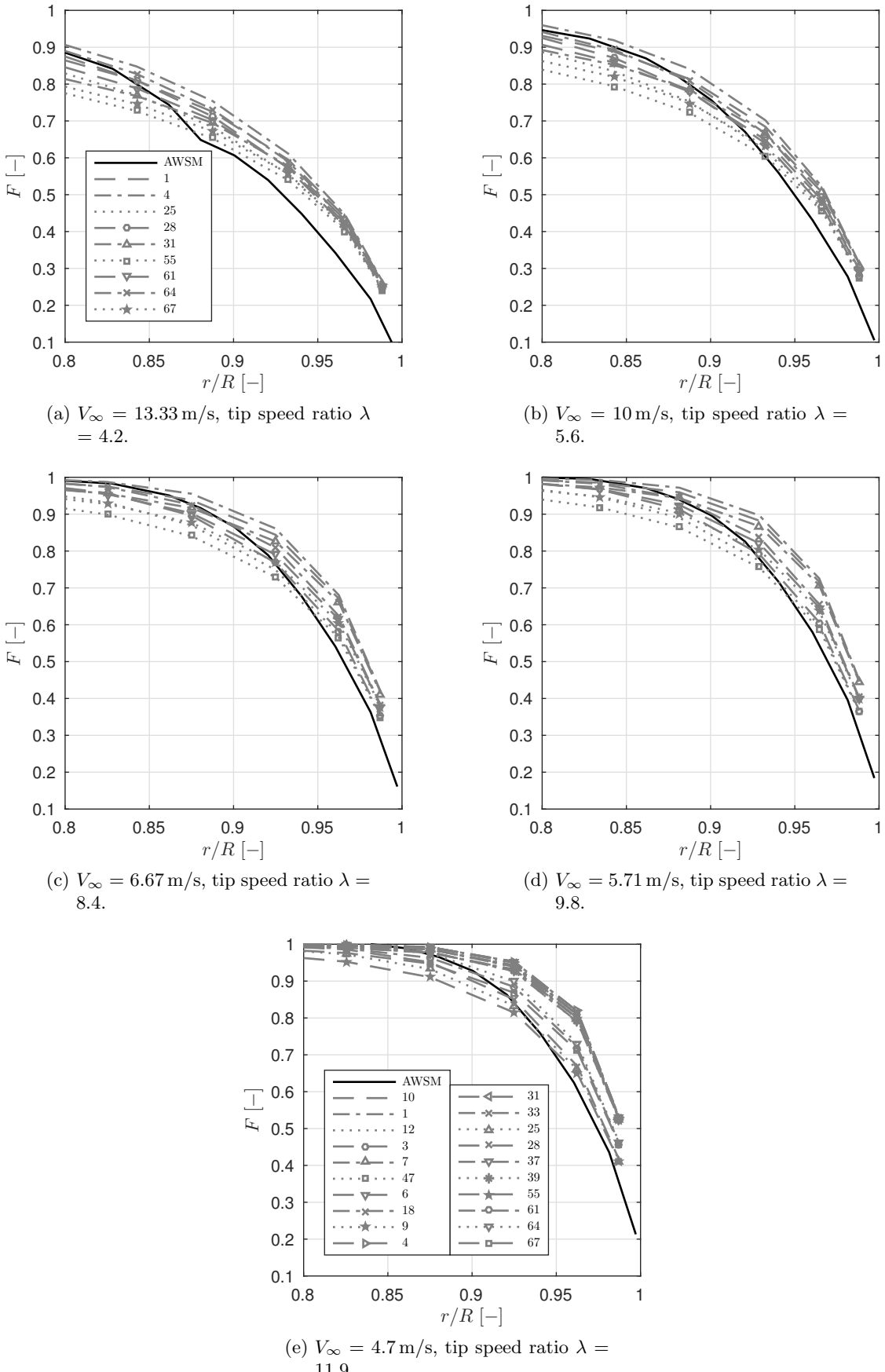
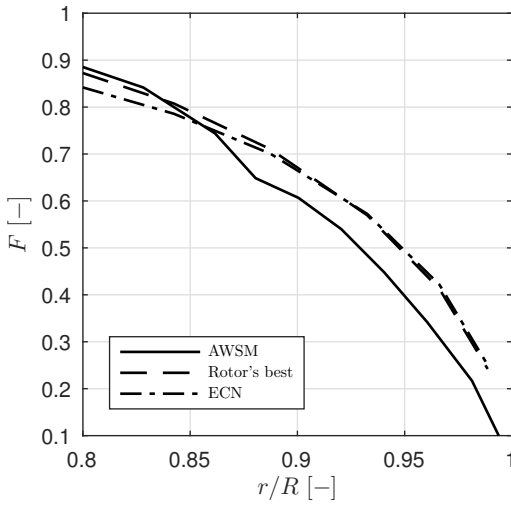
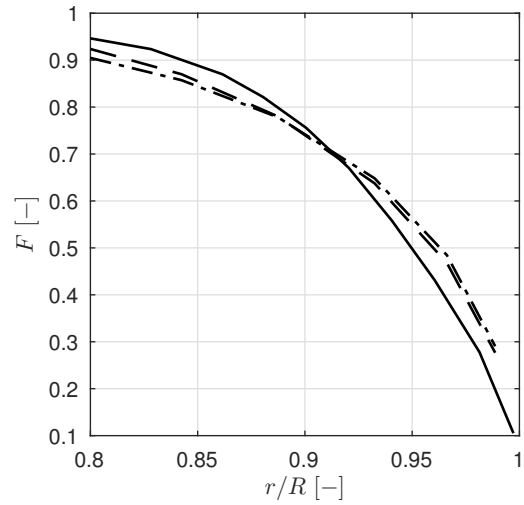


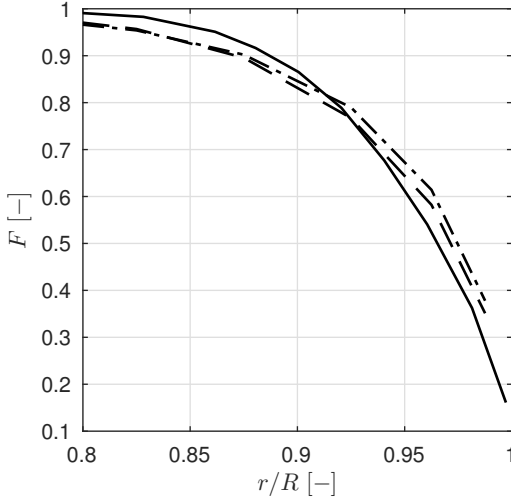
Figure 5.33: The AWSM tip loss factors and a variety of Prandtl tip loss factors at 4 wind velocities V_∞ and thus 4 tip speed ratios. The differences can be explained by the effect of the loading and the modelling of the wake expansion and trailedd tip vortex. The numbering of the tip loss factors can be found in table 5.3.



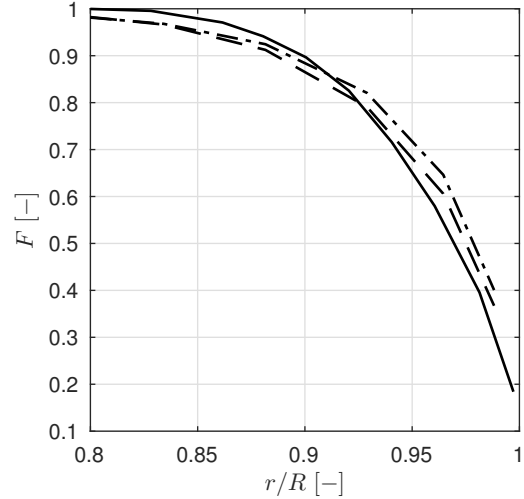
(a) $V_\infty = 13.33 \text{ m/s}$, tip speed ratio $\lambda = 4.2$.



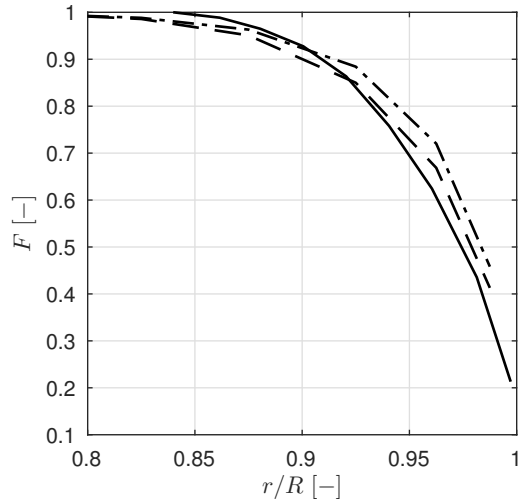
(b) $V_\infty = 10 \text{ m/s}$, tip speed ratio $\lambda = 5.6$.



(c) $V_\infty = 6.67 \text{ m/s}$, tip speed ratio $\lambda = 8.4$.



(d) $V_\infty = 5.71 \text{ m/s}$, tip speed ratio $\lambda = 9.8$.



(e) $V_\infty = 4.7 \text{ m/s}$, tip speed ratio $\lambda = 11.9$.

Figure 5.34: The AWM, the rotor's best (F_{30}) and the ECN (F_{71}) tip loss factor for the 4 wind velocities V_∞ settings. Comparable to what has been shown before, both Prandtl tip loss factors do no show large differences with each other and with the AWM tip loss factor.

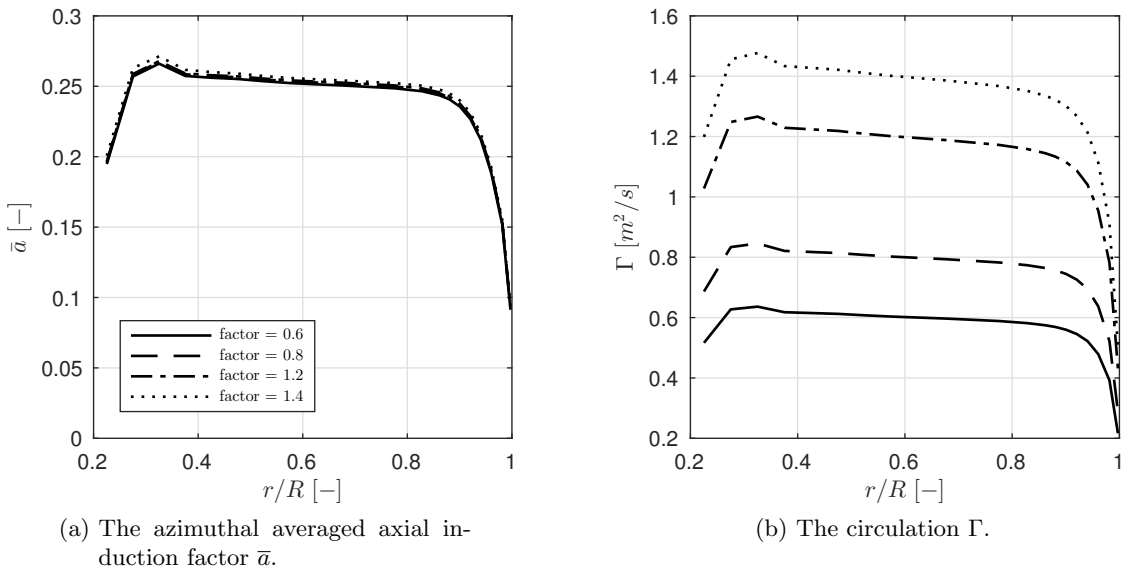


Figure 5.35: The results for the azimuthal averaged axial induction factor \bar{a} and circulation Γ , by multiplying the rotational velocity Ω and wind velocity V_∞ with the same factor, resulting in an unchanged tip speed ratio λ .

figure 5.37b for the 0.6 and 1.4 cases, to visualize the difference in the extreme cases. Note that the x-axis shows the distance downstream (the rotor is located at $x = 0$) in rotor diameters and the y-axis shows the top tip region (the total rotor span is from 1 to -1). From this figure it can be concluded that the wake velocity near the blade is close to identical, independent on the tip speed ratio λ although the wind velocity V_∞ and rotational velocity Ω are changed with the same multiplication factor. This verifies the assumption that the angle between helical wake sheets ϵ_w is equal to the inflow angle ϕ for at least the near blade wake. Deviations of the wake velocities are only visible for far wake distances. This explains that there are no differences visible in figure 5.36.

From the AWSM results it can be concluded that tip speed ratio λ is also an dimensionless indicator on the wake velocity near the blade: although the self-induction of the wake will be different due to the changed settings, this will only affect the wake far downstream.

Blades Lastly, the effect of the number of blades N_b is investigated, because it is interesting to see if the results confirm the expectations and because the NREL Phase VI has one blade less compared to the other rotors. ECN Aero-Module only allows 2 to 4 blades, so this limits the investigation.

Figure 5.38 shows that the azimuthal averaged axial induction factor \bar{a} and circulation Γ . With more blades, there will be more energy extraction from the flow by the rotor, shown by the increase of the azimuthal averaged axial induction factor \bar{a} . Though, keeping the operational conditions the same, the forces on the blades will be lower for a rotor with more blades, shown in figure 5.38b.

The spread of the Prandtl tip loss factors and the AWSM tip loss factor show similar observation to what is explained before: 1) lower loading results in lower values of the

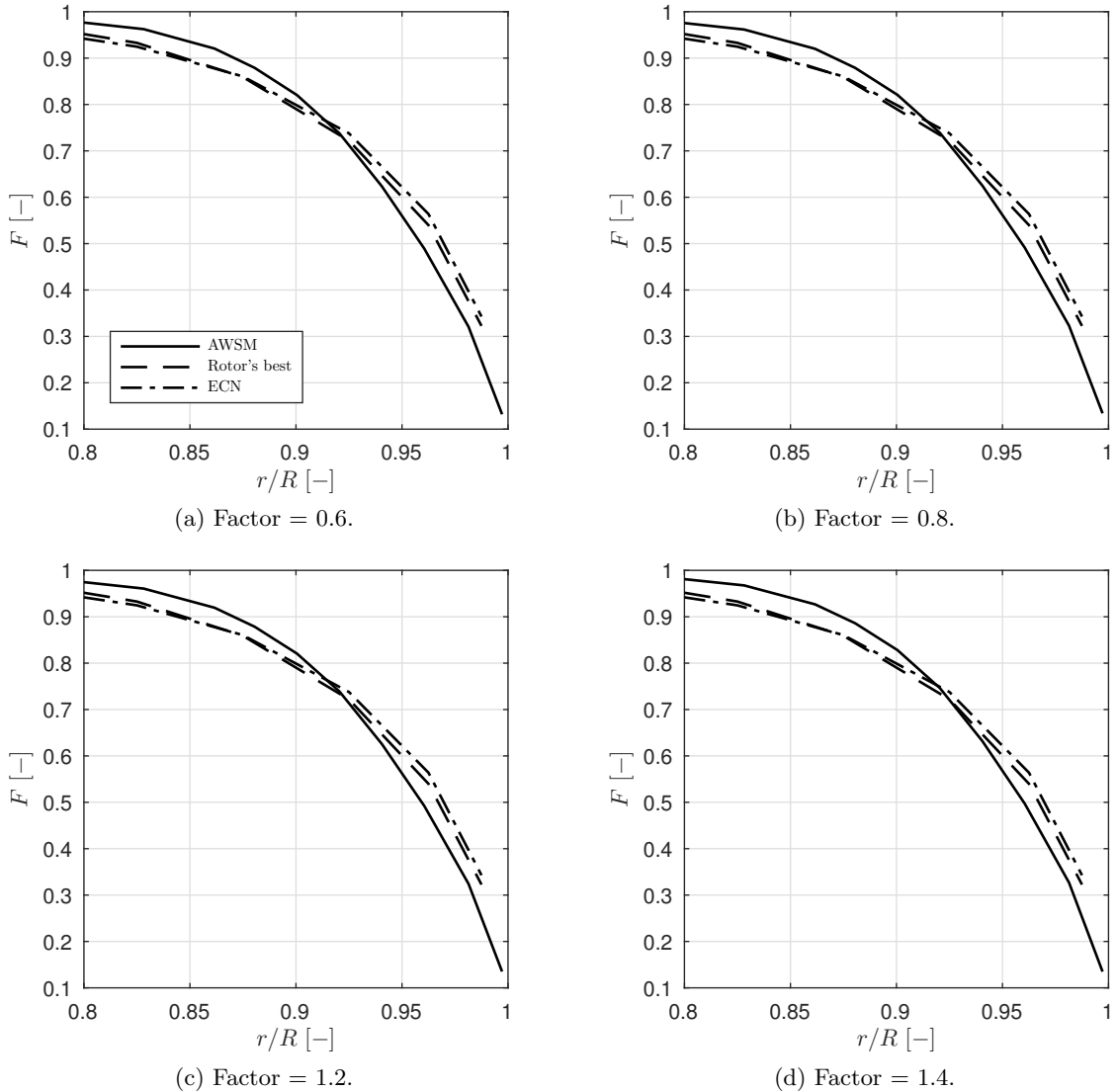
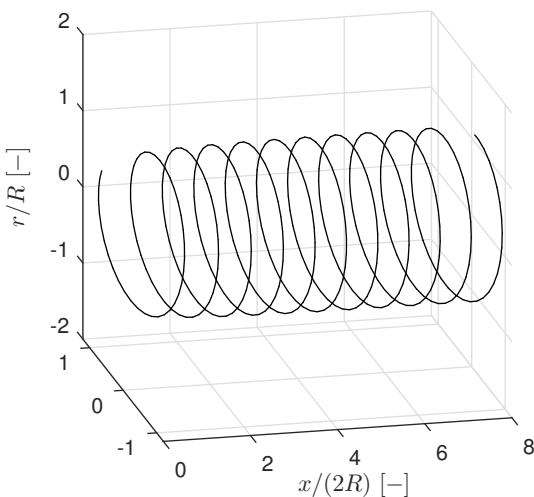
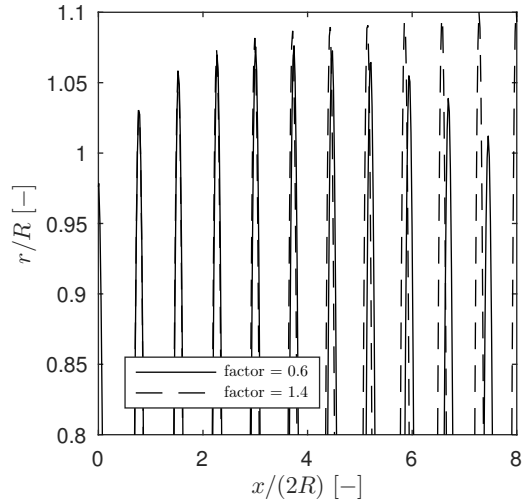


Figure 5.36: The AWSM tip loss factor, the rotor's best (F_{30}) and the ECN tip (F_{71}) loss factor after multiplying the rotational velocity Ω and wind velocity V_∞ with the same factor, resulting in an unchanged tip speed ratio λ .



(a) Three-dimensional view.



(b) Two-dimensional view.

Figure 5.37: The left sub-figure shows one tip wake streamline originating from one blade versus the downstream distance in rotor diameters. This sub-figure is thus partly similar to figure 3.1. The right sub-figure shows an enlarged two-dimensional view, but now with two streamlines plotted, which are the result of two settings of the multiplication factor. The wind velocity V_∞ and rotational velocity Ω are both multiplied with this factor such that the tip speed ratio λ is maintained at 7. It can be seen that the two streamlines only start to deviate significantly after 5 rotor diameters downstream the rotor.

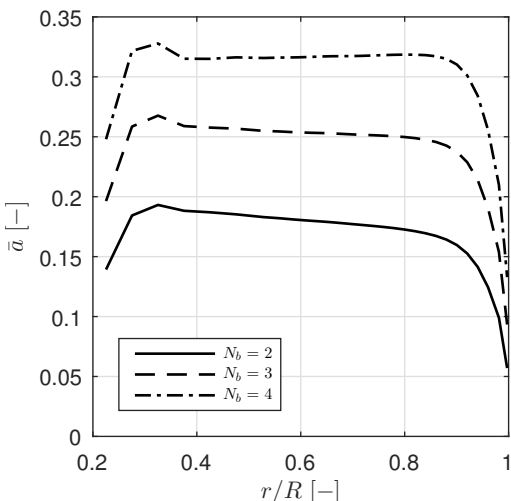
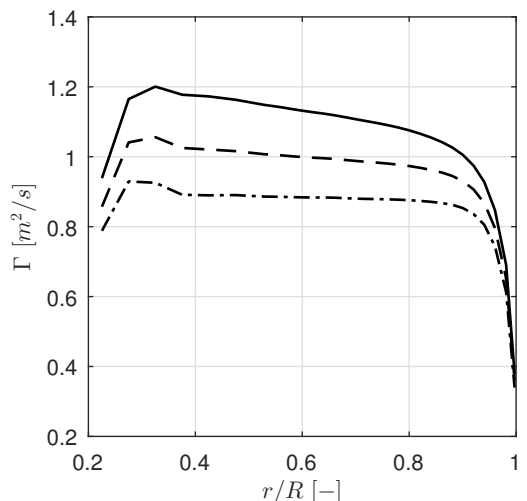
(a) The azimuthal averaged axial induction factor \bar{a} .(b) The circulation Γ .

Figure 5.38: The azimuthal averaged axial induction factor \bar{a} and circulation Γ with equipping the NewBlade rotor with 2, 3 and 4 blades.

tip loss factor, 2) the Prandtl tip loss factors agree more when the loading is lower and 3) the AWSM tip loss factor decays faster when the loading is lower.

The first observation is explained by the fact that for a high number of blades N_b , the value for the distance between two helical wake sheets d will be smaller, with remembering equation (3.20) and noting that the wake velocity is not changed since the operational conditions are the same. Therefore, the curving flow will be less pronounced for a rotor with more blades, explaining the higher values for the tip loss factors for these rotors.

However, the axial induction factor a and the a' will be also higher for the rotors with more blades, indicated by figure 5.38a. Consequently, the differences between the tip loss factors will be higher because the variations are formed by evaluating these variables differently. This is shown in figure 5.39c.

The explanation of the third observation is not different to what was discussed earlier: due to the lower loading, the wake expansion is less, resulting in that the tip vortex remains closer to the blade and thus is the origin of more non-uniform flow at the tip. Though this is only shown by AWSM because the trailed tip vortex is not modelled by BEM.

Figure 5.40 shows that the rotor's best tip loss factor and the ECN tip loss factor are comparable, independent of the N_b and are very close to the AWSM tip loss factor.

Conclusion From these cases it can be concluded that for the assessment of the Prandtl tip loss factor the focus can be on the tip speed ratio λ , as this ratio determines the loading on the blade and the wake effects including wake expansion, distortion and convecting velocity. In the next section the variety of the Prandtl tip loss factors will not be shown, because the observations made in this section are general applicable.

5.4 Real rotors

Now that the behaviour of the AWSM and Prandtl tip loss factors is understood for the constant circulation NewBlade rotor, this section will discuss the results for the tip loss factors for four reference rotors. First the results per rotor are shown in a similar way as was done previously. After this, the results of the assessments concerning these four rotors are taken together, to be able to create the general insights.

5.4.1 Per rotor

As discussed in section 5.3, the non-uniform flow is a function of the tip speed ratio λ . Therefore, the tip speed ratio λ is changed, but differently per rotor in order to be in line with defined operational conditions in literature for each rotor. Hence, table 4.1 gives the conditions used in this thesis which also are commonly used in other studies.

Each tip loss factor figure will now also show, besides the AWSM, rotor's best and ECN tip loss factor, the overall best tip loss factor. When available, the CFD tip loss factor will be also shown. The overall best tip loss factor is computed in a similar way to the rotor's best tip loss factor, but now for all the five rotors (thus including the NewBlade rotor, however excluding this blade does not change the outcome) and operational conditions:

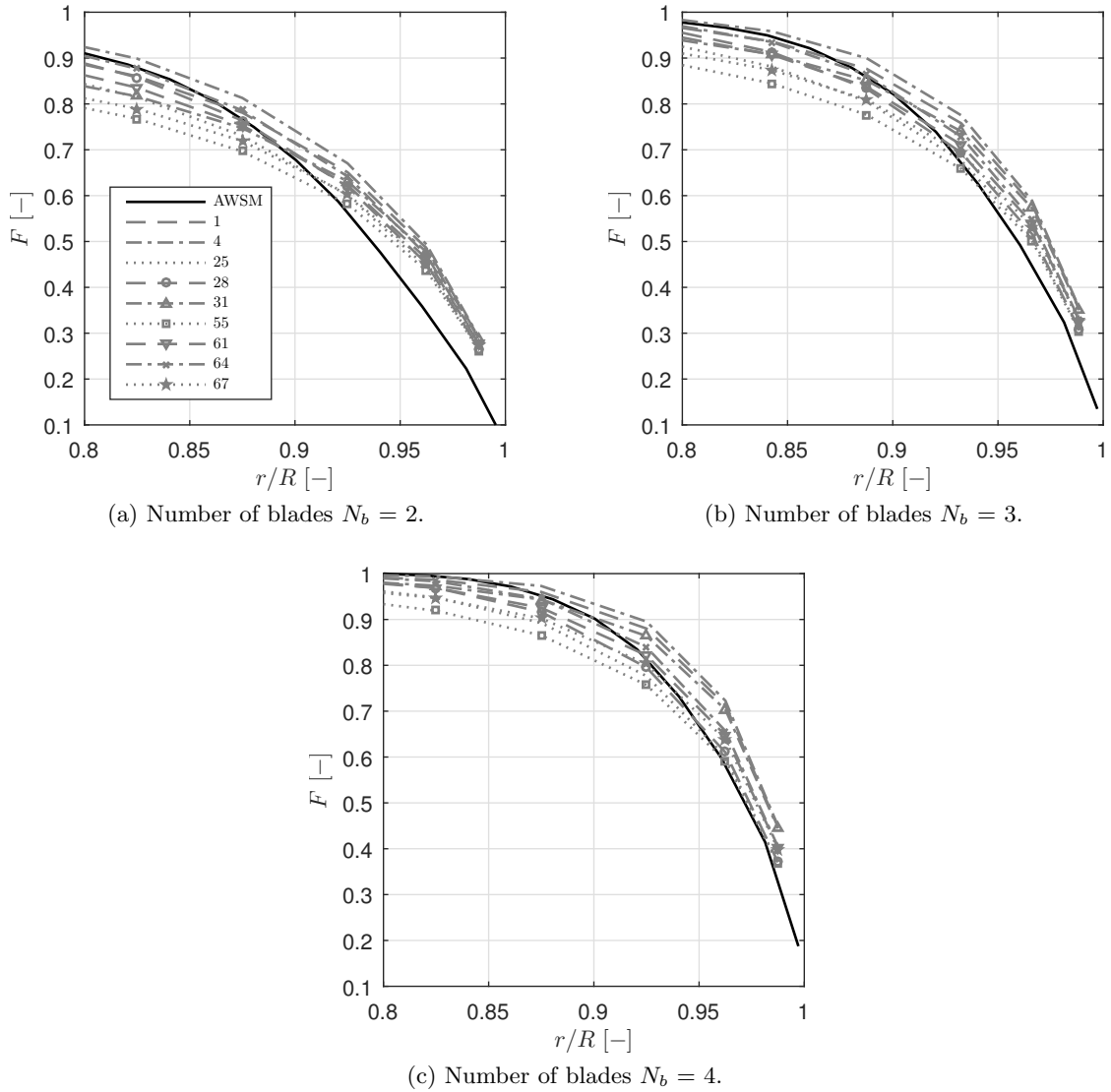


Figure 5.39: The AWSM tips loss factor and a variety of the Prandtl tip loss factors for the NewBlade rotor with 2, 3 and 4 blades. It can be seen that the amount of non-uniform flow near the tip decreases with increasing the number of blades. The numbering of the tip loss factors can be found in table 5.3.

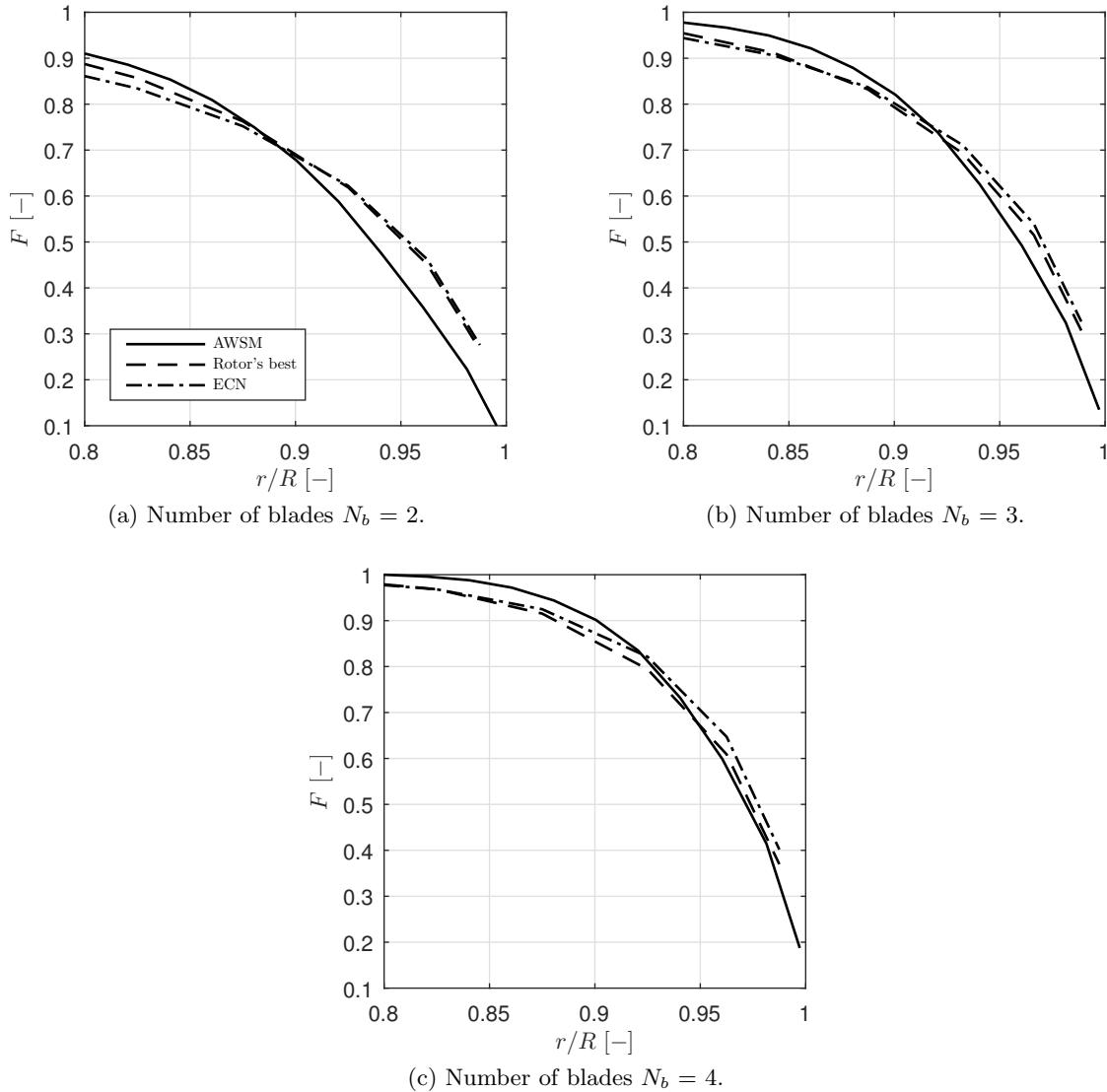


Figure 5.40: The AWM tip loss factor, the rotor's best (F_{30}) and the ECN (F_{71}) tip loss factor for the rotor with 2, 3 and 4 blades. Once more are the difference between the rotor's best and the ECN tip loss factor small. Also the same trends of deviations compared to the AWM tip loss factor has been seen earlier.

all 72 Prandtl tip loss factors are compared to the AWSM tip loss factor for each percent point in the last 20 % of the blade span. Note that the rotor's best tip loss factor is defined as the tip loss factor that performs the best considering all conditions for which the rotor has been assessed in this thesis.

Furthermore, each blade is discretized such that there is a high number of sections in the last 75 % of the blade and less sections before this position (the smallest rotor Mexico with $R = 2.25$ m is for example discretized into 39 sections).

Mexico The Mexico rotor is discussed first. Figure 5.41 shows the azimuthal averaged axial induction factor \bar{a} and the circulation Γ as before. It can be seen that for the tip speed ratio $\lambda = 10.02$ and $\lambda = 8.42$, the loading is very high, such that the wake will be in or close to turbulent state. For these conditions it is important to ensure that the wake is fully developed in the simulation.

Compared to the cases seen so far, figure 5.41b shows a non-constant circulation Γ distribution. The dip in the circulation for $\lambda = 4.17$ can be explained by that at these locations the airfoil RISO-A121 is used (from roughly 45 % R to 74 % R). Given the angle of attack α along the span for $\lambda = 4.17$ in figure 5.42a and the lift polars in figure 5.42b (obtained from experiments, see Boorsma and Schepers (2011)), it can be concluded that the lift coefficient C_l is lower, compared to the other regions due to the use of this airfoil.

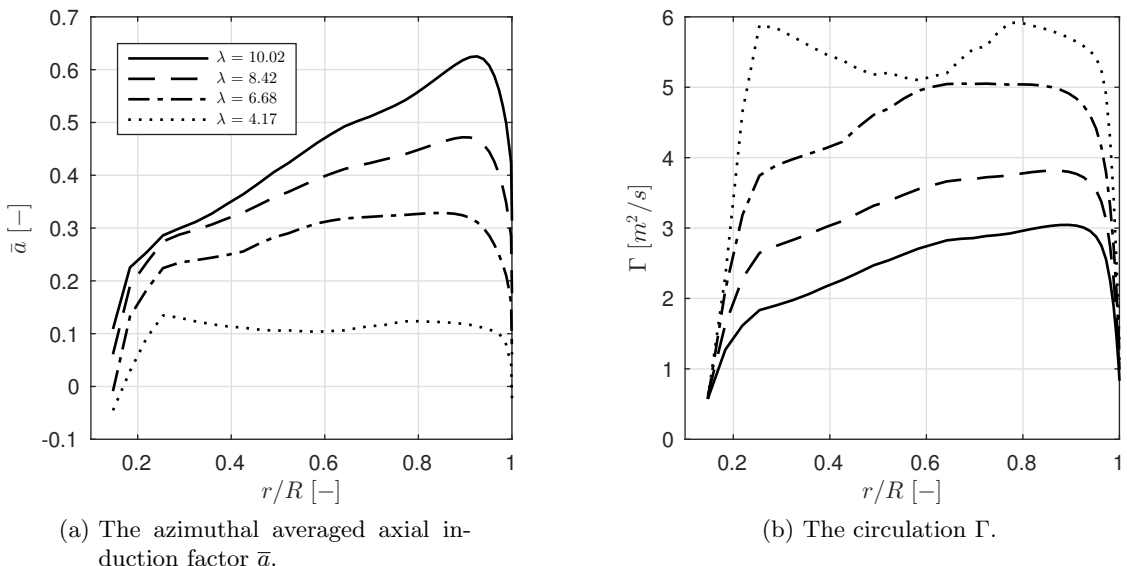


Figure 5.41: The results for the azimuthal averaged axial induction factor \bar{a} and circulation Γ for the Mexico rotor at 4 conditions.

The four tip loss factors are shown in figure 5.43. All the observations done in section 5.3 will be also visible in this section. For example, higher tip speed ratios lead to less non-uniform flow described by the Prandtl tip loss factor, as the helical wake sheets are closer to each other, giving the flow less opportunity to interact with the sheets. This explains that the values of the tip loss factors are higher in figure 5.43a compared to the other sub-figures and decrease with the tip speed ratio λ .

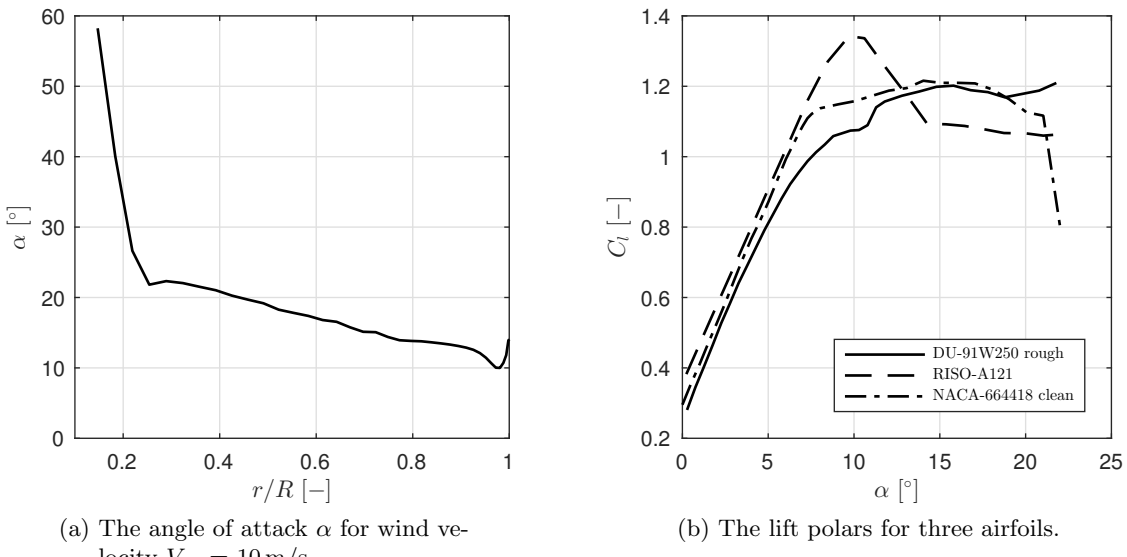


Figure 5.42: This figure shows for the Mexico rotor, the angle of attack α when the wind velocity $V_\infty = 10 \text{ m/s}$ and the lift polars for the three airfoils which are used in the blade design. The DU-91W250 airfoil is used for the inboard sections to 45 % R , the RISO-A121 airfoil is used for sections between 45 % R to 74 % R and the NACA-664418 airfoil is used for the outboard sections (note that there are transition airfoils used, so these percentages are taken roughly). With the high angles of attack, the dip in circulation Γ midboard the blade (shown in figure 5.41b) can be explained by the different stall behaviours of the RISO-A121 airfoil.

Furthermore, the spread of the tip loss factor is explained by the fact that Prandtl derived his tip loss factor for lightly loaded conditions. When this is not the case, the difference between the axial induction factor a , the angular induction factor a' and azimuthal averaged axial induction factor \bar{a} are large along the span of the blade, especially at the tip. Because the origin of the Prandtl tip loss factor variations lie in the question on which and where these variables should be evaluated, large deviations between the outcome of the tip loss factors are expected, when the conditions are such that the loading is high. As illustrated by figure 5.41a, this is the case for $\lambda = 10.04$. This explains the wide spread of the results in figure 5.43a. The opposite is true for the lower tip speed ratios.

In this last sub-figure the peak close to the end of the span is due to the vortex singularity: evaluating the induction close to the core results in induced velocities that go to infinity with the Biot-Savart law. This can be controlled by the lifting line cut-off radius LCO , as discussed in section 5.2. Because it concerns the only last 0.56 % R for the worst case, the results are accepted.

The faster decay of the AWSM tip loss factor for the lower tip speed ratios is once more explained by the movement of the tip vortex, which stays closer to the tip, compared to the higher tip speed ratios, although the convective velocity is also higher. In any case, BEM does not model these effects, leading to the larger differences between the two models.

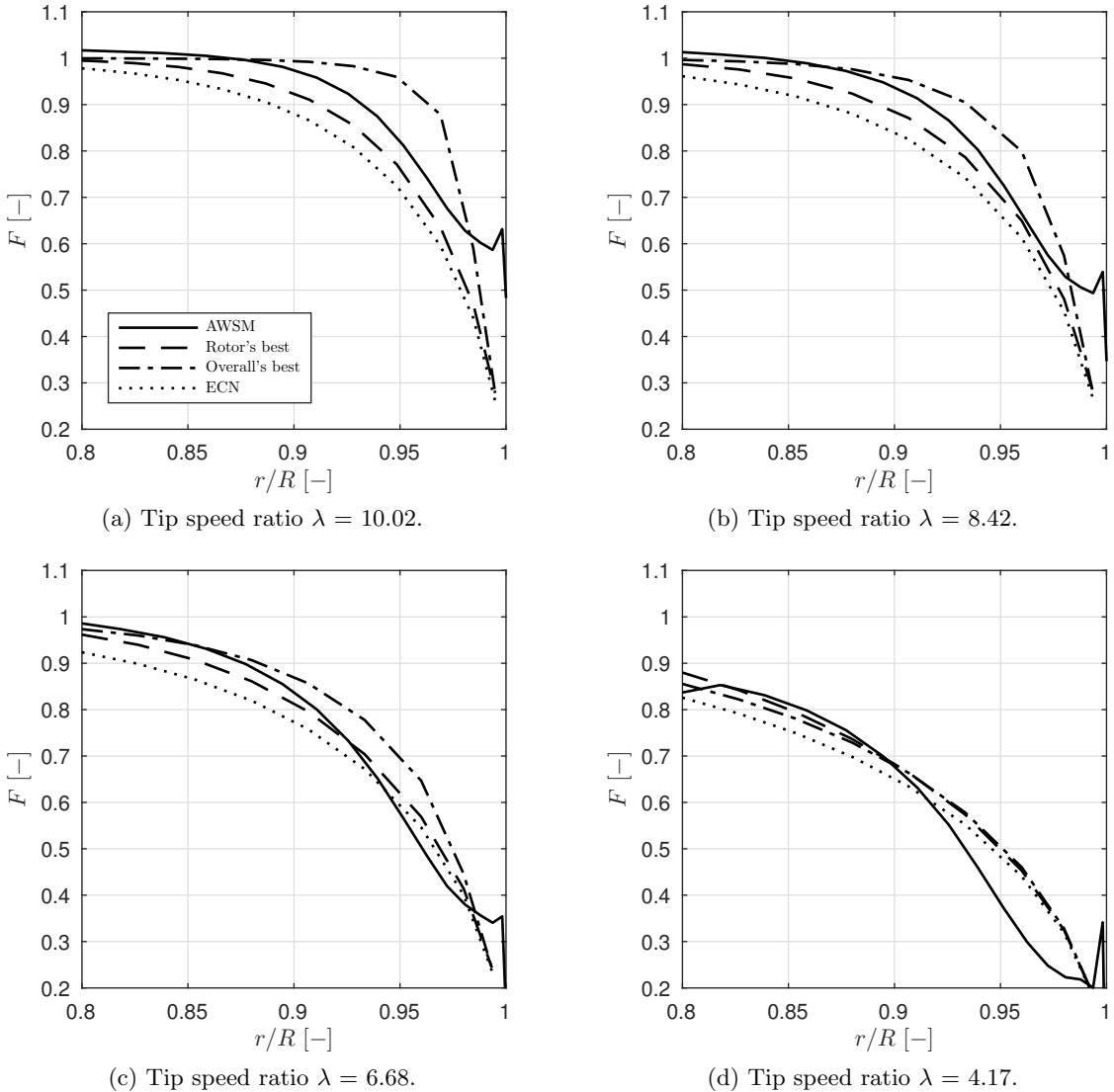


Figure 5.43: The AWSM tip loss factor versus the rotor's best (F_{22}), overall best (F_{13}) and the ECN (F_{71}) Prandtl tip loss factors for the Mexico rotor at 4 different operational conditions. In contrary to the NewBlade rotor results, the differences between the three Prandtl tip loss factors are significant explained by the non-constant circulation distributions.

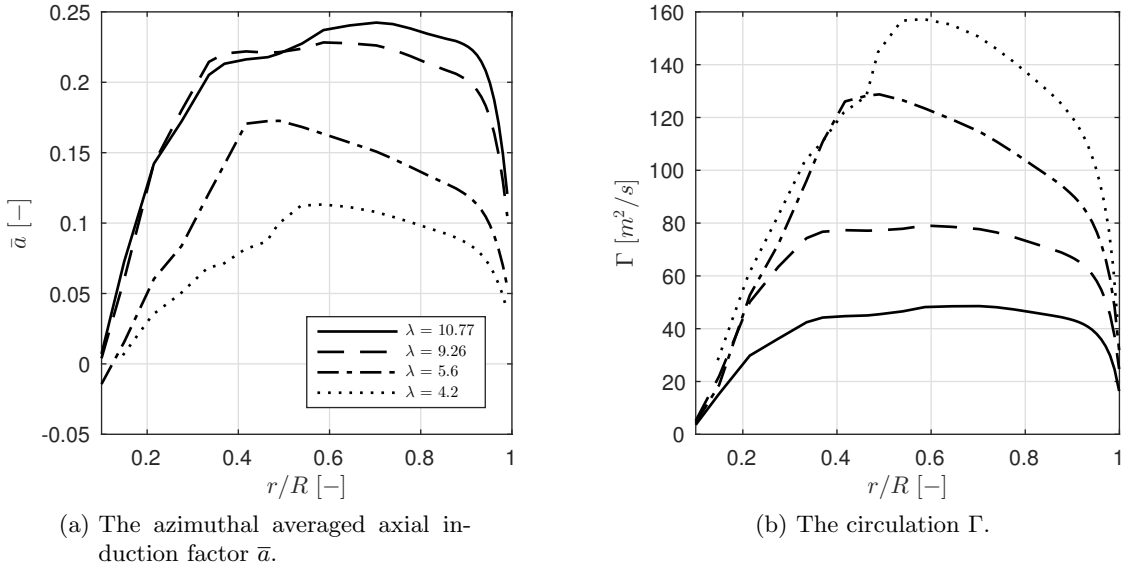
(a) The azimuthal averaged axial induction factor \bar{a} .(b) The circulation Γ .

Figure 5.44: The azimuthal averaged axial induction factor \bar{a} and circulation Γ for the AVATAR rotor at 4 different operational conditions.

The overall best tip loss factor seems to underpredict the non-uniform flow for three out of the four cases, compared to the AWSM tip loss factor. However, compared to ECN's tip loss factor, the overall best is closer to AWSM for the region before 90 % R . ECN's tip loss factor is more conservative for the Mexico rotor.

AVATAR The AVATAR rotor is known to be a low induction reference rotor. This is clearly visible for all the operational conditions in figure 5.44a. The circulation plot (figure 5.44b) shows interesting distributions. This means that the wake structures will be also diverse.

However, as seen in figure 5.45, the lightly loading conditions lead to very small differences between the tip loss factors. Similar to the observations done for the Mexico rotor, the ECN tip loss factor tends to overpredict the non-uniformities.

For $\lambda = 10.77$ and $\lambda = 9.26$ CFD results are available. The CFD tip loss factor was determined in section 5.1.2, with the important doubts on the results discussed. It can be seen that the CFD tip loss factor states that the amount of non-uniform flow is higher before reaching the tip. This can be explained due to that two-dimensional airfoil data is used for AWSM and BEM, where CFD incorporates the three-dimensional effects intrinsically. Several corrections exist to correct the use of the two-dimensional polar data, and are also implemented in ECN Aero-Module, but it might be that the correction is not sufficient enough, if one would say that the CFD tip loss factor is correct. It seems that at the tip there is good agreement, however because it is not known if the used CFD methods are accurate and the number of sections is low, this might be a coincidence.

Innwind For the Innwind rotor, five simulations are run, showing a wide-spread of loading in figure 5.46a. The design of the Innwind rotor is such that the circulation Γ is

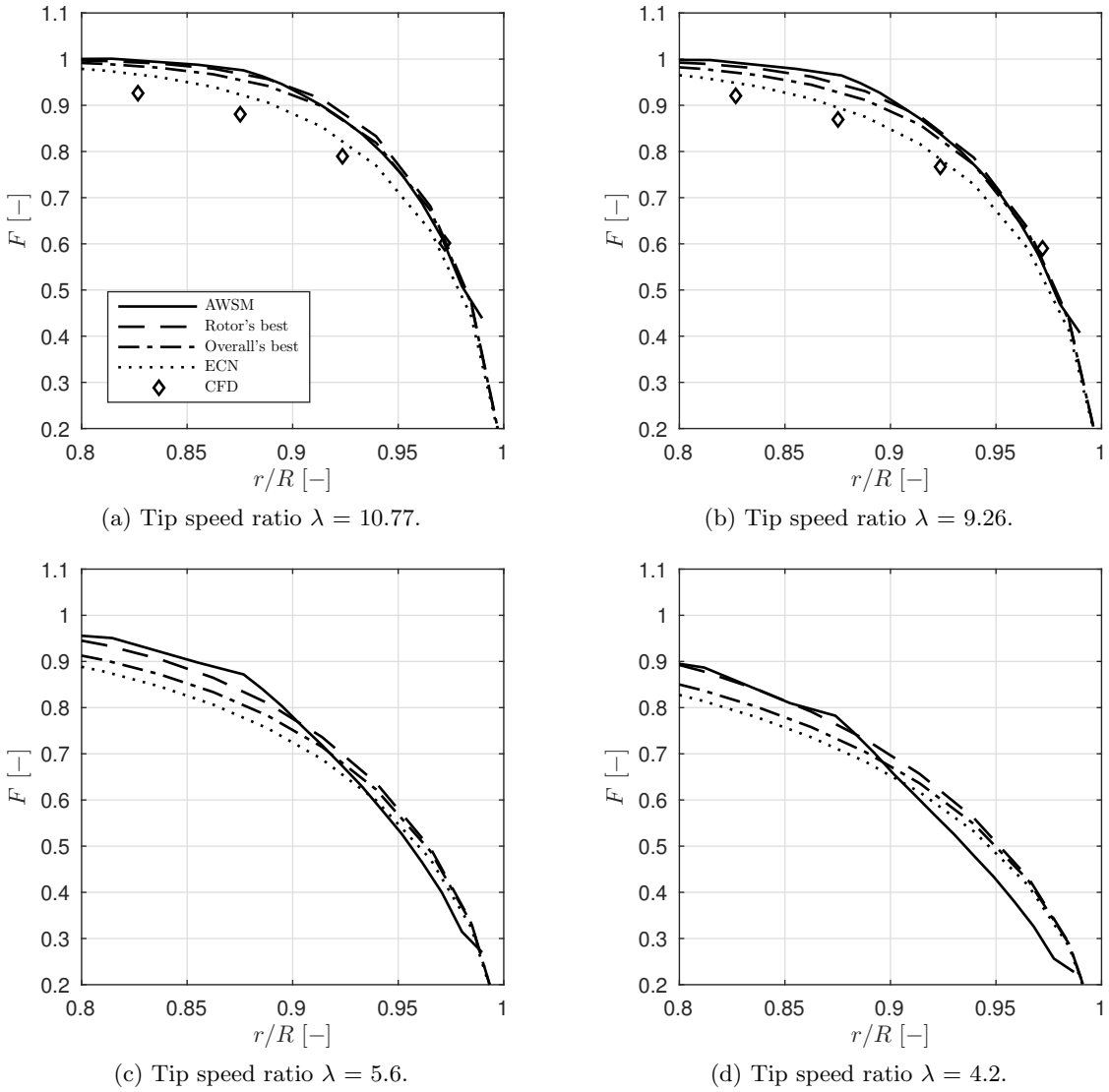


Figure 5.45: The AWSM tip loss factor versus the rotor's best (F_6), overall best (F_{13}) and the ECN (F_{71}) Prandtl tip loss factors for the AVATAR rotor at 4 different operational conditions. For the tip speed ratio $\lambda = 10.77$ and 9.26, the CFD tip loss factor is also plotted. The differences compared to the CFD tip loss factor can be explained by the fact that the other two aerodynamic models use two-dimensional airfoil data, however it should be noted that the CFD data is validated. In most cases the ECN tip loss factor overpredicts the non-uniform flow, except for region very close to the tip when the tip speed ratio λ is lowered.

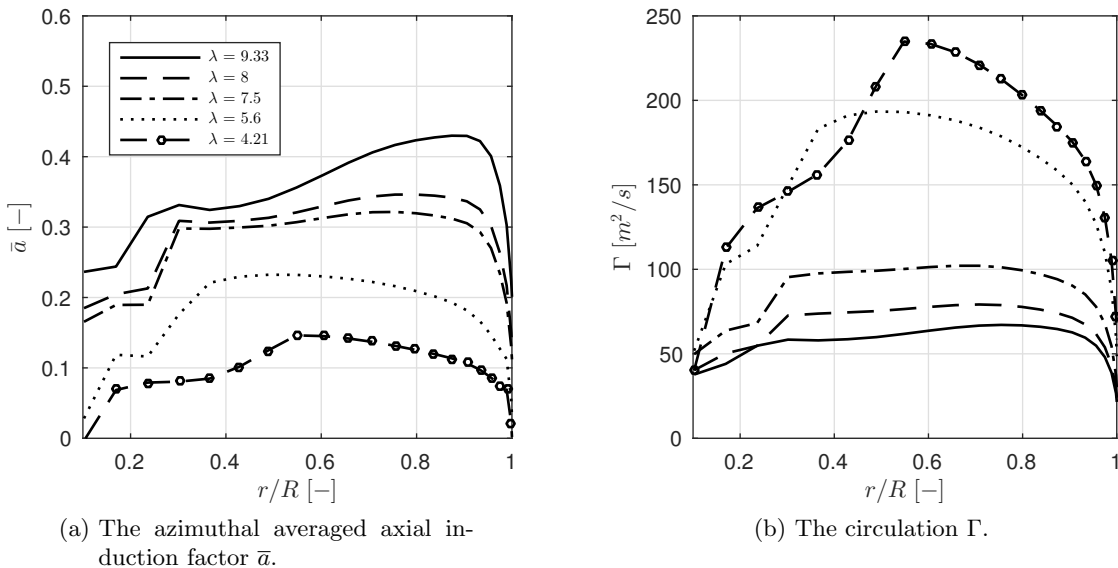
(a) The azimuthal averaged axial induction factor \bar{a} .(b) The circulation Γ .

Figure 5.46: The azimuthal averaged axial induction factor \bar{a} and circulation Γ for the Innwind rotor at 5 different operational conditions.

constant when the wind velocity is between 6 m/s to 9 m/s. For the other two conditions, V_∞ is higher than 15 m/s, for which separated flow is expected. The resulting tip loss factors are given in figure 5.47.

It can be seen that the ECN tip loss factor does not perform well for the normal conditions. For the lower induction conditions, the tip loss factor are once again more similar and the faster decay of the AWSM tip loss factor compared to the Prandtl tip loss factors at the very tip is also visible.

Furthermore, the CFD tip loss factor is determined for $\lambda = 9.33$ and $\lambda = 7.5$. Similar observations to what was discussed for the AVATAR rotor for the CFD tip loss factor can be done for these two cases. Closer to the end of the blade the tip loss factors are comparable, but the CFD tip loss factor is lower in value for the region before the tip. For these regions, the ECN roller bearing tip loss factor shows almost identical results, but it should be noted that the CFD tip loss factor is developed with methods, for which there are unresolved questions on the validity of these methods (as discussed in section 5.1).

NREL Phase VI For the NREL Phase VI rotor, AWSM experiences convergence problems, especially at the root section and for some wind velocities. Therefore, some sections are removed in the input files and the conditions equal to the CFD simulations could not be run. The removal of the root sections leads to, though not shown in the figures, high computed non-uniform flow at the inboard sections. As the focus is on the tip loss factor, this observation is taken as noted, but it does not affect the discussion in this thesis.

With setting the wind velocities to 5 m/s, 6.74 m/s and 10 m/s and the rotational velocity Ω at 71.7 rpm results in three very different conditions (a turbulent wake state condition, close to design condition and a stalled condition, respectively), shown in figure 5.48.

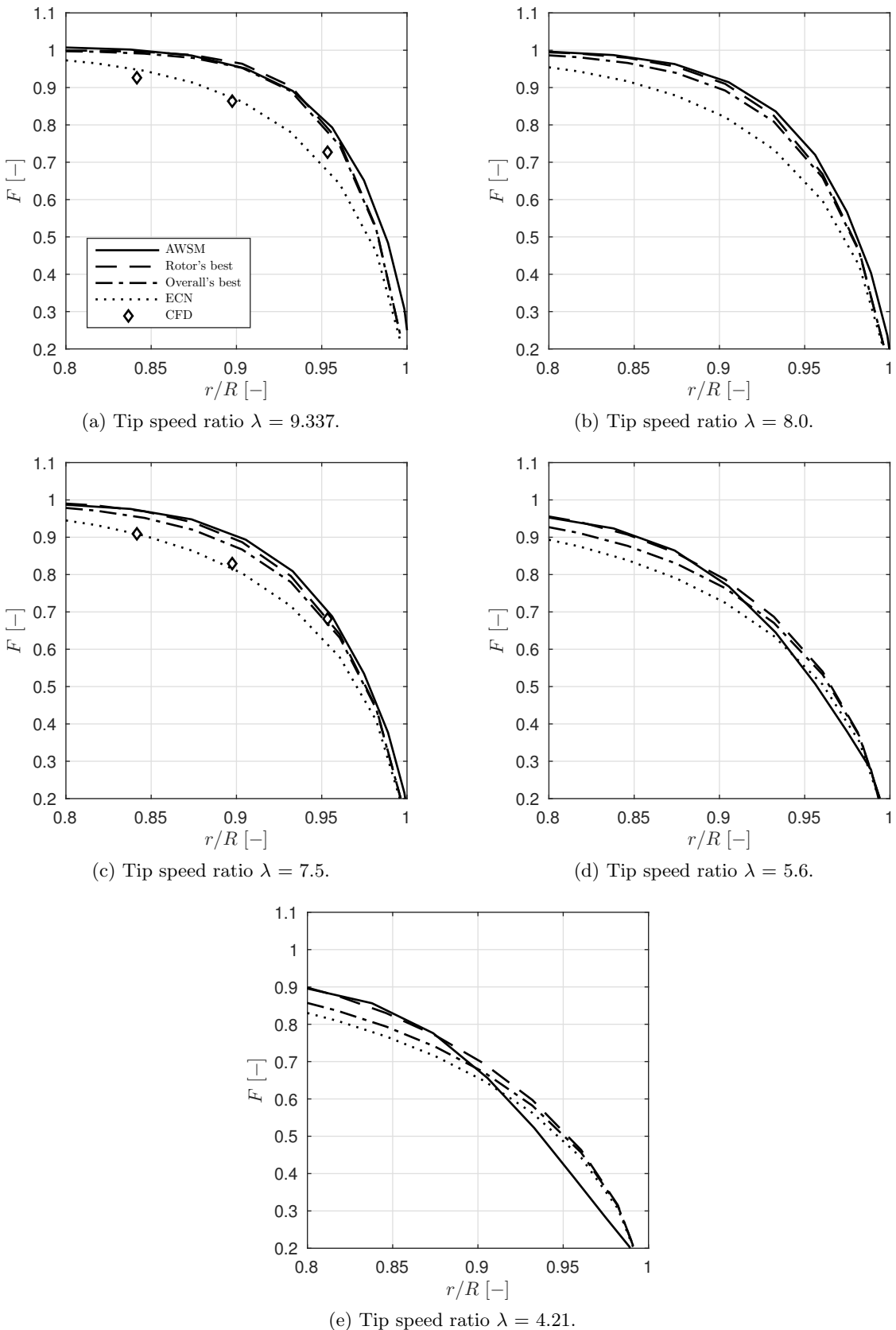


Figure 5.47: The AWSM tip loss factor versus the rotor's best (F_6), overall best (F_{13}) and the ECN (F_{71}) Prandtl tip loss factors for the Innwind rotor at 5 different operational conditions. For the tip speed ratio $\lambda = 9.33$ and 7.5, the CFD tip loss factor is also plotted. The comparisons are similar to what has been seen with the AVATAR results shown in figure 5.45.

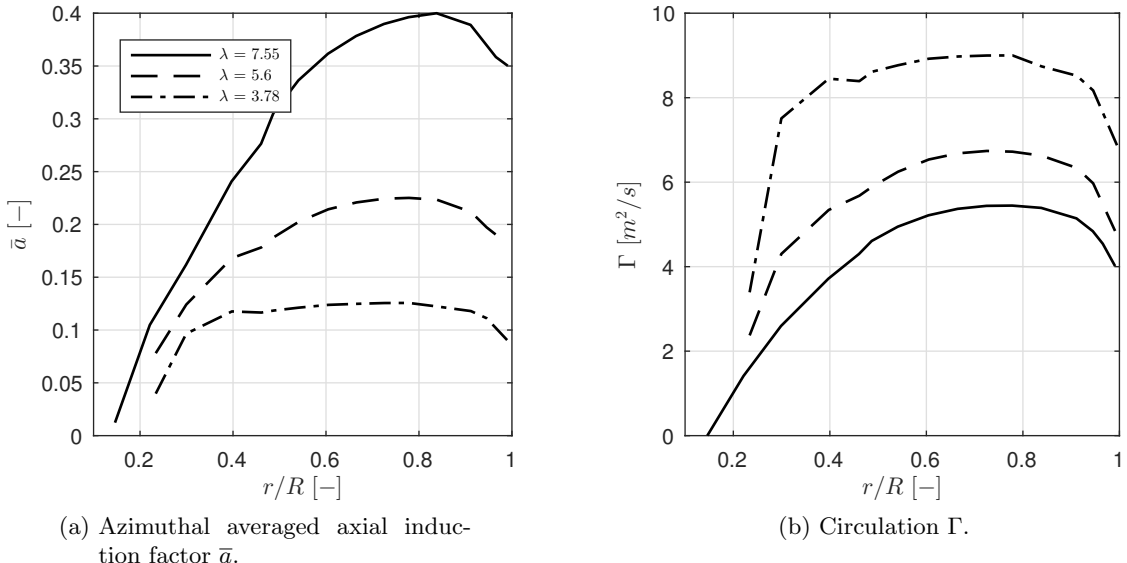


Figure 5.48: The azimuthal averaged axial induction factor \bar{a} and circulation Γ for the NREL Phase VI rotor at 3 operational conditions.

The tip loss factors are given in figure 5.49. By no surprise, the tip loss factors disagree more for the higher tip speed ratios. Also, the general overprediction of the non-uniform of the ECN tip loss factor is illustrated. Lastly, the differences between the AWSM tip loss factor and the Prandtl tip loss factors at the last part of the blade for the lower loaded condition is explained by the lower wake expansion.

5.4.2 General trends

The results per rotor did not show many surprises, except that it was observed that the ECN tip loss factor is overpredicting the tip losses for higher tip speed ratios. Though, the CFD tip loss factor seemed to agree better with the ECN tip loss factor, but because the accuracy of the CFD tip loss factor is questionable and the CFD tip loss factor is not available for all conditions and rotors, the AWSM tip loss factor will still be considered as the desired results for the Prandtl tip loss factors.

The difference between the AWSM tip loss factor and a Prandtl tip loss factor can be computed at different radial locations. This is done for the overall best Prandtl tip loss factor and the ECN tip loss factor for the four rotors at locations $r/R = 84\%$, 92% and 98% . The results are shown in figure 5.50 as function of the tip speed ratio λ .

As a check, it can be seen that the overall tip loss factor performs indeed better than the ECN tip loss factor. Next, it is visible that at more inboard regions (two top sub-figures), the differences are more constant, compared to the outer tip region (two bottom sub-figures), where a dependency on the tip speed ratio λ is clearly shown, especially for the ECN tip loss factor. It seems that the Prandtl tip loss factors are underpredicting the non-uniform flow at the very tip for lower values of the tip speed ratio. For higher values of the tip speed ratio, the overall best tip loss factor is better comparable to the AWSM tip loss factor, in contrary to the ECN tip loss factor.

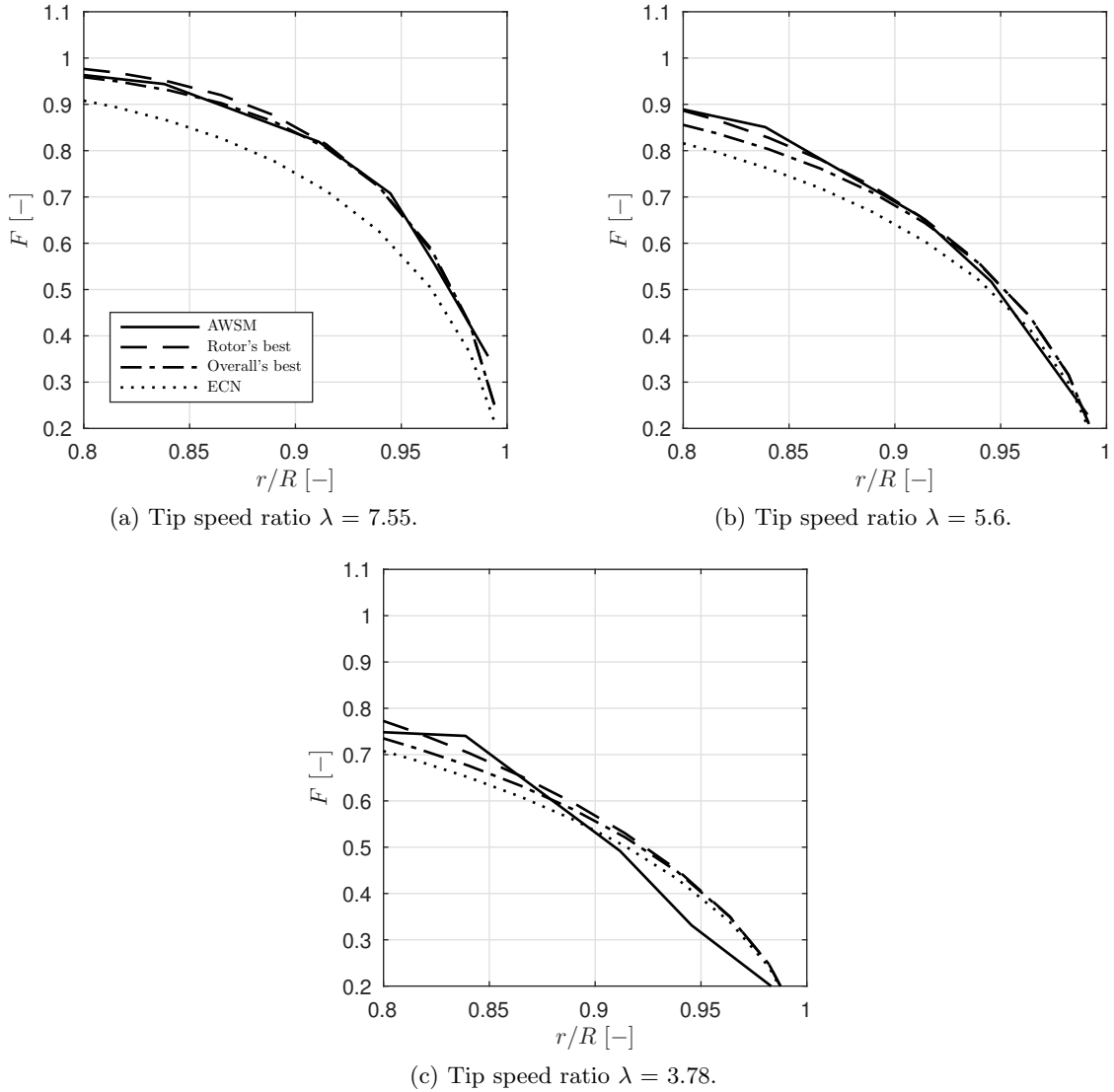


Figure 5.49: The AWSM tip loss factor versus the rotor's best (F_{24}), overall best (F_{13}) and the ECN (F_{71}) Prandtl tip loss factors for the NREL rotor at 3 different operational conditions. The results are similar to what has been seen for the AVATAR and Innwind rotors.

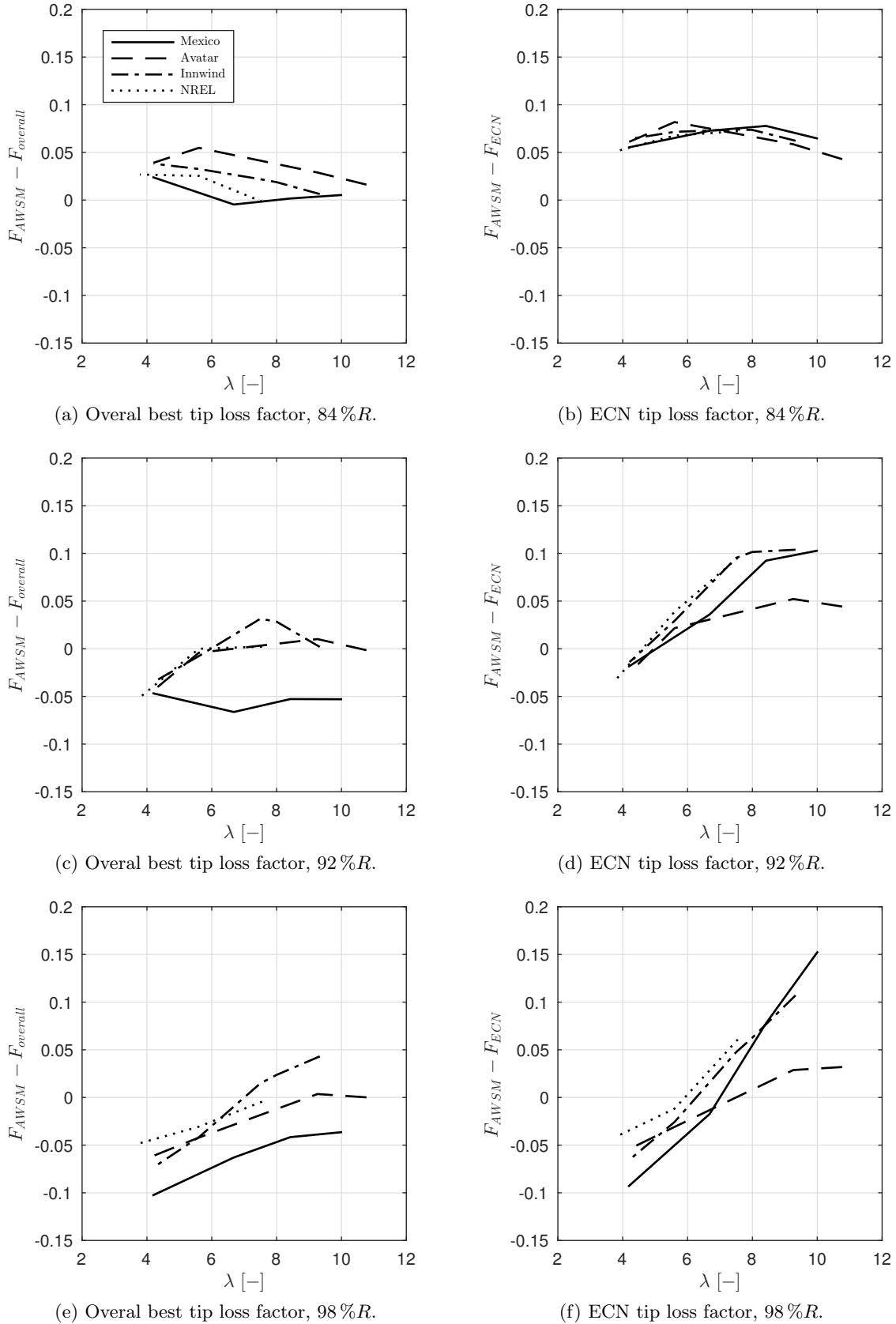


Figure 5.50: The differences of the overall best tip loss factor (F_{13}) and the ECN tip loss factor (F_{71}) compared to the AWSM tip loss factor measured at three radial positions for the 4 rotors as a function of the tip speed ratio λ . It can be seen that the dependency of the differences on the tip speed ratio λ is more pronounced for the computations done at 98 %R.

When lowering the tip speed ratio (by increasing the wind velocity V_∞ or decreasing the rotational velocity Ω), it is known that the induction will be lower. This leads to less wake expansion and thus less radial movement of the tip vortex. The opposite is true for when the tip speed ratio λ is increased. A modification to the AWSM code was done to investigate the effect of the radial movement of the tip vortex. In this modified code, the radial velocity V_z of the wake is set to zero and all the simulations for the real rotors given in table 4.1 are run with this modified AWSM version. The results are given in figure 5.51.

For the evaluation locations 84% R and 92% R , there are only small deviations visible when comparing the results to what is shown in figure 5.50. However, for 98% R there is a shift visible. The difference between the AWSM tip loss factor and the overall best tip loss factor when the radial velocity is set to zero are more negative for the lower tip speed ratios, as illustrated by figure 5.51e compared to figure 5.50e. From figure 5.51e it is also clear that the differences are now less dependent on the tip speed ratio λ when the radial velocity is fixed to zero, except for the Mexico rotor at $\lambda = 10$. In these simulations, there is no wake expansion and therefore the tip vortex modelled in AWSM stays closer to the blade. This results in a lower AWSM tip loss factor and thus the difference between the AWSM tip loss factor minus the overall best Prandtl tip loss factor decreases, compared to when there is wake expansion. The same observation and explanation is true for the ECN tip loss factor results shown in figure 5.51f when comparing them to figure 5.50f.

The shift of difference at the highest λ between the simulations from normal AWSM code and the simulations from the modified AWSM code is roughly the same magnitude of the overprediction of the Prandtl tip loss factor at the lowest λ shown in figure 5.50e and figure 5.50f. Though, this comparison may be bluntly, it indicates, besides the observations on the AWSM tip loss factor when setting the radial velocity to zero, that the lacking of the Prandtl tip loss factor can be found in the disability to account for the wake expansion and tip vortex movement.

However, in this thesis one of the 72 Prandtl tip loss factor is appointed to be the overall best one, besides the rotor's best tip loss factors, comparing the results to the AWSM results in the same manner as described in section 5.3. These are investigated next. Table 5.4 gives an overview of the results. The numbering can be found in table 5.3.

Rotor	NewBlade	Mexico	AVATAR	Innwind	NREL Phase VI	Overall
Best tip loss factor	30	22	6	6	24	13

Table 5.4: Per rotor the best Prandtl tip loss factor and the overall best tip loss factor. With this overview it is interesting to see that all best tip loss factors are in the range of the first 30, with the numbering given in table 5.3. These have in common that the radius r_2 is evaluated locally ($r_2 = r$).

From table 5.4 it can be observed that all stated best tip loss factors belong to the first 30 tip loss factors in table 5.3. These tip loss factors have one thing in common: r_2 in equation (3.26) is evaluated locally ($r_2 = r$). This radius is used to calculate the distance between two helical wake sheets d . Physically, this means that the non-uniform flow is not only dependent on the distance between two helical wake sheets at the tip of the wake, but also in between the sheets. This may sound reasonable, but it should be noted that

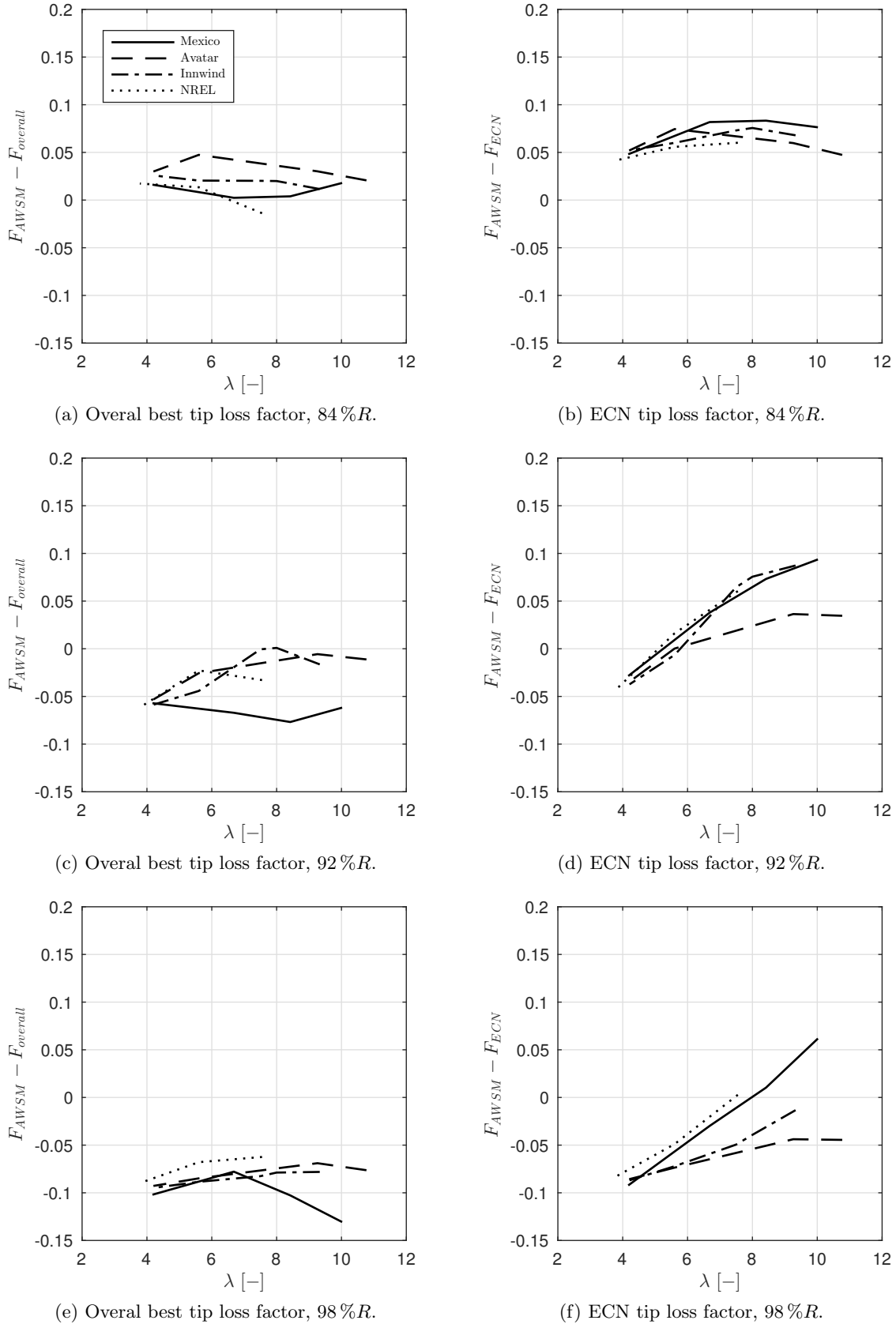


Figure 5.51: The differences of the overall best tip loss factor (F_{13}) and the ECN tip loss factor (F_{71}) compared to the AWSM tip loss factor measured at three radial positions, with the modified AWSM code in where the radial velocity V_z is fixed to zero. When comparing to figure 5.50 it can seen that the results at 98 %R significantly change, in contrary to the other positions.

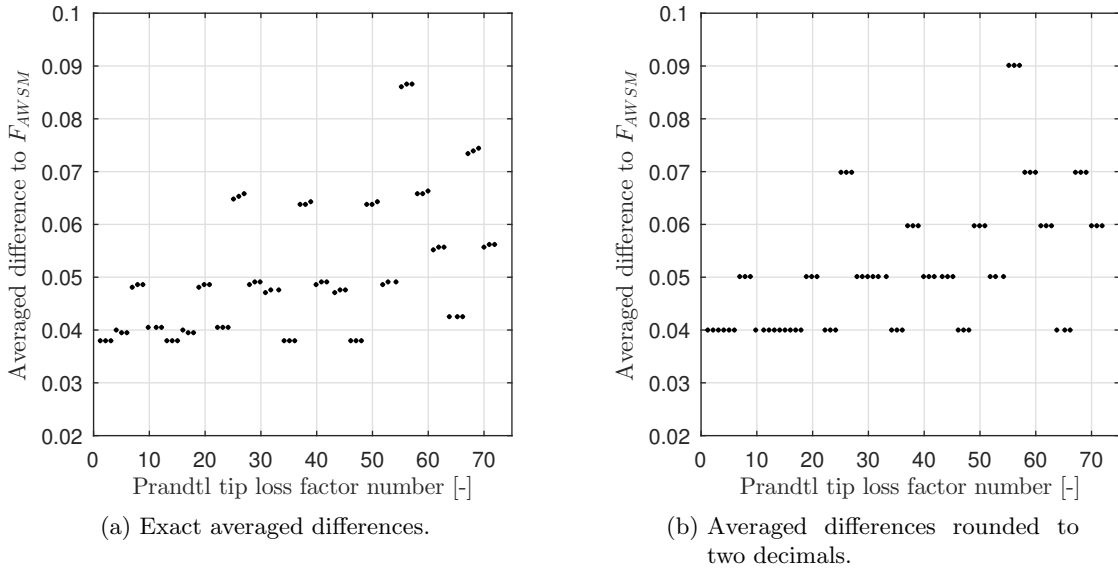


Figure 5.52: The averaged differences of the 72 Prandtl tip loss factor compared to the AWSM tip loss factor considering all simulations done in this thesis, with the exact values (left) and rounding the results to two decimals (right). It can be concluded that there are multiple tip loss factor that perform similar to the best tip loss factor (F_{13}).

the derivation of the Prandtl tip loss factor is based on the describing the curving flow over the tips of the wake sheet. It is not known how to describe the movement of the flow in between the blades and sheet. However, these results show that the Prandtl tip loss factor can be used to approach this movement of the flow when r_2 is set to r , due to that the results are closer to the AWSM tip loss factor when doing so.

The overall best tip loss factor is number 13, which evaluates the r_2 , a , r_3 and a' locally and using $a = \bar{a}$. When plotting the averaged differences of the 72 Prandtl tip loss factor compared to the AWSM tip loss factors of all simulations, it can however be seen that the differences between results are small. Figure 5.52 gives the comparison when not rounding the values (left) and when rounding the computations to 2 decimals. Although hardly visible, figure 5.52a illustrates that F_{13} is the best performing tip loss factor (lowest difference), but figure 5.52b shows that there are more that perform almost identical.

Thus, there is not just one best tip loss factor but 27 best tip loss factors, at least when considering the simulations done in this thesis. Except for 6 tip loss factors, they all evaluate r_2 locally. The question is then which one to choose? The most obvious choice would be the one for which the least amount of calculations are needed. This would exclude the tip loss factors for which the azimuthal averaged axial induction factor \bar{a} are used, because this requires the tip loss factor to be known, resulting in an extra loop in the BEM iteration. Furthermore, for the three roller bearing and for some other tip loss factors, the axial induced velocity u_{ind} is required to be known up front, as the value at the tip is used (for these BEM codes the axial induced velocity u_{ind} is first estimated). Therefore, these can also be excluded from the list to be used. The same holds for the tip loss factors that evaluate the angular induction factor a' at the tip, which is also not

known from the start of the computations.

These considerations narrow the best tip loss factors down to 6 variations (tip loss factors 1, 2, 4, 6, 34 and 36 in table 5.3), for which the averaged results for the simulations in this thesis show identical values, when rounding this average to two decimals. With the observations deducted from table 5.4 that each rotor's best tip loss factor evaluates r_2 locally, it is recommended to also not use tip loss factors 34 and 36, as these evaluate r_2 at the tip.

For completeness, the settings of the four best Prandtl tip loss factors are given in table 5.5, which should be used in equations (3.21) to (3.23), considering the simulations done in this thesis. From this table it can be seen that, besides r_2 , also the axial induction factor a should be taken locally in order to obtain the best predictions of non-uniform flow.

Furthermore, figure 5.52a shows that there are always three tip loss factors that give almost identical results compared to each other (indicated by the cluster of three consecutive dots). With table 5.3 it can be concluded that this is due to that the results are insensitive on the choice of the angular induction factor a' . The choice of the radius r_3 is also less important compared to the parameters r_2 and a .

	r_2	a	r_3	a'
F_1	local	local	local	local
F_2	local	local	local	tip
F_4	local	local	tip	local
F_6	local	local	tip	0

Table 5.5: The parameter settings for the best performing Prandtl tip loss factors, which show identical results. The labelling of the tip loss factors is done to distinguish the 72 Prandtl tip loss factor variations. The settings of the parameters should be used in equations (3.21) to (3.23).

$$F = \frac{2}{\pi} \arccos \left[\exp \left(-\frac{N_b}{2} \frac{R-r}{r_2} \frac{\sqrt{V_n^2 + V_t^2}}{V_n} \right) \right] \quad (3.21 \text{ revisited})$$

$$V_n = U_\infty(1-a) \quad (3.22 \text{ revisited})$$

$$V_t = \Omega r_3(1+a') \quad (3.23 \text{ revisited})$$

Chapter 6

Conclusion and recommendations

In this chapter the conclusions of this study and the recommendations that will allow further research will be presented. First, section 6.1 will discuss the conclusion following the order of the objectives and section 6.2 will list the recommendations.

6.1 Conclusion

In this thesis the Prandtl tip loss factor used in Blade Element Momentum theory (BEM) is investigated on its ability to accurately predict the non-uniform flow in the rotor plane of a horizontal axis wind turbine. The insights are based on results from higher fidelity models such as Computational Fluid Dynamics (CFD) and vortex methods.

In this thesis a full and complete derivation of the Prandtl tip loss factor is given, which is rarely found in literature. This derivation leads to a basic general expression for the Prandtl tip loss factor. The derivation also makes clear that when applying the Prandtl tip loss factor in a BEM code, there are still several underlying parameters open to be chosen, although this has not been discussed in literature. The freedom is basically related to the way how the angle between the helical wake sheets should be interpreted in BEM, which leads to freedom in choice of local versus tip values or in blade versus azimuthally averaged values of the induction factors. It is striking to note that this freedom in the Prandtl tip loss factor parameters is never realized when assessing results from BEM codes, even though this thesis shows that there are at least 72 Prandtl tip loss factors variations which can be considered feasible.

The performance of the different variations has been assessed for five rotors in a wide-range of operational conditions. In order to do so, four sub-objectives have been stated in this thesis. The conclusions corresponding to these objectives are given in the respective order.

1. The first objective is to obtain a tip loss factor from CFD that is apparent to the Prandtl tip loss factor. The challenge of this objective is to extract the induced

velocities from the CFD results in order to be able to compute the angle of attack, which are defined in the engineering methods. Although within the thesis project much insights have been gained on the performance of several methods to extract these engineering variables from CFD results, no firm conclusions can be drawn yet. For the reasons that the Upwash from bound Vortex Line (UVL) method agreed better with the expectations and this method showed perfect agreement with the same method coded by the University of Stuttgart, this method is used to obtain a CFD tip loss factor.

2. The second objective is to obtain a tip loss factor from the vortex method, which can be compared to the Prandtl tip loss factors. Much effort had to be spent on the discretization and on the locations of the evaluation points, which should be chosen not close to the edges of the cross-sections in order to avoid non-physical results. Eventually, the discretization at the tip region of the blade is increased, such that the induced velocities on the blade are directly outputted by the free wake lifting line code AWSM with keeping the computational time low, in contrary to the usual procedure in where a so-called external flow field module is called.
3. In the third part of the thesis, the 72 Prandtl tip loss factor variations are assessed for a simplified rotor that is developed in this thesis, which satisfies the assumptions made by Prandtl. From the sensitivity study it is explained that the loading of the blade affects
 - the mutual agreement in Prandtl tip loss factors due to that the variations of the induction factors (which are dependent on the loading of the blade) are largely responsible for the differences between the Prandtl tip loss factor variations,
 - the general behaviour of the AWSM tip loss factors due to the radial movement of the tip vortex,
 - the faster decay of the AWSM tip loss factors compared to the Prandtl tip loss factors due to the movement of the tip vortex.

Furthermore it is concluded that the rotor's best Prandtl tip loss factor and the ECN tip loss factor show similar results for the simplified rotor, but tend to overpredict the non-uniform flow and the beginning of the tip region (defined as the last 20 % of the span) and underpredict the non-uniform flow near the very tip of the blades.

4. The fourth objective is to identify trends and possible improvements that hold for multiple more complex rotors. The tip loss factors from the three aerodynamic models are compared for the Mexico, AVATAR, Innwind and NREL Phase VI rotors. Due to that these rotors are not conform the assumptions made by Prandtl, the tip loss factors show more significant differences, especially at the higher loading conditions. It is also shown that there is a pronounced dependency of the tip speed ratio on the performance of the Prandtl tip loss factor, which is related to the lack of modelling the radial flow component.

Finally, four Prandtl tip loss factors are discussed to be the best performing Prandtl tip loss factors. The parameters are given in table 5.5, which should be used in

equations (3.21) to (3.23). From these results it is concluded that the radius r_2 , related to the distance between the helical sheets, and the axial induction factor a should be evaluated locally. The results are negligibly sensitive on the radius r_3 , which is related to the tangential velocity component, and the angular induction factor a' .

	r_2	a	r_3	a'
F_1	local	local	local	local
F_2	local	local	local	tip
F_4	local	local	tip	local
F_6	local	local	tip	0

Table 5.5 revisited: The parameter settings for the best performing Prandtl tip loss factors, which show identical results. The labelling of the tip loss factors is done to distinguish the 72 Prandtl tip loss factor variations. The settings of the parameters should be used in equations (3.21) to (3.23).

$$F = \frac{2}{\pi} \arccos \left[\exp \left(-\frac{N_b}{2} \frac{R-r}{r_2} \frac{\sqrt{V_n^2 + V_t^2}}{V_n} \right) \right] \quad (3.21 \text{ revisited})$$

$$V_n = U_\infty(1-a) \quad (3.22 \text{ revisited})$$

$$V_t = \Omega r_3(1+a') \quad (3.23 \text{ revisited})$$

With this thesis the limitations of the Prandtl tip loss factors are identified with the use of higher fidelity aerodynamic models for multiple rotors at a wide-range of operational conditions. It is furthermore presented that from the 72 Prandtl tip loss factor variations, four outperform the others. This study therefore increases the insurance of computing the loads at the tip in the most accurate way with the current Prandtl tip loss factor, consequently leading to more efficient wind turbine blade designs.

6.2 Recommendations

With this thesis the limitations of the Prandtl tip loss factor are clear, but further research has to be done in order to increase the accuracy of the Prandtl tip loss factor and thus the BEM simulation. The recommendations concerning this further research are listed next.

- The Prandtl tip loss factor should be improved on the ability to account for the non-uniform flow due to the radial movement of the flow which is shown to be a function of the tip speed ratio. However, because the Prandtl tip loss factor is not initially designed to correct the effects of wake expansion or tip vortex movement, it is recommended to take the derivation of the Prandtl tip loss factor into account when improvements on a fundamental level are of interest.

- In this thesis the effect of the radial movement of the flow is only investigated by comparing the original results with results for which the radial flow component is set zero. It is therefore recommended to investigate and map this radial flow component in more detail for several rotors and operational conditions.
- In order to use CFD results in the manner described in this thesis, the extraction of the engineering variables, such as the induced velocities and the angle of attack, should be validated. From CFD data the amount of non-uniform flow can also be investigated by directly looking at the flow field computations.
- In this thesis the tip loss factor from the lifting line method are treated as the desired Prandtl tip loss factor. The use of a panel vortex method can help to distinguish the effect of chordwise distribution of the bound vorticity on the loading of the blade, in contrary to the lifting line method in where there is no chordwise vorticity distribution modelled.
- One of the four best Prandtl tip loss factor should be used in further BEM computations when the lacking of the current form of the Prandtl tip loss factor described in the first point is accepted. These tip loss factors have in common that the distance between the helical wake sheets and the axial induction factor should be evaluated locally. Further research may also show that one tip loss factor outperforms the other three.
- Only non-yawed uniform inflow conditions are simulated in this thesis. The wake structure and movement is altered heavily when the conditions deviate from these assumptions. Therefore it is expected that the amount of non-uniform flow and thus also the performance of the tip loss factor will be different. It is recommended to extend this study for more complex operational conditions.

In the ideal case, when the stated recommendations are successfully carried out, BEM is able to compute the loads at the tip of the blades accurately, despite the fact that the theory is not considering three-dimensional flow and the wake development.

References

- Anderson, J. D. (2011). *Fundamentals of aerodynamics* (5th ed.). New York: McGraw-Hill.
- Bahaj, A., Molland, A., Chaplin, J., & Batten, W. (2007). Power and thrust measurements of marine current turbines under various hydrodynamic flow conditions in a cavitation tunnel and a towing tank. *Renewable Energy*, 32(3), 407-426.
- Bak, C., Johansen, J., & Andersen, P. (2006). Three-dimensional corrections of airfoil characteristics based on pressure distributions. *European Wind Energy Conference & Exhibition (EWEC)*.
- Betz, A., & Prandtl, L. (1919). Schraubenpropeller mit geringstem energieverlust - mit einem zusatz von L. Prandtl. *Göttinger Klassiker der Strömungsmechanik Bd. 3*, 1-92.
- Boorsma, K., & Grasso, F. (2016). *Ecn aero-module user's manual v221 (confidential)* (Tech. Rep.). ECN.
- Boorsma, K., Grasso, F., & Holierhoek, J. (2011). *Enhanced approach for simulation of rotor aerodynamic loads* (Tech. Rep. Nos. ECN-M-12-003). ECN.
- Boorsma, K., Hartvelt, M., & Orsi, L. (2016). Application of the lifting line vortex wake method to dynamic load case simulations. *Journal of Physics: Conference Series*, 753.
- Boorsma, K., & Schepers, J. G. (2011). *Description of experimental setup - Mexico measurements* (Tech. Rep. Nos. ECN-X-11-120). ECN.
- Boorsma, K., & Schepers, J. G. (2014). *New Mexico experiment - preliminary overview with initial validation* (Tech. Rep. Nos. ECN-E-14-048). ECN.
- Branlard, E. (2011). *Wind turbine tip-loss corrections* (Master thesis). Technical University of Denmark.
- Branlard, E., Dixon, K., & Gaunaa, M. (2013). Vortex methods to answer the need for improved understanding and modelling of tip-loss factors. *IET Renewable Power Generation*, 7(4), 311-320.
- Breton, S. P., Coton, F. N., & Moe, G. (2008). A study on rotational effects and different stall delay models using a prescribed wake vortex scheme and NREL phase VI experiment data. *Wind Energy*, 11(5), 459-482.

- Burton, T., Sharpe, D., Jenkins, N., & Bossanyi, E. (2001). *Wind energy handbook*. Chichester: John Wiley & Sons Ltd.
- Chaviaropoulos, P. K., & Hansen, M. O. L. (2000). Investigating three-dimensional and rotational effects on wind turbine blades by means of quasi-3d navier stokes solver. *Journal of Fluids Engineering*, 122, 330-336.
- De Vries, O. (1979). *Fluid dynamic aspects of wind energy conversion* (Company report No. AG-243). Advisory Group of Aerospace Research & Development (AGARD).
- Dumitrescu, H., & Cardos, V. (2011). Inboard stall delay due to rotation. *Journal of Aircraft*, 49(1), 101-107.
- Eggers, A. J., & Digumarthi, R. (1992). Approximate scaling of rotational effects of mean aerodynamic moments and power generated by the combined experiment rotor blades operating in deep-stalled flow. *Proceedings of the 11th ASME Wind Energy Symposium 1992*, 33-43.
- European Wind Energy Association. (2015). *Wind energy scenarios for 2030* (Tech. Rep.). European Wind Energy Association.
- European Wind Energy Association. (2016). *Wind in power - 2015 European statistics* (Tech. Rep.). European Wind Energy Association.
- Glauert, H. (1926). *The analysis of experimental results in the windmill brake and vortex ring states of an airscrew* (Tech. Rep.). Great Britain Aeronautical Research Committee.
- Glauert, H. (1935). Airplane propellers, division 1. *Aerodynamic Theory* 4, 169-360.
- Goldstein, S. (1929). On the vortex theory of screw propellers. *Proceedings of the Royal Society of London*, 123(792), 440-465.
- Guntur, S., Bak, C., & Sørensen, N. N. (2012). Analysis of 3d stall models for wind turbine blades using data from the Mexico experiment. *Proceedings of the 13th International Conference on Wind Engineering 2012*.
- Hand, M., Simms, D., Fingersh, L., Jager, D., Cotrell, J., Schreck, S., & Larwood, S. (2001). *Unsteady aerodynamics experiment phase vi: wind tunnel test configurations and available data campaigns* (Tech. Rep. No. NREL/TP-500-29955). National Renewable Energy Laboratory (NREL).
- Hansen, M. O. L. (2008). *Aerodynamics of wind turbines* (2nd ed.). London: Earthscan.
- Hansen, M. O. L., Sørensen, N. N., Sørensen, J. N., & Michelsen, J. A. (1997). Extraction of lift, drag and angle of attack from computed 3-d viscous flow around a rotating blade. *Proceedings of the European Wind Energy Conference 1997*, 499-501.
- Harris, F. D. (1966). Preliminary study of radial flow effects on rotor blades. *Journal of the American Helicopter Society*, 11(3), 1-21.
- Herráez, I., Stoevesandt, B., & Peinke, J. (2014). Insight into rotational effects on a wind turbine blade using navier-stokes computations. *Energies*, 7, 6798-6822.
- Himmelskamp, H. (1945). *Profile investigations on a rotating airscrew* (Ph.D. thesis). Gottingen University.
- Ivanell, S., Mikkelsen, R., Sørensen, J. N., & Henningson, D. (2008). *Validation of methods using ellipsys3d* (Tech. Rep.). Linné Flow Center, KTH Mechanics, Technical University of Denmark.
- Johansen, J., & Sørensen, N. N. (2004). Aerofoil characteristics from 3d CFD rotor computations. *Wind Energy*, 7(4), 283-294.
- Koh, W. X. M., & Ng, E. Y. K. (2016). Effects of reynolds number and different tip loss models on the accuracy of BEM applied to tidal turbines as compared to experi-

- ments. *Ocean Engineering*, 111, 104-115.
- Lindenburg, C. (2003). *Investigation into rotor blade aerodynamics* (Technical report Nos. ECN-C-03-025). Energy research Center of the Netherlands (ECN).
- Maniaci, D., & Schmitz, S. (2016). Extended Glauert tip correction to include vortex rollup effects. *Journal of Physics: Conference Series*(753 - The Science of Making Torque from Wind (Torque 2016)).
- Manwell, J. F., McGowan, J. G., & Rogers, A. L. (2009). *Wind energy explained* (2nd ed.). Chichester: John Wiley & Sons Ltd.
- Micallef, D. (2012). *3d flows near a HAWT rotor* (Ph.D. thesis). University of Technology Delft.
- Montgomerie, B. (2004). *Methods for root effects, tip effects and extending the angle of attack range to 180 degrees, with application to aerodynamics for blades on wind turbines and propellers* (Technical report Nos. FOI-R-1305-SE). Swedish Defence Research Agency.
- Mycek, P., Gaurier, B., Germain, G., Pinon, G., & Rivoalen, E. (2014). Experimental study of the turbulence intensity effects on marine current turbines behaviour. part i. one single turbine. *Renewable Energy*, 66, 729-746.
- Pozrikidis, C. (2011). *Introduction to theoretical and computational fluid dynamics* (2nd ed.). New York: Oxford University Press.
- Prandtl, L. (1921). *Applications of modern hydrodynamics to aeronautics* (Technical report No. 116). National Advisory Committee for Aeronautics (NACA).
- Clay Mathematics Institute. (2016). *Millennium problems — Clay Mathematics Institute*. Retrieved from <http://www.claymath.org/millennium-problems>
- Ronsten, G. (1992). Static pressure measurements on a rotating and a non-rotating 2.375m wind turbine blade. comparison with 2d calculations. *Journal of Wind Engineering and Industrial Aerodynamics*, 39, 105-118.
- Schepers, J. G. (2012). *Engineering models in wind energy aerodynamics* (Ph.D. thesis). University of Technology Delft.
- Schepers, J. G., Boorsma, K., Cho, T., Gómez-Iradi, S., Schaffarczyk, P., Jeromin, A., ... Sørensen, N. N. (2012). *Final report of IEA task 29, Mexnext (phase 1)* (Tech. Rep. No. ECN-E-12-004). ECN.
- Schepers, J. G., Boorsma, K., Gomez-Iradi, S., Schaffarczyk, P., Madsen, H. A., Sørensen, N. N., ... Schreck, S. (2014). *Final report of IEA wind task 29: Mexnext (phase 2)* (Tech. Rep. No. ECN-E-14-060). ECN.
- Schepers, J. G., Ceyhan, O., Savenije, F., Stettner, M., Kooijman, H., Chaviaropoulos, P. K., ... Gonzalez, A. (2015). AVATAR: Advanced aerodynamic tools for large rotors. *33rd Wind Energy Symposium*.
- Schreck, S., & Robinson, M. (2002). Rotational augmentation of horizontal axis wind turbine blade aerodynamic response. *Wind Energy*, 5, 133-150.
- Shen, W. Z., Hansen, M. O. L., & Sørensen, J. N. (2006). Determination of angle of attack (aoa) for rotating blades. *Wind Energy, Proceedings of the Euromech Colloquium*, 205-209.
- Shen, W. Z., Hansen, M. O. L., & Sørensen, J. N. (2009). Determination of the angle of attack on rotor blades. *Wind Energy*, 12, 91-98.
- Shen, W. Z., Mikkelsen, R., Sørensen, J. N., & Bak, C. (2005). Tip loss corrections for wind research turbine computations. *Wind Energy*, 8(4), 457-475.
- Snel, H., Houwink, R., & Bosschers, J. (1994). *Sectional prediction of lift coefficients on*

- rotating wind turbine blades in stall* (Tech. Rep. Nos. ECN-C-93-052). ECN.
- Snel, H., & Schepers, J. G. (2009). Mexico project: the database and results of data processing and interpretation. *AIAA Aerospace Sciences, 47*.
- Snel, H., & Van Holten, T. (1995). *Review of recent aerodynamic research on wind turbines with relevance to rotorcraft* (Technical report No. CP-552). Advisory Group of Aerospace Research and Development (AGARD).
- Sørensen, J. N., Dag, K. O., & Ramos-Garcia, N. (2014). A refined tip correction based on the decambering approach. *Wind Energy, 19*(5), 787-802.
- Sørensen, N. N., Hansen, M. O. L., García, N. R., Florentie, L., & Boorsma, K. (2014). *Power curve predictions WP2 deliverable 2.3* (Tech. Rep.). AVATAR project.
- Sørensen, N. N., Michelsen, J. A., & Schrek, S. (2002). Navier-stokes predictions of the NREL phase VI rotor in the NASA Ames 80 ft x 120 ft wind tunnel. *Wind Energy, 5*, 151-169.
- Van Garrel, A. (2003). *Development of a wind turbine aerodynamics simulation module* (Tech. Rep. Nos. ECN-C-03-079). Energieonderzoek Centrum Nederland.
- Wilson, R. E. (1986). A wind turbine flow field model. *Trans. ASME, 108*, 344-345.
- Wilson, R. E., & Lissaman, P. B. S. (1974). *Applied aerodynamics of wind power machines* (Technical report No. PB-238595). Oregon State University.
- Yang, H., Shen, W. Z., Xu, H., Hong, Z., & Liu, C. (2014). Prediction of the wind turbine performance by using BEM with airfoil data extracted from CFD. *Renewable Energy, 70*, 107-115.

Appendix A

Additional explanations and results of determining the angle of attack from CFD

The Upwash from bound Vortex Line (UVL) method and the Upwash from Distributed Vorticity (UDV) method are explained in more detail in this appendix. These methods are used to extract the angle of attack α from the CFD results in section 5.1. The articles from Shen et al. (2006, 2009) describe both methods respectively, but during this thesis it is experienced that the implementation is not straightforward. This chapter will provide a step by step explanation for both methods, with the objective to show the methods in more detail and to provide a clear description which can be used for further research. The last section of this appendix will show the results that are not discussed in the main report.

A.1 Post-processing

For both methods the blades have to be discretized into two-dimensional sections. Furthermore, the flow field data can be reduced in size when it is known where it is desired to evaluate the angle of attack. Depending on the structure of the CFD data, the programs Tecplot or Paraview can be used to visualize the results but they also can perform the required discretization and extraction of data. In this thesis Matlab is used to further perform the calculations with the reduced data sets.

The CFD mesh used in this thesis was not structured. This required additional computations to order the data points such that the airfoil geometries (i.e. leading edge position, trailing edge position, etc) are known before starting the use of the UVL and UDV methods. A code was written that 'walked' along the surface of each airfoil cross-section, although it is not initially known what the shape of airfoil is. Extra attention was required on the sharp corners at the trailing edge. When the sectional geometries

are known for one blade, the rotation matrix R_m can be used for the other blades, with azimuth angle ψ .

$$R_m = \begin{bmatrix} \cos(\psi) & -\sin(\psi) \\ \sin(\psi) & \cos(\psi) \end{bmatrix} \quad (\text{A.1})$$

Each rotor consists of a number of blades N_b which are discretized into number of sections N . Depending on the CFD mesh each section has approximately 250 data points along the surface. This data is stored in surface slices. The flow field is discretized into domain slices containing all the data points of the flow up- and downstream each section. The difference between the surface and domain slices is visualized in figure A.1 shown for five sections. The monitor points where the angle of attack will be evaluated are placed in the domain slices.

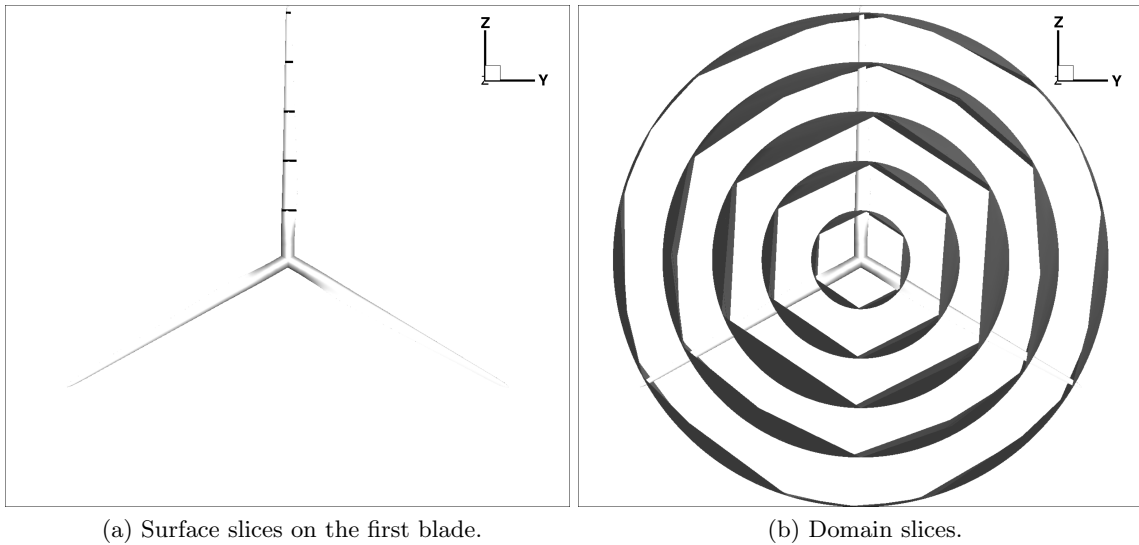


Figure A.1: The two types of slices in Tecplot used to reduce the CFD data set. Note that the orientation of the reference frame in figure A.1 is not conventional and different from what is used in this thesis:

A.2 UVL method

With Upwash from bound Vortex Line (UVL) the upwash felt at a monitor point is induced by modelling the sections as point vortices. The upwash is calculated with the Biot-Savart law, given in equation (2.3). The strength of each point vortex is calculated by the Kutta-Joukowski equation, in where the lift force L is related to the local blade forces and the inflow angle ϕ . The inflow angle is estimated in the monitor point, located in front of the cross-section. As the point vortex is a singularity, this monitor point should not be chosen close to the cross-section. The results show that a distance of at least a half chord from the leading edge is acceptable. The upwash felt in the monitor point due to the point vortex is subtracted from the computed velocities in the monitor point.

Thus, as the inflow angle is an input for the method and the induced velocities, which are outputs of the method, are required to calculate the inflow angle, an iterative process is needed. Note also that for one monitor point, there are five point vortices along each blades of the rotor shown in figure A.1 that induce a velocity at this monitor point.

Next, the implementation is discussed step-wise. Note that the equations are shown concerning one monitor point, although there are the same number of monitor points as cross-sections.

1. The local blade forces, normal force F_n and tangential force F_t , are calculated for each cross-section along each blades, with equations (A.2) and (A.3) respectively.

$$F_{n,i} = \oint p \cdot e_n ds \quad (\text{A.2})$$

$$F_{t,i} = \oint p \cdot e_t ds \quad (\text{A.3})$$

The index i indicates the cross-section numbering. For the discrete integration in Matlab, the locations of where the pressure acts on the airfoil are treated as the middle points of the panels. Each panel has therefore a certain panel length ds and a certain angle with respect to the reference frame. This panel angle is used to calculate the unit vectors e_n and e_t . The summation of all the forces along the airfoil boundary results in the normal force and tangential force.

2. The placement of the monitor point is chosen in the rotor plane, as the induced velocities varies across the rotor plane. In this report the location is made dependent on the chord length times an integer, allowing comparisons with other papers, although in theory it can be chosen anywhere. Furthermore, to ensure uniform inflow for each cross-section, the monitor point is in the azimuthal direction, explaining the choice of circular domain slices. Concluding from these placements constraints, only a part of the circular domain slices are needed, depending on the which cross-section is taken. To reduce the computational time, the domain slices are therefore cut, leading to reduction up to a factor of 8.
3. At the monitor point the initial inflow angle ϕ and relative velocity V_{rel} are calculated. This angle and velocity are the uncorrected values at iteration step $n = 0$. The equations (A.4) and (A.5) show the dependency of the azimuthal velocity V_θ , which is calculated in equation (A.6). In these equations the velocity components V_x , V_y and V_z are known from the CFD computations.

$$\phi^0 = \tan^{-1} \frac{V_x}{\Omega r_i - V_\theta^0} \quad (\text{A.4})$$

$$V_{rel}^0 = \sqrt{V_x^2 + (\Omega r_i - V_\theta^0)^2} \quad (\text{A.5})$$

$$V_\theta^0 = V_y \cos(\psi) + V_z \sin(\psi) \quad (\text{A.6})$$

4. The first estimation for the lift force L and circulation Γ can now be calculated with equations (A.7) and (A.8). Equation (A.8) represents the Kutta-Joukowski theorem at the two-dimensional cross-sections, which calculates the strength of the point vortex. The point vortex is located at the quarter chord point, which can be estimated from the positions of the leading and trailing edge points and the twist angle between them. The calculated twist angle and the chord length can be compared to the design tables of the specific rotor. Both comparisons are identical, indicating that the geometry post-processing is done correctly.

$$L_i^n = F_n \cos(\phi_i^n) + F_t \sin(\phi_i^n) \quad (\text{A.7})$$

$$\Gamma_i^n = \frac{L_i^n}{\rho V_{rel,i}^n} \quad (\text{A.8})$$

To obtain the directional influences of the point vortex, the circulation strength is multiplied with the radial unit vector e_r , which can be calculated with equation (A.9), remembering that the reference frame is such that the y-axis is parallel to the cross-sections of the first blade and the z-axis is parallel along the first blade. Equation (A.10) shows the new notation form, emphasizing that the circulation is now a vector, with \mathbf{y} being the coordinates of the quarter chord point where the point vortex is located.

$$\mathbf{e}_r = R_m(\psi) \begin{bmatrix} 0 \\ 0 \\ 1 \end{bmatrix} \quad (\text{A.9})$$

$$\boldsymbol{\Gamma}_i^n(\mathbf{y}) = \Gamma_i^n \mathbf{e}_{r,i} \quad (\text{A.10})$$

5. With the strengths of all the point vortices along the blades are calculated, the Biot-Savart law can be used to calculate the induced velocity at a monitor point. The general Biot-Savart law in aerodynamic context is given in equation (2.3) and repeated below.

$$\mathbf{dV} = \frac{\Gamma}{4\pi} \int_{-\infty}^{+\infty} \frac{dl \times r}{|r|^3} \quad (2.3 \text{ revisited})$$

with segment dl and the distance vector r from the point of interest to the segment. In this context the length of the segment is fixed (equal to the blade radius R) and the induced velocity at a monitor point is composed of the induced effects due to all the blades. The resulting Biot-Savart equation for one monitor point is given in equation (A.11).

$$\mathbf{u}_{ind}^n = (u_x^n, u_y^n, u_z^n) = \frac{1}{4\pi} \sum_{k=1}^{N_b} \int_0^R \frac{\boldsymbol{\Gamma}_i^n(\mathbf{y}) \times (\mathbf{x} - \mathbf{y}_i)}{|\mathbf{x} - \mathbf{y}_i|^3} dr \quad (\text{A.11})$$

in where \mathbf{x} is the location of the monitor point. The discrete integration over the blade is done by trapezoidal integration with setting the integrand at the root ($r =$

- 0) and at the tip ($r = R$) to zero.
6. With the induced velocity calculated at the monitor point, the inflow angle and relative velocity at iteration step n excluding the upwash created by the blades can be calculated with equations (A.12) and (A.13).

$$\phi^n = \tan^{-1} \frac{V_x - u_x^n}{\Omega r_i - V_\theta^n} \quad (\text{A.12})$$

$$V_{rel}^n = \sqrt{(V_x - u_x^n)^2 + (\Omega r_i - V_\theta^n)^2} \quad (\text{A.13})$$

with azimuthal velocity V_θ given in equation (A.14).

$$V_\theta^n = (V_y - u_y^n) \cos(\psi) + (V_z - u_z^n) \sin(\psi) \quad (\text{A.14})$$

7. The results are accepted if there is convergence of the inflow angle, by comparing the results at iteration step $n + 1$ with the results of the previous iteration step n . If this is not the case, steps four to six are repeated using the values of the inflow angle and relative velocity at iteration step $n + 1$.

A.3 UDV method

The Upwash from Distributed Vorticity (UDV) method differs from the first method by the fact that in the UDV method the upwash felt at a monitor point is now induced by a bound circulation distribution along the cross-section. To calculate the bound circulation distribution, the velocity on the surface wall should be determined. As it is assumed that the flow is steady and incompressible, the Bernoulli equation is used to calculate the magnitude of this edge velocity. The sign is resolved by finding the stagnation point, separation point (if there is separated flow) and reattachment point (if there is reattachment), and knowing that for a positive angle of attack,

- the local bound circulation is positive between the stagnation point and the leading edge and between the leading edge and separation point or trailing edge in case of no separation;
- local bound circulation is negative between the separation point and the attachment point or the trailing edge in case of no reattachment of flow and between the trailing edge and stagnation point.

The difficulty of this method lies in correctly finding these points, but it has the advantage that because the bound circulation distribution does not change for the given solution set, no iteration loop is required to calculate the inflow angle. Furthermore, the monitor point can be chosen closer to the cross-section. The surface and domain slices containing information about the mesh, flow field and pressure values resulting from the post-processing of the CFD data as discussed in appendix A.1 are also used for this method. Similar to the previous section, the method is explained step-wise.

- From the pressure values along the surfaces of the cross-sections the velocity at the surface can be calculated with the Bernoulli equation, stating that the total pressure in the flow is constant for steady, incompressible flow. Equation (A.15) compares the flow at infinity upstream location to the flow at the boundary of the closed surface s .

$$p + \frac{1}{2}\rho|V_s|^2 = p_\infty + \frac{1}{2}\rho V_\infty^2 \quad (\text{A.15})$$

Note that the pressures calculated with CFD are not the absolute pressures, but this is of no issue here as only differences of pressures are important. Solving the previous equation gives the magnitude of the velocity at the surface V_s .

- With boundary layer theory this velocity at the surface can be related with the bound circulation on the cross-section. When a flow is treated as a viscous flow, a boundary layer on the surface will be formed. The flow outside this boundary layer can be treated as inviscid, but inside the boundary layer the flow changes rapidly due to the no-slip condition at the wall of the surface. This no-slip condition states that the tangential velocity along the boundary of the surface is zero. The velocity at the edge of the boundary layer should however match the flow outside of the boundary layer. The gradient of the tangential velocity normal to the wall will be therefore large. In contrary, the component of the normal velocity along the wall is small as potential theory states that the normal velocity is zero along the horizontal axis. Now with the knowledge that vorticity is defined as the curl of the velocity, given in equation (A.16), and remembering that the flow is two-dimensional in this case, equation (A.17) states that the vorticity is related to the gradient of the tangential velocity normal to the wall ($\frac{\partial u}{\partial y}$) and the normal velocity along the wall ($\frac{\partial v}{\partial x}$).

$$\boldsymbol{\xi} = \nabla \times \mathbf{V} = \left(\frac{\partial w}{\partial y} - \frac{\partial v}{\partial z} \right) \mathbf{i} + \left(\frac{\partial u}{\partial z} - \frac{\partial w}{\partial x} \right) \mathbf{j} + \left(\frac{\partial v}{\partial x} - \frac{\partial u}{\partial y} \right) \mathbf{k} \quad (\text{A.16})$$

$$\xi_{2D} = \left(\frac{\partial v}{\partial x} - \frac{\partial u}{\partial y} \right) \mathbf{k} \quad (\text{A.17})$$

As $\frac{\partial u}{\partial y} \gg \frac{\partial v}{\partial x}$, the vorticity in the boundary layer is thus related one to one with the derivative of the tangential velocity to the local normal axis, or in other words, the velocity jump over the boundary layer in normal direction. Furthermore, because it is known that the velocity at the wall is zero, the jump is from zero to a non-zero value, where the magnitude of this non-zero value is equal to the velocity calculated with the Bernoulli equation. Therefore, the vorticity vector on the cross-section can be calculated with equation (A.18), showing the velocity jump from the wall and the undetermined sign.

$$\boldsymbol{\xi} = \pm(V_s - 0)\mathbf{e}_r \quad (\text{A.18})$$

For both rotors, there are approximately 250 data points available on each cross-section, leading to vorticity distribution over each cross-section. This vorticity distribution is to be called the local bound circulation, as the relation between vorticity

and circulation is defined with the use of contour integral over the boundary of the cross-section.

3. The sign in equation (A.18) is determined by looking where the data point is located with respect to the stagnation point, separation point, reattachment point, leading and trailing edge, which is explained at the beginning of this section. The stagnation point can be found by the knowledge that at this point the pressure is at its maximum and the velocity magnitude close to zero (in theory exactly zero). The separation and reattachment points can be found by looking at the skin friction coefficient, which in case of separated flow will be changed in a negative sign in the region between the separation and reattachment points. This is due to the fact that in a separated condition, the flow at the surface is in opposite direction (from trailing edge to leading edge).
4. The location of where each local vorticity element is acting, is equal to the coordinates of the data points on the cross-sections, because the pressure values in these points are used to determine the magnitude of the local vorticity. As in the first step of the UVL method, these points are treated as middle points of panels, where each panel has a panel length ds . These lengths will be used later in contour integral over the boundary of the cross-section.
5. The placement of the monitor points is exactly the same as described in step 2 of the UVL method.
6. The next two steps are similar to the 5th and 6th steps of the UVL method, excluding the iteration part which is not necessary. Again, the Biot-Savart law is used to calculate the velocity at a monitor point induced by the blades. This velocity represents the created upwash and the cross-sections resemble the blades. As only the vorticity distribution is known and the Biot-Savart law uses the circulation, there is the need of a second integral corresponding to the already discussed contour integral. The resulting Biot-Savart law for one monitor point for this method is given next.

$$\mathbf{u}_{\text{ind}} = (u_x, u_y, u_z) = \frac{1}{4\pi} \sum_{k=1}^{N_b} \int_0^R \oint_s \frac{\xi_{ij}(\mathbf{y}) \times (\mathbf{x} - \mathbf{y}_{ij})}{|\mathbf{x} - \mathbf{y}_{ij}|^3} ds dr \quad (\text{A.19})$$

Two indices can be seen; similar to the previous section, the cross-section is labelled with index i . Index j indicates a data point on this cross-section. Furthermore, the vector \mathbf{y} corresponds to the coordinates of the data point and the vector \mathbf{x} is the location of the monitor point.

The inner integral is discretely solved by multiplying the integrand parts with the panel lengths ds and summing the intermediate results. The outer integral is calculated as described for the UVL method (trapezoidal integration with setting the integrand at the root and at the tip to zero) where after the induced effects from N_b blades are summed, resulting in the induced velocity at one monitor point.

7. The inflow angle and relative velocity at the monitor point can now be calculated with equations (A.20) and (A.21), where it is shown that the upwash is deducted

from the velocity components computed by CFD at the monitor point.

$$\phi = \tan^{-1} \frac{V_x - u_x}{\Omega r_i - V_\theta} \quad (\text{A.20})$$

$$V_{rel} = \sqrt{(V_x - u_x)^2 + (\Omega r_i - V_\theta)^2} \quad (\text{A.21})$$

with azimuthal velocity V_θ given in equation (A.22).

$$V_\theta = (V_y - u_y) \cos(\psi) + (V_z - u_z) \sin(\psi) \quad (\text{A.22})$$

A.4 Remaining results

In section 5.1 the results for the AVATAR rotor at 6 m/s are used to discuss the performance of the methods to extract the angle of attack from CFD computations. In this section the results for the other rotors and conditions are given.

A.4.1 Monitor point location dependency

Figures A.2 to A.6 give the results of the axial induced velocity u_{ind} and the inflow angle ϕ versus the monitor point location.

A.4.2 Spanwise dependency

Figures A.7 to A.10 give the results of the axial induced velocity u_{ind} and the inflow angle ϕ along the span of each blade for choosing the monitor point at $1.0c$ and $4.0c$ from LE.

A.4.3 Tip loss factor

Figures A.11 to A.14 give the computed axial induction factor a , azimuthal averaged axial induction factor \bar{a} and tip loss factor F with the use of the UVL method.

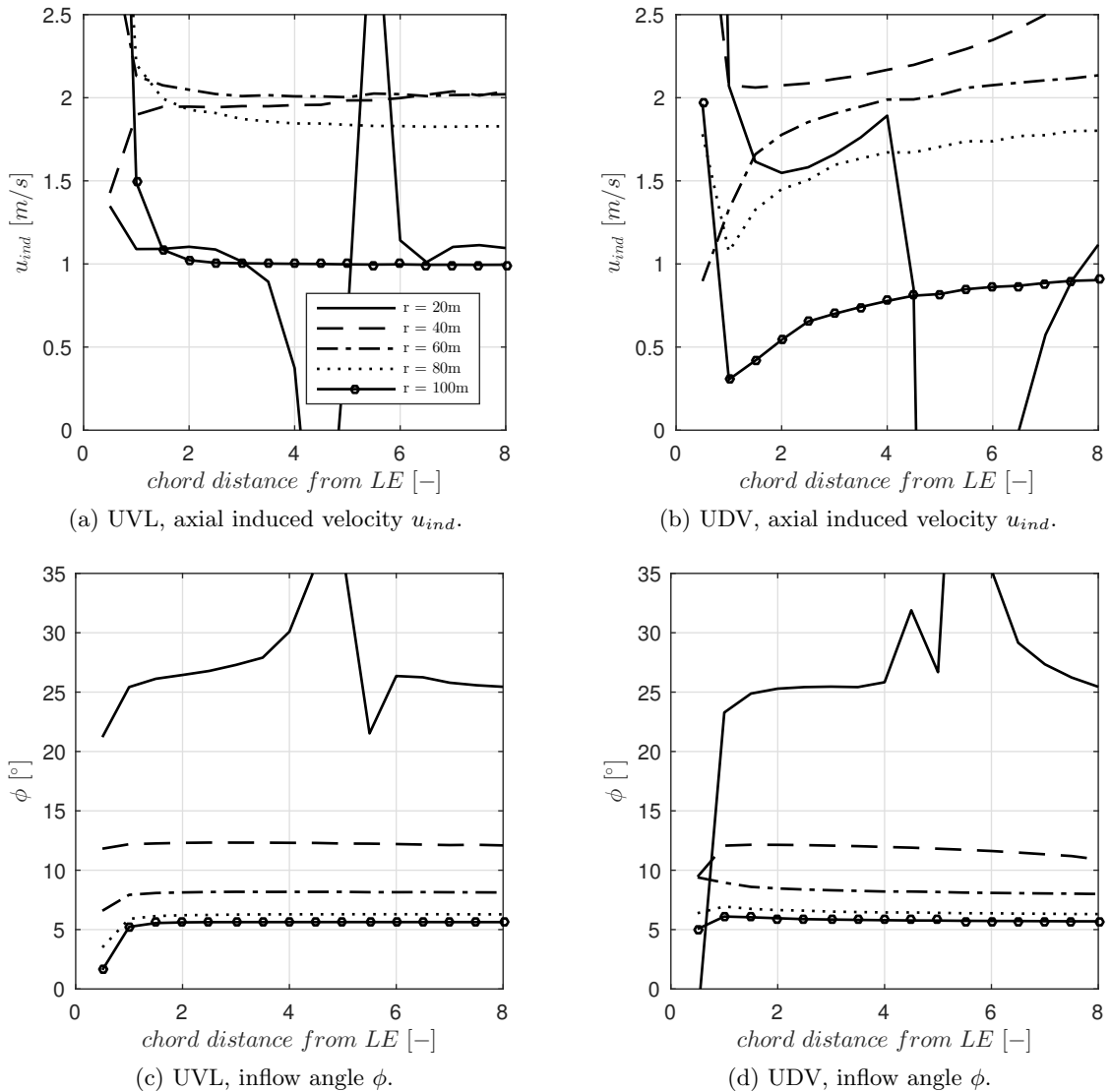


Figure A.2: The axial induced velocity u_{ind} and inflow angle ϕ results from UVL and UDV for the AVATAR rotor at 9 m/s shown for five sections and monitor points located from $0.5c$, $1.0c$, $1.5c$, etc, to $8.0c$.

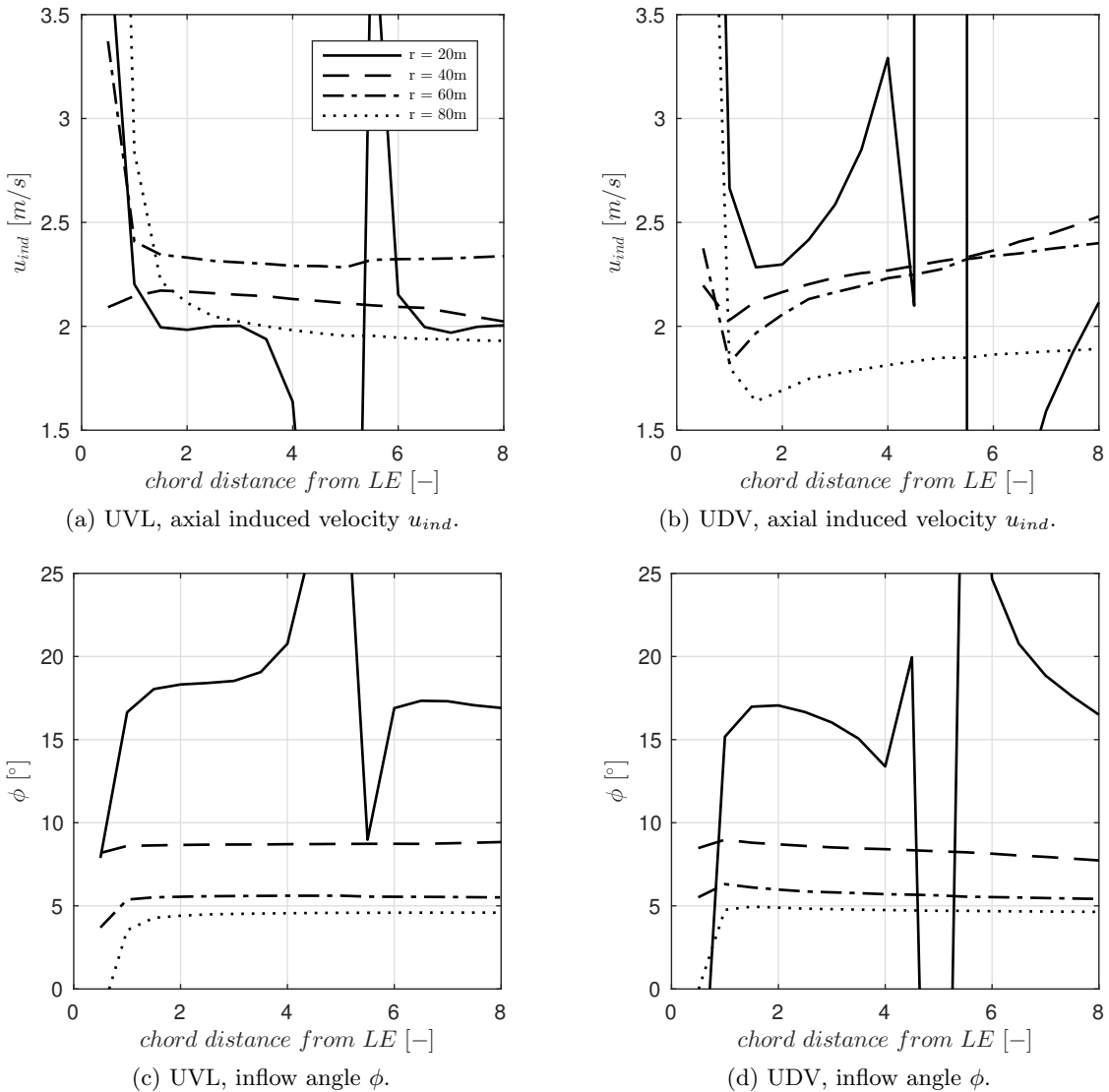


Figure A.3: The axial induced velocity u_{ind} and inflow angle ϕ results from UVL and UDV for the Innwind rotor at 6 m/s shown for four sections and monitor points located from $0.5c$, $1.0c$, $1.5c$, etc, to $8.0c$.

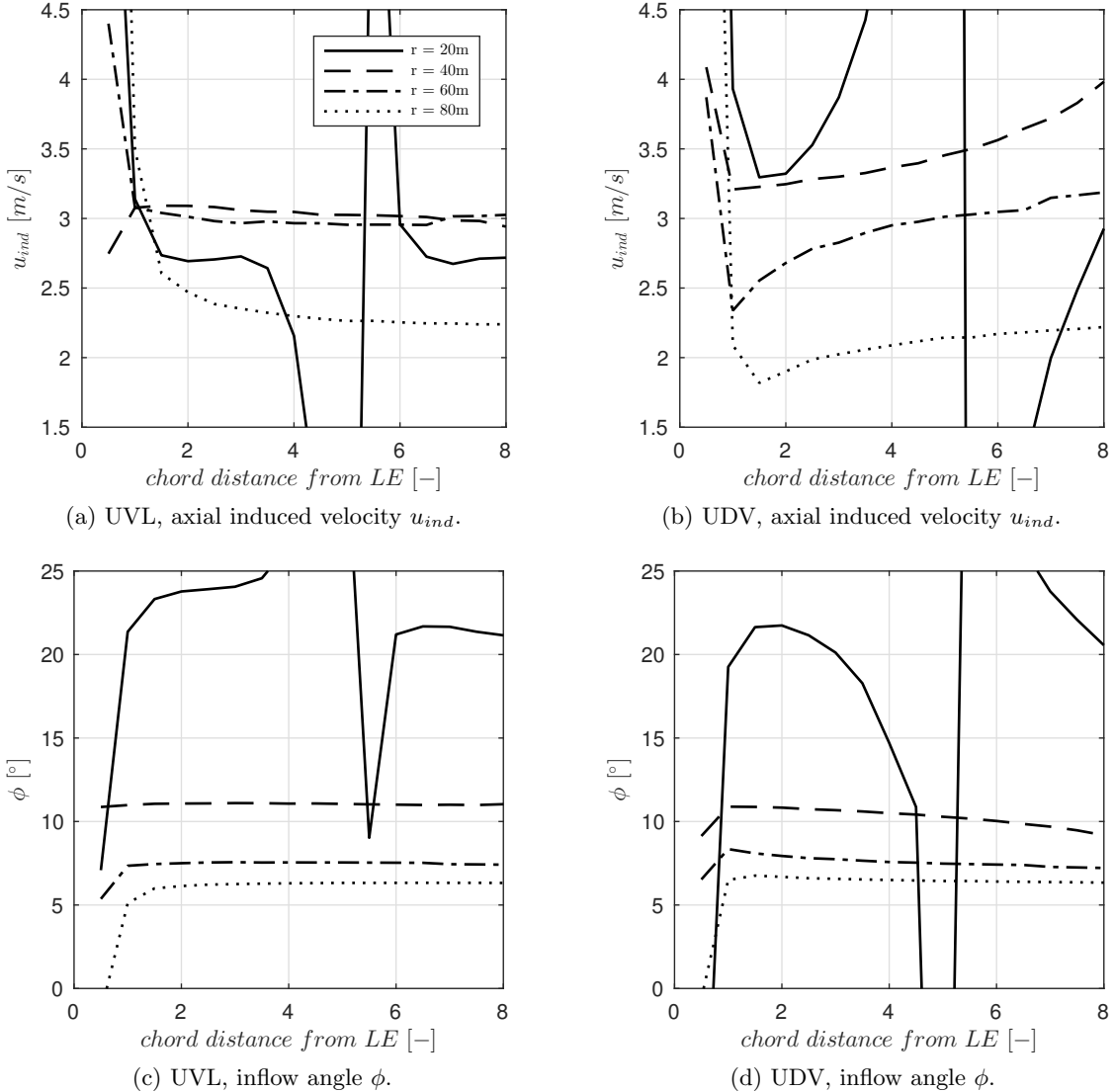


Figure A.4: The axial induced velocity u_{ind} and inflow angle ϕ results from UVL and UDV for the Innwind rotor at 9 m/s shown for four sections and monitor points located from $0.5c$, $1.0c$, $1.5c$, etc, to $8.0c$.

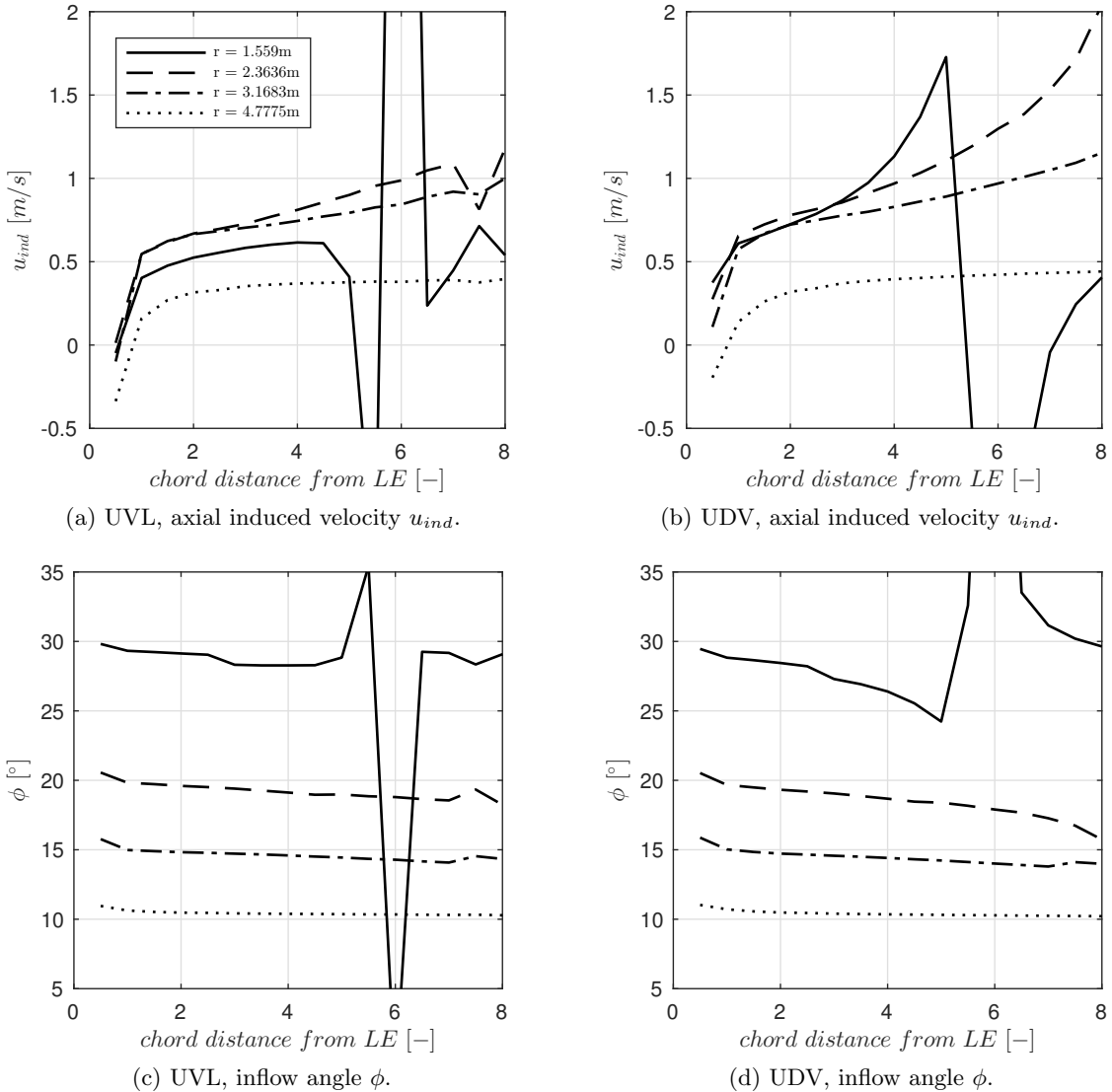


Figure A.5: The axial induced velocity u_{ind} and inflow angle ϕ results from UVL and UDV for the NREL Phase VI rotor at 7 m/s shown for four sections and monitor points located from $0.5c$, $1.0c$, $1.5c$, etc, to $8.0c$.

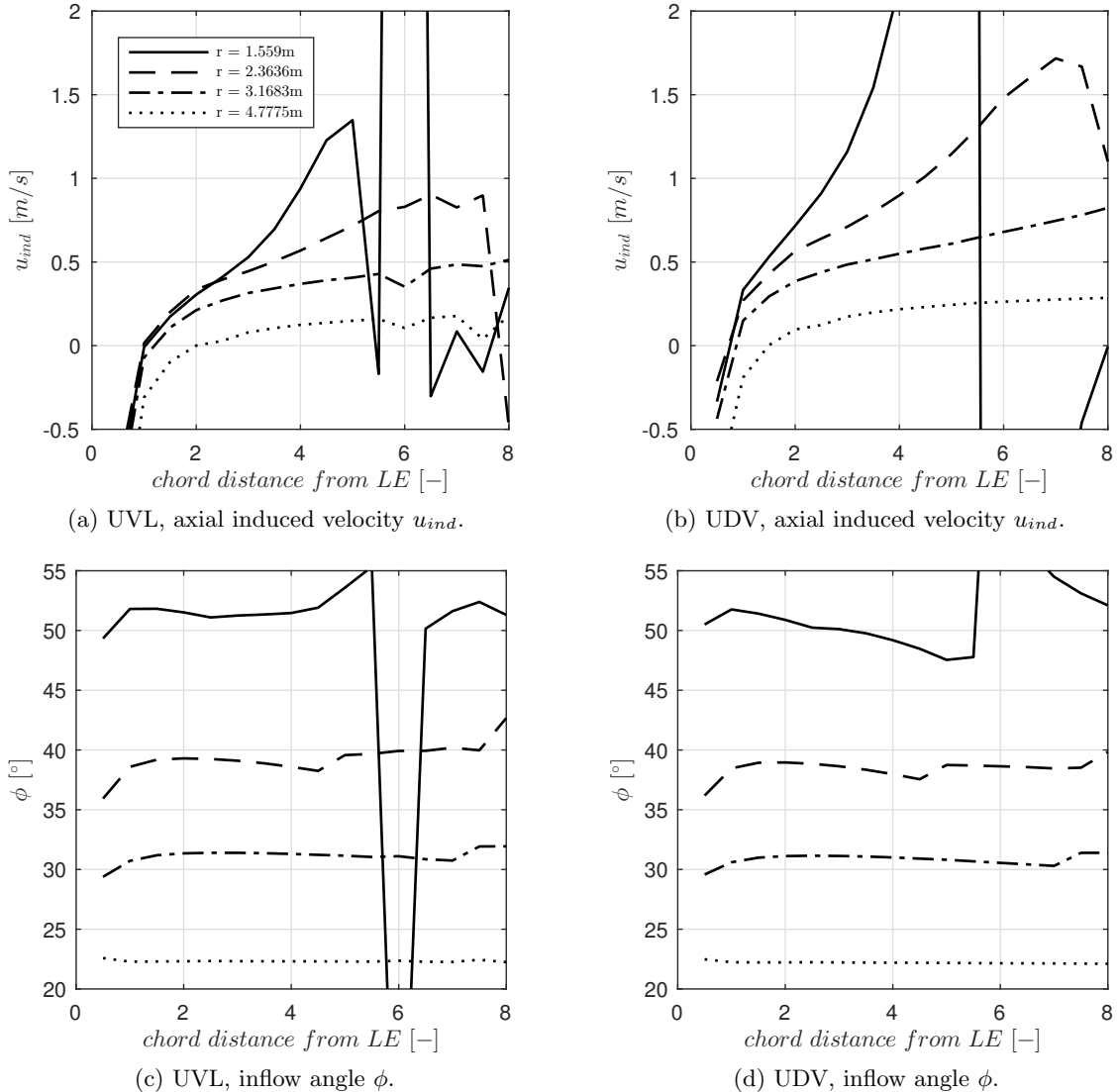


Figure A.6: The axial induced velocity u_{ind} and inflow angle ϕ results from UVL and UDV for the NREL Phase VI rotor at 15 m/s shown for four sections and monitor points located from $0.5c$, $1.0c$, $1.5c$, etc, to $8.0c$.

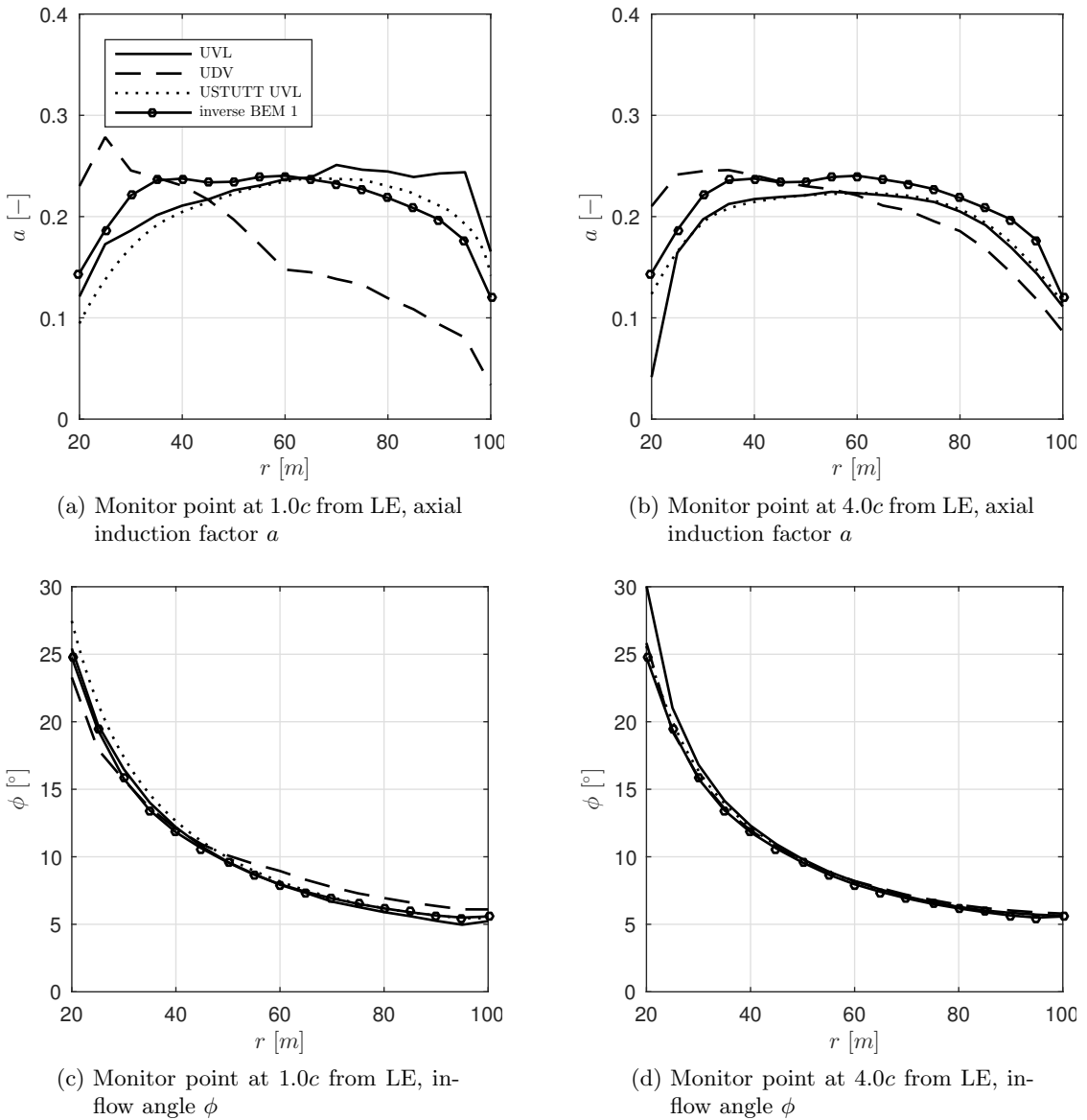


Figure A.7: The results from all four methods to extract the angle of attack α from the CFD results for the AVATAR rotor at 9 m/s, shown for two monitor point positions. The UVL results from the University of Stuttgart (USTUTT) are obtained with discretizing the blade in 103 section compared to 17 sections in this thesis.

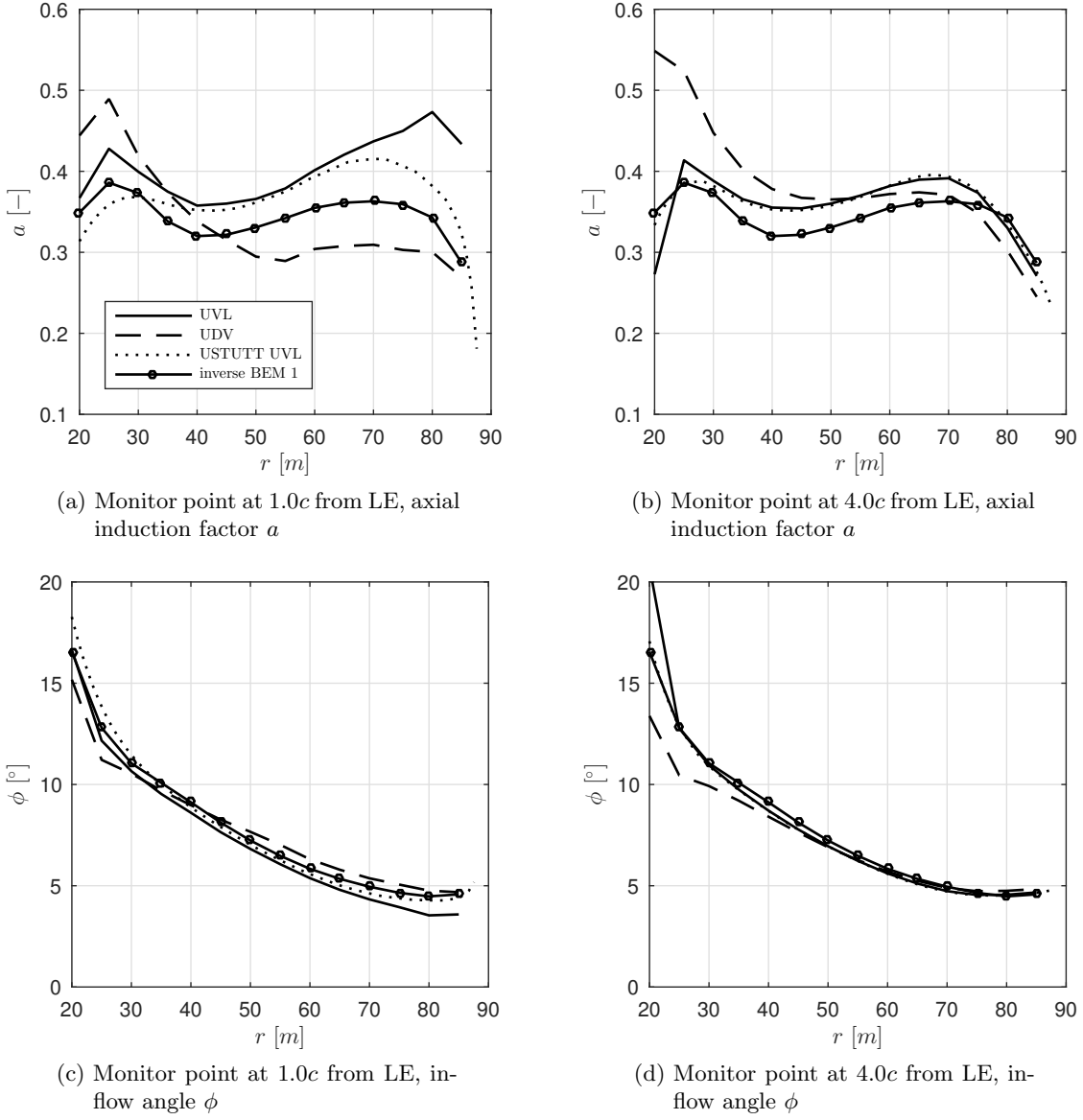


Figure A.8: The results from all four methods to extract the angle of attack α from the CFD results for the Innwind rotor at 6 m/s , shown for two monitor point positions. The UVL results from the University of Stuttgart (USTUTT) are obtained with discretizing the blade in 89 section compared to 13 sections in this thesis.

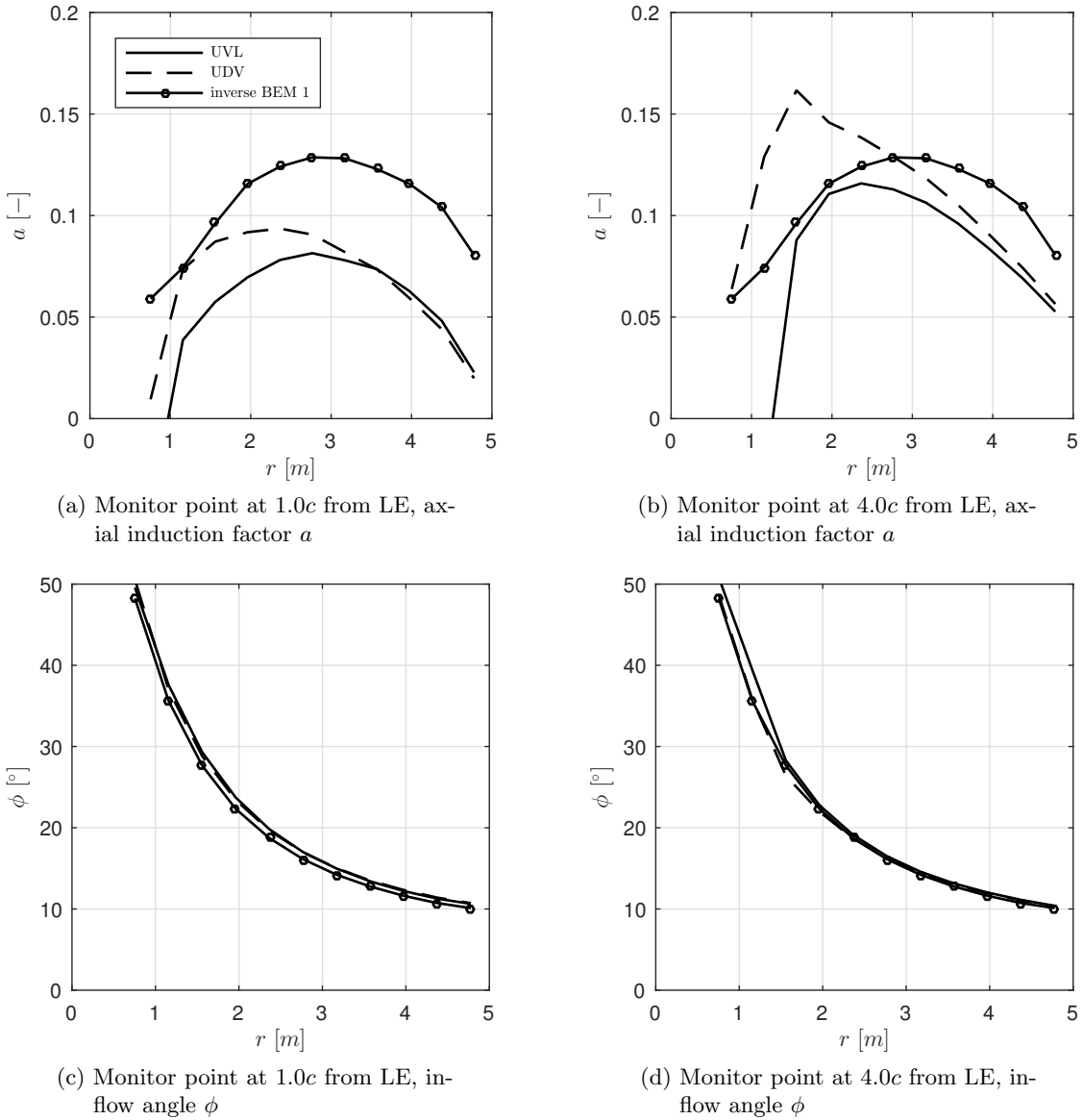


Figure A.9: The results from all four methods to extract the angle of attack α from the CFD results for the NREL Phase VI rotor at 7 m/s, shown for two monitor point positions. Results from the University of Stuttgart (USTUTT) are not available for the NREL Phase VI rotor.

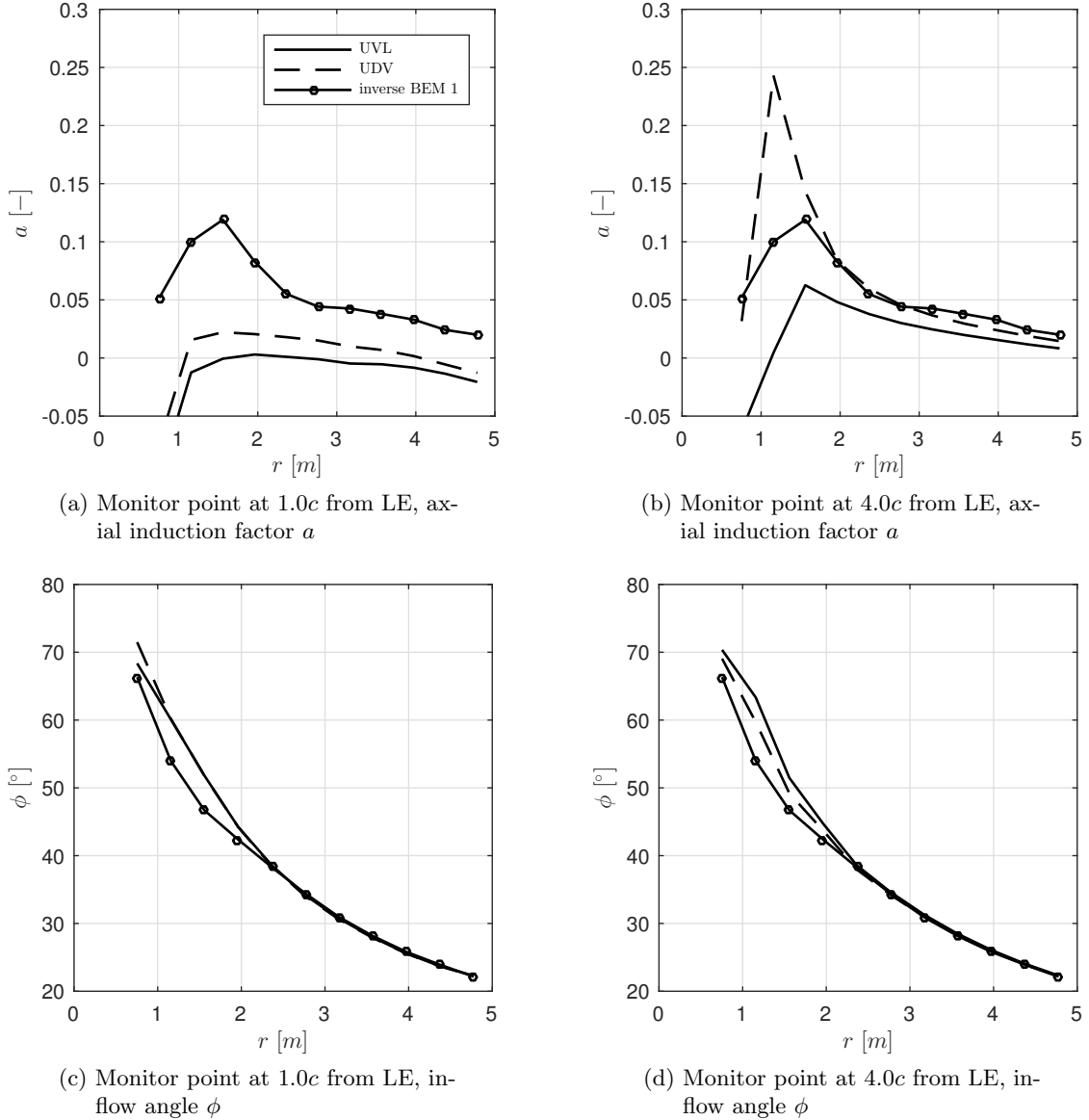


Figure A.10: The results from all four methods to extract the angle of attack α from the CFD results for the NREL Phase VI rotor at 15 m/s, shown for two monitor point positions. Results from the University of Stuttgart (USTUTT) are not available for the NREL Phase VI rotor.

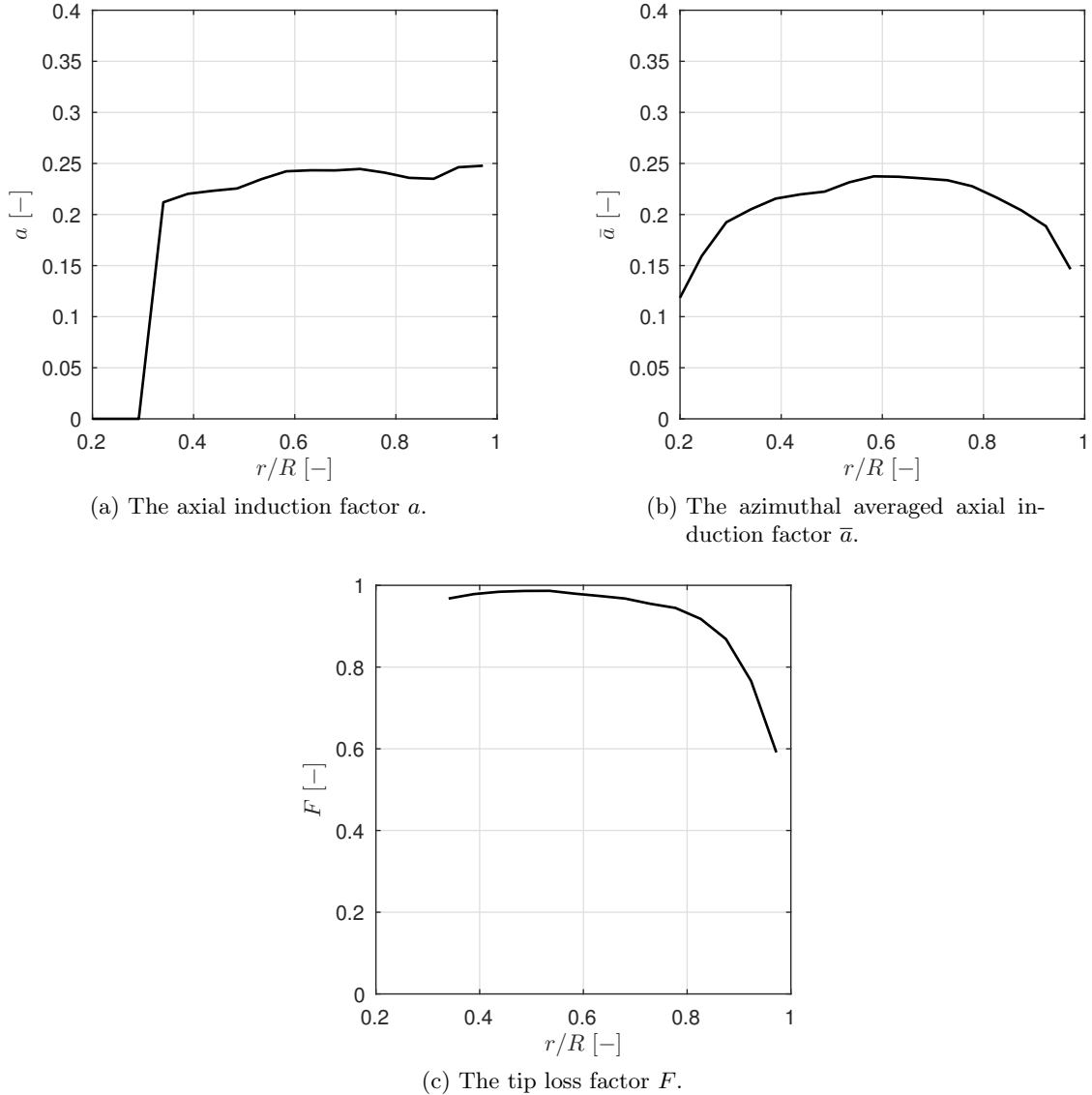


Figure A.11: The computed axial induction factor a , azimuthal averaged axial induction factor \bar{a} and tip loss factor F extracted from the UVL method for the AVATAR rotor at 9 m/s.

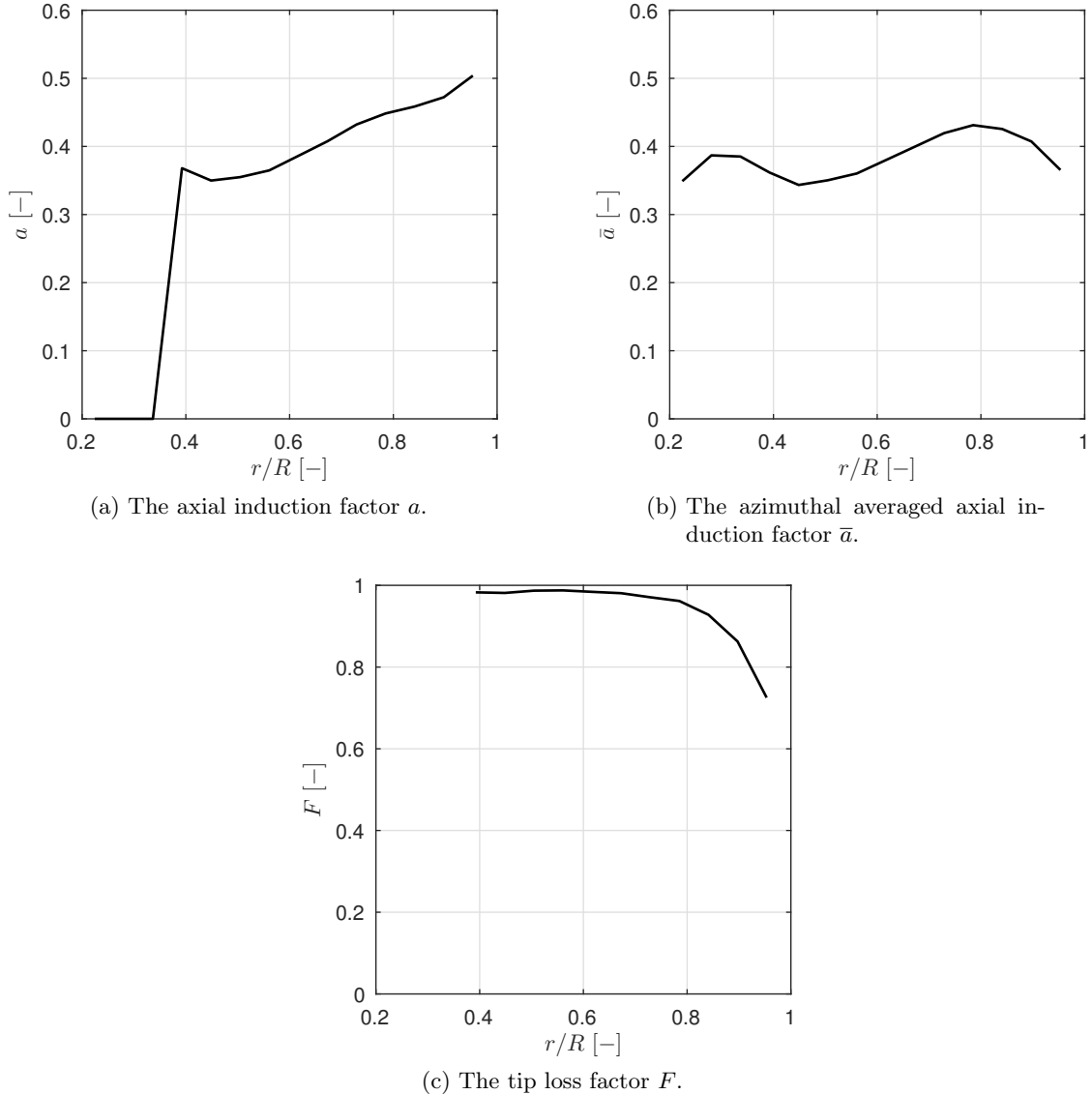


Figure A.12: The computed axial induction factor a , azimuthal averaged axial induction factor \bar{a} and tip loss factor F extracted from the UVL method for the Innwind rotor at 6 m/s.

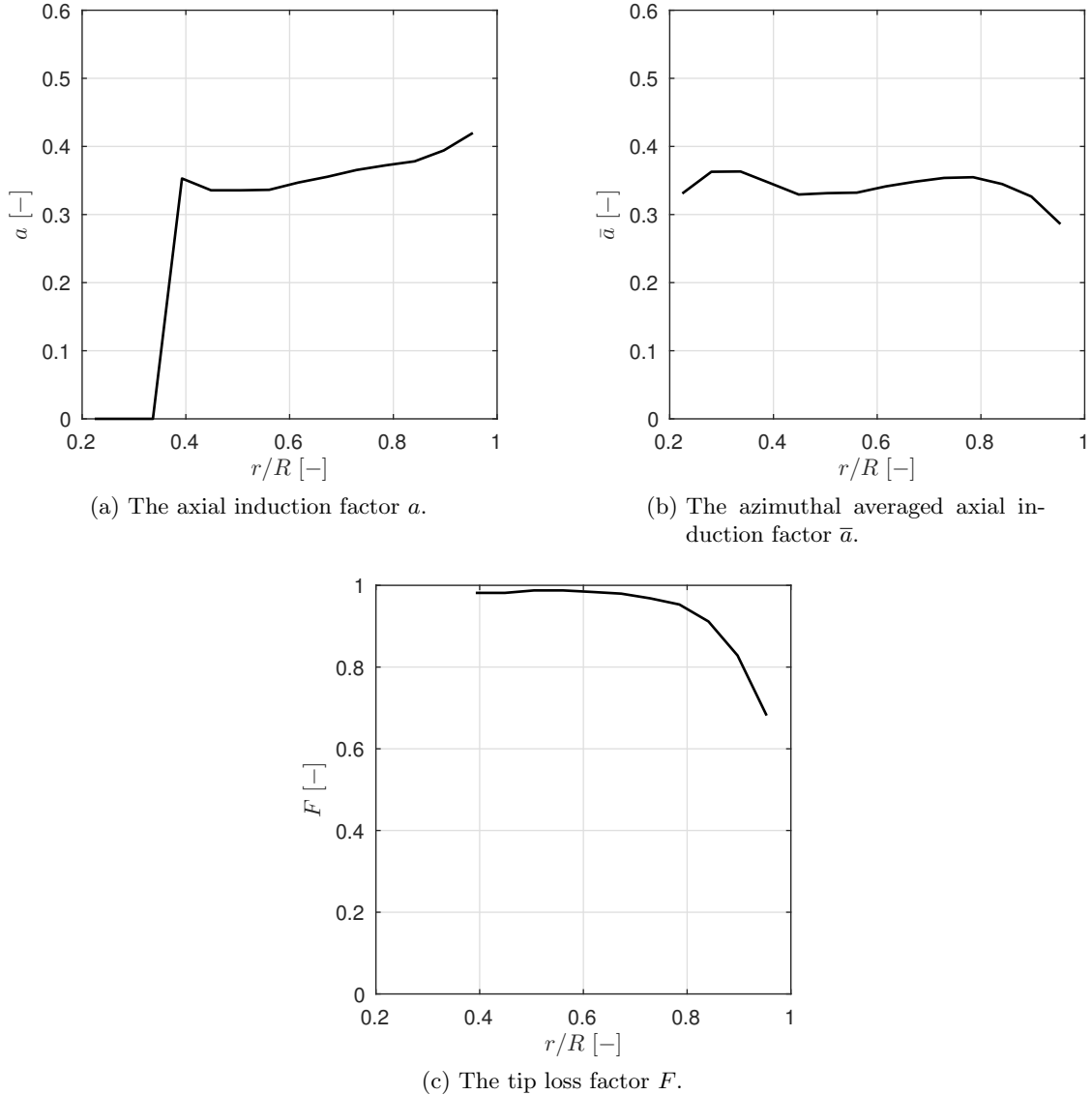


Figure A.13: The computed axial induction factor a , azimuthal averaged axial induction factor \bar{a} and tip loss factor F extracted from the UVL method for the Innwind rotor at 9 m/s.

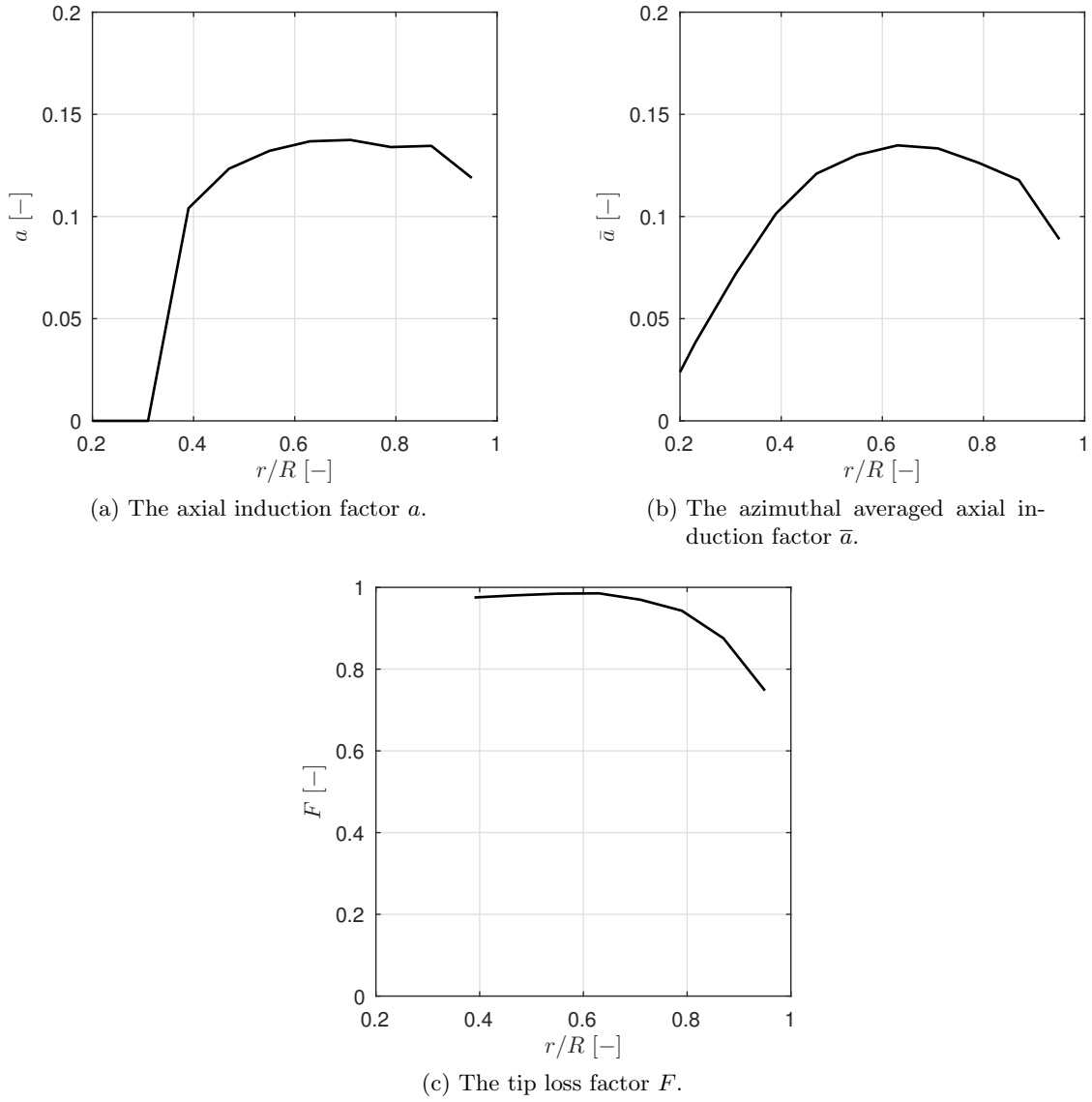


Figure A.14: The computed axial induction factor a , azimuthal averaged axial induction factor \bar{a} and tip loss factor F extracted from the UVL method for the NREL Phase VI rotor at 7 m/s.

Appendix B

Remaining vortex method validation results

In this appendix the axial, radial and azimuthal traverse results for 10 m/s and 24 m/s are given. These results show similar behaviour to what is discussed in section 5.2.1.

B.1 Axial traverse

Figures B.1 and B.2 give the axial traverse for 10 m/s and 24 m/s, respectively.

B.2 Radial traverse

Figures B.3 and B.4 give the radial traverse for 10 m/s and 24 m/s, respectively.

B.3 Azimuthal traverse

Figures B.5 and B.6 give the radial traverse for 10 m/s and 24 m/s, respectively.

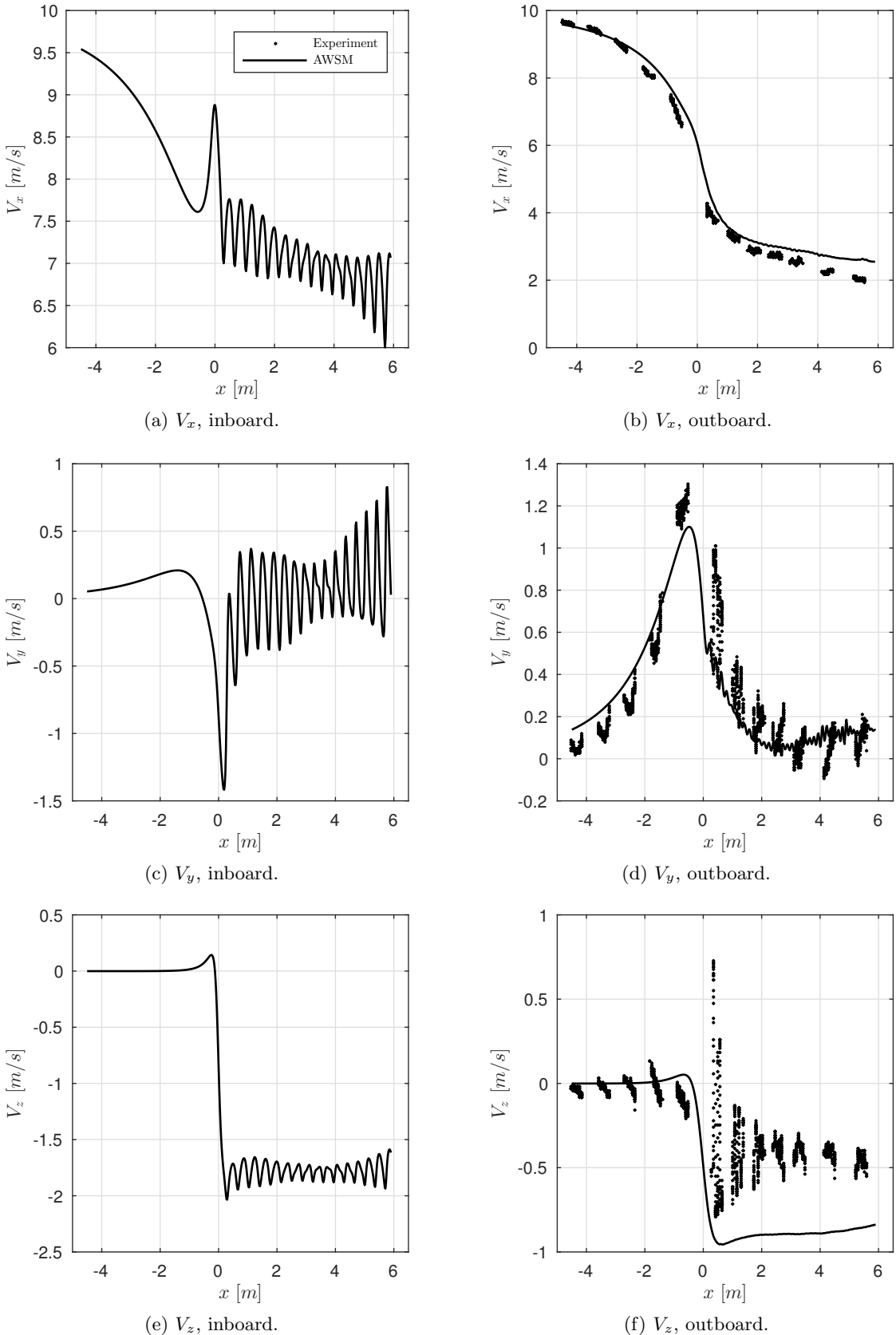


Figure B.1: Inboard ($r = 0.5$ m) and outboard ($r = 1.5$ m) axial traverse for 10 m/s measured in the New Mexico experiment and computed by AWSM at the 9 o'clock position, with the first blade in 12 o'clock position. No experimental results are available for the inboard position.

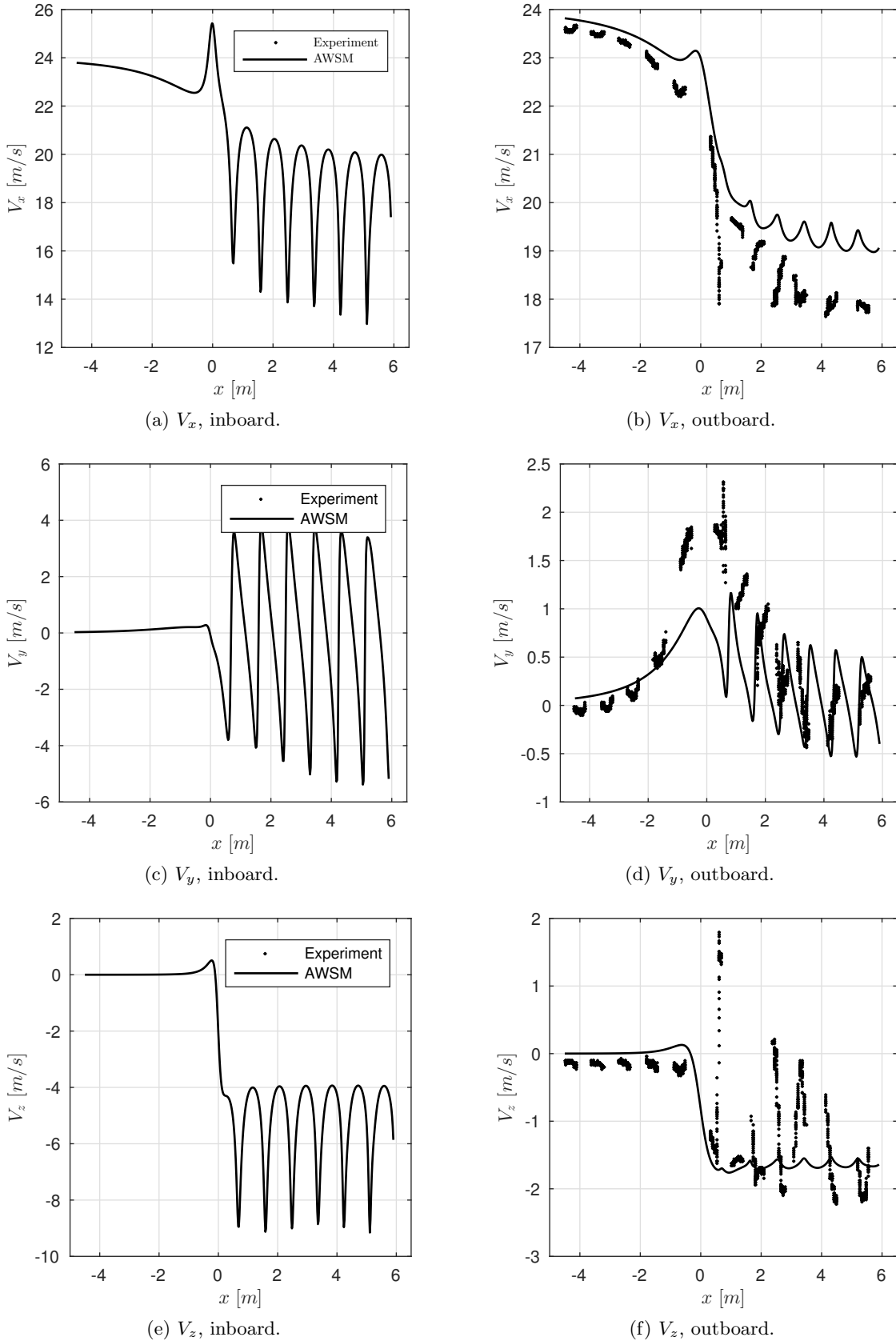


Figure B.2: Inboard ($r = 0.5$ m) and outboard ($r = 1.5$ m) axial traverse for 24 m/s measured in the New Mexico experiment and computed by AWM at the 9 o'clock position, with the first blade in 12 o'clock position. No experimental results are available for the inboard position.

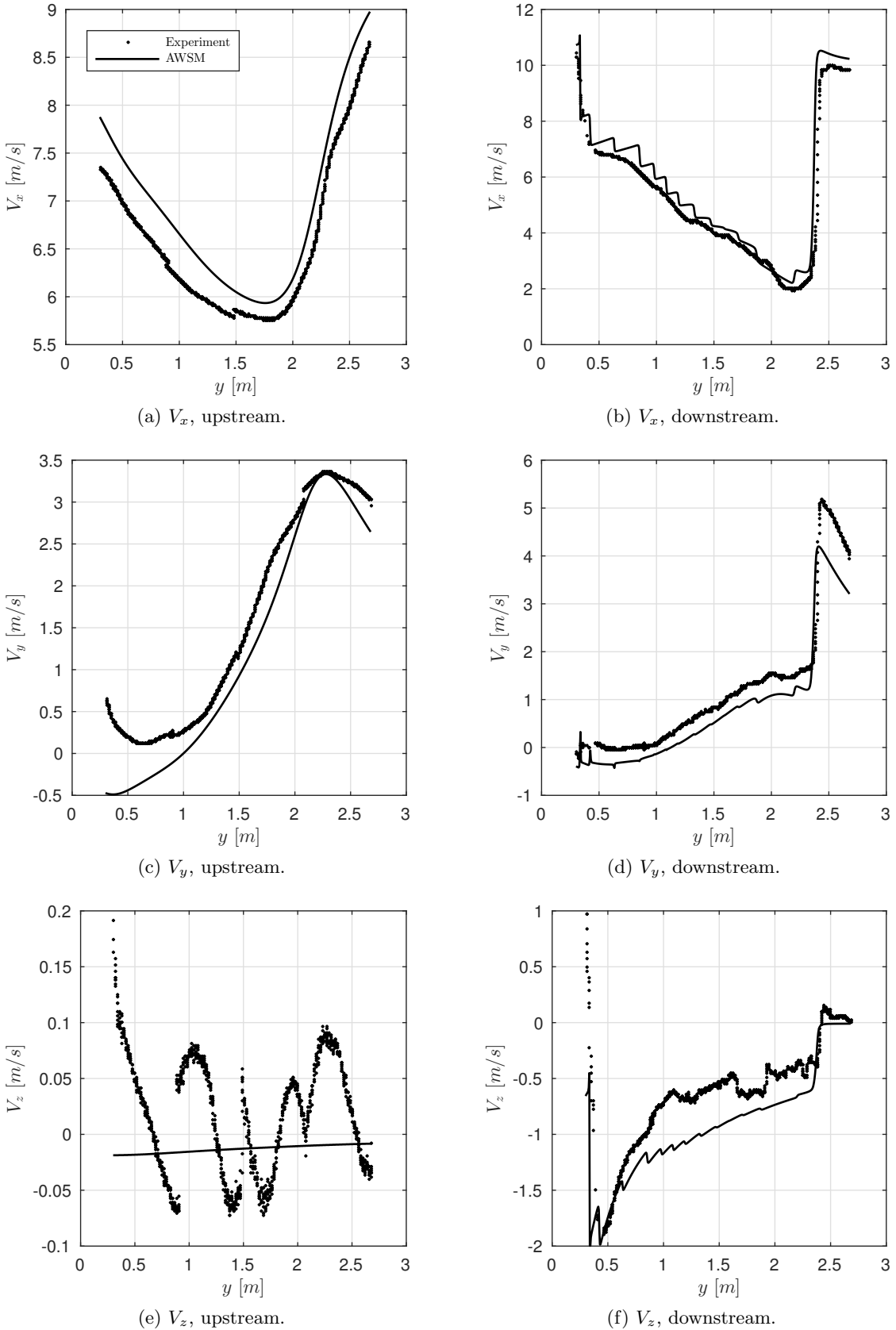


Figure B.3: Upstream (-0.30 m) and downstream (0.30 m) radial traverse for 10 m/s measured in the New Mexico experiment and computed by AWSM. The velocity components are averaged over 13 rotor positions.

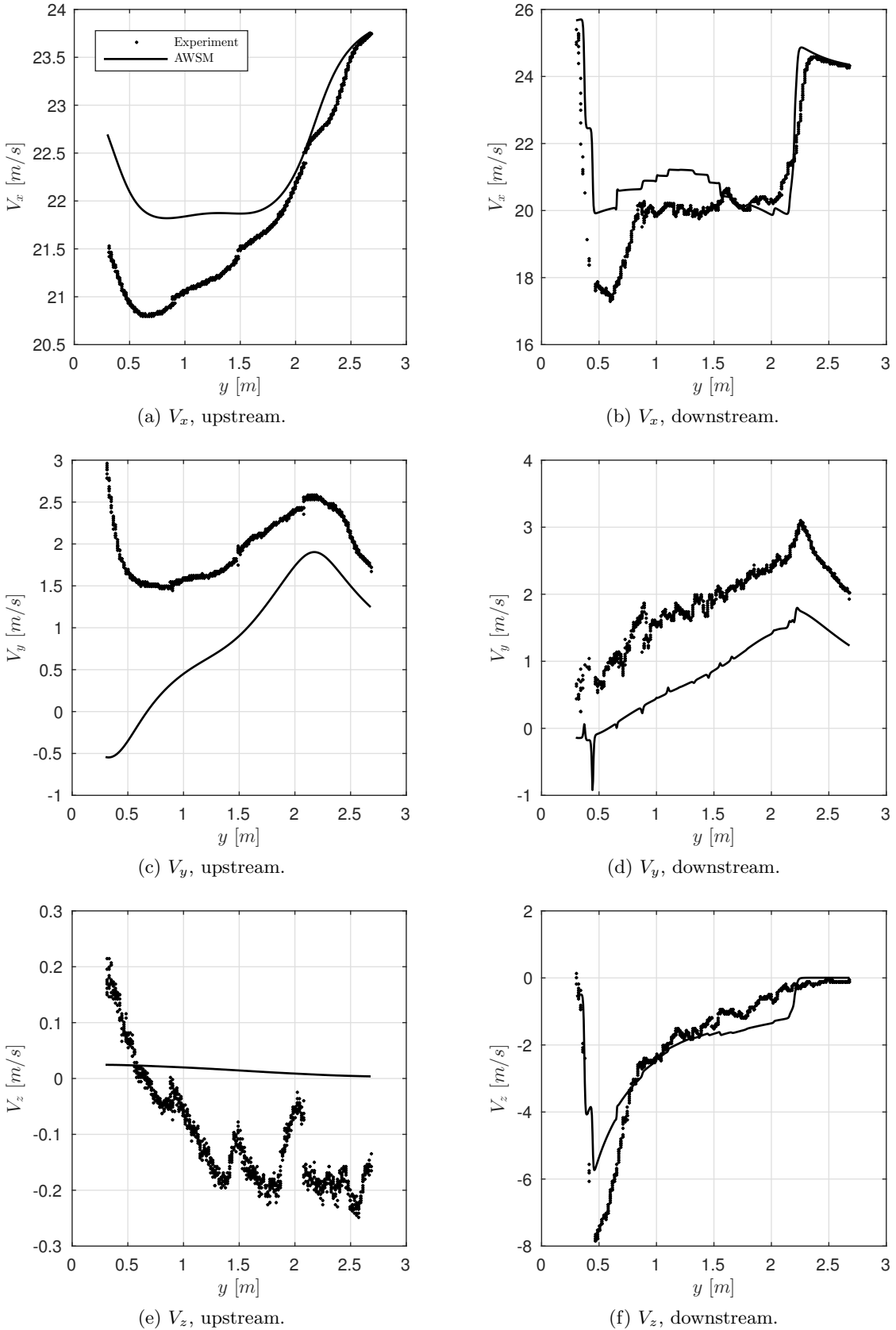


Figure B.4: Upstream (-0.30 m) and downstream (0.30 m) radial traverse for 24 m/s measured in the New Mexico experiment and computed by AWSM. The velocity components are averaged over 13 rotor positions.

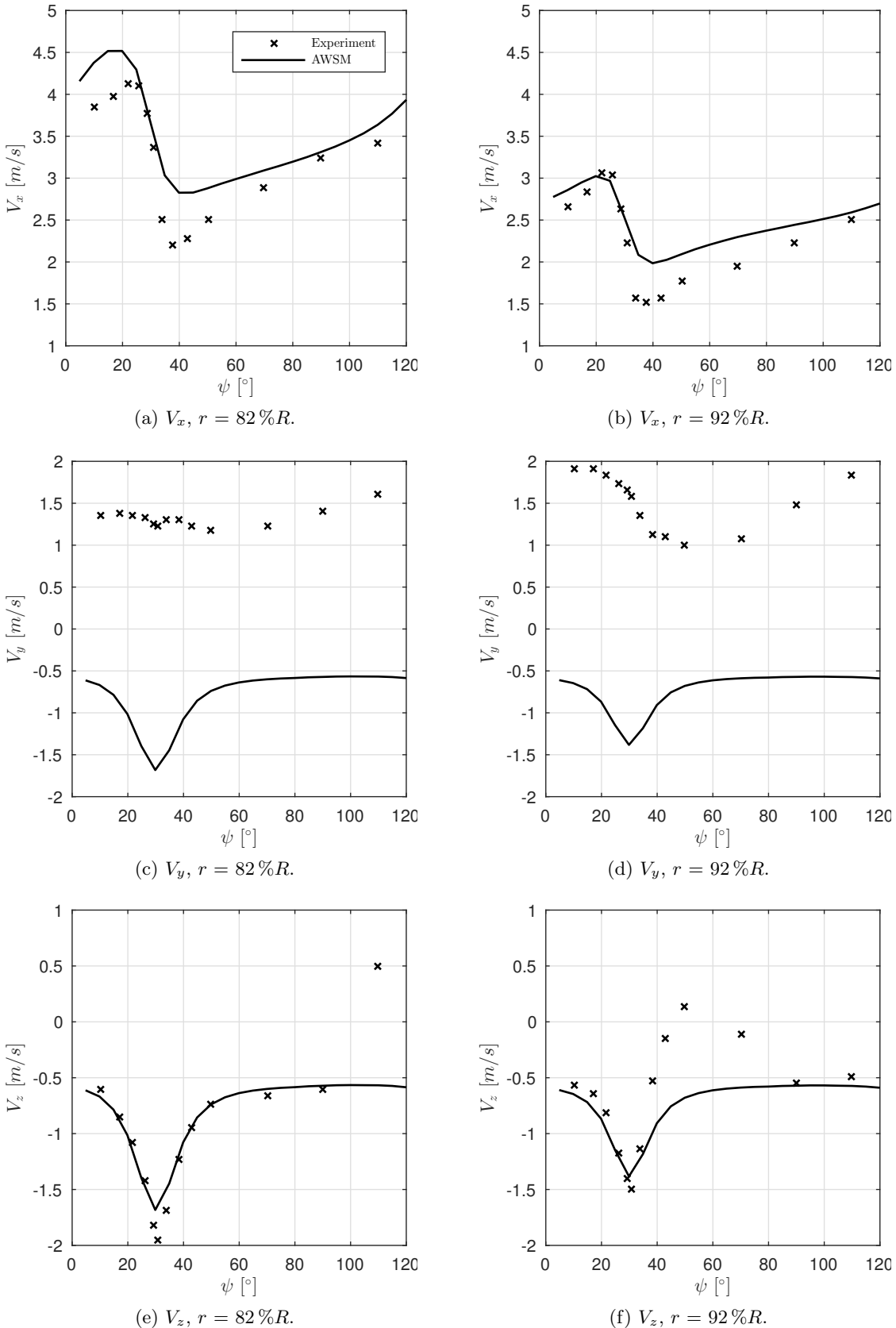


Figure B.5: Azimuthal traverse for 10 m/s at sections $r = 82\%R$ and $92\%R$ measured and computed downstream (0.30 m) and averaged over 13 rotor positions, with the blade passage at $\psi = 30^\circ$.

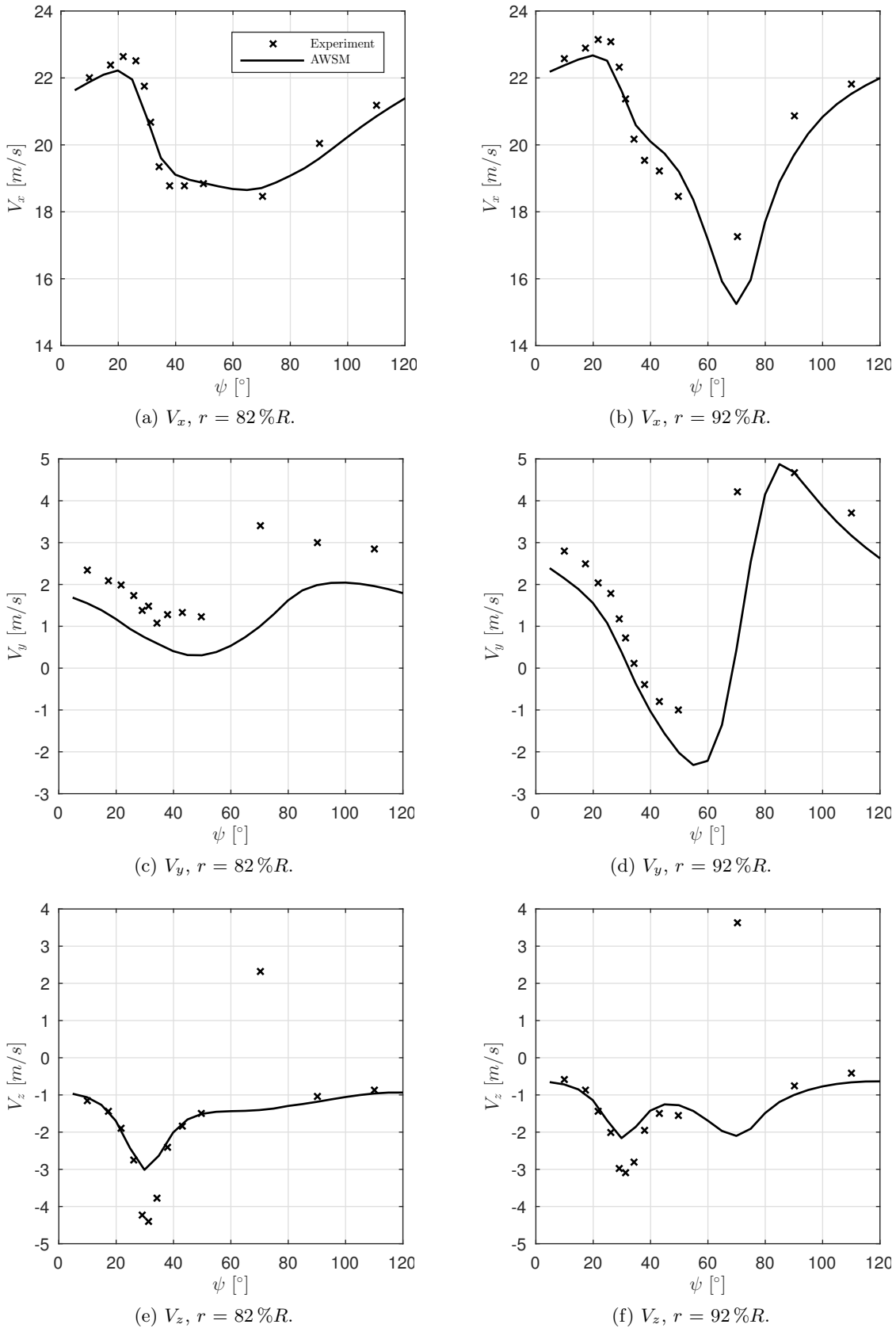


Figure B.6: Azimuthal traverse for 24 m/s at sections $r = 82\%R$ and $92\%R$ measured and computed downstream (0.30 m) and averaged over 13 rotor positions, with the blade passage at $\psi = 30^\circ$.

